19 June 2009 | $10

Science

AAAS

Biacore systems

from inspiration ...to publication

Highest quality, information-rich interaction data from Biacore™ systems deepen your understanding of molecular mechanisms and interaction pathways and enable you to add function to structure.

Select the perfect solution for your application and draw conclusions with confidence – from the company that continues to set the standard for label-free protein interaction analysis.

For further information or register to have one of our scientific experts contact you, please visit **www.gelifesciences.com/biacore-science**

Biacore T100
unmatched performance

Biacore X100
ready to run research system

Biacore Flexchip
array-based comparative profiling

imagination at work

The next BIG scientific breakthrough

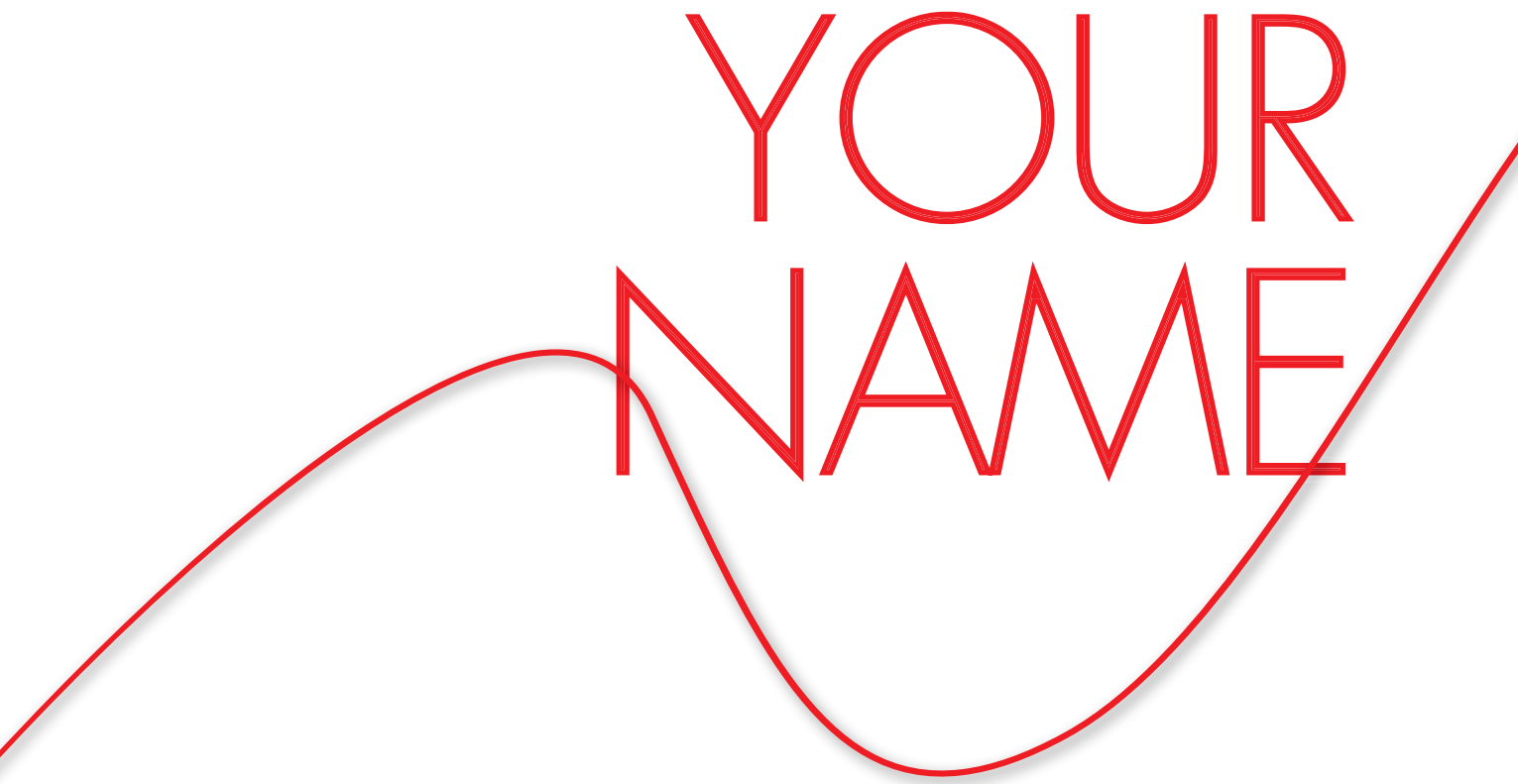

SIGMA® Life Science

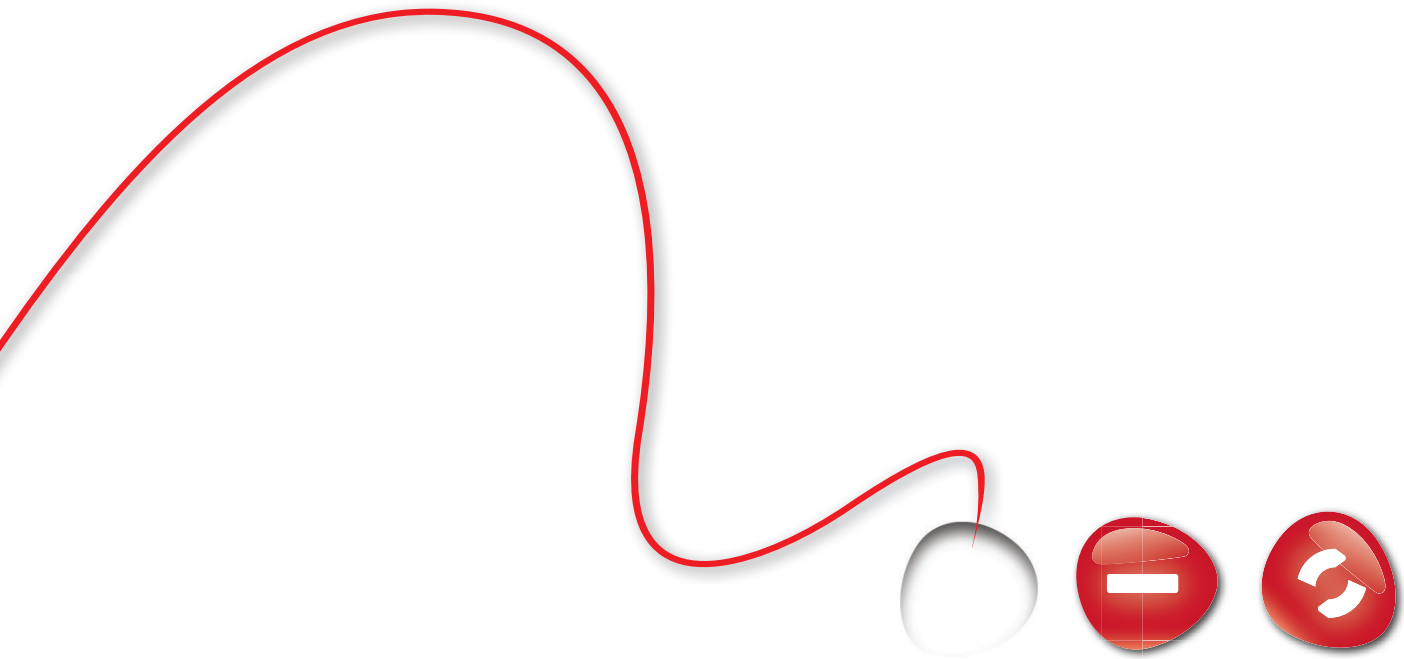

EDIT FOR THE BETTER.

What will be the next scientific breakthrough?

We can only tell you it's guaranteed to be a knockout.

CompoZr™ ZFN technology enables simple and efficient genomic editing and is offered exclusively from Sigma Life Science. Zinc Finger Nuclease (ZFN) technology allows easy creation of novel cell lines and model organisms with precise and heritable gene additions, deletions or modifications. A proven technology with unimaginable potential.

The future of genomic research is at your fingertips.
***Discover ZFN technology at* compozrzfn.com**

SIGMA-ALDRICH®

Coming Fourth Quarter 2009

A new journal from the publisher of *Science*, AAAS

Introducing *Science Translational Medicine*, the new journal from AAAS and *Science*.

This fall, AAAS and *Science* will launch *Science Translational Medicine*, a new journal focused on how basic research knowledge can be applied to positively impact human health.

The goal of *Science Translational Medicine* is simple: to help the scientific community harness decades of progress in basic research and translate these complex biological discoveries into medical advances.

Headed by Editor Katrina Kelner, Ph.D., and Chief Scientific Adviser, Elias Zerhouni, M.D., former Director of the NIH, the journal will feature original research articles, in-depth reviews, and commentary. Both in print and online, *Science Translational Medicine* promises a unique forum where biologists, engineers, chemists, and physicians can come together to exchange ideas and information.

Science Translational Medicine is now accepting manuscripts. To submit your work for consideration please visit: **www.sciencemag.org/marketing/stm/papers.dtl.**

For information on institutional or individual subscriptions, please contact **sciencemedicine@aaas.org**.

Science Translational Medicine
AAAS

www.ScienceTranslationalMedicine.org

EDITORIAL

NEWS OF THE WEEK

NEWS FOCUS

LETTERS

BOOKS *ET AL.*

POLICY FORUM

PERSPECTIVES

CONTENTS continued >>

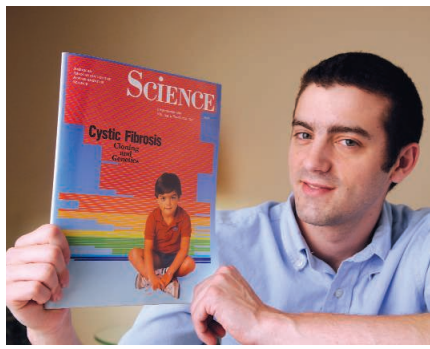

page 1504

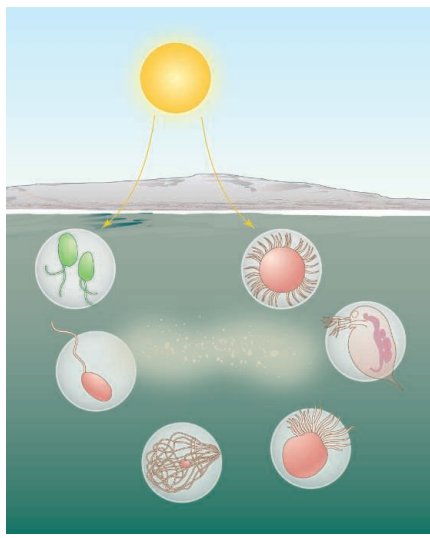

page 1521

COVER

The current global outbreak of influenza A (H1N1) in humans appears to have originated in Mexico from infected pigs. The cover portrait is of "Patient Zero" from La Gloria, Veracruz, who is now well. Fraser *et al*. (page 1557) report on an initial epidemiological analysis and offer baseline estimates for transmissibility while acknowledging the prevailing uncertainties at this early stage of the epidemic.

Photo: Erich Schlegel/Rapport/Newscom

DEPARTMENTS

Published by AAAS

Making improvements in life possible

QIAGEN is making improvements in life possible in:

- Molecular diagnostics
- Pharma
- Animal and veterinary testing
- Genetic identity and forensics
- Life science research

QIAGEN®

Sample & Assay Technologies

Corporate0109S1WW

REVIEW

BREVIA

RESEARCH ARTICLE

REPORTS

CONTENTS continued >>

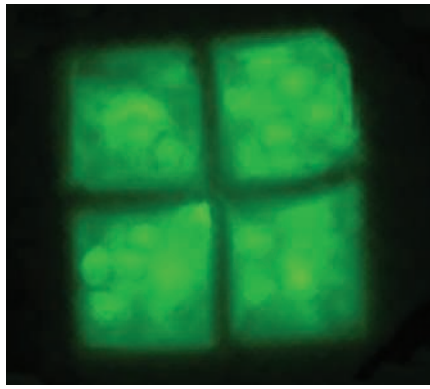

page 1523

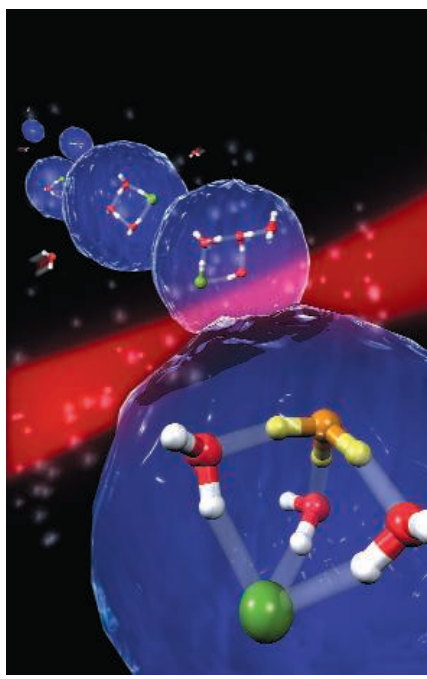

pages 1522 & 1545

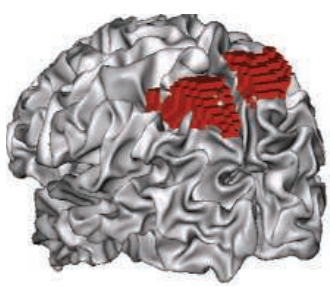

page 1583

Eppendorf Consumables – it's your sample

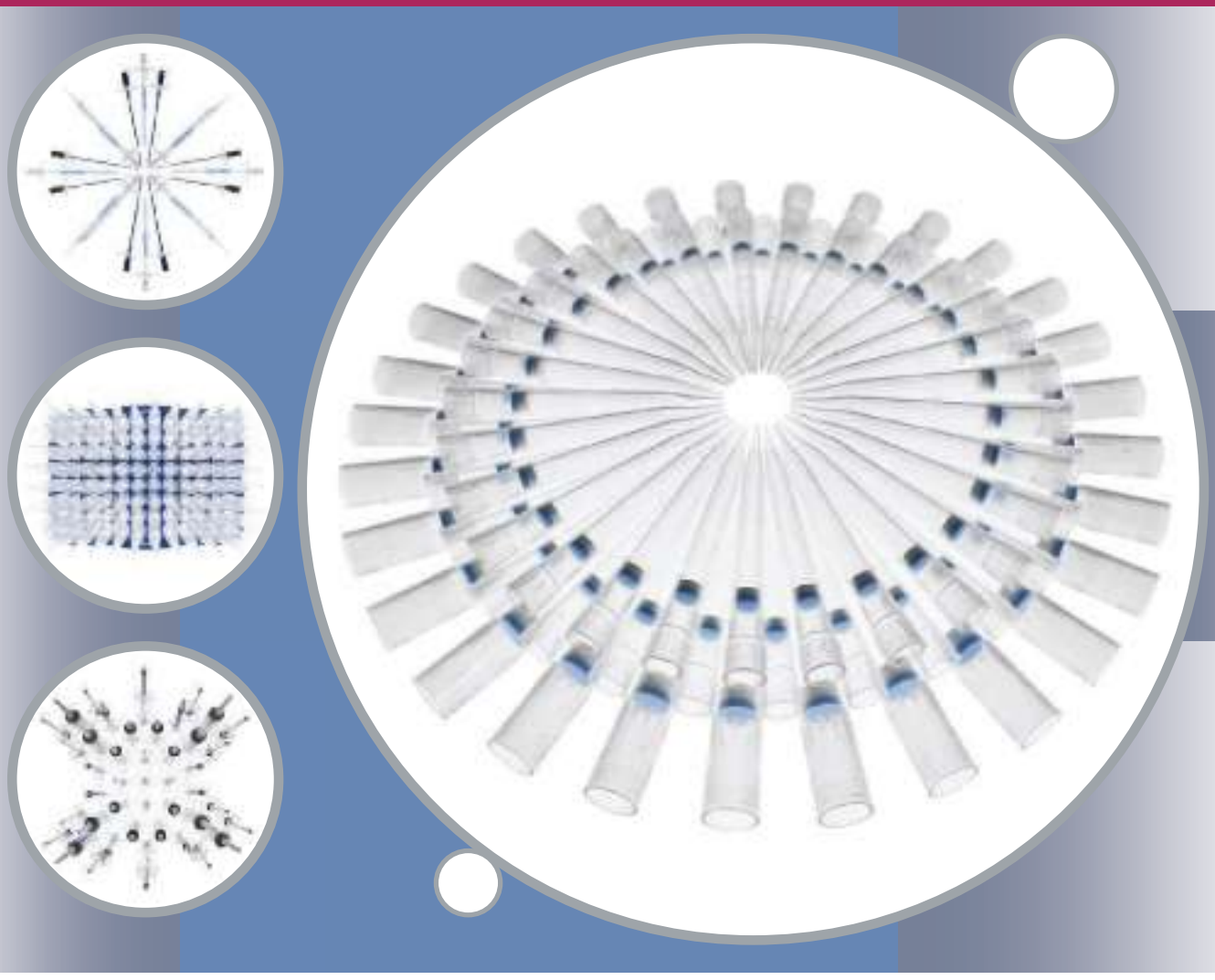

Make the best of it!

Top quality for your sample

Each of your valuable samples deserves the best treatment. See for yourself how the Eppendorf tips will save time and reduce costs.

With respect to material, fit, design and operating forces our tips set new standards. The close environment of each sample should be adapted to its specific quality and purity needs. This can involve a specific purity level or the absence of certain substances, but also stability, reliability, or geometry. The Eppendorf tips are designed to cover all of the specific needs of your samples!

Stop Aerosols! Eppendorf ep Dualfilter T.I.P.S.®

- Maximum protection of pipette and sample by our unique two phase filter technology
- Ultimate absorption of aerosols and biomolecules
- Free from PCR inhibiting additives and particles from the filter material itself

Learn more about Eppendorf ep Dualfilter T.I.P.S.®:
www.eppendorf.com/dualfilter
Learn more about Eppendorf consumables:
www.eppendorf.com/consumables

eppendorf

In touch with life

Your local distributor www.eppendorf.com/worldwide · **Application Support** E-Mail: support@eppendorf.com
Eppendorf AG · Hamburg · Germany · Tel: +49 40 538 01-0 · Eppendorf North America, Inc. · USA · Tel.: +1 800 645 3050

SCIENCEONLINE

SCIENCEXPRESS
www.sciencexpress.org

Successful Conservation of a Threatened *Maculinea* Butterfly
J. A. Thomas et al.

Prediction of population dynamics in relation to habitat requirements has led to a conservation success in the UK.
10.1126/science.1175726

Penumbral Structure and Outflows in Simulated Sunspots
M. Rempel et al.

Simulations of sunspots show that their structure and outflows can be understood in terms of convection in a magnetic field.
10.1126/science.1173798

Consistency Between Satellite-Derived and Modeled Estimates of the Direct Aerosol Effect
G. Myhre

Observational data and modeling narrows the large range of uncertainty about how much aerosols influence climate.
>> Science *Podcast*
10.1126/science.1174461

Functional Amyloids as Natural Storage of Peptide Hormones in Pituitary Secretory Granules
S. K. Maji et al.

Peptide and protein hormones are stored in secretory granules in a non-pathological amyloid conformation.
10.1126/science.1173155

Translocator Protein (18 kD) as Target for Anxiolytics Without Benzodiazepine-Like Side Effects
R. Rupprecht et al.

Possible drug alternative for rapid treatment of anxiety disorders could replace benzodiazepines.
10.1126/science.1175055

TECHNICALCOMMENTS

Comment on "Experimental Test of Self-Shielding in Vacuum Ultraviolet Photodissociation of CO"
J. R. Lyons et al.

full text at www.sciencemag.org/cgi/content/full/324/5934/1516-a

Comment on "Experimental Test of Self-Shielding in Vacuum Ultraviolet Photodissociation of CO"
S. R. Federman and E. D. Young

full text at www.sciencemag.org/cgi/content/full/324/5934/1516-b

Comment on "Experimental Test of Self-Shielding in Vacuum Ultraviolet Photodissociation of CO"
Q.-Z. Yin et al.

full text at www.sciencemag.org/cgi/content/full/324/5934/1516-c

Response to Comments on "Experimental Test of Self-Shielding in Vacuum Ultraviolet Photodissociation of CO"
S. Chakraborty et al.

full text at www.sciencemag.org/cgi/content/full/324/5934/1516-d

SCIENCENOW
www.sciencenow.org
Highlights From Our Daily News Coverage

Recipe for Life: Water and a Little Lava
Habitable planets require just the right amount of volcanism.

On the Road to a New Species
A small gene change is a big deal for an island bird.

Warp-Speed Raindrops
Some raindrops fall to the ground much faster than expected.

SCIENCESIGNALING
www.sciencesignaling.org
The Signal Transduction Knowledge Environment

RESEARCH ARTICLE: Suppression of LPS-Induced TNF-α Production in Macrophages by cAMP Is Mediated by PKA-AKAP95-p105
E. A. Wall et al.

PERSPECTIVE: Putting on the Brakes—Cyclic AMP as a Multipronged Controller of Macrophage Function
M. Peters-Golden

Distinct anchoring proteins enable cAMP signaling to selectively modulate macrophage responses to pathogens.

REVIEW: The Vitamin D Sterol–Vitamin D Receptor Ensemble Model Offers Unique Insights into Both Genomic and Rapid-Response Signaling
M. T. Mizwicki and A. W. Norman

Different vitamin D conformations binding to different pockets of a flexible receptor could elicit distinct responses.

PROTOCOL: Using a Microfluidic Device for High-Content Analysis of Cell Signaling
R. Cheong et al.

This method for analyzing individual cells reveals differences in responses masked by averaging across the population.

SCIENCECAREERS
www.sciencecareers.org/career_magazine
Free Career Resources for Scientists

Professional Polish
S. Webb

When dressing for a job interview, it pays to cultivate conformity and attention to detail.

Following in Darwin's Footsteps
E. Pain

Jordi Serrallonga has developed a career where research and travel are both adventures.

Tooling Up: Four Must-Haves for Convincing Communication
D. Jensen

Anyone can learn to communicate effectively by learning a few key points.

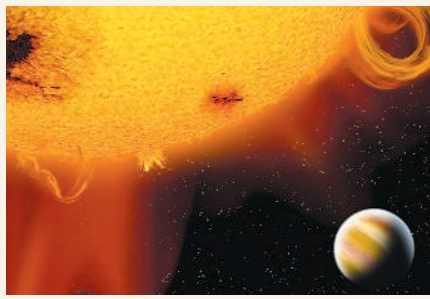

SCIENCENOW
Tidal forces need to be just right for life.

SCIENCESIGNALING
Single-cell analysis with microfluidics.

SCIENCEPODCAST
www.sciencemag.org/multimedia/podcast
Free Weekly Show

Download the 19 June *Science* Podcast to hear about narrowing in on aerosols' contribution to climate change, the latest in cystic fibrosis research, demystifying Merkel cells, and more.

ORIGINSBLOG
blogs.sciencemag.org/origins
A History of Beginnings

SCIENCEINSIDER
blogs.sciencemag.org/scienceinsider
Science Policy News and Analysis

SCIENCE (ISSN 0036-8075) is published weekly on Friday, except the last week in December, by the American Association for the Advancement of Science, 1200 New York Avenue, NW, Washington, DC 20005. Periodicals Mail postage (publication No. 484460) paid at Washington, DC, and additional mailing offices. The title SCIENCE is a registered trademark of the AAAS. Domestic individual membership and subscription (51 issues): $146 ($74 allocated to subscription). Domestic institutional subscription (51 issues): $835; Foreign postage extra: Mexico, Caribbean (surface mail) $55; other countries (air assist delivery) $85. First class, airmail, student, and emeritus rates on request. Canadian rates with GST available upon request, GST #1254 88122. Publications Mail Agreement Number 1069624. **Printed in the U.S.A.**

Change of address: Allow 4 weeks, giving old and new addresses and 8-digit account number. **Postmaster:** Send change of address to AAAS, P.O. Box 96178, Washington, DC 20090–6178. **Single-copy sales:** $10.00 current issue, $15.00 back issue prepaid includes surface postage; bulk rates on request. **Authorization to photocopy** material for internal or personal use under circumstances not falling within the fair use provisions of the Copyright Act is granted by AAAS to libraries and other users registered with the Copyright Clearance Center (CCC) Transactional Reporting Service, provided that $20.00 per article is paid directly to CCC, 222 Rosewood Drive, Danvers, MA 01923. The identification code for *Science* is 0036-8075. *Science* is indexed in the *Reader's Guide to Periodical Literature* and in several specialized indexes.

AAAS
ADVANCING SCIENCE, SERVING SOCIETY

Published by AAAS

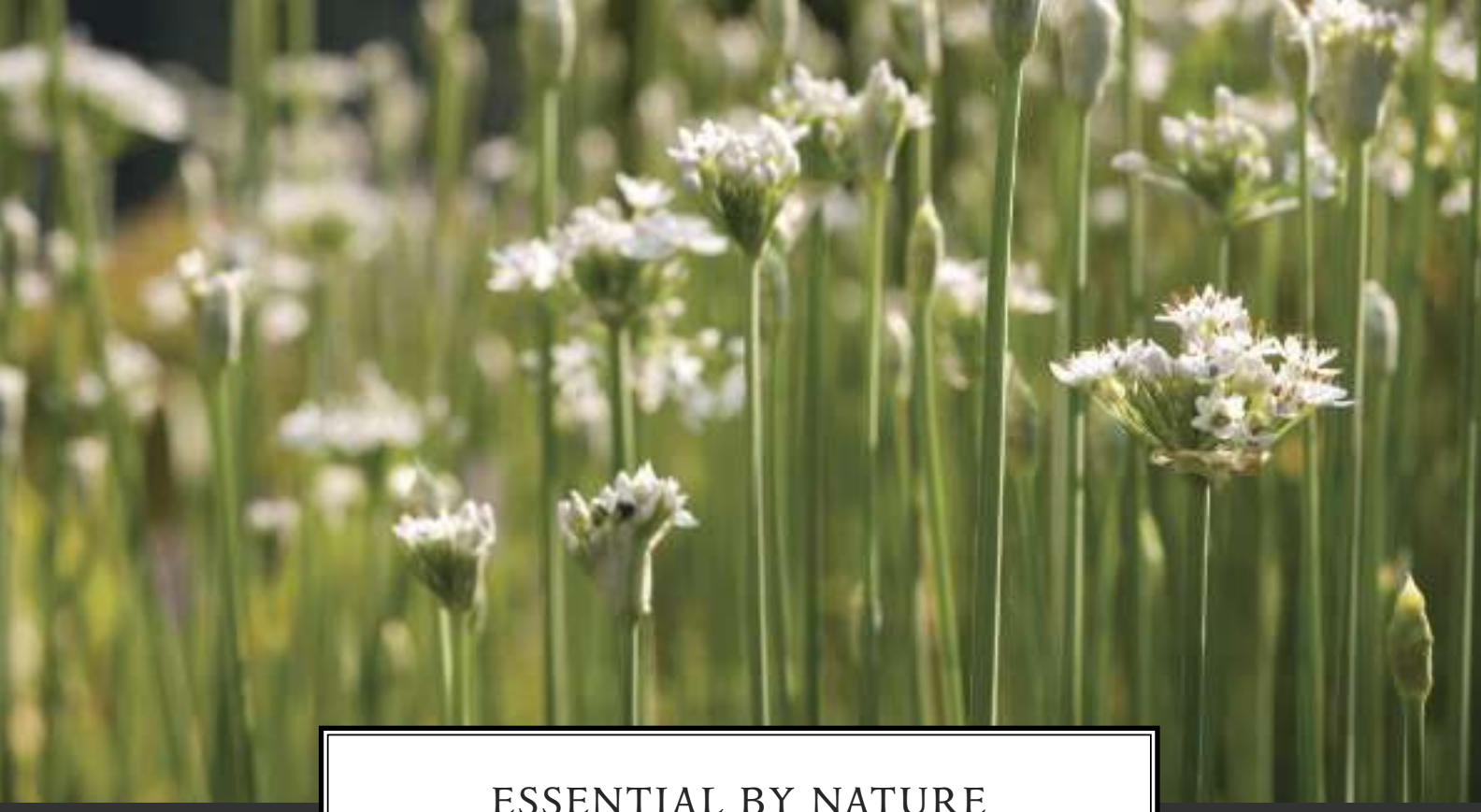

ESSENTIAL BY NATURE

The 2009|10 NEB Catalog & Technical Reference

This year's catalog features minireviews focused on renewable energy generated from natural resources.

Highlights

- High Fidelity (HF) Restriction Enzymes - the next generation in restriction enzyme technology
- A comprehensive offering of PCR reagents
- The latest innovation in competent cells for protein expression
- An extensive selection of markers and ladders for DNA, RNA and protein
- A new gene expression and cellular analysis section showcasing a powerful protein labeling technology unique to NEB
- A range of expression systems, including a novel kit for cell-free expression
- Tools for glycobiology
- Tools to enable RNA research
- A substantial technical reference section

To request a copy, visit www.neb.com

NEW ENGLAND BioLabs® Inc.
enabling technologies in the life sciences

CLONING & MAPPING	DNA AMPLIFICATION & PCR	RNA ANALYSIS	PROTEIN EXPRESSION & ANALYSIS	GENE EXPRESSION & CELLULAR ANALYSIS

www.neb.com

Extinction Distinction

The Triassic-Jurassic extinction approximately 200 million years ago is one of the five major extinctions in Earth's history. It has been primarily recognized through the loss of marine species, as well as the subsequent emergence of dinosaurs, but its pace, both on land and in sea, has been unclear. **McElwain *et al.*** (p. 1554) now provide evidence from the plant fossil record from rocks in East Greenland. The total number of taxa and the number of common taxa decreased across the extinction boundary. The decrease was fairly abrupt and seemed to coincide with a period with increased atmospheric CO_2 levels.

Sensorin Reporter

Long-term memory and synaptic plasticity require changes in gene expression and yet can occur in a synapse-specific manner. Messenger RNA (mRNA) localization and regulated translation at synapses have been proposed as mechanisms for spatially restricting gene expression during transcription-dependent, synapse-specific forms of neuronal plasticity. In the sea slug *Aplysia*, which is a frequently used model system for studying learning and memory, sensorin is a sensory cell–specific peptide neurotransmitter. The mRNA encoding sensorin localizes to distal sensory neurites and further concentrates at sites of synaptic contact between sensory and motor neurons. **Wang *et al.*** (p. 1536, published online 14 May; see the Perspective by **Korte**) demonstrate, using translational reporters of sensorin mRNA expressed in individual cultured *Aplysia* sensory and motor neurons, that local translation occurs at synapses during transcription-dependent, learning-related forms of synaptic plasticity.

Star Gazing

Seismology of stars provides a unique insight into physical mechanisms taking place in their interior. Like the Sun, some stars have low-amplitude pulsations that are excited by turbulent convection in their outer layers. **Belkacem *et al.*** (p. 1540), using data gathered by the CoRoT satellite, report on low-amplitude, solar-like oscillations in a massive star that undergoes radial pulsations as a result of expanding and contracting layers in its interior. The finding opens the possibility of probing the interiors of this type of massive star, which can be the progenitors of supernovae.

Minimally Acidic

Acidity is usually construed in the context of a bulk liquid solvent: billions of trillions of molecules such as HCl, added to hundreds of billions of trillions of water molecules. What happens under sparser conditions, for example, in atmospheric or interstellar environments, when a single HCl molecule might interact with just three or four water molecules? **Gutberlet *et al.*** (p. 1545; see the Perspective by **Zwier**) explored this question using theoretical simulations together with vibrational spectroscopy in ultracold helium droplets that effectively isolated small aqueous HCl clusters. HCl remained intact upon solvation by one, two, or three water molecules. Dissociation into an ion pair, as occurs in bulk water, required the approach of a fourth water molecule and was facilitated by the geometry of the existing $(H_2O)_3$ cluster.

Reaping Gain from Decay

In photovoltaic devices, absorbed light excites electrons into a conduction band and thereby initiates electric current flow. Unfortunately, if the energy of the incident photons exceeds the threshold for this excitation (the bandgap), the excess tends to be wasted. Initially, a photon bearing several multiples of the bandgap energy may correspondingly promote several electrons, but before these can begin to travel through a circuit, most of them drop back down to the immobile state, transferring their packet of energy to a lone remaining carrier in a process termed "Auger decay." **Sukhovatkin *et al.*** (p. 1542) show that a photoconductive device design can actually leverage the Auger decay process to improve sensitivity in ultraviolet detection. Their detector, a thin film assembled from lead sulfide quantum dots, improves its response by up to a factor of four when the incident light frequency rises to several multiples of the bandgap.

Expanding Flatland

Since its discovery and isolation some 5 years ago, research on graphene has exploded. The sheets of carbon atoms, just one atom thick, exhibit a vast array of properties—mechanical, optical, and electrical—that make it an ideal test bed to probe fundamental problems in physics, as well as lending itself to a wide portfolio of applications. **Geim** (p. 1530), the discoverer of this remarkable material, reviews recent advances and discusses what other developments may be in store for this material.

A Change in the Air?

Between around 1.2 million and 500,000 years ago, Earth's glacial cycle changed from one with a period of roughly 40,000 years to one with a period of about 100,000 years. Although there has been much speculation about why this transition may have occurred, no potential explanation seemed more likely than that it was caused by decreasing concentrations of atmospheric CO_2. **Hönisch *et al.*** (p. 1551) present a record of atmospheric pCO_2 for the past 2.1 million years, derived from the boron isotopic composition of planktonic foraminifera, and show that the amount of CO_2 in the atmosphere has remained relatively constant over that period. While pCO_2

Continued on page 1490

CREDITS (TOP TO BOTTOM): MARLENE HILL-DONNELLY/FIELD MUSEUM; KOSTYA NOVOSELOV

This Week in *Science*

Continued from page 1489

was approximately 30 ppm higher before the start of the mid-Pleistocene transition than after the transition, atmospheric CO_2 did not decrease gradually as would be expected were it to be the driver of the transition.

Antiporter Antics

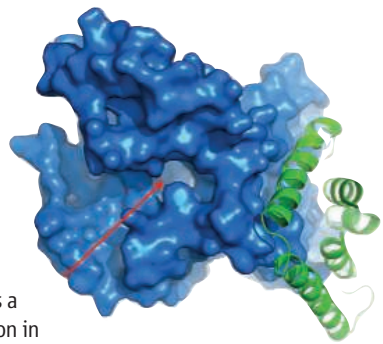

Bacteria that survive in the acidic environment of the stomach have mechanisms to maintain a high intracellular pH. In *Escherichia coli*, glutamate (Glu) and arginine (Arg) are decarboxylated intracellularly and the reaction products are exchanged with extracellular Glu and Arg. **Gao *et al.*** (p. 1565, published online 28 May) now report a crystal structure of AdiC, an arginine:agmatine antiporter from *E. coli*. AdiC exhibits the same fold as that of the Na^+-coupled symporters, including LeuT. It contains 12 transmembrane segments, forms a homodimer, and exists in an outward-facing, open conformation in the crystals. The structure, together with biochemical data, suggests how the antiporter senses the pH and responds to transport the reaction product agmatine out of the cell and Arg into the cell.

Controlling Chronic Viral Infections

Chronic viral infections such as HIV and hepatitis B and C viruses are major public health concerns. T cell–mediated immune responses are critical for controlling viral infections. In contrast to acute infections, chronic viral infections are characterized by "exhausted" cytotoxic $CD8^+$ T cells, cells which exhibit reduced proliferative capacity, cytokine secretion, and cytotoxicity. Treatments that reverse exhaustion result in increased viral control. Despite their exhaustion, these $CD8^+$ T cells eventually help to control chronic infections by killing virally infected cells, and require $CD4^+$ T cell help to do so. How do $CD4^+$ T cells provide help to $CD8^+$ T cells during chronic infection (see the Perspective by **Johnson and Jameson**)? **Elsaesser *et al.*** (p. 1569, published online 7 May), **Yi *et al.*** (p. 1572, published online 14 May), and **Fröhlich *et al.*** (p. 1576, published online 28 May) now show that the cytokine, interleukin-21 (IL-21), known to be critical for the differentiation of certain $CD4^+$ T cell effector subsets, is an essential factor produced by $CD4^+$ T cells that helps $CD8^+$ T cells to control chronic lymphocytic choriomeningitis virus infection in mice. Acute and chronic infections resulted in differing amounts of IL-21 production by virus-specific $CD4^+$ T cells. $CD8^+$ T cells required IL-21 directly, and when $CD8^+$ T cells were unable to signal through IL-21 or IL-21 was not available, they were reduced in number, exhibited a more exhausted phenotype, and were not able to control the virus. In contrast, the absence of IL-21–dependent signaling did not affect primary $CD8^+$ T cell responses to acute infection or responses to a viral rechallenge, suggesting that differentiation of memory $CD8^+$ T cells is independent of IL-21.

Mysterious Merkel cells

Anatomists have known about the existence of Merkel cells in our skin for over a century. However, the function of these cells has been unclear and controversial. To solve this mystery, **Maricich *et al.*** (p. 1580) created a genetic deletion of Merkel cells. When Atoh1, a transcription factor expressed by Merkel cells, was conditionally deleted in the skin, Merkel cells were completely absent from Atoh1CKO mice. Using ex vivo skin and nerve preparations from the animals showed that Merkel cells are needed to properly encode light touch sensation in the skin.

Addition to the Right, Subtraction to the Left

High-level cognitive achievements, such as writing and mathematics, have appeared relatively recently in the evolutionary record in comparison to low-level skills, such as the perception of bright-dark boundaries. The latter have been demonstrated to arise from the coding properties of neurons in visual cortical centers, but what do the former map onto? **Knops *et al.*** (p. 1583, published online 7 May) provide evidence that addition and subtraction are encoded within the same cortical region that is responsible for eye movements to the right and left, such that the neural activity associated with addition could be distinguished from that associated with subtraction by a computational classifier trained to discriminate between rightward and leftward eye movements.

CREDIT: GAO *ET AL.*

Cristine Russell is a senior fellow at Harvard's Belfer Center for Science and International Affairs and president of the Council for the Advancement of Science Writing. E-mail: russellcris@nasw.org

Science Journalism Goes Global

WHEN SWINE FLU STRUCK SWIFTLY IN MEXICO, IT CREATED A CHALLENGE NOT ONLY FOR international public health officials but also for journalists around the world assigned to follow the unfolding story. They needed to explain, in the face of great uncertainty and a nonstop news cycle, what the novel influenza A (H1N1) virus was and the potential dangers it posed. It was a difficult story handled most capably by experienced health and science reporters.

Swine flu is the latest in a string of important global stories across the spectrum of science: stem cell research, the human genome, climate change, new energy technologies, evolution, space exploration, and HIV/AIDS, to name a few.

At a time when global science-based stories such as these are more prevalent than ever, international science journalism faces both great opportunities and great peril. A sense of crisis has gripped the American science writing community, as traditional staff jobs in mainstream print and electronic media have increasingly fallen victim to hard economic times. Content has also shifted toward "science-lite," with consumer health and fitness often trumping important developments in scientific research and policy. Similar problems have arisen in Canadian, United Kingdom, and European science journalism.

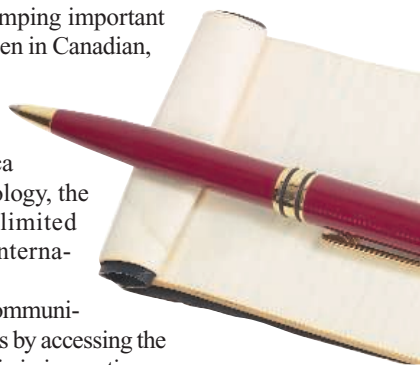

There is growing excitement, however, about emerging opportunities for global expansion of science journalism, particularly in developing countries. Reporters in Asia, Africa, the Middle East, and Latin America report increasing demand for local stories involving science and technology, the environment, and public health. Although they may struggle with limited resources and political obstacles, they are eager to join the ranks of international science writers.

For journalists from Boston to Beijing, the rapidly changing world of communication technology also offers myriad multimedia options for crossing borders by accessing the latest science, interviewing experts, mining research, and reaching the public in innovative ways. While these new tools—blogs, podcasts, Skype, Facebook, YouTube, and Twitter—offer creative outlets, mindless chatter can gobble up precious time. Countless new Web sites provide a dizzying array of science information, misinformation, and commentary that can be hard to sort through. These sites also run the risk of preaching to the converted and subdividing the audience in ways that may narrow the science knowledge base and reinforce uninformed opinion.

In the face of this changing media landscape, journalism and science organizations need to explore better ways to train reporters, scientists, and other communicators around the world in the substance and process of science writing. In doing so, it is crucial that the old-fashioned virtues of good journalism—accurate information, multiple sources, context over controversy, and editorial independence—not be lost in the enthusiasm for communicating content in novel ways.

Opportunities for professional development of international journalists are expanding. Mid-career journalism programs at places such as Harvard, the University of California, and the Massachusetts Institute of Technology seek fellows from around the world. The Gates Foundation funds training and travel programs to improve global health coverage in Africa, while international nonprofit groups train reporters from developing regions in global climate change reporting. American science journalists have an ongoing partnership with Arab journalists that widens the horizons of both groups.

Perhaps the best evidence of the growing international nature of this field is the upcoming 6th World Conference of Science Journalists, which is expected to draw about 600 attendees from 70 countries to London later this month. Organized by British science writers working with the World Federation of Science Journalists, a 6-year-old network of 40 science journalism groups, the conference builds skills in covering science and policy, from theoretical physics to food security, while providing a forum for examining common concerns and actions to improve the quality and quantity of science journalism.

Hopefully, the recent crisis in science journalism in Western countries will be tempered by optimism about the overall future of international science journalism and the importance of reaching a global public in dire need of the best science and technology information.

– Cristine Russell

10.1126/science.1176995

Published by AAAS

Submission deadline August 1

"It's truly exhilarating to be recognized for your hard work. This prize will motivate young generations of scientists and encourage new discoveries."

Dr. Christine Jacobs-Wagner
Grand Prize winner 1997

The GE & Science Prize for Young Life Scientists. Rewarding brilliance since 1995.

Imagine standing on the podium at the Grand Hotel in Stockholm, making your acceptance speech. Imagine joining the ranks of those published in Science magazine and having your essay on your work in molecular biology read by your peers around the world. Imagine taking part in a seminar with the other Prize winners and Nobel Prize laureates and discussing your work with leaders in the field. Imagine what you could do with the US$25,000 prize money. Imagine this brilliant start to your career and where it could lead you. Now stop imagining, and make it a reality.

Dr. Christine Jacobs-Wagner did just that. In 1997, she entered in the GE & Science Prize for Young Life Scientists and won the grand prize. So why not you? If you are one of those who were awarded a Ph.D in 2008, then submit your 1000-word essay by August 1, 2009. Your brilliant idea could well be on its way to building a better reality, for you and for those around you.

All the information you need awaits you at: www.gelifesciences.com/science

GE & Science Prize for Young Life Scientists

imagination at work

Science AAAS

For the purpose of this prize, molecular biology is defined as "that part of biology which attempts to interpret biological events in terms of the physico-chemical properties of molecules in a cell".

(McGraw-Hill Dictionary of Scientific and Technical Terms, 4th Edition).

ECOLOGY

Wetting One's Appetite

Ecological studies of food webs and their resources tend to focus on the limited availability of and competition for nutrients and energy. In some systems, however, water may exert an important influence on species interactions. McCluney and Sabo have investigated the impact of distinct water regimes on ecological systems in the San Pedro River in southern Arizona. In a field setting, they furnished cages containing field crickets with an ample supply of cottonwood and willow leaves, and they varied two factors: the presence/absence of wolf spiders (which prey on crickets) and mesic/xeric conditions. They found that when water was scarce, crickets consumed significantly more green leaves, rather than old litter, and experienced significantly higher mortality, presumably due to wolf spider predation, in comparison to cages lacking spiders. In contrast, in cases of rainfall or when water was provided, the cricket-spider interaction strength diminished almost to zero, suggesting that crickets were more important as a source of water than as nutrient. These data indicate that in some ecosystems, interactions between species can differ depending on water availability, and thus the local effects of global climate change—including derived aridification, droughts, and increases in precipitation—may alter food webs significantly. — LMZ

Ecology **90**, 1463 (2009).

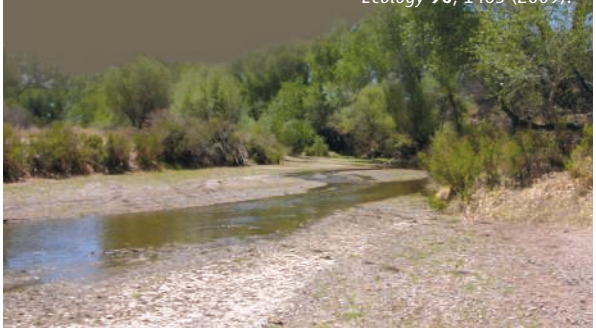

CREDITS (LEFT TO RIGHT): KEVIN MCCLUNEY; SCHÖFFEL *ET AL.*, *ANGEW. CHEM. INT. ED.* **48**, 4734 (2009)

CHEMISTRY

A Late Triple

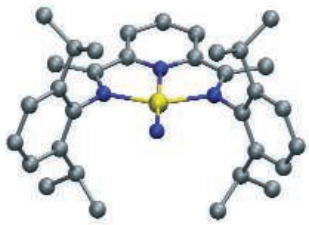

Transition metals with comparatively few valence electrons, such as titanium and chromium, tend to form multiple bonds with carbon, oxygen, and nitrogen (N) atoms fairly easily. In contrast, late metals such as iridium (Ir) and platinum engage more rarely in this mode of bonding, an observation that has been justified by repulsive interactions between the ligand's lone pairs and residual *d* orbital electrons at the metal center. Schöffel *et al.* show that mild heating of an azide-substituted Ir complex in the solid state leads efficiently to N_2 loss and resultant formation of a stable Ir-N triple bond. The compound was characterized crystallographically, and the observed bond length, coupled with in-depth theoretical analysis, supports a formal bond order between 2 and 3. Reaction with hydrogen led to very clean direct reduction at nitrogen, forming an Ir amide complex that was also structurally characterized by x-ray diffraction. An isotopic labeling study confirmed H_2 as the proton source. — JSY

Angew. Chem. Int. Ed. **48**, 4734 (2009).

VIROLOGY

Lessons from the Pros

Human cells contain tens of thousands of protein-encoding genes that are transcribed into a much larger numbers of mRNAs. Viruses, on the other hand, are far simpler, carrying with them only a handful of genes and proteins, yet they have developed countless ways of hijacking specific host cellular functions for their own benefit. Discovering these survival mechanisms often offers fascinating insights into normal host cell biology. Eukaryotes use sophisticated ways of regulating gene expression, including polyadenylating the 3′ end of mRNAs to enhance their stability for eventual translation into protein, and possibly also to promote mRNA degradation. Some herpesviruses, including Kaposi's sarcoma–associated herpesvirus (KSHV), manipulate host cells by promoting the widespread destruction of cellular mRNAs. KSHV achieves this via its Sox protein, and Lee and Glaunsinger show that human cells expressing the viral Sox protein contain mRNAs with unusually long poly(A) tails (hyperadenylation), which was mediated by the host enzyme poly(A) polymerase II. This effect of viral Sox was linked to its ability to accelerate mRNA turnover, suggesting that the virus induces host mRNA degradation by modulating poly(A) length. — HP

PLoS Biol. **7**, e1000107 (2009).

CHEMISTRY

Lining up for Photos

Transient diffraction techniques can be used in the gas phase to probe molecules in the midst of transformation, but structural information is limited by the random orientation of the sample. In contrast, static diffraction techniques applied to crystals that keep the constituent molecules well aligned can provide exquisite three-dimensional structures. Reckenthaeler *et al.* show that ultrafast optical methods can begin to bridge these two limiting cases. The authors use femtosecond laser pulses to dissociate gas phase diiodotetrafluoroethane molecules, creating a C_2F_4I ensemble briefly aligned on account of the laser polarization. Before the alignment is lost, a short pulse of electrons is fired through the sample, allowing the determination of transient molecular structure. Because the alignment persists for several picoseconds, the method may offer the opportunity to study a range of more complex molecular structures and dynamics. — ISO

Phys. Rev. Lett. **102**, 213001 (2009).

www.sciencemag.org

Science

1200 New York Avenue, NW
Washington, DC 20005
Editorial: 202-326-6550, FAX 202-289-7562
News: 202-326-6581, FAX 202-371-9227
Bateman House, 82-88 Hills Road
Cambridge, UK CB2 1LQ
+44 (0) 1223 326500, FAX +44 (0) 1223 326501

Subscription Services For change of address, missing issues, new orders and renewals, and payment questions: 866-434-AAAS (2227) or 202-326-6417, FAX 202-842-1065. Mailing addresses: AAAS, P.O. Box 96178, Washington, DC 20090-6178 or AAAS Member Services, 1200 New York Avenue, NW, Washington, DC 20005

Institutional Site Licenses please call 202-326-6755 for any questions or information

Reprints: Author Inquiries 800-635-7181
Commercial Inquiries 803-359-4578

Permissions 202-326-7074, FAX 202-682-0816

Member Benefits AAAS/Barnes&Noble.com bookstore www.aaas.org/bn; AAAS Online Store www.apisource.com/aaas/ code MKB6; AAAS Travels: Betchart Expeditions 800-252-4910; Apple Store www.apple/eppstore/aaas; Bank of America MasterCard 1-800-833-6262 priority code FAA3YU; Cold Spring Harbor Laboratory Press Publications www.cshlpress.com/affiliates/aaas.htm; GEICO Auto Insurance www.geico.com/landingpage/go51.htm?logo=17624; Hertz 800-654-2200 CDP#343457; Office Depot https://bsd.officedepot.com/portalLogin.do; Seabury & Smith Life Insurance 800-424-9883; Subaru VIP Program 202-326-6417; VIP Moving Services www.vipmayflower.com/domestic/index.html; Other Benefits: AAAS Member Services 202-326-6417 or www.aaasmember.org.

science_editors@aaas.org	(for general editorial queries)
science_letters@aaas.org	(for queries about letters)
science_reviews@aaas.org	(for returning manuscript reviews)
science_bookrevs@aaas.org	(for book review queries)

Published by the American Association for the Advancement of Science (AAAS), *Science* serves its readers as a forum for the presentation and discussion of important issues related to the advancement of science, including the presentation of minority or conflicting points of view, rather than by publishing only material on which a consensus has been reached. Accordingly, all articles published in *Science*—including editorials, news and comment, and book reviews—are signed and reflect the individual views of the authors and not official points of view adopted by AAAS or the institutions with which the authors are affiliated.

AAAS was founded in 1848 and incorporated in 1874. Its mission is to advance science, engineering, and innovation throughout the world for the benefit of all people. The goals of the association are to: enhance communication among scientists, engineers, and the public; promote and defend the integrity of science and its use; strengthen support for the science and technology enterprise; provide a voice for science on societal issues; promote the responsible use of science in public policy; strengthen and diversify the science and technology workforce; foster education in science and technology for everyone; increase public engagement with science and technology; and advance international cooperation in science.

Information for Authors
See pages 807 and 808 of the 6 February 2009 issue or access www.sciencemag.org/about/authors

EDITOR-IN-CHIEF **Bruce Alberts**
EXECUTIVE EDITOR **Monica M. Bradford**
NEWS EDITOR **Colin Norman**
MANAGING EDITOR, RESEARCH JOURNALS **Katrina L. Kelner**
DEPUTY EDITORS **R. Brooks Hanson, Barbara R. Jasny, Andrew M. Sugden**

Editorial senior editor/perspectives Lisa D. Chong; **senior editors** Gilbert J. Chin, Pamela J. Hines, Paula A. Kiberstis (Boston), Marc S. Lavine (Toronto), Beverly A. Purnell, L. Bryan Ray, Guy Riddihough, H. Jesse Smith, Phillip D. Szuromi (Tennessee), Valda Vinson; **associate editors** Kristen L. Mueller, Nicholas S. Wigginton, Jake S. Yeston, Laura M. Zahn; **online editor** Stewart Wills; **associate online editors** Robert Frederick, Tara S. Marathe; **web content developer** Martyn Green; **book review editor** Sherman J. Suter; **associate letters editor** Jennifer Sills; **editorial manager** Cara Tate; **senior copy editors** Jeffrey E. Cook, Cynthia Howe, Harry Jach, Barbara P. Ordway, Trista Wagoner; **copy editors** Chris Filiatreau, Lauren Kmec; **editorial coordinators** Carolyn Kyle, Beverly Shields; **publications assistants** Ramatoulaye Diop, Carlos L. Durham, Joi S. Granger, Jeffrey Hearn, Lisa Johnson, Scott Miller, Jerry Richardson, Jennifer A. Seibert, Brian White, Anita Wynn; **editorial assistants** Emily Guise, Michael Hicks, Patricia M. Moore; **executive assistant** Sylvia S. Kihara; **administrative support** Maryrose Madrid

News deputy news editors Robert Coontz, Eliot Marshall, Jeffrey Mervis, Leslie Roberts; **contributing editors** Elizabeth Culotta, Polly Shulman; **news writers** Yudhijit Bhattacharjee, Adrian Cho, Jennifer Couzin, David Grimm, Constance Holden, Jocelyn Kaiser, Richard A. Kerr, Eli Kintisch, Andrew Lawler (New England), Greg Miller, Elizabeth Pennisi, Robert F. Service (Pacific NW), Erik Stokstad; **intern** Jackie D. Grom; **contributing correspondents** Dan Charles, Jon Cohen (San Diego, CA), Daniel Ferber, Ann Gibbons, Robert Koenig, Mitch Leslie, Charles C. Mann, Virginia Morell, Evelyn Strauss, Gary Taubes; **copy editors** Linda B. Felaco, Melvin Gatling, Melissa Raimondi; **administrative support** Scherraine Mack, Fannie Groom; **bureaus** New England: 207-549-7755, San Diego, CA: 760-942-3252, FAX 760-942-4979, Pacific Northwest: 503-963-1940

Production director James Landry; **senior manager** Wendy K. Shank; **assistant manager** Rebecca Doshi; **senior specialists** Steve Forrester, Chris Redwood; **specialist** Anthony Rosen; **Preflight director** David M. Tompkins; **manager** Marcus Spiegler; **specialist** Jason Hillman

Art director Yael Kats; **associate art director** Laura Creveling; **illustrators** Chris Bickel, Katharine Sutliff; **senior art associates** Holly Bishop, Preston Huey, Nayomi Kevitiyagala; **art associates** Jessica Newfield, Matthew Twombly; **photo editor** Leslie Blizard

***Science* International**

Europe (science@science-int.co.uk) **editorial: international managing editor** Andrew M. Sugden; **senior editor/perspectives** Julia Fahrenkamp-Uppenbrink; **senior editors** Caroline Ash, Stella M. Hurtley, Ian S. Osborne, Peter Stern; **associate editor** Maria Cruz; **locum editor** Helen Pickersgill; **editorial support** Deborah Dennison, Rachel Roberts, Alice Whaley; **administrative support** John Cannell, Janet Clements, Louise Moore; **news: europe news editor** John Travis; **deputy news editor** Daniel Clery; **contributing correspondents** Michael Balter (Paris), John Bohannon (Vienna), Martin Enserink (Amsterdam and Paris), Gretchen Vogel (Berlin); **intern** Claire Thomas

Asia Japan Office: Asca Corporation, Eiko Ishioka, Fusako Tamura, 1-8-13, Hirano-cho, Chuo-ku, Osaka-shi, Osaka, 541-0046 Japan; +81 (0) 6 6202 6272, FAX +81 (0) 6 6202 6271; asca@os.gulf.or.jp; **asia news editor** Richard Stone (Beijing: rstone@aaas.org); **contributing correspondents** Dennis Normile (Japan: +81 (0) 3 3391 0630, FAX +81 (0) 3 5936 3531; dnormile@gol.com); Hao Xin (China: +86 (0) 10 6307 4439 or 6307 3676, FAX +86 (0) 10 6307 4358; cindyhao@gmail.com); Pallava Bagla (South Asia: +91 (0) 11 2271 2896; pbagla@vsnl.com)

EXECUTIVE PUBLISHER **Alan I. Leshner**
PUBLISHER **Beth Rosner**

Fulfillment Systems and Operations (membership@aaas.org); **director** Waylon Butler; **senior systems analyst** Nomuna Nyamaa; **customer service supervisor** Pat Butler; **specialists** Latoya Casteel, LaVonda Crawford, Vicki Linton, April Marshall; **data entry supervisor** Cynthia Johnson; **specialists** Shirlene Hall, Tarrika Hill, William Jones

Business Operations and Administration director Deborah Rivera-Wienhold; **assistant director, business operations** Randy Yi; **manager, business analysis** Michael LoBue; **manager, business operations** Jessica Tierney; **financial analysts** Priti Pamnani, Celeste Troxler; **rights and permissions: administrator** Emilie David; **associate** Elizabeth Sandler; **marketing director** Ian King; **marketing manager** Allison Pritchard; **marketing associates** Aimee Aponte, Alison Chandler, Mary Ellen Crowley, Julianne Wielga, Wendy Wise; **marketing executive** Jennifer Reeves; **director, site licensing** Tom Ryan; **director, corporate relations** Eileen Bernadette Moran; **publisher relations, eresources specialist** Kiki Forsythe; **senior publisher relations specialist** Catherine Holland; **publisher relations, east coast** Phillip Smith; **publisher relations, west coast** Philip Tsolakidis; **fulfillment supervisor** Iquo Edim; **fulfillment coordinator** Laura Clemens; **marketing associate** Mary Lagnaoui; **electronic media: manager** Lizabeth Harman; **project manager** Trista Snyder; **assistant manager** Lisa Stanford; **senior production specialists** Christopher Coleman, Walter Jones; **production specialists** Nichele Johnston, Kimberly Oster

Advertising director, worldwide ad sales Bill Moran

Product (science_advertising@aaas.org); **midwest/west coast/w. canada** Rick Bongiovanni: 330-405-7080, FAX 330-405-7081; **east coast/e. canada** Laurie Faraday: 508-747-9395, FAX 617-507-8189; **uk/europe/asia** Roger Goncalves: TEL/FAX +41 43 243 1358; **japan** Mashy Yoshikawa: +81 (0) 3 3235 5961, FAX +81 (0) 3 3235 5852; **senior traffic associate** Deiandra Simms

Commercial Editor Sean Sanders: 202-326-6430

Project Director, Outreach Brianna Blaser

Classified (advertise@sciencecareers.org); **u.s.: sales manager** Daryl Anderson: 202-326-6543; **inside sales representative** Tina Burks: 202-326-6577; **key account manager/midwest** Joribah Able; **east coast** Alexis Fleming: 202-326-6578; **west/south central** Nicholas Hintibidze: 202-326-6533; **sales coordinators** Rohan Edmonson, Shirley Young; **international: sales manager** Tracy Holmes: +44 (0) 1223 326525, FAX +44 (0) 1223 326532; **sales** Susanne Kharraz, Dan Pennington, Alex Palmer; **sales assistant** Lisa Patterson; **japan** Mashy Yoshikawa: +81 (0) 3 3235 5961, FAX +81 (0) 3 3235 5852; **advertising support manager** Karen Foote: 202-326-6740; **advertising production operations manager** Deborah Tompkins; **senior production specialist/graphic designer** Amy Hardcastle; **senior production specialist** Robert Buck; **senior traffic associate** Christine Hall

AAAS Board of Directors retiring president, chair James J. McCarthy; **president** Peter C. Agre; **president-elect** Alice Huang; **treasurer** David E. Shaw; **chief executive officer** Alan I. Leshner; **board** Alice Gast, Linda P. B. Katehi, Nancy Knowlton, Cherry A. Murray, Julia M. Phillips, Thomas D. Pollard, David S. Sabatini, Thomas A. Woolsey

AAAS
ADVANCING SCIENCE, SERVING SOCIETY

EDITED BY CONSTANCE HOLDEN

Sorghum Hero

Agronomist Gebisa Ejeta of Purdue University in West Lafayette, Indiana, last week won the $250,000 World Food Prize—the "Nobel Prize" for agriculture—for developing drought- and weed-resistant sorghum varieties in Africa. Ejeta, born in Ethiopia, spent 15 years looking for ways to defeat striga, a parasitic weed that devastates sorghum crops. He finally identified the chemical signal from sorghum that striga rootlets pick up and developed sorghum seeds in which the process would be interrupted.

Ejeta has spent his whole career at Purdue, where he got his doctorate in 1978. He'll be honored at a 15 October ceremony in Des Moines, Iowa.

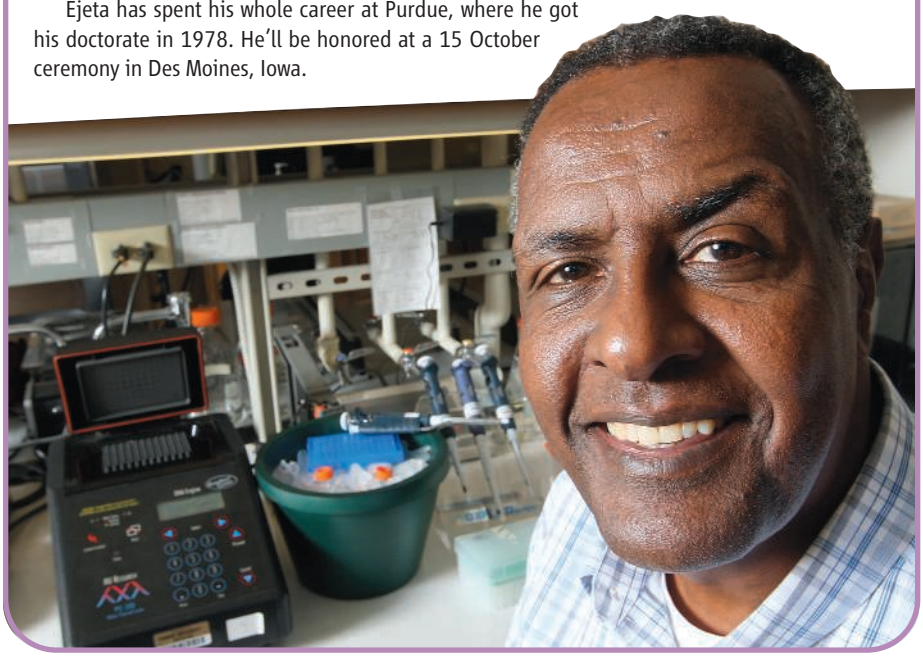

Self-Confidence Genes?

Brains alone don't make a star student. Motivation and self-confidence—what some psychologists call "self-perceived abilities" (SPAs)—are important, too. Now, psychologists report that not only IQ but SPAs as well are strongly influenced by genes.

A team led by Corina Greven of the Institute of Psychiatry in London examined data from a large longitudinal study of British twins. For 1217 identical twin pairs and 1070 same-sex fraternal twin pairs, all 9 years old, the researchers compared school test scores, IQ scores, and results of a test in which the subjects ranked themselves on a five-point scale ranging from "not at all good" to "very good" at English, math, and science subjects.

By comparing scores of identical twins (who share 100% of their genes) and fraternal twins (with 50%), the researchers estimated a heritability for SPAs at 51%. "Contrary to extant theories, SPAs are substantially influenced by genetic factors, … at least as much as IQ is," they wrote online last month in *Psychological Science*. Heritability of IQ, which goes up with age, was estimated at .43 for the 9-year-olds.

"I don't think anyone has looked at this before," says Nicholas Martin, a twin researcher at the Queensland Institute of Medical Research in Brisbane, Australia. "It would be interesting to explore further what the roots of self-confidence are, since it seems to be semi-independent of true ability."

Underwater World

Some time between 10,000 and 7000 years ago, hunters herded caribou on what is now the bottom of Lake Huron. Now researchers are searching the site—a land bridge that once connected Michigan and Ontario when lake levels were about 100 meters lower—for clues about its inhabitants.

Stones believed to have been used as caribou-hunting blind.

Anthropologist John O'Shea and ocean engineer Guy Meadows of the University of Michigan, Ann Arbor, probed the waters with side-scan sonar and a remote operating vehicle to uncover what appears to be a former caribou hunting ground. They identified a long string of boulders, or "drive lane," used to guide caribou to an ambush site with large boulders believed to be a hunting blind. Other signs are suggestive of a campsite, the team reported online on 8 June in the *Proceedings of the National Academy of Sciences*. The researchers plan to explore the area further with scuba divers and an autonomous underwater vehicle. O'Shea says the site may shed light on the transition from nomadic big-game hunters to a more settled society.

"Some of the features they see are really intriguing," says paleontologist Russell Graham of Pennsylvania State University, University Park. "If their interpretations are right, … we might find perishable remains," such as bones and wood artifacts that are typically lost to the acidic soils of the northeast but that could be preserved in the water, he says.

Making It Last

Maybe size doesn't matter with fruit flies, but for the males, at least, longer is better.

In the fruit fly *Drosophila montana*, females who are detained in lengthy copulations with males wait longer before going at it again, a team of European scientists reports in a paper in press at *BMC Evolutionary Biology*. It's to the

males' advantage, as the longer they draw out the encounter, the greater the chance that they will father the ensuing offspring.

In fruit flies, males and females seem to have different ideas about how long they want copulation to last. Not long after a female has permitted a male to mount her, she tries to kick him off, report researchers led by Dominique Mazzi of the University of Jyväskylä in Finland. The scientists found that the males who manage to hang on stayed on 50% longer than those who were successfully rebuffed.

Protracted copulation didn't enhance fertility, the researchers found. Rather, it prevented females from hooking up quickly with competitors. If the scientists interrupted the linkage, the females quickly found someone new.

CREDITS (TOP TO BOTTOM): COURTESY OF PURDUE UNIVERSITY; JENNI KESANIEMI AND ANNE LEHTOVAARA; JOHN O'SHEA AND GUY MEADOWS

Published by AAAS

A prescription for U.S. schools
1498

Radionuclides absent from North Korea's test
1499

Weighing the options. WHO leader Margaret Chan, shown here with flu chief Keiji Fukuda, had to balance science and politics in making her call.

CREDIT: FABRICE COFFRINI/AFP PHOTO/NEWSCOM

SWINE FLU

After Delays, WHO Agrees: The 2009 Pandemic Has Begun

In the end, it was an anticlimactic, almost tedious event. When World Health Organization (WHO) chief Margaret Chan declared last week that for the first time in more than 40 years the world is facing an influenza pandemic, she simply stated what everybody already knew. "The scientific criteria for an influenza pandemic have been met," Chan told reporters in WHO's main assembly hall in Geneva shortly after 5 p.m. local time on 11 June. "I have therefore decided to raise the level of influenza pandemic alert from phase 5 to phase 6," the highest level in WHO's pandemic alert system.

Many leading influenza scientists and public health experts say that those scientific criteria had been satisfied for several weeks and that WHO postponed its decision unnecessarily. "It's a shame it didn't happen sooner," says Marc Lipsitch, an epidemiologist at the Harvard School of Public Health in Boston, who calls the debate over the meaning of pandemic "a big distraction." But WHO says that science wasn't the only factor and that the timing was carefully calibrated to ensure that countries were well-prepared to prevent overreaction. "This was a message to the globe," says Michael Ryan, director of global alert and response at WHO. "We're operating at the intersection of science, policy, and diplomacy."

Scientists hope the end of the debate will lead to a renewed focus on mitigating the virus's effects as it washes over the globe. Chan's declaration brings to the fore many important decisions still to come. Chief among them are the mass production and equitable distribution of a vaccine, a key topic during a New York City meeting between Chan and U.N. Secretary-General Ban Ki-moon earlier this week.

WHO had jumped from phase 3 to 4 and then to 5 in less than a week in late April, as the novel H1N1 virus spread widely in Mexico, the United States, and Canada. Phase 6 requires that the virus make similar inroads in communities in another of WHO's six global regions. By mid-May, many epidemiologists thought the United Kingdom, Spain, and Japan met that criterion. But Ryan contends that those were localized outbreaks, often centered around schools and other institutions, and not the generalized onslaught expected during a pandemic.

At the World Health Assembly (WHA) that began on 18 May, several countries warned Chan that calling the outbreak a pandemic could create panic about a virus that did not seem to cause more serious disease than seasonal flu. Because many preparedness plans were written with the much more deadly avian flu strain H5N1 in mind, the declaration might also trigger draconian measures, they said. WHO has since acknowledged that its phasing system needs fixing, as it relies solely on geographic spread and doesn't factor in severity.

Through the first week in June, as cases began to skyrocket in Australia, WHO continued to put off the final call. Although country representatives at WHA had urged Chan to move slowly before declaring phase 6, Ryan insists that no prolonged lobbying campaign occurred. Then on 10 June, Chan led a teleconference with the eight hardest-hit countries (Mexico, the United States, Canada, Chile, Spain, the United Kingdom, Japan, and Australia) about the extent of their outbreaks. Countries such as Japan and the United Kingdom still weren't ready to say they had a full-blown epidemic, Ryan says. But then, Chan turned the question around: Could they be positive that there was not sustained community transmission within their borders? All agreed that they couldn't. At the end of the call, Chan decided to convene the so-called Emergency Committee the next morning. The advisory group supported the move to level 6, which Chan announced hours later.

In delaying the decision, WHO appears to have allowed politics to trump science, says virologist Albert Osterhaus of Erasmus Medical Center in Rotterdam. But other scientists say they understand the difficult situation WHO confronted. "It's realpolitik for someone like Margaret Chan," says Ian Gust, a veteran flu researcher at the University of Melbourne in Australia. Moreover, the alert system isn't an exact science either, says flu expert Angus Nicoll of the European Centre for Disease Prevention and Control in Stockholm. Under the two-region rule, outbreaks in Thailand and Vietnam—which belong to two different WHO regions—could trigger level 6, whereas similar outbreaks in Canada and Chile, both part of the Americas region, cannot. Ryan says the measured global response last week shows that the balancing act worked: "You don't see people running around like chickens with their heads chopped off."

The delay had one upside for vaccine makers: Companies are only now completing production of the seasonal flu vaccine for next winter in the Northern Hemisphere. Had phase 6 been announced a month ago, some may have been forced to cut short that production to make way for the pandemic vaccine, jeopardizing the

20 years after the CF gene
1504

China's bid for astronomical big time
1508

health of millions of people who might be left unprotected from seasonal flu strains.

One big unknown is whether companies will be able to make enough pandemic vaccine to meet the demand. Based on studies and talks with the vaccine industry, WHO has estimated that companies could churn out a maximum of 4.9 billion vaccine doses the first 12 months after they start production—if everything works in their favor. A more conservative estimate, WHO says, is 1 billion to 2 billion vaccine doses in the first year. For either scenario, a so-called antigen-sparing strategy, which uses a vaccine enhancer called an adjuvant to make the vaccine's viral proteins (the "antigen") trigger stronger immune responses, will be essential. If less antigen is needed per dose, manufacturers can produce more doses in a shorter time.

Many researchers are worried that the adjuvants could slow the regulatory process in the United States. The U.S. Food and Drug Administration licenses vaccines, not adjuvants themselves, but the only adjuvant used in FDA-approved products is an old-fashioned formulation called alum. GlaxoSmithKline and Novartis, two of the largest influenza vaccine makers, both hope to use "next generation" adjuvants, which are included in vaccines already approved for use in many countries. Norman Baylor, director of FDA's office of vaccine research and review, doesn't expect that to pose "a big hurdle," but he does note that antigen-sparing strategies benefit populations, not individuals. "You have to think about those trade offs," he says.

Chan called on the world last week to ensure equitable access to the vaccine. The agency is hoping that poor countries can benefit from donations by drug companies, a tiered pricing system, or funding by rich countries. That may be difficult to realize, however, because an unknown number of doses is already tied up through contracts between pharmaceutical companies and countries that can afford them.

How useful—or crucial—the vaccine will be depends in part on how severe the pandemic is. For now, WHO has classified the severity as "moderate," because it looks nowhere near as severe as H5N1 or the dreaded 1918 pandemic virus. Still, Chan warned last week that nasty surprises could be in store if the virus becomes more pathogenic or develops resistance to drugs that can now stop it. "The virus writes the rules," she said.

Harvard's Lipsitch worries that people are underestimating the dangers, noting that the novel H1N1 virus unusually leads to severe disease in young people, and many common conditions such as asthma, diabetes, and pregnancy are underlying risk factors for severe disease. Tens of thousands of people could die in age groups for which seasonal flu is rarely lethal, he says. "If school kids start dying in substantial numbers, that will cause people to take notice. But at that point, it's too late."

–JON COHEN AND MARTIN ENSERINK

For continuing coverage of the pandemic and an up-to-date timeline, go to www.sciencemag.org/swineflu/.

PUBLIC HEALTH

Expanded U.S. Drug Agency to Control Tobacco

The U.S. Food and Drug Administration (FDA) is on the cusp of gaining power for the first time to regulate cigarettes and other tobacco products. Last week, the U.S. Senate followed the lead of the House of Representatives, voting 79–17 to give FDA this authority, and President Barack Obama has vowed to sign the legislation. It will allow FDA to ban certain ingredients in cigarettes, push for tougher labeling, and create an FDA Center for Tobacco Products within 90 days after the law takes effect.

A government source, speaking on condition of anonymity because he was not authorized to talk to the press, says that the new center could be staffed by as many as 1000 employees, including several hundred scientists. A user fee paid by tobacco companies will finance the expansion, which includes an advisory committee on which tobacco companies will be able to place nonvoting members.

The bill has its problems, antitobacco activists say. For one, this gives cigarettes "the imprimatur of the FDA," says Alan Blum, who directs the Center for the Study of Tobacco and Society at the University of Alabama, Tuscaloosa. Public health researchers are also wary because Philip Morris supported the bill. In a statement, the Altria Group, which owns the company, hailed the legislation for providing "important benefits to adult consumers for many years to come."

Lighting a fire. FDA will regulate tobacco products.

CREDIT: JUPITERIMAGES

Despite the concerns, this action "is long overdue," says Michael Cummings, a tobacco control expert at the Roswell Park Cancer Institute in Buffalo, New York. "There is no government agency right now that can even tell you what products are being sold where."

The bill doesn't permit FDA to ban nicotine. But FDA can keep other components out, such as sugary flavorings that increase the appeal of cigarettes. It also allows FDA to strengthen U.S. warning labels—"the worst warning labels in the world," says Gregory Connolly of the Harvard School of Public Health in Boston, who faults them for not including images of tobacco-driven diseases that have been found to discourage cigarette smoking.

One big unknown is how, exactly, FDA will exercise its newfound authority. Connolly notes a tension in current tobacco-control measures between "product harm reduction"—promoting cigarettes that are deemed less toxic—versus "product use reduction," or preventing smoking in the first place. The latter, he says, has been shown to reduce tobacco-related death and disease, whereas the former has not. Like others in tobacco control, Connolly is skeptical about "safe" cigarettes and hopes FDA will focus on discouraging smoking and making cigarettes less appealing and less addictive. Cummings expects that FDA will do "its own validation in testing products," to ensure the tobacco companies don't make misleading claims.

–JENNIFER COUZIN-FRANKEL AND ROBERT KOENIG

Published by AAAS

U.S. STEM EDUCATION

Report Calls for Grassroots But Comprehensive Changes

Think globally, act locally. That popular slogan, used by activists of various stripes, captures the spirit of what the latest blue-ribbon panel says is needed to improve U.S. math and science education.

The $1.5 million study,* from the Carnegie Corporation of New York, melds the handwringing in previous reports about the overall state of U.S. education with specific warnings about weaknesses in math and science education. It calls for more rigorous math and science content, improved standards and assessment, better training for teachers, and more innovative schools. Those changes, if adopted, would not only improve math and science, says mathematician Phillip Griffiths, past director of the Institute for Advanced Study in Princeton, New Jersey, and commission chair, but also "do school differently."

But nothing will happen, the report warns, until everyone with a stake in U.S. education—from politicians and business leaders to principals and university professors—gets involved. Unlike in countries with a centralized education system, what happens in the 95,000 schools across the United States is determined largely by local and state budgets, policies, and practices. The federal government acts more like a referee, cheerleader, and trendsetter.

For the most part, the report backs a slew of current reform efforts, notably a 46-state consortium hoping to develop a common set of "fewer, clearer, and higher" standards in reading, math, and science. The report plows a bit of new ground, however, with a proposal for an alternative to the standard precalculus pathway in high school mathematics that would focus on statistics, data analysis, and other applied topics. It also calls on reformers to pay more attention to improving science.

The A-list of attendees at the report's Washington, D.C., rollout—including Education Secretary Arne Duncan and Representative George Miller (D–CA), chair of the House education panel and the cream of the education policy community—suggests that the report already has the ear of the Administration and leaders of Congress. The commissioners themselves—18 prominent scientists, politicians, and academics, labor, and business leaders (including Bruce Alberts, editor-in-chief of *Science*)—represent diverse constituencies. "We may be strange bedfellows," says Ellen Futter, commissioner and president of the American Museum of Natural History in New York City, "but we're united behind the same purpose."

One commissioner, Katherine Ward, says she relished her role as "a voice from the trenches." An advanced placement biology and biotechnology teacher in San Mateo, California, Ward thinks that the panel's biggest contribution may be its recognition that producing "a generation of STEM-capable students" (the acronym for science, technology, engineering, and mathematics) can't be achieved by fiat. The current federal law requiring all students in grades 3 through 8 to be tested each year in reading and math, known as No Child Left Behind, isn't mentioned by name in the report, but several commissioners remarked that improving STEM education will require much more than simply mandating that students make annual progress on such tests.

"When there's a problem with our schools, people usually turn to teachers and ask, 'Well, what are you going to do about it?' But many times, the answer lies outside the control of the individual teacher," says Ward, a 13-year veteran teacher. "Of course, we want access to the latest brain research on how children learn, on what's developmentally appropriate, on what strategies are most effective. But the way schools operate can make it hard to obtain that sort of information, much less to apply it in the classroom. So even though the target is better math and science education, you probably can't achieve it without looking at the entire system."

One approach that the report advocates is to scale up what Duncan calls local "islands of excellence." One such program, Urban Advantage, utilizes the resources of museums throughout New York City to teach middle school science. Not only does the program "broaden the definition of the schoolhouse," says Futter, who helped to create it 5 years ago, but it also satisfies a requirement that all eighth-graders in the New York public schools conduct a long-term scientific investigation. Denver and Miami are hoping to launch similar programs this fall, says Futter.

Having a good idea isn't always enough, however. Xavier University of Louisiana, a historically black college in New Orleans with fewer than 3000 undergraduates, decided in the 1970s to beef up its STEM curriculum. Now 62% of its students are STEM majors, says its longtime president, commission member Norman Francis, and it sends more African-American students to medical and dental school than any other U.S. university, regardless of size. But that success is more admired than emulated, admits Francis, who also served on the 1983 report, *A Nation at Risk: The Imperative for Educational Reform*, that famously identified a "rising tide of mediocrity" overtaking U.S. schools.

"It's not rocket science, but it takes hard work," Francis says about Xavier's efforts. "You can't legislate those changes, but you can support them wherever they are taking place. That's what we hope this commission will do."

–JEFFREY MERVIS

Museum-quality science. Museums throughout New York City provide equipment and training for middle schoolers as part of the Urban Advantage program.

CREDIT: AMERICAN MUSEUM OF NATURAL HISTORY

*The Opportunity Equation: Transforming Mathematics and Science Education for Citizenship and the Global Economy (opportunityequation.org)

Published by AAAS

ARMS CONTROL

Verification Experts Puzzled Over North Korea's Nuclear Test

VIENNA—When North Korea declared on 25 May that it had carried out a second underground nuclear test—a blast that clearly showed up on seismometers across the globe—it seemed to confirm what most observers feared about the country's nuclear ambitions. But at a scientific conference it convened here last week, the Comprehensive Nuclear-Test-Ban Treaty Organization (CTBTO) revealed that its global network of radionuclide detectors, which sniff out faint wind-borne traces of radioactive elements such as xenon, had not picked up anything it could pin on the Korean test. Press reports say that South Korean sensors have also detected nothing, and neither has a U.S. Air Force plane over the East Sea, causing some to speculate that the test was faked with nonnuclear explosives.

Yet researchers at the conference weren't buying the conspiracy theory. Seismologist and verification expert Paul Richards of Columbia University's Lamont-Doherty Earth Observatory in Palisades, New York, acknowledges that it is possible to make a chemical explosion look nuclear up to a certain size, but "it's very difficult and highly implausible. … Personally, I have no doubt [that it was nuclear]."

The mystery of the missing radionuclides comes at a time when there's renewed attention on the test ban treaty, thanks to President Barack Obama's campaign pledge to see the United States ratify it. Although the treaty has been signed by 180 nations, it will not come into force until all countries that have nuclear weapons or reactors have adopted it. Nine such states have yet to ratify it, including North Korea and the United States. Nevertheless, CTBTO is building a global network of 337 detector stations from Spitsbergen to Antarctica. Currently more than 70% complete, the network has sensors for seismic signals, airborne radionuclides, and acoustic signals in the oceans and atmosphere.

On 25 May, 23 of CTBTO's 40 operational primary seismic stations picked up tremors from Korea and relayed data to the organization's headquarters here. One and a half hours later, CTBTO officials sent a bulletin to treaty signatory governments detailing the time, location, depth, and likely nature of the event. "There could not be a clearer indication of the need for these verification tools," says CTBTO chief Tibor Tóth.

Arctic sniffer. CTBTO's Yellowknife station in Canada detected Korean xenon in 2006, but not this time.

In 2006, when Korea carried out its first nuclear test, a U.S. plane detected radionuclides within days, and a CTBTO station as far away as Yellowknife in Canada picked them up 12 days after the test. This time around, there has been nothing, which is concerning verification experts. "Radioxenon is most likely the only conclusive evidence of a nuclear explosion," says Anders Ringbom of the Swedish Defence Research Agency in Stockholm. Ringbom says CTBTO's xenon detectors, which can pick up a couple of hundred atoms from a cubic meter of air, "were working fine" in the days following last month's explosion in North Korea. The relevant xenon isotopes have half-lives measured in hours and days, so "the opportunity is … perhaps closing rapidly," he says.

Researchers are speculating that North Korea this time deliberately sought to prevent leakage of radionuclides by, for example, carrying out the test deep underground and in rock that melts easily, forming a seal around the explosion chamber. The blast, which produced a magnitude-4.5 tremor, is thought to be larger than the one in 2006 (magnitude 4.1), and that may also have played a role. "There is evidence from earlier tests that a bigger explosion leads to more melting and so better containment," says planetary scientist Raymond Jeanloz of the University of California, Berkeley.

Verification experts point out that doubts about the test would easily be dispelled by the test ban treaty's ultimate tool: an onsite inspection. But such intrusive investigations can take place only when the treaty is ratified and fully in force.

–DANIEL CLERY

CREDITS (TOP TO BOTTOM): COURTESY OF CTBTO PUBLIC INFORMATION; ROBERT MOYLE

ScienceNOW.org

From *Science*'s Online Daily News Site

Warp-Speed Raindrops It's a rain race out there. In the meteorological equivalent of breaking the light-speed barrier, new research shows that the smaller droplets in a rainstorm often surpass what appears to be the speed limit for rain. The findings should help scientists devise models that could lead to more accurate weather forecasts.
http://tinyurl.com/m4zkms

Stressed Cells Cause Gray Hair. If you've ever blamed your gray hair on stress, you weren't far from the truth. Genotoxic stress—the kind that can damage a cell's DNA—causes hair to whiten over time, according to a new study. The results challenge accepted ideas about how stem cells age and may eventually lead to new ways to prevent graying and treat the more serious conditions caused by genotoxic stress, such as cancer.
http://tinyurl.com/m4jqha

Lava for Life. Astronomers scanning the skies for another Earth might need to narrow their search. New research suggests that even if a world lies within the Habitable Zone, in which water is liquid, too much or too little volcanic activity can render it lifeless.
http://tinyurl.com/mgve5q

On the Road to a New Species. Catching one species in the act of becoming two is no easy feat. Yet evolutionary biologists working in the Solomon Islands may have done just that. They have found that a single genetic change turns a small, brown-bellied bird black, possibly leading it to mate with like-colored birds—and setting it on the road to becoming a new species.
http://tinyurl.com/lvzk9f

Read the full postings, comments, and more on **sciencenow.sciencemag.org**.

Published by AAAS

LAW OF THE SEA

A Final Push to Divvy Up the Sea by All the Rules

ANNAPOLIS—Is this the year that the United States finally ratifies an international agreement to conserve and manage the wealth of the ocean?

Since coming into effect 15 years ago, the United Nations Convention on the Law of the Sea (UNCLOS) has been guiding how 156 countries settle maritime boundary disputes, watch over their natural resources, and—especially in the Arctic—extend their rights to any riches on or beneath the adjacent seafloor. But the United States doesn't have the legal right to extend its claims or a seat on the commission that reviews the plans of other countries, because it has never ratified UNCLOS.

Last week, at a symposium* here on the implications of the dramatic shrinking of summer Arctic sea ice, scientists discussing the results of four summer mapping expeditions shared the podium with policymakers saying that the time has come for the U.S. Senate to act. "I believe it is crucial for the United States to be a party to this Treaty," said Senator Lisa Murkowski (R–AK) in a statement read at the meeting, adding that this year represents "the best opportunity for Senate accession."

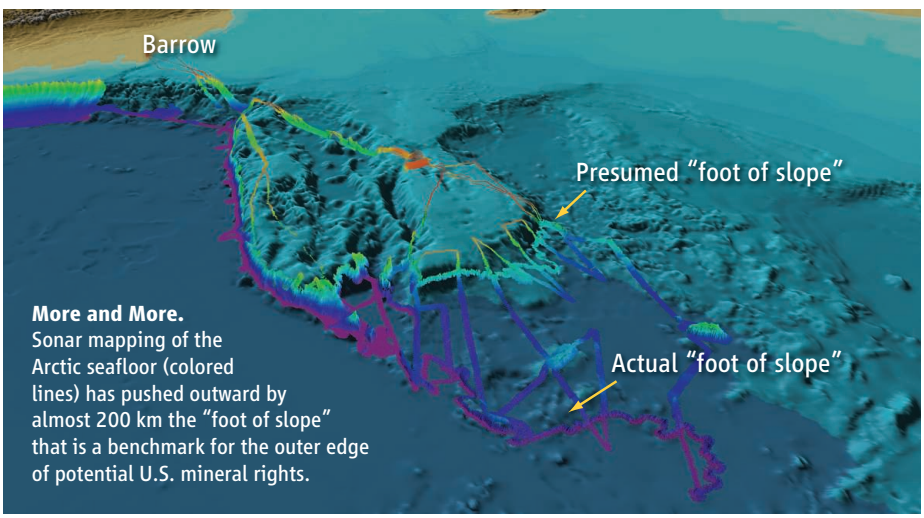

More and More. Sonar mapping of the Arctic seafloor (colored lines) has pushed outward by almost 200 km the "foot of slope" that is a benchmark for the outer edge of potential U.S. mineral rights.

CREDIT: IMAGE CREATED BY LARRY MAYER; DATA COLLECTED BY THE UNIVERSITY OF NEW HAMPSHIRE CENTER FOR COASTAL AND OCEAN MAPPING/JOINT HYDROGRAPHIC CENTER; BASE MAP IS IBCAO COMPILATION (JAKOBSSON *ET AL.*, 2008)

Two U.S. agencies now oversee the spending of about $7 million a year on research aimed at exploring the geographical limits of the country's maritime rights as defined under UNCLOS. That work has gone ahead because the government recognizes the convention as "customary" international law, says marine geologist Larry A. Mayer of the University of New Hampshire, Durham, who codirects the mapping project. He and colleagues are searching for the point at which the sloping pile of sediment washed off the continent peters out, which under UNCLOS's definition marks the boundary of a country's seafloor claims.

The Arctic expeditions have considerably

*Impacts of an Ice-Diminishing Arctic on Naval & Maritime Operations, 9–11 June, Annapolis, Maryland.

CHINA

After Outcry, Government Backpedals Over Internet-Filtering Software

Last week, the Chinese government provoked a firestorm of criticism when it announced that starting 1 July, all computers sold in China must have a new software program meant to filter pornographic images and block content that offends government sensibilities, such as discussion of the banned sect Falun Gong. But scientists whose work was the basis for text filtering are distancing themselves from the controversial software. And as *Science* went to press, it appeared that the government may not force computer users to run the "censorware" after all.

China's information ministry spent $6.1 million last year on a 1-year license of an Internet-filtering software that dynamically blocks Web sites by detecting "harmful" images and text for "constructing a green, healthy, harmonious network environment and protecting the healthy growth of youths," according to the published government procurement notice. After requiring installation of the *Lü Ba-Hua Ji Hu Hang* (Green Dam-Youth Escort) software on all school computers and on computers sent to the countryside, the ministry had intended to impose protection on all of China's 300 million netizens—who already face government censorship of the Internet. But even state media have turned against Green Dam-Youth Escort, questioning its value. And Chinese lawyers have called for public hearings on the information ministry's directive, which they assert may violate China's antimonopoly law.

Netters who have tested Green Dam, developed by the firm Zhengzhou Jin Hui in Henan, say that it blocks many harmless pictures while letting some pornographic ones pass. If Green Dam finds a certain number (preset by the user) of objectionable images on a Web site, it automatically adds the address to its blacklist and blocks access to the site from that computer until it is reset by the password holder. In a test conducted by *Science*, Green Dam added *The Wall Street Journal* Web site to the blacklist because it detected too many "harmful" images, including a picture of U.S. Secretary of State Hillary Clinton.

The text-filtering component, Youth Escort, "seems to use a more intelligent method," says J. Alex Halderman, a computer security expert at the University of Michigan, Ann Arbor. It was created by the Beijing Da Zheng Linguistic Knowledge Processing SciTech Company Ltd., a software company spun off from the Institute of Acoustics (IOA) of the Chinese Academy of Sciences. Da Zheng's Web site says the software implements a natural language-processing method developed by IOA's Huang Zengyang in the 1990s. The theory, called Hierarchical Network of Concepts (HNC), posits that different natural languages can be mapped onto a symbolic representation of concepts, enabling machine understanding and translation with an accuracy greater than 90%, says Huang, who is listed on Da Zheng's Web site as chief scientist. But Huang is distancing himself from the company and Youth Escort. "I don't

Published by AAAS

enlarged the area where the United States will claim rights to oil, gas, and other seafloor and sub-seafloor resources. Beyond Barrow, Alaska, in the Chukchi Sea, surveying has pushed the likely boundary northward by more than 185 km from where earlier, sketchy observations would have placed it, Mayer reported. Along the way, researchers have discovered a seafloor scoured by a grounded ice sheet and crustal rock that doesn't fit with conventional ideas of how the Arctic Ocean formed.

Those advances in scientific understanding have yet to be matched in the political realm, however. "The mapping is really quite consequential for us," Murkowski told reporters this week. "If the treaty is not ratified, we can't make a claim before the [UNCLOS] commission. That's to our detriment; there's so much at stake."

John Norton Moore, a law professor at the University of Virginia, Charlottesville, says that opponents have held up ratification by using "a series of distortions and untruths repeated over and over again," including the false claim that ratification would constitute "turning two-thirds of Earth over to the United Nations." But even with the political stars aligned—support from President Barack Obama, a sympathetic chair of the Senate Foreign Relations Committee, Senator John Kerry (D–MA), and a likely super-majority of the Senate in favor of ratification—the issue has not made it onto the Senate calendar for floor debate.

Proponents of ratification see an opening, but it will not come easily. Senator James Inhofe (R–OK) and others who regard UNCLOS as a threat to U.S. sovereignty have successfully prevented the treaty from coming up for an expedited vote after only limited debate, notes Inhofe spokesperson Jared Young. The other option—a large block of floor time—has proved elusive until now.

Both Murkowski and Inhofe think that's now likely, possibly this fall. To prepare for that opportunity, Murkowski says she's working with Kerry and Senate Foreign Relations Committee ranking minority member Senator Richard Lugar (R–IN) to "see what members we need to encourage." One key issue is whether the United States is better off not ratifying the treaty and instead choosing which sections to abide by while enjoying the treaty's benefits. Supporters say being a player beats being an outsider.

Murkowski isn't promising victory. "It will require some floor time, which is a precious commodity, especially these days," she says. And Young says his boss will be ready: "It is more than likely it will come up in the Senate, [where] Senator Inhofe will be a leader against it." **–RICHARD A. KERR**

think I have been chief scientist for even a day. That's just a company advertisement," he says. "They don't listen to me."

Huang's former Ph.D. student, Jin Yaohong, wrote the original demonstration software as an HNC application and invented "standpoint filtering" in the early 2000s. Jin has described the filtering as "based on the standpoint of the article, filter reactionary speech." For example, the software can detect whether the phrase "Falun Gong" appears in a complimentary or derogatory context. Da Zheng developed this software into Youth Escort, says Jin, who adds that "how the company will use it is out of our control." Halderman found that entering "Falun Gong" in combination with certain words in Notepad, a basic Windows text editor, triggered filtering and that the program closed abruptly.

At a press briefing last week, foreign ministry spokesperson Qin Gang said that the government's goal is to prevent information harmful to the public from spreading on the Internet. However, earlier this week, an information ministry official told the state-owned newspaper *China Daily* that people would not be compelled to run the Green Dam-Youth Escort that comes with new computers. The ministry did not respond to requests from *Science* for an unfiltered explanation. **–HAO XIN**

Green damned. In a test by *Science*, *The Wall Street Journal*'s Web site was blacklisted and blocked.

CREDIT: (FRAME ONLY) JUPITERIMAGES

ScienceInsider

From the *Science* Policy Blog

This week, *Science*Insider reported on a plan to build a cleaner coal-powered plant, the elimination of a key scientific instrument on a European mission to Mars, and a demand that **HIV-positive people be allowed to attend** an international AIDS meeting in the United States.

A **model electric plant** is getting help from the U.S. Department of Energy (DOE). Designed to burn gas from coal and pump carbon dioxide emissions into geological reservoirs, FutureGen II could cost $2 billion or more. Last week, DOE pledged up to $1 billion for the Illinois-based project, pending private backing.

It's still early in the 2010 U.S. budget cycle but sobering all the same: House of Representatives appropriators disapproved of plans by the **National Science Foundation** to spend $100 million on its Major Research Instrumentation program, saying the program has enough money for now. Legislators also shrank by two-thirds the requested funding for advanced technological education at community colleges.

Researchers who accept U.S. grants should be held to **rigorous standards for disclosing outside income**—such as from drug companies—according to a couple of heavyweight institutions. The Association of American Medical Colleges and the Association of American Universities told the National Institutes of Health last week that far too little income is being reported. But at the same time, they warned of "over-zealous" regulation.

Canadian academics want science minister Gary Goodyear to resign over his latest statements involving religious views. In March, Goodyear linked possible doubts about evolution to his beliefs. This time around, the minister suggested that a government funding body review its support for an upcoming conference on prospects for peace in the Middle East after pro-Israel groups complained that the list of speakers favored the Palestinian position.

Stay on top of the latest science policy news at **blogs.sciencemag.org/scienceinsider**.

Published by AAAS

EUROPE

Italy's MIT Grows, And So Does Controversy Over It

Everyone wants to emulate the Massachusetts Institute of Technology (MIT), but Italy is discovering that not everyone agrees on how to do it.

Six years ago, the Italian government launched the Italian Institute of Technology (IIT) with the grand goal of using scientific and engineering research to boost the country's struggling economy. It was established as a unique public-private research foundation, with government funding of about €50 million to €100 million a year for a decade—a huge investment for a country where researchers complain of chronic underfunding.

On the surface, the institute is growing up nicely. It now employs 380 scientists, based in a newly renovated massive lab building outside Genoa, in external research centers at nine Italian universities, and in IIT-affiliated labs abroad. "We've been able to attract researchers from 38 countries," says Roberto Cingolani, IIT's scientific director. "There is no other institution in Italy with such an international environment."

Last month, IIT released its second 3-year strategic plan, outlining goals of awarding Ph.D.s independent of Italy's universities and expanding from its research themes of neuroscience, robotics, nanotechnology, and drug development into areas such as energy technologies and smart materials. The plan notes that almost 400 peer-reviewed articles have been credited to IIT and boasts: "We can conclude to date that IIT has filled all its promises."

Not so, say the institute's critics. IIT was expected to partner with Italian industry, but not a single Italian company has funded research with it so far, Cingolani confirmed to *Science*. And although Cingolani points to a string of positive evaluations by IIT's own scientific committee, the Italian government has declined to release a recent independent assessment of IIT that, according to its authors, is highly critical. "IIT is a fascinating idea and one of the biggest investments the Italian government ever made in science," says theoretical physicist Mario Rasetti of the Polytechnic University of Turin, one of the authors. "However, the way it is directed is leading it into a big fog."

The Italian media have begun to ask questions. Last week, the major newspaper *L'Espresso* reported that only €108 million of the €518 million allocated to IIT since 2004 have been spent so far. Cingolani, however, explains that IIT spent relatively little during its initial design years, building its endowment for when it would have a full roster of scientists to fund. And he says that some of the money noted by *L'Espresso* wasn't originally budgeted to IIT, as it came from another foundation the government just closed.

Lab sites. IIT's scientists work at this headquarters outside Genoa or in universities in Italy or abroad.

IIT has been controversial from its early days. The idea originated within Italy's treasury department in 2003, back when Silvio Berlusconi was the country's prime minister, as he is once again. Giulio Tremonti, the current Italian minister of economy and finance who held the same role at that time, envisioned something like MIT that would attract industrial investments and world-class scientists. Two dozen international scientists and industrial managers, including four Nobel Prize winners, were asked to help design IIT.

But several of those scientists told *Science* that IIT officials ignored their calls for international competitions to pick the facility's research themes and scientists. "Our proposals were never discussed nor acted on," recalls Hans Wigzell, former president of the Karolinska Institute in Sweden. "We felt like hostages there. We weren't listened to at all." Francesco Salamini, director of the Plant Breeding department at Max Planck Institute for Plant Breeding Research in Germany, says "We felt we were just icons to be displayed but not asked for a real contribution."

The IIT assessment authored by Rasetti and Elio Raviola, a neurologist at Harvard Medical School in Boston, was commissioned last year by former Minister of Treasury Tommaso Padoa Schioppa—he was replaced when Berlusconi returned to power. The report, which involved extensive site visits, evaluated the overall scientific activity of IIT. Cingolani says he considers it a positive evaluation, but Rasetti says he and Raviola judged IIT as underperforming.

Three of IIT's main areas of research—neuroscience, robotics, and nanotechnology—are intended to merge results and focus on the creation of intelligent machines, in particular humanoid robots and high-tech bioelectronic interfaces such as those between the brain and prostheses or artificial sensors. IIT researchers, for example, have helped create a humanoid robot called iCub produced as part of European Union-wide collaboration. Yet Rasetti says he and Raviola concluded that there is little coordination among the three research areas and that much of IIT's research is outside the areas laid out in the institute's plans.

IIT's management structure has also raised eyebrows. IIT's president, Vittorio Grilli, is the director general of the Italian treasury. "Grilli is in charge of allocating money to the same institution he chairs," says Rasetti. "This cannot be accepted."

IIT has also been criticized for padding its scientific roster with big names who primarily work elsewhere, much as some have accused China of doing (*Science*, 22 September 2006, p. 1721). "This situation penalizes young researchers [at IIT] who are left alone, without any leadership. I think one person shouldn't lead two research groups at the same time," says Rasetti. "We consider this as a major problem. This situation won't help IIT to reach top-quality research."

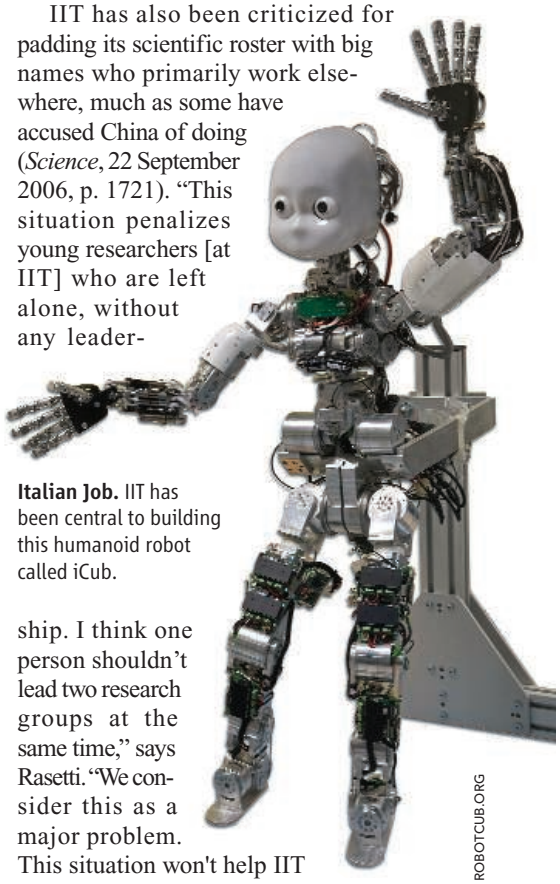

Italian Job. IIT has been central to building this humanoid robot called iCub.

CREDITS (TOP TO BOTTOM): WIKIPEDIA; ROBOTCUB.ORG

Cingolani, however, contends IIT's "brilliant scientists" have already achieved that goal. Whether IIT will ever compare to MIT is an open question, but there appears little doubt Italian scientists will continue to argue about the contentious and costly venture.

–LAURA MARGOTTINI

Laura Margottini is a freelance writer based in London.

Published by AAAS

Dark-Matter Model Multiplies Mass of Galactic Black Holes

Distant quasars harbor at their centers black holes as massive as 10 billion suns. The black holes in the middle of nearby galaxies are featherweights by comparison. Why the difference? According to new research presented at the meeting, astronomers may have been systematically underestimating nearby black hole masses by a factor of two to three.

Researchers figure out the mass of a galaxy by measuring the velocity of stars orbiting within it and calculating the amount of gravity required to keep them moving. The galaxy's light provides a mass measure for all the stars in it. Subtracting that from the galactic mass gives the mass of the central black hole.

Karl Gebhardt of the University of Texas (UT), Austin, and Jens Thomas of the Max Planck Institute for Extraterrestrial Physics in Garching, Germany, applied new computer models to work out the mass of the black hole in the middle of M87, a giant galaxy relatively near our Milky Way. Unlike previous estimates, their work factored in the dark halo—the invisible sphere of dark matter surrounding the galaxy. Gebhardt says he and other researchers had always assumed the halo wasn't important for the calculation.

It was. Running the model on a powerful supercomputer called Lonestar at UT Austin, the team found the black hole's mass to be 6.4 billion times the mass of our sun, between two and three times previous estimates. The magnitude of the effect "caught us off guard," says Gebhardt.

Earlier models underestimated the effects of dark matter on the outskirts of a halo, says Avi Loeb of Harvard University. As a result, they assumed the wrong "mass-to-light ratio"—a crucial factor for calculating a galaxy's mass. Including the dark matter reduces the estimated mass of the galaxy's stars and confers more mass on the black hole. "With the new estimate for the black hole mass in M87, M87 is now closer to being a remnant of a luminous quasar," Loeb says.

"Knowing just how big black holes within galaxies are" will have a fundamental impact on "efforts to understand how galaxies grow and change," says Tod Lauer, an astronomer at the National Optical Astronomy Observatory in Tucson, Arizona. **–Y. B.**

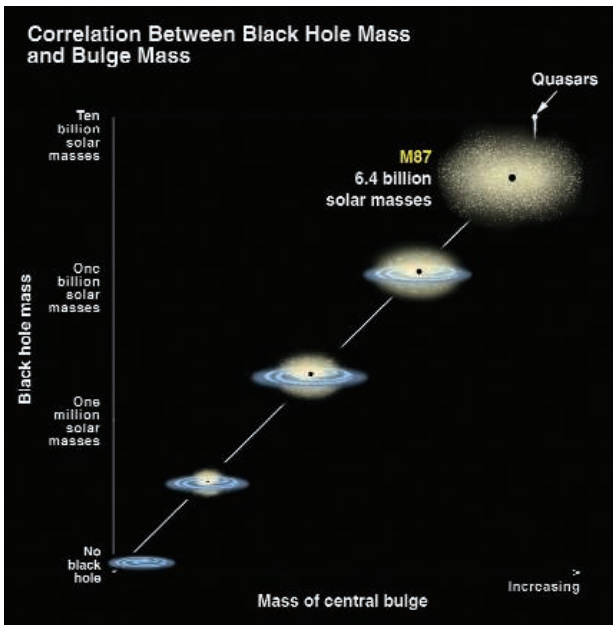

Lining up. New calculations bring M87's black hole mass closer to that of black holes in quasars.

Star Studies Yield Better Yardsticks

Measuring cosmic distances is a tricky business. At the meeting, researchers presented findings that could make the job easier and help refine estimates of the rate of expansion of the universe.

Astronomers determine the distance to galaxies by looking at stellar objects of known brightness, often called standard candles. Comparing their actual brightness with their apparent brightness from Earth reveals how far they are.

Jonathan Bird, a graduate student at Ohio State University, Columbus, reported results that could triple the distances measurable using standard candles known as Cepheid stars. Cepheids, which brighten and dim over a time period proportional to their intrinsic luminosity, are trusted mile-markers of distances up to 100 million light-years. But at periods longer than 80 to 100 days, the correlation between brightness and period breaks down, making their actual luminosity difficult to figure out. That's too bad for astronomers because Ultra Long Period (ULP) Cepheids are bright enough to be observed at distances of up to 300 million light-years.

Combing the literature, Bird and colleagues found 18 ULP Cepheids in nearby galaxies. Because the galaxies' distances are known, the researchers could calculate the intrinsic luminosities of the Cepheids. They all turned out to be similar, regardless of period. "Cepheids that fall off the correlation between period and brightness seem to fall into the same place," says Bird. Now researchers can use distant Cepheids as standard candles, he says.

James Braatz, a researcher at the National Radio Astronomy Observatory, unveiled another signpost: a galaxy called UGC 3789 that he and colleagues determined to be about 160 million light-years away. What makes the galaxy special is the presence of water molecules that act as a maser, amplifying radio waves emanating from the gas clouds rotating around the galactic center.

The maser effect allowed Braatz and colleagues to map the galactic disk and infer the rotational velocity of the gas clouds from the Doppler shift in their spectra. In follow-up observations, the researchers derived the acceleration of the clouds by watching their velocities change over time. Combining their data, they were able to get the diameter of the galactic disk, which, compared with the disk's apparent size from Earth, provided the distance to the galaxy.

The findings could lead to better estimates of the Hubble constant, which gauges how quickly the universe is flying apart, says Adam Riess, an astrophysicist at Johns Hopkins University in Baltimore, Maryland. "It would be fantastic to find more ULP Cepheids," he says, noting that "they are pretty rare."

–YUDHIJIT BHATTACHARJEE

CREDIT: TIM JONES/UNIVERSITY OF TEXAS, AUSTIN, AFTER K. CORDES & S. BROWN/STSCI

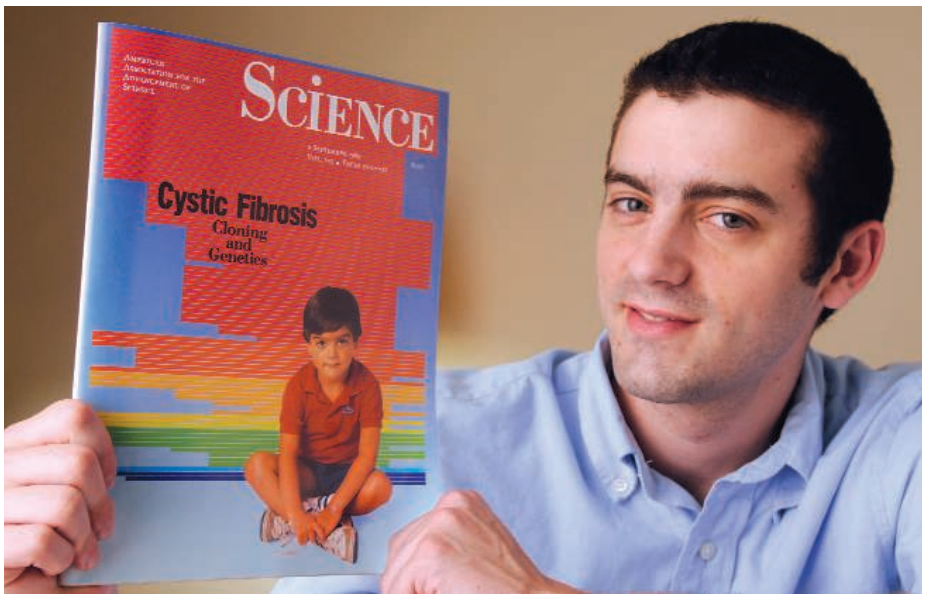

All grown up. Danny Bessette, a 24-year-old with CF, was 4 years old when he appeared on the cover of *Science* announcing the discovery of the CF gene.

The Promise of a Cure: 20 Years and Counting

The discovery of the cystic fibrosis gene brought big hopes for gene-based medicine; although a lot has been achieved over 2 decades, the payoff remains just around the corner

The gene hunt began quietly, with few theatrics and much uncertainty.

For Mitch Drumm, the starting gate lifted in the fall of 1985. He and geneticist Francis Collins met on opposite sides of a volleyball net, during a faculty-student mixer at the University of Michigan, Ann Arbor. Drumm, shorter than the lanky Collins, was outmatched in volleyball. But Collins quickly recruited Drumm to join the lab he was setting up, as its first graduate student. There, Drumm began experimenting with a gene-hunting technique Collins had developed. As a test case, they chose cystic fibrosis (CF), an inherited disease in which sticky mucus accumulates in the lungs and elsewhere, eventually killing the patient. At the time, life expectancy hovered in the early 20s.

Coincidentally, CF had been on Drumm's mind. Just months before, the infant son of his family's next-door neighbors, close friends in New Philadelphia, Ohio, had been diagnosed with the disease. Drumm still recalls the phone call from his mother relaying the devastating news. Like many others studying CF, he became immersed in the field by a personal connection, which carried him through ups and downs in the decades ahead. A big triumph came nearly 4 years after signing up with Collins, in the spring of 1989. In collaboration with a large research group in Toronto, Canada, that had started an aggressive chase for the CF gene years earlier, the team cloned the CF gene—called the cystic fibrosis transmembrane conductance regulator (*CFTR*)—and nailed a crucial, disease-causing mutation (*Science*, 8 September 1989, pp. 1059, 1066, 1073).

Everyone in the CF community recalls the electric moment when they heard the news. "I remember seeing it roll off the fax machine, gathering people in the lab, and thinking, 'What did we need to know' " now? says Michael Welsh, a pulmonary physician at the University of Iowa, Iowa City. Most believed that the disease had grown vastly less complex overnight and would soon be eliminated, probably by gene therapy.

On the 20th anniversary of the identification of the CF gene, as new gene discoveries pile up weekly and hype over the power of genes to transform medicine flows fast, CF offers an object lesson in how difficult it is, and how long it takes, to convert genetic knowledge into treatments. Every CF expert agrees that the gene discovery transformed their understanding of the disease's pathology. But even after so much hard work, not a single therapy based on the CF gene has reached the market. Some promising treatments, especially gene therapy, have proven bitterly disappointing.

"We were naïve," says Johanna Rommens, who at the time was a postdoc in Lap-Chee Tsui's lab at the Hospital for Sick Children in Toronto, the counterpart to Collins's group in Michigan. In her 20s and relatively new to science back then, Rommens couldn't imagine a problem that defied resolution. "I thought I could do anything," she says. "I sometimes feel discouraged that this was so hard." Keen to experiment with other

CYSTIC FIBROSIS KEY DATES

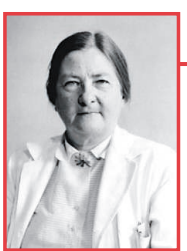

1938: Physician Dorothy Hansine Andersen provides the first clinical description of cystic fibrosis.

1983: Chloride transport is identified as the major defect in CF.

1989: *CFTR*, the cystic fibrosis gene, is found. Median life expectancy for those with CF is about 29.

1990: Scientists suggest that protein folding is behind CF.

CREDITS: (TOP) STEVE BARRETT; (BOTTOM, LEFT TO RIGHT) LIBRARY OF MEDICINE/WIKIPEDIA; *SCIENCE*

Published by AAAS

genetic diseases, Rommens subsequently left the CF field.

Although gene therapy hasn't paid off, prospects have improved for those with CF: Their median life expectancy has stretched almost 10 more years and now exceeds 37. This is thanks not to genetic knowledge, however, but to more aggressive and earlier treatment to keep the lungs clear.

Soaring hopes

In October 1989, a month after the CF gene was published in *Science*, gene therapist James Wilson strode to the speaker's podium at a Florida cystic fibrosis conference to discuss prospects for gene therapy. Thousands of people—physicians, scientists, families—packed the meeting. "I get shivers talking about it right now," says Wilson, who then worked down the hall from Collins at Michigan and is now at the University of Pennsylvania. "The excitement was palpable. I have never felt energy like that ever before."

There was broad consensus that the time for CF gene therapy had arrived. Two advances buoyed hopes that this new technique, still in its infancy, would eliminate CF. First, scientists had managed to "cure" the disease in test tubes. They introduced a normal version of *CFTR* into cells from CF patients, compensating for a defective gene that produced no protein, or none the cell could use. In addition another researcher, W. French Anderson, then at the National Institutes of Health, began the first-ever clinical trial of gene therapy to treat an immune deficiency syndrome, demonstrating that gene transfer in people was feasible. By then, in the fall of 1990, says Wilson, "expectations for the success of gene therapy for CF were as high as I've ever seen for any disease, under any circumstances, in the 20 years I've been involved in this."

Looking back, many CF experts consider an excessive focus on gene therapy in the early years to have been a big mistake. Like an investor who gambles much of his or her fortune on a single stock, "people kind of stopped doing the other things they were doing" and turned instead to strategies for getting the gene into lung cells, says Raymond Frizzell, a physiologist at the University of Pittsburgh in Pennsylvania.

Then and now. Geneticist Mitch Drumm (*inset, right*) worked with Francis Collins (*inset, left*) in the 1980s and helped identify the CF gene. He remains in the CF field today (main picture).

Early successes in basic CF research also convinced scientists that new treatments were right around the corner. In addition to correcting the gene defect in cells, having *CFTR* in hand revealed that the healthy CFTR protein was an ion channel that helped transport chloride and control the movement of water across cell membranes. Researchers determined that several mutations led to a protein-folding defect—one of the first protein-folding diseases identified. Then in 1992, Welsh and his colleagues published a paper in *Nature* explaining that the protein-folding problem could be corrected by chilling the cells. Although this tactic wasn't useable in patients, it allowed "people to say, 'It's misfolded but you can overcome that,' " Welsh says.

Even with these heartening advances in the early 1990s, there were hints that choppy waters lay ahead. The CF protein was a bear to work with because it didn't respond well to classic analytical tools like Western blots and antibody assays, recalls Margarida Amaral, now on sabbatical at the European Molecular Biology Laboratory in Heidelberg, Germany, who worked on the protein at the University of Lisbon in Portugal. "Nothing seemed to work."

In Wilson's lab, meanwhile, postdoc John Engelhardt, now at the University of Iowa, was running into difficulties getting gene therapy to work. The gene's expression varied wildly depending on which parts of the lung researchers examined. One great appeal of gene therapy for CF was that a vector carrying a working CF gene could easily be introduced into the lung with aerosols. But Engelhardt found that only about 1% of cells lining the lung's airway—the cells that come into contact with aerosols—boasted high levels of CFTR protein.

Each advance provoked more questions. When Richard Boucher, an adult pulmonologist at the University of North Carolina, Chapel Hill, won a three-way race to create the first mouse model of CF in 1992, he and others were dismayed to find that the rodents didn't mimic human disease. They shared the gut afflictions of CF patients, who must take pancreatic enzymes for life to break down thick secretions. But the lungs of CF mice, unlike those of their human counterparts, were healthy.

Like Drumm, Boucher traces his passion for CF to a personal experience: His daughter suffered several bouts of pneumonia as a baby and was suspected of having CF. Panicked, he read up on the disease; this drew him to a career teasing apart its mysteries. The CF mouse was a big one: Why were its lungs clear? Boucher and others determined that the animals had a second chloride channel that was unaffected by CF. This led to a new understanding of how the airway surfaces stayed healthy: As long as chloride could pass

1990: Patients with the same gene mutation don't share the same severe disease, suggesting a role for other genes or the environment.

1992: Scientists describe the first mouse model of CF, but the mice don't have lung disease.

1993: A 23-year-old man with CF receives the first dose of gene therapy.

1993: The number of mutations in *CFTR* surpasses 200. Today, we know of over 1500 different mutations.

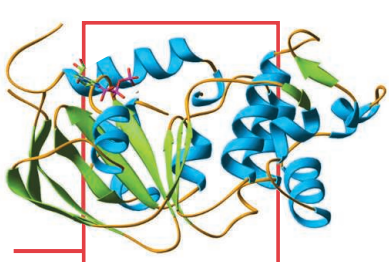

CREDITS: (TOP) ANTOINETTE HILLIAN; (INSET) DOUG MARCHUK; (BOTTOM, LEFT TO RIGHT) COURTESY OF RICHARD BOUCHER; CFF

Published by AAAS

through, the lungs fared well. But in other ways, the mouse proved of virtually no value. It would be 15 years before other researchers found a better animal model.

Meanwhile, gene therapy plowed ahead. In 1993, a 23-year-old became the first CF patient to receive a dose of healthy *CFTR* by gene transfer. Three small clinical trials began: one led by Wilson, one by Welsh, and one by Ronald Crystal at Weill Cornell Medical College in New York City. "Boy, there were all kinds of issues," Wilson recalls. Among them: potent fears that the virus carrying healthy *CFTR* into a patient's nasal passages or lungs would recombine with another virus, be shed by that patient, and "create an environmental catastrophe." Volunteers in the trials were put in strict isolation.

"We have miles to go before we sleep."

—PAUL QUINTON, UC SAN DIEGO

The bigger issue, as it turned out, was that gene therapy simply didn't work. Few lung cells took up the gene. There were also concerns about inflammation, as the lung rebelled against a viral intruder. "You had to confront the reality of eons of evolution" that had built barriers against toxins and infections, says Boucher, who also worked in CF gene therapy. Researchers in the United States spent several more years trying to get around this, tinkering with gene therapy in baboons, rhesus macaques, and other animals, before largely giving up.

Shifting gears

Although the trials failed to help CF patients, they mattered to clinical research: For the first time, viral vectors were injected directly into a patient (as opposed to affected cells being removed, modified, and reinfused), and this became the new model for a nascent specialty. The CF trials also underscored the problem of immune reactions to treatment, which hadn't previously been appreciated, says Wilson.

In a funny way, "science has benefited more from the CF gene than CF has benefited from the science," says John Riordan, a biochemist and, with Tsui and Collins, one of the co-discoverers of the CF gene when he worked at the Hospital for Sick Children. Now at the University of North Carolina, Chapel Hill, Riordan never thought he'd still be working on CF 20 years later. But he points out that CFTR, which belongs to a large family of membrane proteins, is unusual, using several different mechanisms to carry out its functions. As the years passed, biologists studying CFTR learned much about how chloride is transported across cells, and that the protein may also influence inflammation, cell signaling, and other processes. They found that cells build complexes of CFTR and other proteins to keep the system humming.

But what about a cure for this genetic disease, for which there'd been such high hopes? By 1998 or so, researchers knew far more about CF than they had 10 years before. They knew, for example, that hundreds of different mutations in *CFTR* could cause the disease and that not all disabled the protein in the same way—suggesting that different treatments might be needed for different patients. They knew, too, that *CFTR* couldn't explain everything. Some severely affected 12-year-olds needed lung transplants, and some 28-year-olds were running marathons—even when the quirk in their *CFTR* gene was identical. This led researchers to consider that other genes also play a role in CF, as do environmental factors.

None of this was quickly leading to new treatments. "1997, 1998 was really the point where we said, 'Academics are great, but if we really want to discover drugs, we've got to become more businesslike,' " says Robert Beall, president and CEO of the Cystic Fibrosis Foundation. The CF Foundation had been instrumental in funding the gene hunt and subsequent CF research, raising and investing tens of millions of dollars. In the late 1990s, Beall began shopping around plans to develop small-molecule, traditional drugs—back to basics after gene therapy had failed.

"A lot of people thought that Bob Beall was going far out on a limb to put a lot of money into a strategy that was clearly risky," says Collins. Multiple drugs might be needed to tackle different CFTR defects. Companies apparently were wary, too. Beall telephoned seven; two called back. One was Aurora Biosciences in San Diego, California, which was bought by Vertex Pharmaceuticals in 2001. It agreed, with generous support from the CF Foundation, to see what it could do.

Progress at last

More than $75 million and another 10 years later, two Vertex drugs are taking the CF world by storm. One, VX-809, is designed for the most common CF mutation and helps CFTR get to the surface of the cell. Only safety data are available on VX-809 so far.

The other Vertex drug, VX-770, aims to boost the function of CFTR protein that's already made its way to the cell surface—which would help in at least one of the CF mutations, accounting for a few percent of cases of the disease. Last October, Vertex reported that in a phase II trial, lung function of volunteers improved by 12% in 4 weeks of treatment. "That's more than any drug ever improved the disease" in any span of time, says Beall. The excitement around Vertex is so great that at a recent CF fundraising walk, organizers gave two Vertex employees the bib numbers 770 and 809, says Paul Negulescu, a vice president of research at the company's San Diego office. And everyone knew what those numbers meant.

The CF field has enjoyed other recent breakthroughs. In September 2008, Welsh and his colleagues described a CF pig model in *Science*—the first animal model that closely resembles human CF. More recently at Iowa, Engelhardt, who worked in Wilson's lab in the old days and also collaborated on the pig, has developed a CF ferret, the culmi-

Online
sciencemag.org
Podcast interview with author Jennifer Couzin-Frankel.

1995: Gene therapy fails to help CF patients.

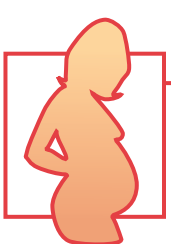

2001: Two medical professional groups recommend prenatal CF carrier screening.

2005: Researchers show that the gene TGFß modifies the severity of CF.

2006: The first drug designed to target a CF protein defect, by Vertex Pharmaceuticals, enters clinical trials.

2008: Pigs become the second animal model of CF.

CREDIT: COURTESY OF GREG DAVIS

Published by AAAS

nation of 10 years' work. (The group spent more than 2 years just trying to understand ferret lung biology.) "Not having good animal models has really slowed the field down," says Engelhardt. Therapies can have harmful side effects, so "when you think about treating a kid before they have overt disease, you've got to be pretty sure you've got a great treatment." Testing in animals offers some reassurance.

Gene therapy, too, is experiencing a resurgence. In the United Kingdom, a team of 80 investigators is launching a 100-person trial using fat particles—unlike the viral vectors in earlier U.S. studies—to carry *CFTR* to cells. The U.K.'s Cystic Fibrosis Trust has dedicated considerable effort, and $50 million, to gene therapy. "Someone needs to find out" if this works, says Eric Alton, a gene therapist at Imperial College London who's heading up the trial, which he hopes will reveal how distant the goal is. "We're either sitting on the therapy, or we're a million miles away from it." Despite earlier setbacks, Alton still feels that gene therapy offers more hope than drugs, because in theory at least, it's more comprehensive. Researchers have found at least 20 functions for the CFTR protein. A drug can correct only one or two at once—whereas gene transfer, if it works, can do it all. Results from Alton's trial, which is just beginning, will come in 2012.

There have been other developments: Prenatal testing is increasingly offered to couples contemplating pregnancy, potentially reducing the number of babies born with CF, although figures are difficult to come by. Forty-seven states and many countries now test newborns for CF, enabling treatment to start right away rather than months or years later, when a child fails to thrive.

Humbling science

Many CF experts say that, after 20 long, frustrating years, it's possible now, finally, to look patients in the eye and assure them that in a few years, treatment will be vastly improved. And patients are optimistic, too. "I can't imagine where we're going to be in another 25 years if it's not cured," says Ryan Ress, a 24-year-old with CF. Ress was Drumm's infant next-door neighbor who inspired the geneticist, now at Case Western Reserve University in Cleveland, Ohio, to stick with CF, and the two remain in touch. Ress majored in biochemistry in college and spent a summer working in a CF lab next door to Drumm's. He's now studying to be a neonatal nurse practitioner. Ress is convinced that CF will be conquered, based on his reading of the disease literature and the belief that "there will be a reward" for CF researchers for their backbreaking years of work.

Needle in a haystack. Capsules, each containing DNA that might harbor the CF gene, filled the freezer in Lap-Chee Tsui's lab in Toronto.

But with lessons learned the hard way, caution abounds, too: "We have miles to go before we sleep," says Paul Quinton, a physiologist at the University of California, San Diego. Quinton is a rare bird. At 20, in college and thinking about his own mortality, he says, he began combing through textbooks in his campus library, hunting for an explanation for the abdominal troubles, chronic cough, and lung problems that had plagued him for years. In books he found an answer: CF. Soon after, Quinton abandoned his dream to become a poet and turned to understanding his disease. In 1983, he determined that chloride transport was the fundamental defect in CF, one of the biggest breakthroughs in the field.

Quinton learned via genetic testing that he harbors one severe mutation and one that's milder, a combination that may explain why he's survived as long as he has. Now 64, he admits that he was as optimistic as the next person when the CF gene was found, even declaring in an editorial in *Nature* that the chance to cure CF had become reality. These days, though, he sees questions everywhere. How, exactly, does normal CFTR function? How does the absence of CFTR lead to the thick mucus of CF? Will even today's most promising drugs work in more than a very narrow slice of patients?

The case of CF, agrees Amaral, is "a lesson in being humble in science."

What does this mean for the flood of genes identified in the years since—both for single-gene diseases and more complex ailments? One shouldn't generalize from the CF story, says the irrepressibly optimistic Collins, former director of the National Human Genome Research Institute, because every disease is different. He knows of at least one—progeria, which causes accelerated aging—in which a gene he helped identify led to a drug within 5 years that's now being tested in nearly every child with the disease.

Collins's early competitor and later collaborator in the CF gene hunt, Tsui, treads more carefully. "Because of the excitement, some scientists, perhaps even disease funding agencies, … wanted to give people hope, or give themselves hope," says Tsui, who in 2002 left Toronto to become vice-chancellor and president of the University of Hong Kong. "They were a little bit optimistic at predicting when a cure would be there. … [It] taught a lesson to other gene researchers." Namely: don't spin prophecies, don't assume that the gene is the end of the story. Rather, it's just the end of the beginning, with a long road still ahead.

–JENNIFER COUZIN-FRANKEL

2008: Forty-seven U.S. states are screening newborns for CF.

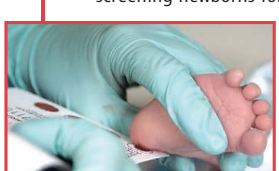

2008: The United Kingdom launches a new CF gene therapy trial.

2009: A gene for type 2 diabetes predisposes children to CF-associated diabetes.

2009: The phase 3 clinical trial for one Vertex drug opens after lung function improved in an earlier study.

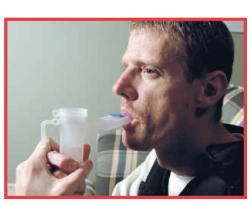

2009: Median life expectancy for those with CF exceeds 37 years old, thanks to more aggressive and earlier treatment.

CREDITS: (TOP) JOHANNA ROMMENS; (BOTTOM, LEFT TO RIGHT): USAF PHOTOGRAPHIC ARCHIVES/WIKIPEDIA; ZUMA PRESS/NEWSCOM

Published by AAAS

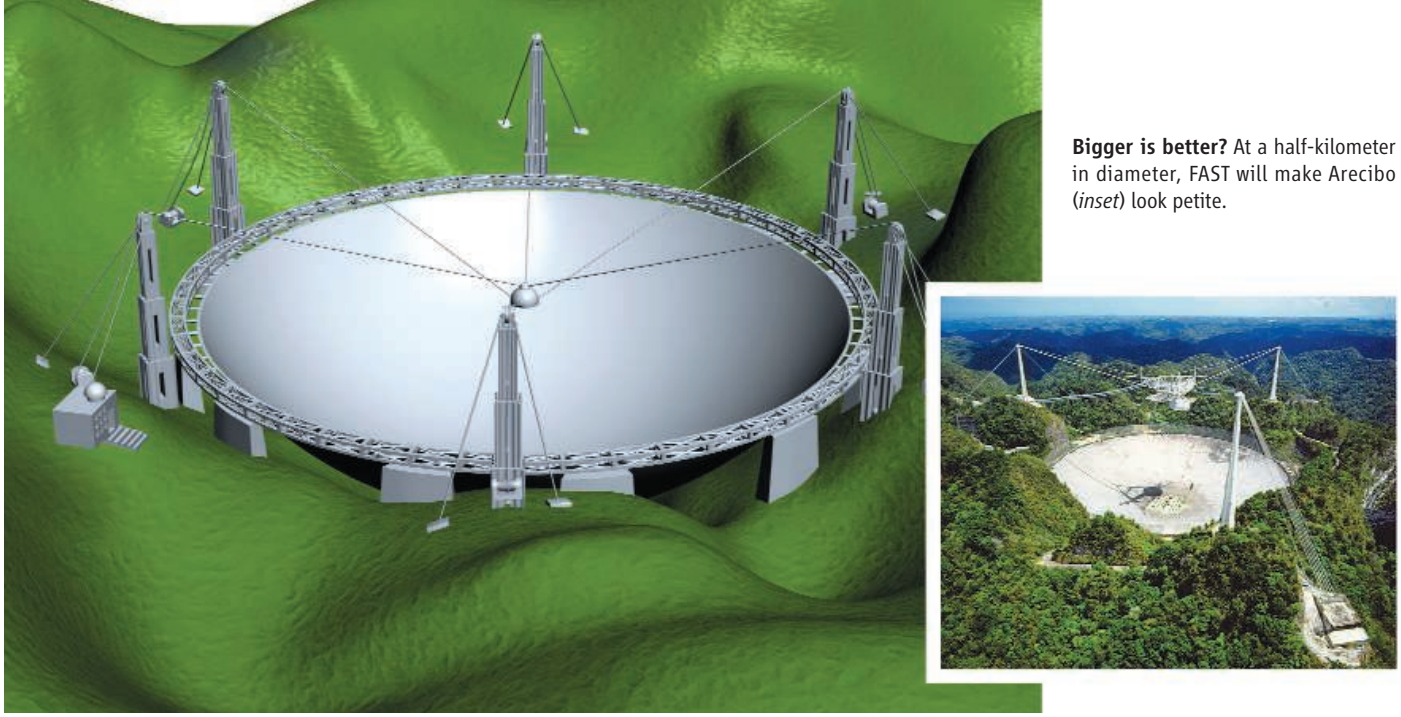

Bigger is better? At a half-kilometer in diameter, FAST will make Arecibo (*inset*) look petite.

CHINA

Radio Astronomers Go for High Gain With Mammoth Telescope

Construction is about to commence on the world's biggest single-dish radio telescope, which will take aim at exotic beasts such as pulsars and dark galaxies

DAWODANG, CHINA—Descending into the limestone valley where China has chosen to build its paramount telescope is a treacherous hike. So steep and vast is the depression that the few dozen villagers who live at the bottom rarely leave.

Scale is precisely what China is going for with the 500-meter Aperture Spherical Radio Telescope (FAST), a massive instrument that the government hopes will thrust China to the forefront of radio astronomy. This month, engineers from the Chinese Academy of Sciences' National Astronomical Observatories in Beijing will drill into this remote corner of Guizhou Province for a final round of geoengineering studies before breaking ground later this year. When FAST sees first light in 2014, it will measure more than five football fields in diameter, making it the largest single-dish radio telescope in the world.

FAST is modeled on Arecibo, the 305-meter-diameter radio telescope cradled in a limestone karst valley in Puerto Rico—a sight so arresting that the dish is a popular setting for science-fiction movies. But with a collecting area twice that of Arecibo's, FAST will be even more striking. "It's going to be an extremely impressive project," says Donald B. Campbell, an astronomer at Cornell University and associate director of the National Astronomy and Ionosphere Center, which operates Arecibo. "We're expecting them to do some good science with it."

Nearing the finish line. Nan Rendong has been laying plans for FAST since the early '90s.

Since Arecibo was completed in 1963, radio astronomy has charted some important advances. Key among these is the development of radio interferometry, or antennas linked in a network to achieve high resolution and high frequency by covering a wide geographic area. Today's radio telescopes include both interferometric arrays and single dishes, which operate at a lower resolution but simplify data collection. "You can build a large number of small dishes, or you can build a small number of large dishes," says Nan Rendong, FAST's chief scientist and engineer.

China's decision to opt for a single dish was partly strategic. "I looked around and thought, 'We cannot compete in phased arrays,' " Nan says. Even so, astronomers say single-dish telescopes are valuable for studying everything from magnetic fields to pulsars. FAST's jump in size will mean a leap for astronomy in those areas.

FAST will boast twice the sensitivity of Arecibo, allowing astronomers to cut through cosmic dust to detect weaker signals from a greater distance. And although Arecibo can eavesdrop on a swath of sky ranging 20 degrees from the zenith, FAST will tune in signals from an arc twice as wide, a difference that will expand access to parts of the universe out of Arecibo's reach. "They will be able to sample a large portion of the Milky Way," says James M. Cordes, a radio astronomer at Cornell who observes at Arecibo. That's important, he says, for surveying pulsars and using the rapidly spinning neutron stars to shed light on gravitational waves and general relativity in our galaxy.

Plans for China's behemoth dish date to the early 1990s, when astronomy in the country was opening up to the outside world. In 1993, astronomers from China joined colleagues from around the globe in Kyoto for an International Union of Radio Science meeting, at which they discussed plans for a Large Telescope, the precursor to today's international Square Kilometre Array (SKA). The next year, Nan and Peng Bo, both of National Astronomical Observatories, began surveying sites in western China.

The astronomers saw Arecibo as a compelling model, figuring that they could

CREDITS (TOP TO BOTTOM): NATIONAL ASTRONOMICAL OBSERVATORIES BEIJING; (INSET) COURTESY OF NAIC - ARECIBO OBSERVATORY, A FACILITY OF NSF; COURTESY OF NAN RENDONG

reproduce the dish with updated technology. It helped that China abounds in karst, much of it in underdeveloped areas with low radio interference. "FAST takes advantage of our geography," says Shen Zhiqiang, an astronomer at the Shanghai Astronomical Observatory.

In the mid-1990s, at the Beijing observatory's request, the Chinese Academy of Sciences' Institute of Remote Sensing Applications surveyed karst formations in southwest China using QuickBird satellite photos. Nan and his colleagues looked for round, uniform sinkholes that were middle-aged in geological terms, meaning they weren't yet filled with debris from erosion. Smaller candidates were marked for China's SKA proposal—the Kilometer-square Area Radio Synthesis Telescope (KARST), which would have entailed a series of 200-meter reflectors spread out over 30 smaller depressions. A larger depression was reserved for FAST, described as an SKA prototype.

China's plan disintegrated in 2006, when SKA's steering committee opted for an array of smaller antennas, a choice that ensures better imaging. But preparations for FAST continued. Last year, China's National Development and Reform Commission authorized $97 million for the project. By that point, Nan and his colleagues had settled on Dawodang, a nearly perfectly circular valley ringed by karst peaks. Spaced between the peaks will be six towers strung with cables supporting FAST's focus. Curving down from the towers will be the dish itself.

For searches that require sensitivity but not imaging, a single dish offers quicker processing speeds. "If you look back at the history of Nobel Prizes for physics, several have been awarded for work done using a single dish," says Nan. For example, Russell Hulse and Joseph Taylor Jr. of Princeton University discovered binary pulsars using Arecibo in 1974, a landmark find that earned them the 1993 prize.

FAST will be structurally different from its U.S. cousin, however. Arecibo's focus is suspended over its reflector by a 900-ton movable platform, a design that is both unwieldy and expensive at a larger scale. FAST's reflector will instead do the tweaking through 4600 adjustable parabolic plates, and the cabin containing its focus will be lighter.

More critical to the science, FAST will have 19 feed horns, whereas Arecibo currently has just seven. That will allow FAST's surveys to be conducted with more sensitivity or, well, FASTer. That's a boon for observations, says Nan: "If you have a larger field of view, it's much easier to capture blinking transient phenomena" such as comets, meteors, and supernovae.

KARST's home. Before construction of the gigantic dish can begin, Huang Huamei and other villagers must be resettled.

A chief astronomical target for the new telescope is pulsars. Arecibo has excelled at pulsar hunting, and FAST's heightened sensitivity means it should find many more. Once the Chinese scope starts looking for pulsars, in just 230 days of operation it stands to increase the number of known pulsars nearly fourfold to about 7000, says Richard Manchester, a pulsar expert at Australia's Commonwealth Scientific and Industrial Research Organisation who served on a panel that evaluated FAST in 2006. Astronomers hope at least one of the new crop will be a pulsar orbiting a stellar-mass black hole, which would enable them to test general relativity and other theories with great precision. "That's one of the holy grails of astronomy," Manchester says.

Neither Arecibo nor FAST are in the right location to tune in to chatter from Sagittarius A*, the black hole believed to lie at our galaxy's center; SKA is better positioned for that task because it will be sited in the Southern Hemisphere, in Australia or South Africa. But FAST's high sensitivity will expand knowledge of distant galaxies that formed when the universe was young. Specifically, FAST will enable astronomers to detect the weak hydrogen line that is crucial to locating starless clusters of dark matter known as "dark galaxies." "They are little beacons out there that could be used for studying the structure of the universe," says Richard Strom, an astronomer at the Netherlands Institute for Radio Astronomy in Dwingeloo who has advised China on FAST.

On a more fantastic quest, Nan hopes the telescope will advance the search for extraterrestrial intelligence (SETI). Under Project Phoenix, the SETI Institute in Mountain View, California, has surveyed about 800 sunlike stars using Arecibo and other radio telescopes. Nan says FAST will increase that number to 5000. Uncovering signs of life in other solar systems is a "long shot," says Manchester. "But it's something that FAST might be able to do."

For now, however, FAST's founders are training their sights on the rugged landscape of southeastern Guizhou. "It's a huge construction job," notes Arecibo's Campbell. In April, engineers visited Dawodang to survey the site and inspect locations for the telescope's towers. After this month's drilling is completed, workers will widen the canals leading out of the valley to ensure that monsoon rains don't turn FAST into the world's largest swimming pool.

Among the remaining challenges is relocating the dozen families who have been eking out a subsistence living in the karst depression for as long as anyone can remember. The local government is building two-story houses for the villagers several kilometers away, but they're reluctant to move. "I haven't left [Dawodang] for 10 years," says 74-year-old Huang Huamei.

Once the farmers are resettled, FAST's construction team can bring in bulldozers and lay the colossal dish's foundations. The project is running a few months behind schedule. But when the telescope is complete, the country will have an instrument of epic proportions. Cue the film crews.

–MARA HVISTENDAHL

Mara Hvistendahl is a writer in Shanghai.

CREDITS: MARA HVISTENDAHL

Published by AAAS

ECONOMIC RECOVERY

ISO . . . 3.5 Million U.S. Jobs

Economists are shaking their heads at the Obama Administration's claim to be able to count the jobs that will flow from the stimulus package

Last week, the White House announced that the massive stimulus package approved this winter has created or saved more than 150,000 jobs in its first 100 days. The next 100 days will add another 600,000 jobs, predicted Jared Bernstein, economic adviser to Vice President Joe Biden, whose office is responsible for tracking the impact of the nation's $787 billion spending spree, known officially as the American Recovery and Reinvestment Act (ARRA).

In fact, no data on job creation yet exist. The numbers come from economic models. "Once you know the spend-out and the type of spending that you're engaged in, then you can derive an estimate of how many jobs you believe you created relative to what would have occurred in the job market were you not doing that spending," Bernstein explained. "This is an absolute tried-and-true economic methodology." In a May report on job creation, the President's Council of Economic Advisers (CEA) does not sound quite so confident, stating that "this is an exercise that should be done despite [a] likely large margin of error."

Welcome to Economics 101, Washington-style. When he signed it into law in Denver, Colorado, on 17 February, President Barack Obama proclaimed that ARRA "will create or save three-and-a-half-million jobs over the next 2 years, including nearly 60,000 in Colorado." Most economists take such predictions with more than a grain of salt. In normal times, they say, modeling can do a fair job at coming up with useful prognostications. But in times like these, as Princeton University economist Harvey Rosen puts it, "all bets are off."

Phillip Swagel, former chief economist at the Treasury Department, says that CEA has tried so hard to be specific about job creation over time and in individual states that its numbers are "as close to meaningless as you can get." What's more, says economist Andrew Reamer of the Brookings Institution in Washington, D.C., even if the numbers turn out to be right, ARRA contains no provisions for predicting the longer term contributions to the economy. "You can have a lot of jobs [in which] people are just chasing their tails," Reamer observes.

There's also a political dimension to counting jobs, says Donald Marron, a member of CEA under President George W. Bush. Recipients of ARRA money, he says, "have a lot of incentive to make this look effective." That could lead, he says, to reports of jobs being "saved" that in fact were never slated for the chopping block.

Observers give the White House credit for doing its darnedest to try to make sense of the confusion. Even before Obama took office, economists worked feverishly to calculate the job impact of a recovery plan, anticipating that the package would be in the neighborhood of $770 billion in tax cuts, "fiscal relief" to states, and direct government spending. In January, 10 days before the inauguration, Bernstein and Christina Romer, now chief of CEA, predicted that 3,675,000 jobs would have been created or retained by September 2010.

That number came with some footnotes, however. It features three definitions of the word "job"—direct, indirect, and induced—offered in two flavors—created and preserved. Relying heavily on a quarterly macroeconomic model of the U.S. economy from the Federal Reserve Board and data from economy.com, a Web site run by Moody's Investors Service, Bernstein and Romer predicted that the stimulus would increase gross domestic product by 3.7%. Each percentage point corresponds roughly to a 1% increase in employment, or 1 million jobs. Tax cuts are responsible for about 1 million jobs, with the rest being generated by infusions of cash into numerous state and federal programs. Construction projects alone claim 18%, the largest single share.

But Bernstein and Romer didn't stop there. They went on to make state-by-state and industry-by-industry employment estimates. The state analyses drew upon three sets of data: the working-age population of the state; the state's proportion of total U.S. employment; and employment in particular industries as of 2007. A state with 10% of the nation's aluminum manufacturing jobs was assumed to get 10% of the jobs created or retained in that industry as of the end of 2010. Bernstein's estimate of 150,000 new or salvaged jobs—the models can't predict which they are—was based on such assumptions.

In their January report, Bernstein and Romer forecast an unemployment rate by the middle of 2009 of about 8% with the stimulus, and 8.5% without it. When the May unemployment rate, announced last week, turned out to be 9.4%, Bernstein didn't miss a beat. Even though the economy contracted more violently than expected in late 2008, he

CREDITS: PHOTOS.COM

Published by AAAS

Defining a job. A highway contract can also generate "indirect" jobs for parts suppliers and "induced" jobs for waitresses.

said, the expectation of 3.5 million jobs from the Recovery Act remains intact.

That economic legerdemain highlights a point made by critics of the approach: With no baseline—there is no parallel universe with an unstimulated U.S. economy—there is no way to test the prediction. Rosen, who also served in Bush's CEA, says the Obama Administration can take credit for millions more jobs regardless of what happens to the economy. "I'm not claiming that the Bush Administration would do it any better," adds Rosen. Rather, he says, following conventional models "makes more sense when things are proceeding normally."

Telling Uncle Sam

How, in fact, do you know when a job is "sustained" that might otherwise have been lost? How can you distinguish a "created" job from one that is being filled by someone who already had one? And what's the definition of a job, anyway? In May, CEA said it anticipates that ARRA jobs will fall into three categories. The first is those financed directly from stimulus money. The second type is created "indirectly": when a cement company, for example, gets business from a highway contractor receiving ARRA money. The third kind is "induced," for example, a waitress hired to serve workers employed on a nearby ARRA-funded construction project, or a mall employee serving customers spending their tax rebates.

CEA hasn't figured out a way to separate direct from indirect jobs, but it predicts that the two categories, combined, will account for about two-thirds of job creation or retention. Induced jobs make up the rest. For example, ARRA's $288 billion in tax cuts will lead to about a million jobs by CEA's calculations. But the council acknowledges that "there is no mechanism available [in ARRA] for collecting data on actual job creation" either from tax cuts, from $81 billion in payments to people hurt by the recession, or from the $144 billion in "fiscal relief" to states.

The burden of reporting how many jobs have been created or preserved will fall upon those who receive the $271 billion in direct government spending. That mechanism, which includes stimulus money flowing to academic research projects, is also expected to generate the biggest bang for the buck in jobs, according to CEA, which estimates that a contract or grant worth $92,000 translates into one job for 1 year.

The rules for how to report job creation or preservation were due out this week, according to the Office of Management and Budget (OMB). Preliminary OMB guidelines say that quarterly reports should include "a narrative description of the employment impact," including estimates of numbers of jobs created or retained, measured as full-time equivalent positions.

However it is defined, the task of counting jobs won't be easy. "They're not going to have a clue," says a government economist who asked not to be quoted by name. In addition to the elusive nature of the jobs themselves, there's also the question of duration. Many jobs are like fireflies, flashing on one minute, off the next. "Fifteen percent of jobs last for less than a quarter [of the year]," says labor economist Julia Lane, director of a new program at the National Science Foundation called the Science of Science and Innovation Policy. That transient nature is at odds with CEA's definition of a job retained as "an existing position that would not have been continued were it not for ARRA funding." Continued, but for how long?

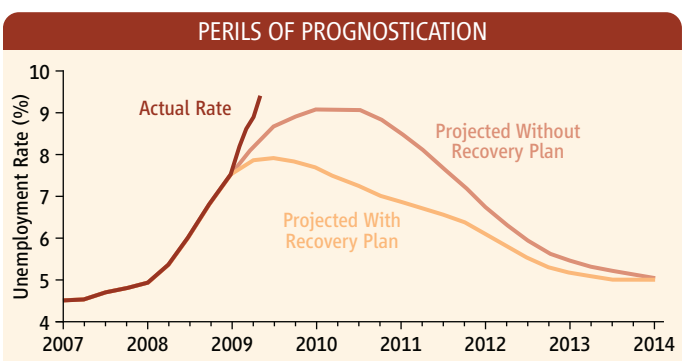

Keeping it real. The unemployment rate as of May was higher than January projections with or without the stimulus.

SOURCE: ROMER AND BERNSTEIN/U.S. BUREAU OF LABOR STATISTICS

Universities and state and federal agencies are scrambling to figure it all out, and their strategies are likely to vary by type of recipient. In academia, for example, there's the question of whether a graduate student counts as an employee or a student. Even if universities gear up to collect data that relates to job creation or retention, questions remain. "There's a lot of concern in the community about how we could, even with the best of guidance, ensure that we report comparable data," says Tobin Smith of the Association of American Universities in Washington, D.C. "What kind of work can be counted toward a job retained? If one university counts one way and one another, then none of the data becomes comparable."

Lane hopes to find a way out of the swamp, taking an approach that is intended to relieve scientists of most of the burden. It calls for coordinating administrative records that already exist within the offices of finance, human resources, and research at most universities. Creating an administrative tracking system would mean developing uniform definitions of what is a "created" and what is a "retained" job, she says. There would still be issues of privacy and confidentiality, feasibility, and cost. But, she says, such a system shouldn't be too costly because the data will already have been generated. Lane says a pilot project is planned at perhaps a half-dozen universities.

Prem Paul, vice chancellor for research and development at the University of Nebraska, Lincoln, thinks that such a system would be "extremely helpful." Research universities are setting up Web sites and advertising positions to help administer the expected windfalls from ARRA, which includes $21.5 billion for R&D. Paul says Nebraska is applying for a total of $75 million in ARRA funds, and the university will have to hire "hundreds" of additional staff to do the reporting if all the applications are successful.

Although universities are required to report only on "direct" job creation, recipients of other types of funding, such as from the Department of Transportation, must track not only direct but also indirect jobs from billions of dollars in construction projects. The Federal Highway Administration alone will be doling out $26.7 billion to states and localities for highway construction and maintenance. The department plans to tell funding recipients to use expenditure data and apply rules of thumb supplied by the CEA such as the $92,000-per-job-year figure.

One thing that is already clear is that ARRA is having a salubrious effect on government job creation. Thousands are being hired to send out the checks and to handle reporting from ARRA recipients. Using job reports that are starting to pour in, CEA hopes that its next report in August will contain some real numbers. But theory—some would say guesswork—will still loom large.

–CONSTANCE HOLDEN

Published by AAAS

PHYSICS

Is Quantum Mechanics Tried, True, Wildly Successful, and Wrong?

A skeptical physicist charges that his field has been wandering in a philosophical wilderness for 80 years. The good news: He thinks he knows the way out

Antony Valentini has never been happy with quantum mechanics. Sure, it's the most powerful and accurate scientific theory ever devised. Yes, its bizarre predictions about the behavior of atoms and all other particles have been confirmed many times over with multi-decimal-place exactitude. True, technologies derived from quantum mechanics may account for 30% of the gross national product of the United States. So what's not to like?

Valentini, a theoretical physicist at Imperial College London (ICL) and the co-author of a forthcoming book on the early history of quantum mechanics, believes that shortly after the theory's birth some 80 years ago, a cadre of influential scientists led quantum physics down a philosophical blind alley. As a result of that wrong turn, Valentini says, the field wound up burdened with paradoxical dualities, inexplicable long-distance connections between particles, and a pragmatic "shut up and calculate" mentality that stifled attempts to probe what it all means. But there is an alternative, Valentini says: a long-abandoned "road not taken" that could get physics back on track. And unlike other proposed remedies to quantum weirdness, he adds, there's a possible experiment to test whether this one is right.

"There isn't a more insightful or knowledgeable critic in the whole field of quantum theory," says Lee Smolin, a theoretical physicist at the Perimeter Institute for Theoretical Physics in Waterloo, Canada. Smolin, who researches a subfield known as quantum gravity, has long held that current quantum theory is incomplete at best.

In a book to be published later this year by Cambridge University Press, Valentini and co-author Guido Bacciagaluppi, a philosopher of physics at the University of Aberdeen in the United Kingdom, reassess a pivotal and contentious meeting at which 29 physics luminaries—including Louis de Broglie, Niels Bohr, Werner Heisenberg, Erwin Schrödinger, and Albert Einstein—butted brains over how to make sense of quantum theory.

The book, *Quantum Theory at the Crossroads*, includes the first English translation of the proceedings of the historic 1927 Solvay conference. The gathering was the fifth in an ongoing series of invitation-only conferences in Brussels, Belgium, launched in 1911 by the Belgian industrialist Ernest Solvay. At the meeting, blandly titled "Electrons and Photons," attendees grappled with issues that were—and remain—among the most perplexing ever addressed by physicists. Quantum mechanics confounds commonsense notions of reality, and the physicists in Brussels disagreed sharply about the meaning of the theory they had created.

"Quantum physics ... is a special case of a much wider physics, with many new possible phenomena that are just there waiting to be explored."

—ANTONY VALENTINI
IMPERIAL COLLEGE LONDON

A classic experiment demonstrates the sheer strangeness of the new physics they were struggling to understand. Light—a stream of photons—shines through two parallel slits cut in a barrier and hits a strip of film beyond the slits. If the experiment is run with detectors near each slit so physicists can observe the passing light particles, the result is unsurprising: Every photon goes through either one slit or the other, just as particles should, leaving two distinct clusters of dots where the individual photons strike the film.

Remove the detectors, however, and something exceedingly strange happens: A pattern of alternating light and dark stripes appears on the film. The only explanation is that photons sometimes behave like waves. As light waves emerge from the two slits, bright lines form on the screen where wave crests overlap; dark lines, where a crest and trough cancel each other. As long as no detectors are present, the same pattern appears even if the photons hit the screen one by one. Over the decades, physicists have tried the experiment with photons, electrons, and other particles, always with the same bizarre results.

The experiment highlights two of the conundrums that dominated discussions at the 1927 Solvay conference: How can photons, electrons, and all other bits of matter and energy behave like waves one moment, particles the next? And how does one explain that the mere act of observation seems to affect physical reality—at least on the quantum level?

Unreality rules

Bohr and Heisenberg answered such questions with an austere vision of the theory now called the Copenhagen interpretation. With no observer present, they said, any given particle exists here, there, and everywhere in between, dispersed like a wave. Introduce an observer to measure the wave, however, and the quantum wave "collapses" into a single particle. Before the measurement, the particle could be described only by an equation that specified the probability of finding it in one location rather than another. The act of measurement itself forces a particle to assume a single, definite position. The sharp boundary between an objective world "out there" and subjective observations blurs in this version of quantum theory.

"Bohr believed that it was meaningless to try to describe the quantum world because we have no direct experience of it," says Valentini. "Bohr and Heisenberg thought that quantum mechanics showed we had reached the limits of human understanding. … Physics no longer told us how things *are*—it only told us how human beings perceive and measure things."

Some conference participants, most notably Einstein, de Broglie, and Schrödinger, rejected Bohr's arguments. Physicists today remember Einstein as Bohr's chief antagonist. But their famed disputes over the validity of quantum theory must have taken place off the record, Valentini says; the published conference proceedings don't mention them at all.

The proceedings do, however, contain 24 pages of discussion of a rival interpretation by de Broglie. Unlike Bohr, who viewed the quantum wave equation describing a particle as a mathematical abstraction, de Broglie

CREDIT: COURTESY OF ANTONY VALENTINI

Published by AAAS

Debate team. Physicists at the 1927 Solvay conference clashed over quantum enigmas.

CREDITS (FROM TOP): PHOTOGRAPH BY BENJAMIN COUPRIE, INSTITUT INTERNATIONAL DE PHYSIQUE SOLVAY; W. F. MEGGERS GALLERY OF NOBEL LAUREATES; PHOTOGRAVURE BY A. BORTZELLS TRYCKERI, WEBER COLLECTION; (ALL) COURTESY AIP EMILIO SEGRE VISUAL ARCHIVES

thought such waves were real—he called them pilot waves. In de Broglie's picture, particles never exist in more than one place at the same time. All the mysterious properties of quantum theory are explained by pilot waves guiding particles along their trajectories. In the two-slit experiment, for example, each particle passes through only one slit. The pilot wave, however, goes through both slits at once and influences where the particle strikes the screen. There is no inexplicable wave collapse triggered by observation. Instead, Valentini says, "the total pilot wave, for the particle and the detectors considered as a single system, evolves so as to yield an *apparent* collapse."

Bohr, Heisenberg, and their supporters at the Solvay conference were unimpressed. The details of the particle trajectories were unobservable, and Bohr insisted that physicists shouldn't traffic in hidden, unmeasurable entities. "De Broglie wasn't happy with the Copenhagen interpretation," says Valentini, "but he gave up trying to argue about it."

Bohr and Heisenberg's vision of quantum theory prevailed; de Broglie's languished. David Bohm, a prominent American physicist, rediscovered de Broglie's work in the early 1950s and expanded on it. But Bohm's work, like de Broglie's, failed to attract much support, because it could not be distinguished experimentally from conventional quantum mechanics.

The past decade has seen renewed interest in understanding the foundations of quantum mechanics, and physicists have devised several competing interpretations of the theory (*Science*, 25 June 2004, p. 1896). Valentini has been in the thick of this quantum renaissance. In the early 1990s, as a graduate student studying with the late Dennis Sciama, a cosmologist who also mentored Stephen Hawking, he learned about the work of de Broglie and Bohm and became convinced that it had the potential to resolve all the mysterious paradoxes of quantum mechanics. He has spent most of his career almost singlehandedly building on their work.

His single-mindedness has cost him. Although Valentini's colleagues acknowledge the originality and importance of his research, spadework on the foundations of quantum theory has not been a fast track to tenure. For years, he has survived from grant to grant in a succession of temporary positions; his current one at ICL ends this year.

"I used to do private teaching just to get by," Valentini says. "Things have changed in recent years, but I'm still just living year by year. It is a field where there are these wide-open, in-your-face problems with interpretation that are staggeringly fundamental, with virtually nobody in the world really dedicating the bulk of their time and attention to working on them. So how do you expect there to be much progress?"

Beyond the quantum?

In Valentini's physics, the "laws" of quantum mechanics are not really laws at all but accidents of cosmic history. Particles in the universe today conform to the supposed rules of quantum mechanics, Valentini suggests, because they settled into a sort of quantum equilibrium immediately after the big bang, in a process roughly analogous to the way a mixture of hot and cold gases gradually reaches a uniform temperature. Immediately after the big bang, particles could have existed in states not allowed by the normal rules of quantum mechanics but permitted in pilot-wave theory.

At odds. Niels Bohr (*left*) blasted Louis de Broglie for trying to link the quantum world to familiar reality.

"Quantum physics is not fundamental; it's a theory of a particular equilibrium state and nothing more," says Valentini. "To my mind, pilot-wave theory is crying out to us that quantum physics is a special case of a much wider physics, with many new possible phenomena that are just there waiting to be explored and tested experimentally."

The place to look, Valentini says, is in the cosmic microwave background (CMB), the remnant radiation from the big bang that fills all of space. The radiation is almost perfectly uniform, with only slight variations in temperature. Theorists think those small temperature differences resulted from quantum fluctuations that were magnified as the universe expanded. In a paper Valentini has submitted to *Physical Review D*, he argues that if his pilot-wave theory is correct, some of those temperature variations will not have the distribution that standard quantum theory predicts. Deviations are more likely to survive at long wavelengths, he says. CMB measurements by the WMAP probe have revealed "intriguing" anomalies in precisely that domain, Valentini says, but pursuing them will take time and effort. "I need to do a lot more work to refine my predictions," says Valentini. "Part of the problem is that I'm the only person working on it. It is a difficult thing."

Confirmation of Valentini's idea would be one of the biggest advances in physics in decades. The Planck spacecraft, launched in May by the European Space Agency (*Science*, 1 May, p. 584), will take a closer look at CMB and could conceivably find evidence supporting Valentini's predictions.

"One of the most attractive features of Antony's proposals is that they're testable," says David Wallace, a philosopher of physics at the University of Oxford in the United Kingdom. "If tomorrow there is some experiment that Antony's theory gets right and quantum mechanics gets wrong, then end of story."

Valentini knows he faces steep odds. "Maybe in 200 years people will look back and say the time wasn't right to reexamine the foundations of quantum mechanics," he says. "Or it might be that they'll say, 'My God, it opened up a whole new world.' We can't tell. One thing is certain: We won't find out if we don't try." **–TIM FOLGER**

Tim Folger is a contributing editor at *Discover*.

LETTERS

edited by Jennifer Sills

Venezuelan Science at Risk

THE VENEZUELAN ACADEMY OF PHYSICAL, MATHEMATICAL, AND NATURAL SCIENCES WOULD like to share with the international scientific community our fears for the present and future fate of science and higher education in our country. A number of worrisome recent events and our interpretations of their implications motivate our concern:

1. The president of our country has stated what he believes science should be in Venezuela and has created his own initiatives for workable lines of scientific research (*1*).

2. At all levels of the national scientific establishment, inexperienced professionals with little scientific or technical knowledge or background have been appointed to positions of authority. They have been chosen on the basis of their loyalty to the political party in power. This approach precludes a constructive dialogue with the R&D community and curtails academic freedom of research.

3. The Ministry of State for Science, Technology, and Intermediate Industries controls discretionary use of resources collected from the private sector (*2*). Some of these resources, which were previously allotted to researchers according to the nature and quality of their research proposals, are now being centralized and distributed according to the "social aim" of the research proposal.

4. The government has decided to create some 40 new universities but has not published a plan to provide them with suitable academic staff.

5. Universities and centers of research have been subjected to drastic budget cuts, which severely affect most current research programs. Restrictions have been imposed on the acquisition of scientific literature and information, as well as of access to the Internet (*3*).

6. The loss of intellectual capital to the United States, Canada, Mexico, Brazil, France, Spain, and other countries has accelerated (*4*). Young scientists, technology experts, physicians, and engineers are leaving the country. The process started in 2003 with the firing of more than 800 researchers from the Venezuelan Institute of Petroleum Research.

7. We believe that Dr. Raimundo Villegas, an emblematic researcher of Venezuela and founder of the Institute for Advanced Studies (IDEA), a wide-scope research institute, was forced into retirement by the Directory from his post of tenured professor of IDEA. His departure was accompanied by the cessation of IDEA's support of the Latin American Academy of Sciences (ACAL) (www.acal-scientia.org/); this support was stated in ACAL's foundation charter. ACAL has an office in Venezuela that has been headed by Dr. Villegas since its creation 25 years ago.

8. Dr. Jaime Requena, who had applied for retirement, was instead fired from his tenured post at IDEA. This appears to have been a result of a personal decision of the Institute Director, as it occurred without the expected and due legal procedures.

The above-mentioned observations represent just a fraction of the many actions that clearly reveal an aim of the government to control all of the national scientific activity and the higher education system, putting Venezuela's scientific activities at risk.

CLAUDIO BIFANO

President of the Venezuelan Academy of Physical, Mathematical, and Natural Sciences (ACFIMAN), Caracas, Venezuela. E-mail: cbifano@acfiman.org.ve

References

1. B. Casassus, *Science* **324**, 1126 (2009).
2. Gobierno Bolivariano de Venezuela, Fonacit; www.fonacit.gob.ve/locti/.
3. Gaceta Oficial Numero 38.145, 25 March 2009.
4. I. de la Vega, *Mundos en Movimiento: El Caso de la Movilidad y Migración de los Científicos y Tecnologos Venezolanos* (Ediciones Fundacion Polar-IVIC, Venezuela, 2005).

Cataloguing Names the Old-Fashioned Way

IN HIS NEWS FOCUS STORY "ARE YOU READY to become a number?" (27 March, p. 1662), M. Enserink clearly explains the importance of successful name disambiguation in scholarly online databases and the difficulty in achieving it. Moreover, it's refreshing that the scientific community has recognized the depth of the name ambiguity problem and that researchers have finally realized that computer algorithms alone are not up to the task of separating authors with the same or similar names.

Unfortunately, the article fails to describe a name disambiguation system that has been practiced successfully for over a century: the system used by library cataloguers. Library cataloguing codes prescribe consistent rules for creating a unique name heading, or identifier, for each author. Each heading is preserved in a file called a name authority record, and every record includes a unique number, so the records are both human-friendly (the name heading) and computer-friendly (the number). These records, maintained by the Library of Congress, are open-access and easily transferred from one system to another. Moreover, the records contain cross-references that lead searchers who are using an outdated or variant form to the correct one, including cross-references from non-Roman scripts to Roman ones. Equally important, cataloguing rules state that name headings should be based on how the author's name appears in his or her own publications, a practice that respects the author's own practice and avoids the stigma of being a mere number.

Algorithmic failures (*1*) to achieve quality name disambiguation parallel similar weaknesses in information retrieval systems (*2*) that rely on full-text searching and probabilistic relevance ranking. These failures demonstrate

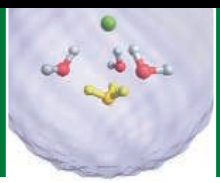

An acidic breakup
1522

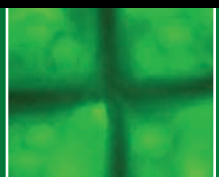

Life in saline habitats
1523

that artificial intelligence has not advanced as much as we would like. Name disambiguation, like information retrieval, needs a deterministic approach and human intervention to be successful and precise.

JEFFREY BEALL

Metadata Librarian, University of Colorado Denver, Denver, CO 80204, USA. E-mail: jeffrey.beall@ucdenver.edu

References

1. Q. M. Vu *et al.*, *Inform. Process Manag*. **44**, 1546 (2008).
2. J. Beall, *J. Acad. Libr*. **34**, 438 (2008).

Too Much Quantification Hinders Creativity

IN HIS NEWS FOCUS STORY "ARE YOU READY to become a number?" (27 March, p. 1662), M. Enserink discusses several new initiatives that would assign each scientist a unique identifying number, used to link all of a given individual's scientific writing. These new über-databases would supposedly make our published writings readily attainable, easily catalogued, and quantifiable.

Scientists and publishing corporations soliciting the use of über-databases claim that this will help review boards that are currently abusing indices such as impact factor. This logic is flawed. Instead of applying common sense to assess the quality of the reviewed scientists, review boards take the easy path and rely on numbers such as the total number of publications and their impact factor. Further quantification of scientific output—through ResearcherID, Scholar Factor, or a new numeric identifier—will increase the dependence of these boards on quantitative measures of productivity.

These factors, by definition, describe the mainstream of the scientific population and research. Increased use of these bean-counting measures will lead to exclusion of nonconformist scientists from our system. However, the very essence of excellent science resides in nonconformity and multidisciplinary thinking. Imposing more rules as requirements for academic survival will narrow the paths by which scientists can travel. In the long run, these limits will greatly damage the creativity of scientists. Science is quantitative, but quantification of scientific creativity may result in its destruction.

MERON GURKIEWICZ AND ALON KORNGREEN*

The Mina and Everard Goodman Faculty of Life Sciences and The Gonda Multidisciplinary Brain Research Center, Bar-Ilan University, Ramat-Gan 52900, Israel.

*To whom correspondence should be addressed. E-mail: korngra@mail.biu.ac.il

Livestock Genomics in Developing Countries

THE RECENT REPORTS ON THE BOVINE GENOME in the 24 April issue ("The genome sequence of taurine cattle: A window to ruminant biology and evolution," The Bovine Sequencing and Analysis Consortium *et al*., p. 522, and "Genome-wide survey of SNP variation uncovers the genetic structure of cattle breeds," The Bovine HapMap Consortium, p. 528) highlight the enormous potential of genomics to increase the understanding of genetic variation of livestock and to provide benefits for well-planned utilization of animal genetic resources for food and agriculture. Genomic selection (*1*) is already being applied to commercial livestock populations and is expected to increase selection response and decrease the costs of phenotyping relative to conventional approaches. The opportunities of genomics may be even greater for local breeds, in developing countries, assuming that complementary animal identification and recording can be established. Genetic variation is greater than in commercial breeds and projected increases in demand for animal products are much larger in developing than developed countries (*2*).

Unfortunately, genomics also presents risks for the sustainable management of animal genetic resources in these countries. Historically, genetic improvement in productivity has commonly been achieved by importation of germplasm and cross-breeding, rendering within-breed improvement less attractive. Increases in productivity have been limited, however, by the poor adaptation of imported breeds to vastly different, and generally harsher, production environments than those in which they were selected. Increasingly precise selection in the same favorable environments is unlikely to overcome this limitation and may even decrease genetic diversity and adaptability. The maximum utility of livestock genomics can only be achieved with research, including collection of phenotypes and genotypes, on developing country breeds (and cross-breeds) in their natural environment. The Bovine HapMap analysis, which included two African and several *Bos indicus* breeds, is an encouraging start, but must be followed through with continued academic and financial investment.

PAUL J. BOETTCHER* AND IRENE HOFFMANN

Animal Production and Health Division, Food and Agriculture Organization of the United Nations, Rome 00153, Italy.

*To whom correspondence should be addressed. E-mail: paul.boettcher@fao.org

References

1. T. H. Meuwissen, B. J. Hayes, M. E. Goddard, *Genetics* **157**, 1819 (2001).
2. FAO, *The State of the World's Animal Genetic Resources for Food and Agriculture,* B. Rischkowsky, D. Pilling, Eds. (FAO, Rome, 2007).

Letters to the Editor

Letters (~300 words) discuss material published in *Science* in the previous 3 months or issues of general interest. They can be submitted through the Web (www.submit2science.org) or by regular mail (1200 New York Ave., NW, Washington, DC 20005, USA). Letters are not acknowledged upon receipt, nor are authors generally consulted before publication. Whether published in full or in part, letters are subject to editing for clarity and space.

Machines Fall Short of Revolutionary Science

THE 3 APRIL ISSUE CONTAINED TWO REPORTS about automated science ("Distilling free-form natural laws from experimental data," M. Schmidt and H. Lipson, p. 81, and "The automation of science," R. D. King *et al.*, p. 85). These Reports are seriously mistaken about the nature of the scientific enterprise, particularly regarding what theorists do and the meaning of physical law. As Thomas Kuhn famously argued, what most scientists do most of the time—which he called "normal science" and Rutherford called "stamp collecting"—does not contribute very much to the advancement of knowledge; rather, this normal science simply fleshes out the consequences of the paradigms that have been established by truly revolutionary advances. Even if machines did contribute to normal science, we see no mechanism by which they could create a Kuhnian revolution and thereby establish new physical law.

In the Report by Schmidt and Lipson, a machine deduces the equation behind a sample of chaotic motion. The discovery of deterministic chaos is an example of true Kuhnian revolution; others were its application to unexpected fields like meteorology and population biology. In the constrained problem in the Report, the relevant physical law and variables are known in advance; it is hardly a template for the creative, exploratory nature of true science.

PHILIP W. ANDERSON[1]* AND ELIHU ABRAHAMS[2]

[1]Physics Department, Princeton University, Princeton, NJ 08540, USA. [2]Department of Physics and Astronomy, Rutgers University, Piscataway, NJ 08854, USA.

*To whom correspondence should be addressed. E-mail: pwa@princeton.edu

TECHNICAL COMMENT ABSTRACTS

COMMENT ON "Experimental Test of Self-Shielding in Vacuum Ultraviolet Photodissociation of CO"

James R. Lyons, Roy S. Lewis, Robert N. Clayton

Chakraborty *et al*. (Reports, 5 September 2008, p. 1328) demonstrated very large, wavelength-dependent mass-independent isotopic effects during carbon monoxide (CO) photodissociation and argued that self-shielding in CO was not responsible. We suggest that variations in band oscillator strengths and linewidths among CO isotopologs are responsible for most of the wavelength dependence observed and that the reported experiments confirm the importance of self-shielding during CO photodissociation.

Full text at www.sciencemag.org/cgi/content/full/324/5934/1516-a

COMMENT ON "Experimental Test of Self-Shielding in Vacuum Ultraviolet Photodissociation of CO"

S. R. Federman and E. D. Young

Chakraborty *et al*. (Reports, 5 September 2008, p. 1328) suggested that experimental results provide support for CO photodissociation having caused the oxygen isotope ratio associated with the early solar nebula. We point out that further analysis is required before other mechanisms, such as self-shielding, are shown to be of little importance.

Full text at www.sciencemag.org/cgi/content/full/324/5934/1516-b

COMMENT ON "Experimental Test of Self-Shielding in Vacuum Ultraviolet Photodissociation of CO"

Qing-Zhu Yin, Xiaoyu Shi, Chao Chang, Cheuk-Yiu Ng

Chakraborty *et al*. (Reports, 5 September 2008, p. 1328) concluded that an anomalously enriched atomic oxygen reservoir can be generated through carbon monoxide photodissociation without self-shielding. We show that this conclusion is based on the incorrect assumption that the spectral shifts of the 97.03-nanometers and 107.61-nanometers vibrational bands for $C^{16}O$, $C^{17}O$, and $C^{18}O$ are negligible and point out shortcomings of the low-resolution light source used in their experiments.

Full text at www.sciencemag.org/cgi/content/full/324/5934/1516-c

RESPONSE TO COMMENTS ON "Experimental Test of Self-Shielding in Vacuum Ultraviolet Photodissociation of CO"

Subrata Chakraborty, Musahid Ahmed, Teresa L. Jackson, Mark H. Thiemens

We address the comments by Lyons *et al*., Federman and Young, and Yin *et al*. regarding the interpretation of our carbon monoxide photodissociation experiments and provide further experimental data analysis, including measured synchrotron beam profiles. The experimental data do not support existing self-shielding models that attempt to explain observed meteoritic oxygen isotopic compositions because they rely on previously untested theoretical assumptions.

Full text at www.sciencemag.org/cgi/content/full/324/5934/1516-d

ENERGY

Can Civilization (at Least the U.K.) Run Sustainably?

Marty Hoffert

Sustainable Energy
Without the Hot Air
by David J. C. MacKay
UIT Cambridge, Cambridge, 2009. 384 pp. £45. ISBN 9781906860011. Paper, £19.99. ISBN 9780954452933. (*1*)

Much that passes for serious discussion of energy and climate policy in legislative halls is "hot air." It is hard to understand the scale of effort needed to transition by midcentury from fossil fuel combustion with CO_2 up the stack or out the tailpipe to "something else" (what some call the terawatt challenge) or what energy "sustainability" or "self-sufficiency" even mean, if one is unwilling to think about actual numbers.

Cambridge physics professor David MacKay doesn't assume fear and loathing of arithmetic: His *Sustainable Energy: Without the Hot Air* is a cold blast of reality that hits hard with numerical estimates, data, and logic. He offers a must-read analysis of cars, jet flights, heating and cooling, food, and manufactured "stuff" on the consumption side, and of energy-generation technologies that might replace fossil fuels on the supply side, in the United Kingdom. For that island country, he delves into the specifics for solar thermal (using sunlight for direct heating), photovoltaics (on rooftops and in "farms"), wind (on land and offshore), biofuels, and tides as well as coal with carbon capture and storage (CCS) and nuclear power. He also covers the critical role of storage in limiting large-scale solar and wind power sources.

McKay holds it instructive to express power in kilowatt-hours per day, and he patiently explains to general readers that we don't say watts (or kilowatts) "per" anything. Fine. In my experience, units for energy and power are endless sources of confusion for students. But the author's use of kilowatt-hour/day doesn't distinguish between electrical and thermal energy. All kilowatt-hours may be equal, but some are more equal than others—with due credit to Sadi Carnot and George Orwell. A rule of thumb is that generating an electrical kilowatt-hour takes about three thermal kilowatt-hours, which might have been worth taking into account.

One challenge in preparing these back-of-the-envelope analyses is deciding what principles limit a given technology. We know, for example, that we may need some 30 terawatts from carbon-neutral sources by midcentury to meet the world's business-as-usual economic targets while staying below the 2°C global warming limit adopted by most nations. Let's say we target a third from renewables, a third from coal with CCS, and a third from fission. MacKay correctly estimates the nuclear fuel extractable from oceans (from the parts per billion concentration of dissolved uranium and ocean volumes) as huge compared with reactor-grade ores. But to provide fuel rods to run ^{235}U thermal reactors at 10 terawatts, the flow through hypothetical collectors in the sea would have to be an order of magnitude greater than the outflow of all the world's rivers (*2*). Nuclear reactors have been proposed as the only serious contender to avoid carbon emissions (*3*), so it is important to understand that the insufficiency of known uranium supplies for "once through" reactors argues for uranium and thorium breeders.

CREDIT: DAVID FAIMAN/BEN-GURION UNIVERSITY

Scope of the problem. This concentrator photovoltaic collector can generate 138 kilowatt-hours per day, half the energy consumption of an average American.

I found MacKay's book by turns exhilarating and terrifying. His calculations are always thought-provoking even when his assumptions had me banging the table in disagreement. My objections often faded as his analysis unfolded. The author dug out a lot of hard-to-find data, and his intelligence, wit, and excellent British humor are in evidence throughout. Some readers—but not Al Gore, who employs offsets to maintain carbon neutrality as he trots the globe—may be surprised that taking even a few jet flights uses as much energy as an average year of car driving.

The author doesn't consider cost or socioeconomic factors, just physics and engineering. With this caveat, MacKay finds there's barely enough "green" power to meet demand in the United Kingdom. But he doesn't believe Britain can live on its own renewables because there is too much opposition due to the costs and not-in-my-backyard arguments. Sustainability is achievable, he concludes, with sun power imported from the Sahara. For the United States, others have independently proposed using high-voltage direct current lines to transmit solar-generated power from Southwestern deserts to the coasts, a "grand plan" that raises well-known issues of transmission and storage (*4*). Continuous solar electricity from space beamed to Earth offers another possibility—and another story (*5*).

Shifting primary power production away from fossil fuels will require substantial investments in energy research, development, demonstration, and deployment. We now have in the United States an administration that understands both the science and the urgency. But I share McKay's concern that for the public at large this is no done deal:

> Given the general tendency of the public to say "no" to wind farms, "no" to nuclear power, "no" to tidal barrages—"no" to anything other than fossil fuel power systems—I am worried that we won't actually get off fossil fuels when we need to. Instead, we'll settle for half-measures: slightly-more-efficient fossil-fuel power stations, cars, and home heating systems; a fig-leaf of a carbon trading system; a sprinkling of wind turbines; an inadequate number of nuclear power stations.…
>
> We need to stop saying no and start saying yes. We need to stop the Punch and Judy show and get building."

Amen. Meanwhile, read *Sustainable Energy*.

The reviewer is at the Department of Physics, New York University, New York, NY 10003–6621, USA. E-mail: marty.hoffert@nyu.edu

Published by AAAS

References

1. The book may be read at or downloaded as a PDF file for free from www.withouthotair.com.
2. M. I. Hoffert *et al.*, *Science* **298**, 981 (2002).
3. J. Lovelock, *The Revenge of Gaia* (Allen Lane, London, 2006).
4. K. Zweibel, J. Mason, V. Fthenakis, *Sci. Am.* **298** (1), 64 (2008).
5. N. Geuder *et al.*, paper presented at the 4th International Conference on Solar Power from Space, Granada, Spain, 30 June to 2 July 2004.

10.1126/science.1175434

ARCHAEOLOGY

Arguments over Early Arrivals

Tim Flannery

First Peoples in a New World
Colonizing Ice Age America
by David J. Meltzer
University of California Press, Berkeley, 2009. 480 pp. $29.95, £20.95. ISBN 9780520250529.

David Meltzer's *First Peoples in a New World* is a double history: an investigation into the initial colonization of the Americas as well as a chronicle of the controversy some finds have engendered. The skeleton of "Kennewick Man," collected in Washington state in 1996 by local archaeologist James Chatters, was particularly fraught. Chatters concluded the remains were those of a middle-aged European. But when dating revealed them to be over 8400 years old, local Indians accused Chatters of forging the European identity to dodge the Native American Graves Protection and Repatriation Act, and an ongoing court case ensued. The idea that Kennewick Man had anything to do with Europe was long ago dismissed in academic circles, but the claim that the Americas were first populated by Caucasians has, according to Meltzer, "seeped into ... the poisonous corners of the Internet where white supremacists continue to claim Kennewick as one of their own."

Meltzer (an anthropologist at Southern Methodist University) argues that America was discovered long before the arrival of the Clovis big-game hunters around 11,200 radiocarbon years ago. (All dates in the book are given in uncalibrated radiocarbon years, although a table allows conversion to calendar years.) This is a contentious position, and the author confesses a partisan stance. Because archaeologists can devote entire careers to excavating a single site, their funding, academic status, and egos can become inextricably tied up with it. James Adovasio claims that Meadowcroft Rockshelter in Pennsylvania had humans living in it by 14,250 radiocarbon years ago, making it the oldest (and only pre-Clovis) site on the continent. A colleague said that he would accept the finding if Adovasio would date a single seed from the critical layer, a request that caused Adovasio to "burst out in derisive laughter" before saying that he would never "accede to any request [his colleague] made for further testing."

The linchpin in Meltzer's argument for a pre-Clovis presence in the Americas is Monte Verde in southern Chile. One of the most extraordinary archaeological sites ever discovered, it has yielded wooden artifacts, human footprints and feces, and pieces of skin and meat from large mammals, all preserved in a bog that radiocarbon dating suggests is around 12,500 years old. In 1997, senior American archaeologists conducted a site visit, which was not entirely satisfactory because excavations had removed almost everything, forcing a shift to collections in museums and labs. Drinks at a tavern afterward saw Monte Verde excavator Tom Dillehay become "short-tempered, even insulting." A row broke out, but not before a show of hands unanimously confirmed Monte Verde as a pre-Clovis site. Although that unanimity has since crumbled, Meltzer continues to argue that Monte Verde is where "the standards of proof" for a pre-Clovis presence "were finally met." However, only radiocarbon dating was done at Monte Verde. Because every dating technique has its own imbedded assumptions (which can lead to error), it's preferable to use multiple methods at such important sites. Optically stimulated luminescence dating and electron spin resonance dating of relevant materials would arguably have shed more light on the age of Monte Verde than a show of hands.

Meltzer devotes much space to explaining why archaeologists have not discovered undisputed pre-Clovis sites north of Chile. Perhaps the people stuck to a coastline now submerged by rising seas or archaeologists are looking in the wrong places. Yet it's striking that excavators have retrieved over 13,000 Clovis points from across North America, yet have been unable to conclusively identify a single site dating to even a few centuries earlier. Archaeologists in Australia and Europe have no such difficulty.

Meltzer discounts Paul Martin's theory that hunting by the Clovis people led to the swift extinction of America's megafauna, but his analysis is based on a selective reading of the evidence. It takes no account of the global pattern of large animal extinction following on the heels of human arrival, nor of the survival until after 8000 years ago of megafauna on islands—including dwarf mammoths on St. Paul Island off Alaska and the sloths and giant rodents on Caribbean islands, all of which go extinct only when humans arrive. And Meltzer never articulates a convincing alternative hypothesis capable of explaining how climate or some other factor could have caused the extinctions. The spores of a fungus that grows on the dung of large herbivores provide a new method with the potential to shed light here. Studies suggest that the spores declined abruptly 10,800 years ago in North America (indicating a collapse of mammalian biomass); a few decades later, there is evidence for an increase in fire. This is the kind of fine resolution required to help untangle the causes of megafaunal extinction.

The questions Meltzer raises in *First Peoples in a New World* are, from a technological perspective, eminently answerable. But doing so will require a broader array of analytical tools than seem, judging from this book, to be currently in use in American archaeology. A more global perspective on the problem would also be helpful.

"In archaeological limbo." The Meadowcroft Rockshelter, western Pennsylvania.

CREDIT: TOM UHLMAN/ALAMY

The reviewer is at the Division of Environmental and Life Sciences, Macquarie University, North Ryde, New South Wales 3800, Australia. E-mail: Tim.Flannery@textpublishing.com.au

10.1126/science.1175691

AGRICULTURE

Nutrient Imbalances in Agricultural Development

Nutrient additions to intensive agricultural systems range from inadequate to excessive—and both extremes have substantial human and environmental costs.

P. M. Vitousek,[1]* R. Naylor,[2] T. Crews,[3] M. B. David,[4] L. E. Drinkwater,[5] E. Holland,[6] P. J. Johnes,[7] J. Katzenberger,[8] L. A. Martinelli,[9] P. A. Matson,[10] G. Nziguheba,[11] D. Ojima,[12] C. A. Palm,[11] G. P. Robertson,[13] P. A. Sanchez,[11] A. R. Townsend,[14] F. S. Zhang[15]

Nutrient cycles link agricultural systems to their societies and surroundings; inputs of nitrogen and phosphorus in particular are essential for high crop yields, but downstream and downwind losses of these same nutrients diminish environmental quality and human well-being. Agricultural nutrient balances differ substantially with economic development, from inputs that are inadequate to maintain soil fertility in parts of many developing countries, particularly those of sub-Saharan Africa, to excessive and environmentally damaging surpluses in many developed and rapidly growing economies. National and/or regional policies contribute to patterns of nutrient use and their environmental consequences in all of these situations (*1*). Solutions to the nutrient challenges that face global agriculture can be informed by analyses of trajectories of change within, as well as across, agricultural systems.

Harvested crops remove nitrogen, phosphorus, and other nutrients from agricultural soils—and sustaining agricultural production requires replacing those nutrients, whether through biological processes like nitrogen fixation or through the addition of animal wastes or mineral fertilizer to fields. Globally, fertilizer is the major pathway of nutrient addition; it has more than doubled the quantities of new nitrogen and phosphorus entering the terrestrial biosphere (*2*, *3*). These inputs have helped to keep world crop productivity ahead of human population growth and can enhance rural economic development. However, environmental costs of nutrient pollution from agriculture have been substantial, including the degradation of downstream water quality and eutrophication of coastal marine ecosystems, the development of photochemical smog, and rising global concentrations of the powerful greenhouse gas nitrous oxide (*4*).

Here, we evaluate nutrient balances (*5*) of three corn-based agricultural systems—low-input corn in Western Kenya, high-input wheat and corn double-cropping systems in Northeast China (see figure, page 1520), and corn-soybean rotations in the upper midwestern United States. Unlike most regions of the world, crop yields have not increased substantially in sub-Saharan Africa, and 250 million people remain chronically malnourished there (*6*). Nutrient additions to most fields do not replenish soil nutrients extracted in crop harvest (*7*). For example, on the 90 smallholder farms sampled in the Siaya District of Kenya, nitrogen inputs from fertilizer were less than the amount taken out as grain and stover (see table, above) (*8*). This system persists by drawing down the nutrient capital of what were once high-fertility soils.

In contrast, agricultural production in China has increased dramatically since ~1975, with per-hectare yields of grain doubling in many areas. Policy-driven increases in fertilizer use contributed to rising crop yields as China strived for food security. Nutrient additions to many fields far exceed those in the United States and Northern Europe (*9*–*11*) (see table, above)—and much of the excess fertilizer is lost to the environment, degrading both air and water quality (*11*).

Finally, increased N and P fertilization in the Mississippi Basin has contributed to increased yields since the 1940s (*12*). From ~1970 to 1995, nutrient additions were well in excess of crop nutrient removals, and hydrologic losses caused eutrophication of freshwaters and the coastal Gulf of Mexico. More recently, nutrient imbalances have been reduced (*13*) (see table, above) (*14*). In Western Europe, post–World War II national

Inputs and outputs	Nutrient balances by region (kg ha $^{-1}$ year $^{-1}$)					
	Western Kenya		North China		Midwest U.S.A	
	N	P	N	P	N	P
Fertilizer	7	8	588	92	93	14
Biological N fixation					62	
Total agronomic inputs	7	8	588	92	155	14
Removal in grain and/or beans	23	4	361	39	145	23
Removal in other harvested products	36	3				
Total agronomic outputs	59	7	361	39	145	23
Agronomic inputs minus harvest removals	-52	+1	+227	+53	+10	−9

Inputs and outputs of nitrogen and phosphorus by managed pathways in a low-input corn-based system in Western Kenya in 2004–2005 (*8*), a highly fertilized wheat-corn double-cropping system in North China (2003–2005) (*9*–*11*), and a tile-drained corn-soybean rotation in Illinois, USA (1997–2006) (*14*). Potential crop yields are similar in these systems, but realized yields of corn were 2000, 8500, and 8200 kg ha^{-1} year^{-1} per crop in the Kenya, China, and U.S. systems, respectively. Wheat yielded another 5750 kg ha^{-1} year^{-1} in China, and soybeans yielded 2700 kg ha^{-1} year^{-1} every other year in Illinois. (Because the Illinois system represents a 2-year rotation, all nutrient inputs and removals were adjusted to place them on an annual basis.)

[1]Department of Biology, Stanford University, Stanford, CA 94305, USA. [2]Woods Institute for the Environment and Freeman Spogli Institute for International Studies, Stanford University, Stanford, CA 94305, USA. [3]Environmental Studies, Prescott College, Prescott, AZ 86301, USA. [4]Department of Natural Resources and Environmental Sciences, University of Illinois, Urbana, IL 61801, USA. [5]Department of Horticulture, Cornell University, Ithaca, NY 14853, USA. [6]National Center for Atmospheric Research, Boulder, CO 80307, USA. [7]Aquatic Environments Research Centre, School for Human and Environmental Sciences, University of Reading, Whiteknights, Reading, RG6 6AB, UK. [8]Aspen Global Change Institute, Aspen, CO 81611, USA. [9]Centro de Energia Nuclear na Agricultura–Universidade São Paulo (CENA-USP), Avenida Centenario 303, 13416-000, Piracicaba, SP, Brazil. [10]School of Earth Sciences, Stanford University, Stanford, CA 94305, USA. [11]The Earth Institute, Columbia University–Lamont Campus, Palisades, NY 10027, USA. [12]The Heinz Center for Science, Economics, and the Environment, Washington, DC 20009, USA. [13]Department of Crop and Soil Sciences, Michigan State University, Hickory Corners, MI 49060, USA. [14]Department of Ecology and Evolutionary Biology and INSTAAR, University of Colorado, Boulder, CO 80309, USA. [15]College of Resources and Environmental Science, China Agricultural University, Beijing, 100094 P. R. C. China.

*Author for correspondence. E-mail: vitousek@stanford.edu

Published by AAAS

and, later, European Community policies to boost food security (*1*) caused many areas to reach nitrogen surpluses within integrated crop and animal production systems as large and damaging as those now observed in China. Since the 1980s, increasingly stringent national and European Union regulations and policies have reduced nitrogen surpluses and have improved indicators of environmental nutrient excess. Despite these steps toward nutrient balance, nitrogen pollution remains substantial in both the air and water of Northern Europe (*15*, *16*), and coastal eutrophication in the Gulf of Mexico is continuing.

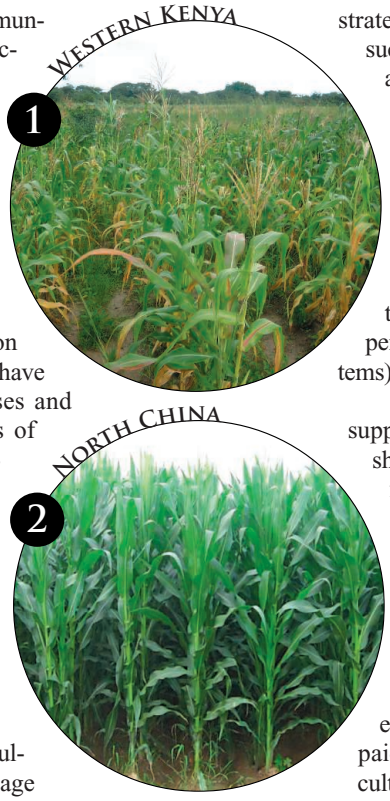

Corn crops in Western Kenya and the North China Plain. Both fields receive sufficient rainfall; they differ primarily in that soil nutrients in the Kenya field have been depleted, whereas the China field receives very large additions of nutrients in fertilizer.

These contrasting agricultural systems (see table, page 1519) require different policies. In sub-Saharan Africa, the initial challenge is to provide more nutrients and to improve cropping practices to build soil organic matter (*17*). Although the reluctance of many policy-makers to accept the economic, environmental, and social costs of subsidized fertilizer use is understandable, inadequate inputs will entrain low productivity, land degradation, and rural poverty until fertilizer for small-holder farmers is subsidized (*18*).

In contrast, the North China Plain wheat-corn systems clearly receive excessive nutrient inputs; Ju *et al*. (*11*) demonstrated experimentally that additions of N fertilizer could be cut in half without loss of yield or grain quality, in the process reducing N losses by >50%. Matson *et al*. (*19*) described a similar overshoot in fertilizer application to intensive wheat systems in Mexico. In these situations, reducing nutrient inputs would be beneficial agronomically, economically, and environmentally. However, this step alone may not suffice to stop environmental damage, as continuing losses of agricultural nutrients and consequent environmental damages in the Mississippi Basin and Northern Europe demonstrate. These systems require further interventions focused on their environmental impacts—and a range of potentially useful strategies and practices have been demonstrated (*20*). Some of these—such as better-targeted timing and placement of nutrient inputs, modifications to livestock diets (*21*), and the preservation or restoration of riparian vegetation strips—can be implemented now. Bolder efforts to redesign agriculture (e.g., by incorporating perennials into cropping systems) also are needed.

More generally, policies supporting nutrient additions should be targeted toward food security objectives early in agricultural development, but those systems should be monitored for changes in soil quality and nutrient losses, as well as for yields. As food security is approached, more attention should be paid to other outputs of agricultural systems—their effects on air and water, on biological diversity, on human health and well-being—and to the ecological and agronomic processes that control them.

One constraint to our ability to diagnose nutrient-driven problems, and to design their solutions, is the scarcity of detailed, on-farm nutrient budgets that quantify multiple pathways of nutrient input and loss over time and under alternative management practices. Both China and the European Union have supported integrated, multiscale biogeochemical research that yields policy-relevant information on nutrient balances and their implications (*11*, *22*). Neither the United States nor most other governments have done as well.

Agricultural systems are not fated to move from deficit to excess. However, most national agricultural agencies lack the means to assess the impacts of changing farm practices at appropriate scales and the incentives to promote the adoption of nutrient-conserving practices and processes. Without these tools, it will be difficult to develop and sustain modern agricultural systems without incurring continuing human and environmental costs.

References and Notes

1. P. J. Johnes, in *Redesigning Animal Agriculture: The Challenge for the 21st Century*, D. Swain, E. Charmley, J. Steel, S. Coffey, Eds. (CAB International, Wallingford, UK, 2007), pp. 185–203.
2. E. M. Bennett, S. R. Carpenter, N. F. Caraco, *Bioscience* **51**, 227 (2001).
3. J. N. Galloway *et al.*, *Science* **320**, 889 (2008).
4. P. M. Vitousek *et al.*, *Ecol. Appl.* **7**, 737(1997).
5. Nutrient budgets can be calculated at different spatial scales and levels of completeness. The agronomic budgets discussed here are based on managed inputs of nutrients and outputs in harvested crops, the most widely available information. More detailed budgets include other nutrient fluxes (atmospheric deposition, emissions of ammonia and other trace gases, denitrification, and leaching) across ecosystem boundaries and changes in nutrient pools within agricultural soils (*11*, *23*).
6. United Nations Food and Agricultural Organization, www.fao.org/news/story/en/item/8836/icode/ (2008).
7. P. A. Sanchez, *Science* **295**, 2019 (2002).
8. Maize and stover yields in 2004 were determined in 90 farms randomly selected from 1000 households in Siaya District, Western Kenya (*24*). Nutrient contents of maize and stover are from the same area of Western Kenya (*25*). Fertilizer applied is from household surveys conducted in the same area in 2005. Small quantities of N and P (relative to fertilizer) in manure are added to this and the other systems; these applications largely represent the recycling of nutrients rather than inputs.
9. Q.-M. Li, X.-P. Chen, F.-S. Zhang, V. Romheld, *Plant Nutr. Fertilizer Sci.* **8**, 152 (2002).
10. X. Tang, J. Li, Y. Ma, X. Hao, X. Li, *Field Crops Res.* **108**, 231 (2008).
11. X.-T. Ju *et al.*, *Proc. Natl. Acad. Sci. U.S.A.* **106**, 3041 (2009).
12. D. B. Egli, *Agron. J.* **100**, S-79 (2008).
13. U.S. Environmental Protection Agency (EPA), *Hypoxia in the Northern Gulf of Mexico: An Update by the EPA Science Advisory Board* (EPA-SAB-08-003, EPA, Washington, DC, 2007).
14. Crop yields are based on county-level National Agricultural Statistics Service data averaged for 1997–2006 for seven east-central Illinois counties. Fertilizer inputs are from 1997–2006 sales to the state of Illinois, with the county sales estimated from Census of Agriculture expenditures on fertilizers. Estimates of N and P in harvested grain and N_2 fixation follow methods in (*26*).
15. J. W. Erisman, A. Bleeker, A. Hensen, A. Vermeulen, *Atmos. Environ.* **42**, 3209 (2008).
16. G. Billen *et al.*, *Sci. Total Environ.* **375**, 80 (2007).
17. C. A. Palm, R. J. K. Myers, S. M. Nandwa, in *Replenishing Soil Fertility in Africa*, R. J. Buresh, P. A. Sanchez, F. Calhoun, Eds. (Special publ. 5, Soil Science Society of America, Madison, WI, 1997), pp. 193–217.
18. G. Denning *et al.*, *PLoS Biol.* **7**, e23 (2009).
19. P. A. Matson, R. Naylor, I. Ortiz-Monasterio, *Science* **280**, 112 (1998).
20. K. A. Cherry, M. Shepherd, P. J. A. Withers, S. J. Mooney, *Sci. Total Environ.* **406**, 1 (2008).
21. T. J. Klopfenstein *et al.*, "Animal diet modification to decrease the potential for nitrogen and phosphorus pollution" (Issue paper no. 21, Council for Agricultural Science and Technology, Ames, IA, 2002), 16 pp.
22. N. Beaudoin *et al.*, *Agric. Ecosys. Environ.* **111**, 292 (2005).
23. W. F. Sheldrick, J. K. Syers, J. Lingard, *Nutrient Cycl. Agroecosys.* **62**, 61 (2002).
24. P. Sanchez *et al.*, *Proc. Natl. Acad. Sci. U.S.A.* **104**, 16775 (2007).
25. E. K. Bünemann, P. C. Smithson, B. Jama, E. Frossard, A. Oberson, *Plant Soil* **264**, 195 (2004).
26. G. F. McIsaac, M. B. David, G. Z. Gertner, D. A. Goolsby, *J. Environ. Qual.* **31**, 1610 (2002).
27. This work is based upon discussions at the Aspen Global Change Institute—supported by U.S. National Aeronautics and Space Administration, the William and Flora Hewlett Foundation, and the David and Lucille Packard Foundation—and at a Scientific Committee on Problems of the Environment (SCOPE)–sponsored meeting of the International Nitrogen Initiative in Paris. G. Billen made helpful comments on an earlier draft.

10.1126/science.1170261

PHOTO CREDITS: KENYA, CHERYL PALM; CHINA, FUSUO ZHANG

MICROBIOLOGY

No Place Too Cold

Simple microbial food webs are found even in the coldest and most remote polar lakes.

Johanna Laybourn-Parry

Even the coldest environments on Earth have enough liquid water to sustain life. The scope for biological productivity in the polar regions is constrained by low temperatures and low annual levels of solar radiation, but free water on or under glaciers or ice sheets nevertheless contains numerous species of mostly microorganisms. These delicate ecosystems are widely regarded as sentinels of climate change. Recent studies of polar and glacial lakes, as well as subglacial environments, have shed light on how these ecosystems function and on the role that they play in nutrient cycling.

The Antarctic is an isolated, largely ice-covered continent with little scope for colonization. Here, bacteria, algae, and flagellated and ciliated protozoans are abundant in the numerous lakes and in free water on and under glaciers, where they form simple truncated food webs. The penguins and seals on Antarctica's margins are not part of this terrestrial biota, but are instead members of the highly productive marine ecosystem. In contrast to Antarctica, the Arctic is an extension of continental land masses such as North America and Asia. Moreover, the climate is generally less severe than in Antarctica. The Arctic therefore has higher plants, land mammals, and birds, and microorganisms are more abundant in the lakes, on glaciers, and in the often well-developed soils. Glaciers at all latitudes represent extreme environments and are always dominated by microorganisms.

The most detailed knowledge of polar ecosystems comes from studies of Antarctic lakes, situated in the small areas of the continent that are ice-free. The lakes contain simple, truncated food webs dominated by microorganisms (see the figure). Cryptophytes are among the most ubiquitous photosynthetic flagellates found in polar lakes. They are microscopic plantlike organisms adapted to low light levels and low temperatures that can feed on bacteria or dissolved organic carbon as well as undertaking photosynthesis (*1*, *2*). This mixed nutrition (mixotrophy) provides photosynthetic flagellates with nutrients for photosynthesis and/or to supplement their carbon budgets. Mixotrophic ciliates (such as *Mesodinium rubrum*) are also common. In general, nutritional versatility is the key to success: For example, some nonphotosynthetic flagellates, such as *Diaphanoeca grandis*, take up dissolved organic carbon but also feed on bacteria.

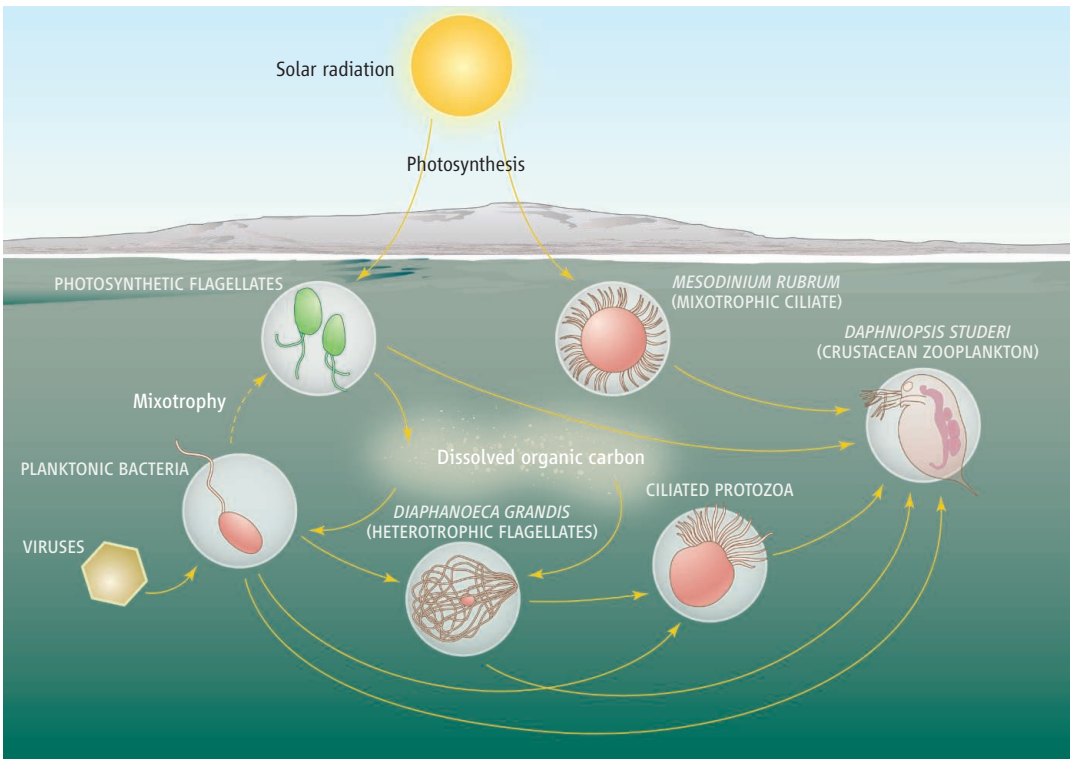

Typical microbial food web structure in the plankton of an Antarctic lake. There are few or no multicellular organisms. The truncated, simple food web is dominated by viruses, bacteria, algae, and protozoans. Dissolved organic carbon includes photosynthate exuded by phytoplankton, used as an energy source by bacteria. Most viruses appear to infect bacteria in these lakes.

Bacteria in Antarctic lakes function throughout the year under lake ice cover. Even in winter, bacterial growth is measurable, but overall rates are much lower than those in lower-latitude systems. Unique selection pressures in polar environments provide an ideal setting to study endemism. Existing data show that many strains are cosmopolitan, but there is clear evidence for novel bacterial species (*3*, *4*).

Viruses in lakes largely infect bacteria and, by lysing the host cell, recycle carbon to the organic carbon pool before it can be transferred up the food chain by protozoan predation on bacteria. They thus effectively shortcircuit the carbon cycle. In low-latitude lakes, only ~0.6% to 4.2% of bacteria may be infected by viruses, whereas in some Antarctic lakes, 22% to 34% of bacteria may be parasitized by viruses (*5*). However, the low rates of bacterial growth in polar waters means that infected bacteria cannot produce many viruses; on average, only 4 viruses are released from a bacterial cell when it is lysed, compared with a mean of 26 viruses across temperate lakes. These high infections rates suggest a significant impact on carbon cycling (*5*).

In glaciers, biologically mediated processes also seem to play an important role in nutrient cycling (*6*). Glacier surfaces develop mini-lakes called cryoconites—near-vertical tubes with a sediment layer at the bottom overlain by water. In Antarctica, cryoconites are entombed

Institute of Antarctic and Southern Ocean Studies, University of Tasmania, Hobart, Tasmania 7001, Australia. E-mail: Jo.Laybourn-Parry@utas.edu.au

CREDIT: P. HUEY/SCIENCE

Published by AAAS

by an ice cover, whereas in the Arctic and in lower-latitude glaciers, they are usually open to the air. They freeze up in winter and have liquid water during summer as solar radiation heats the dark sediment.

The communities in cryoconites resemble those of Antarctic lakes (see the figure). In Antarctica, cryoconites contain viruses, bacteria, cyanobacteria, algae, flagellates, and ciliates. In the Arctic and lower-latitude glaciers, they may also contain microscopic animals such as nematodes and rotifers. Comparative studies, including bacterial ribosomal DNA analyses, indicate that cryoconites are colonized by organisms from nearby lakes and streams (*7*).

Investigations of biogeochemical cycling on glacier surfaces are relatively recent. The evidence from Arctic glaciers suggests that much more organic carbon is deposited from the surrounding environment than is fixed on the glacier during photosynthesis (*8*). On Arctic glaciers, respiration appears to exceed photosynthesis, indicating that surface glacier ecosystems are subsidized by carbon inputs from the environment, rather like streams and estuaries. Whether this is true of Antarctic glaciers remains to be shown.

Liquid water at the bases of glaciers can also support bacterial communities, including aerobic strains and anaerobic nitrate and sulfate reducers and methanogens (*9*). For example, Blood Falls—an iron-rich discharge emanating from the Taylor Glacier in Antarctica—derives from a brine pocket trapped in the glacier 1.5 million years ago. This brine contains a microbial community that mediates a sulfur cycle in which Fe(III) is the terminal electron acceptor; Fe(III) may be an important electron acceptor for many subglacial ecosystems (*10*).

A network of subglacial lakes under the Antarctic ice cap have yet to be sampled. They have been isolated for millions of years, but a molecular analysis of accretion ice above Lake Vostok revealed a bacterial community with species typical of aquatic environments. If these species are characteristic of the underlying lake, this would indicate that it does not possess an evolutionary distinct biota (*11*).

As investigations of polar microbial biodiversity forge ahead, key challenges will be to unravel the roles of different groups in ecosystems and to identify the biochemical mechanisms, such as cold-adapted proteins, that enable survival in extreme environments. Advances in functional genomics and proteomics will provide exciting insights into how life evolved and functions under extreme conditions.

References

1. L. J. Tranvik *et al.*, *Oecologia* **78**, 473 (1989).
2. J. Laybourn-Parry *et al.*, *Freshwater Biol.* **50**, 830 (2005).
3. E. Stackebrandt *et al.*, *Cell. Mol. Biol.* **50**, 517 (2004).
4. D. A. Pearce, P. E. Galand, in *Polar Lakes and Rivers*, W. F. Vincent, J. Laybourn-Parry, Eds. (Oxford Univ. Press, London, 2008), pp. 231–230.
5. C. Säwström *et al.*, *Extremophiles* **12**, 167 (2008).
6. A. Hodson *et al.*, *Ecol. Monogr.* **78**, 41 (2008).
7. C. M. Foreman *et al.*, *J. Geophys. Res.* **112**, G04S32 (2007).
8. M. Stibal *et al.*, *Biogeochemistry* **90**, 1 (2008).
9. M. L. Skidmore *et al.*, *Appl. Environ. Microbiol.* **66**, 3214 (2000).
10. J. A. Mikucki *et al.*, *Science* **324,** 397 (2009).
11. J. C. Priscu *et al.*, in *Polar Lakes and Rivers*, W. F. Vincent, J. Laybourn-Parry, Eds. (Oxford Univ. Press, London, 2008), pp. 119–135.

10.1126/science.1173645

CHEMISTRY

Squeezing the Water Out of HCl(aq)

The controlled formation of clusters confined to helium droplets shows that just four water molecules are sufficient to dissolve hydrochloric acid into its ions.

Timothy S. Zwier

Our earliest encounters with chemistry usually involve measuring the extent to which simple acids dissociate to ions in aqueous solution. For strong acids, such as HCl, dissociation is nearly complete, with the H^+(aq) and Cl^-(aq) ions moving free of one another in a large excess of water. One of the current driving forces in modern science is our interest in studying chemical and physical phenomena in ever-smaller size regimes, seeking to characterize nature strained to its smallest size limits. The fields of molecular electronics (*1*, *2*), single-molecule spectroscopy (*3*), and atomic-scale microscopy (*4*) all operate at or near this limit. On page 1545 of this issue, Gutberlet *et al.* (*5*) consider acid dissociation at its smallest scale, probing the dissociation of a single HCl molecule into its ions under conditions where no more than a handful of water molecules are present. The issue at hand is determining the minimum number of water molecules at which HCl dissociation into $H_3O^+(H_2O)_{n-1}Cl^-$ occurs spontaneously.

Department of Chemistry, Purdue University, West Lafayette, IN 47907, USA. E-mail: zwier@purdue.edu

This "zwitterion" or "ion-pair" structure still carries a net charge of zero but incorporates two opposite charges in close proximity. The tug-of-war between HCl and $(H_2O)_n$ for the proton depends sensitively on the number of water molecules present and the way in which they stabilize the ion pair once formed. As our day-to-day encounters with liquids occur on the scale of Avogadro's number (~10^{23} molecules), it is hard to imagine how to go about answering this question of minimal acidic breakup.

Gutberlet *et al.* used the exotic environment of a superfluid helium droplet (*6*) to form $(HCl)_m(H_2O)_n$ clusters. Formed by expansion of a high-pressure helium gas through a small cooled nozzle into vacuum, typical droplets are at a temperature of 0.37 K and contain about 10,000 helium atoms that move without resistance relative to one another. These helium droplets act as vacuum cleaners for molecules that strike them, absorbing them into the cluster interior, where they can meet and bind to others that have arrived before them, forming molecular clusters embedded in helium (*6*–*8*). The important advantage of the method is that by controlling the pressures of the "pick-up" gases (HCl and H_2O in this case), the size distribution of the molecular clusters can be controlled.

Interrogation of the clusters occurs via laser-based infrared spectroscopy. Absorption of an infrared photon by its molecular constituents is detected indirectly by the change in size of the helium droplet as it boils off helium atoms in response to the droplet's increased energy. Using these methods, Gutberlet *et al.* identified an infrared spectral signature near 2670 cm^{-1} attributable to the H_3O^+ ion in an ion-pair structure. They were able to correlate the occurrence of this unique feature with the $HCl(H_2O)_4$ cluster size.

The calculated structure for this cluster (see the figure) shows three water molecules arranged so as to accept hydrogen bonds from the three hydrogens of H_3O^+, each orienting one of their hydrogens toward the negatively charged chloride anion. The three free OH groups on these bridging water molecules can configure in two different ways with little cost in energy, producing two nearly isoenergetic isomeric forms.

An intriguing aspect of these results is the mechanism proposed for ion-pair formation in the frigid environment of a helium droplet.

One of the trademarks of helium droplets is their ability to trap high-energy cluster structures behind even small energy barriers to rearrangement (*7*, *8*). The constituents come together in the helium droplet one at a time, steered toward one another by long-range electrostatic interactions during their approach, with excess energy removed quickly by the evaporation of helium atoms from the droplet. In such circumstances, even small energy barriers could prevent ion-pair formation and rearrangement of the hydrogen-bonded network of water molecules. Instead, just the opposite occurs. The calculations uncovered a nearly barrierless pathway to formation of the final separated ion pair $H_3O^+(H_2O)_3Cl^-$ involving addition of a fourth water molecule to cyclic $HCl(H_2O)_3$, facilitated by the step-by-step cluster growth process. The single acceptor–single donor water molecules present in both starting and ending structures have been implicated as required sites for attack by HCl leading to ionization on ice surfaces (*9*, *10*).

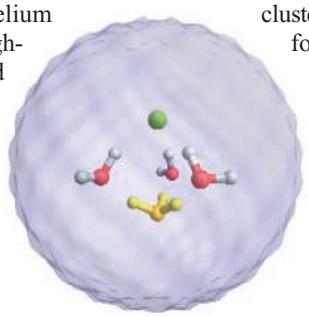

Confine and separate. Calculated structure for the $H_3O^+(H_2O)_3Cl^-$ separated ion pair in a helium droplet, as deduced by Gutberlet *et al*.

The remarkable ability of water to stabilize and solvate ions is clearly exposed in this cluster structure. The fact that a mere four water molecules are sufficient to drive proton transfer and to stabilize the ion-pair products testifies to water's unique assets both as a proton acceptor and as a medium for forming strong hydrogen-bonding networks that stabilize the ions once formed.

Much remains to be done in studying acid-base reactions in this small size limit. We still need to gain a deeper understanding of the development of acid-base reactivity as a function of cluster size. In the $HCl(H_2O)_n$ clusters, for instance, we would hope to understand whether the turn-on of ion-pair formation at $n = 4$ is complete, or whether larger cluster sizes might support certain initial structures as neutrals and others as ion pairs. In those that are trapped as one or the other, we would like to study their temperature-dependent stability, or use laser-initiated excitation to drive proton transfer. Additional ways to characterize these clusters are being developed, including measurements of the vibrational transition moment directions (*8*) and the use of double-resonance spectroscopy (*11*) to identify and study individual structural isomers. In the helium droplets, such double-resonance schemes can also be used to measure the barriers to isomerization or to the proton transfer reaction itself (*12*).

The goal ahead will be to squeeze these clusters for every drop of new understanding of acid-base chemistry in the small size limit.

References and Notes

1. W. Lu, C. M. Lieber, *Nat. Mater.* **6**, 841 (2007).
2. R. M. Metzger, *J. Mater. Chem.* **18**, 4364 (2008).
3. W. E. Moerner, *Proc. Natl. Acad. Sci. U.S.A.* **104**, 12596 (2007).
4. A. M. Moore, P. S. Weiss, *Annu. Rev. Anal. Chem.* **1**, 857 (2008).
5. A. Gutberlet *et al*., *Science* **324**, 1545 (2009).
6. J. P. Toennies, A. F. Vilesov, *Angew. Chem. Int. Ed.* **43**, 2622 (2004).
7. C. J. Burnham, S. S. Xantheas, M. A. Miller, B. E. Applegate, R. E. Miller, *J. Chem. Phys.* **117**, 1109 (2002).
8. M. Y. Choi *et al*., *Int. Rev. Phys. Chem.* **25**, 15 (2006).
9. J. P. Devlin, M. Farnik, M. A. Suhm, V. Buch, *J. Phys. Chem. A* **109**, 955 (2005).
10. J. P. Devlin, N. Uras, J. Sadlej, V. Buch, *Nature* **417**, 269 (2002).
11. T. S. Zwier, *J. Phys. Chem. A* **105**, 8827 (2001).
12. G. E. Douberly, J. M. Merritt, R. E. Miller, *J. Phys. Chem. A* **111**, 7282 (2007).

13. Supported by NSF Experimental Physical Chemistry program grant CHE0551075.

10.1126/science.1175387

ECOLOGY

Thriving in Salt

Saline environments from polar glaciers to the deep sea floor contain a surprising variety of organisms.

Antje Boetius[1] and Samantha Joye[2]

Fluids containing ≥5% salt are classified as brines and exclude most life on Earth, but some microbes thrive at salt saturation (35% salt, 10 times the salinity of seawater). Recent findings of novel saline habitats such as subsurface aquifer seeps, deep-sea brine pools, and ancient subglacial brine (*1*–*4*) extend our knowledge on the limits of life on Earth and beyond (*5*) and elucidate how cycling of sulfur, methane, and iron can support microbial ecosystems in chemically isolated habitats in the absence of light (*2*).

High salt requires microorganisms to minimize water loss and osmotic stress. They accomplish this by concentrating intracellular solutes and by adaptations of their enzymes, which are hence of interest to biotechnology.

The only animal known to tolerate high salt is the "living fossil" brine shrimp *Artemia*, a member of the Branchiopoda. A number of salt lakes have an endemic variety, such as the endangered species *A. monica*, which thrives in Mono Lake, California (see the first figure, panel A). The most famous halophilic algae, *Dunaliella salina*, a very pink member of the Chlorophyceae, survives up to 23% salt (see the first figure, panel B). *Dunaliella* was first

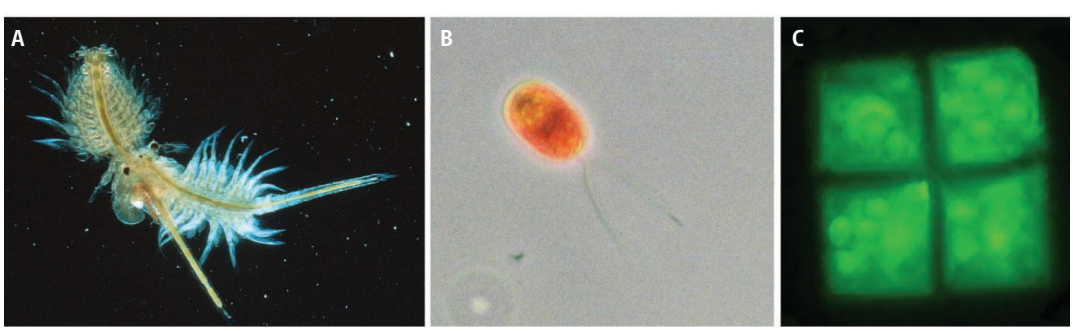

Halophilic life. (**A**) The Mono Lake brine shrimp *Artemia monica* (~1.5 cm long). (**B**) The bright pink phototrophic alga *Dunaliella* (each individual is ~5 μm long). (**C**) A ~5-μm-wide cluster of square archaea *Haloquadratum walsbyi*.

[1]HGF-MPG Joint Research Group for Deep Sea Ecology and Technology, Alfred Wegener Institute for Polar and Marine Research, 27515 Bremerhaven, Germany, and Max Planck Institute for Marine Microbiology, 28359 Bremen, Germany. [2]Department of Marine Sciences, University of Georgia, Athens, GA 30602, USA. E-mail: aboetius@mpi-bremen.de; mjoye@uga.edu

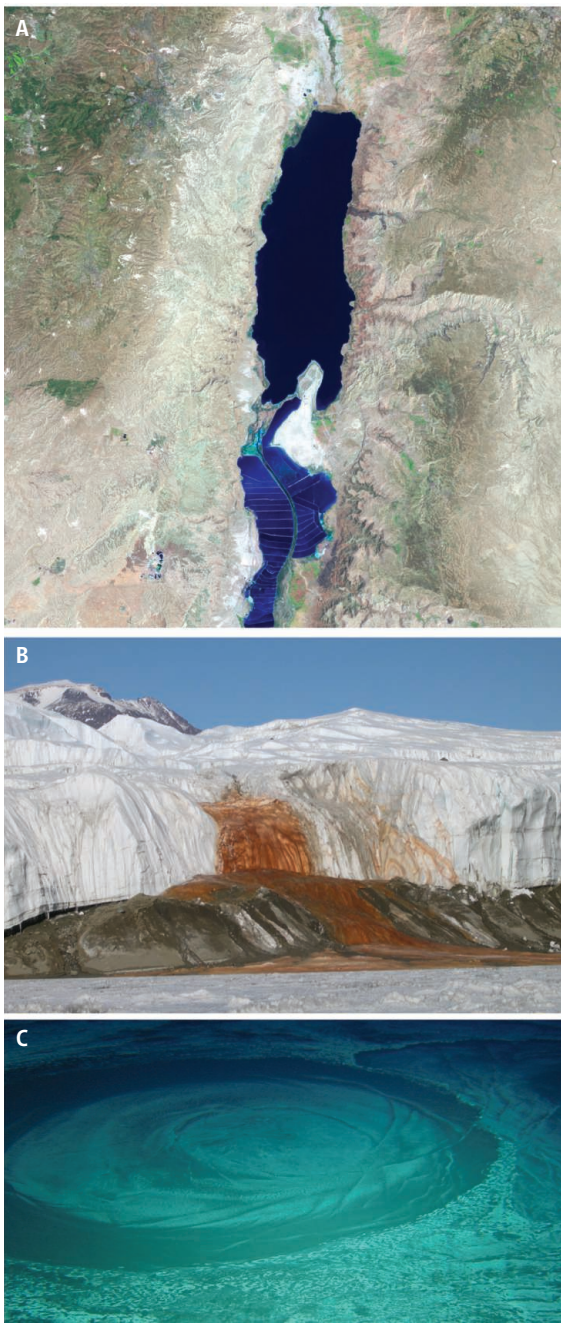

Brine habitats. (**A**) The Dead Sea, where the first halophilic organisms were identified. (**B**) Blood Falls at the base of the Taylor Glacier in Antarctica. (**C**) A bacterial mat–covered brine pool on a deep-sea mud volcano in the Eastern Mediterranean.

studied by Baas-Becking in 1931 (*6*) and was the first life form documented in the Dead Sea (*7*, *8*). The extremely halophilic archaeon *Haloquadratum walsbyi*, first found in a Red Sea salt pond (*9*), has been cultivated and its genome sequenced (*10*). It is <0.1 μm thick and has an unusual rectangular shape (see the first figure, panel C). This and other halophilic archaeae form gas vesicles to float in the sun-lit, aerobic, nutrient-rich brines.

Halophilic organisms are found in many branches of the tree of life, and salt-adapted enzymes occur in both archaea and bacteria. These observations suggest either that similar adaptation mechanisms arose numerous times or that lateral gene transfer is an important mechanism for halophile evolution. Either mechanism can account for the widespread distribution of carotenoid and rhodopsin pigments in halophilic bacteria and archaea. This pigmentation explains the red color of salt lakes, salterns, and salt flats.

Various mechanisms generate the diverse hypersaline habitats found on Earth. Salt lakes such as the giant Aral Sea or Lake Balkhash represent a substantial fraction of inland water bodies. They form when geological processes create a basin in which water evaporation exceeds water input. Evaporation is also used to precipitate salt commercially in human-made shallow salt ponds (salterns) retaining water from the sea or from salt lakes. Salt has been a valuable commodity since the Bronze age, and many ancient cities gained wealth from mining, making, and marketing salt.

Historically, the most intriguing salt lake is the Dead Sea (see the second figure, panel A), mentioned in the Book of Genesis and in Pliny the Elder's *Natural History* as being free of life. The tectonic isolation of the Dead Sea basin from the ocean has contributed to its slow salinization. Today, this natural laboratory is endangered because of ever-decreasing freshwater inputs from the Jordan River. Volcani first described microbial life in Dead Sea waters in his benchmark 1936 paper (*8*). Many halophilic archaeae were isolated from samples of Volcani 57 years after their collection (*11*), indicating low mortality in their salty habitat. For the same reason, thick photosynthetic microbial mats can thrive at the bottom of shallow salt lakes where their grazers are excluded.

Brines also occur in polar habitats. When sea ice forms, 10 to 30% of its volume is comprised by brine channels. Sea-ice microbial communities thrive inside the interconnected brine channels that concentrate nutrients and organic substrates (*12*). In Antarctica, subglacial saline lakes and surficial brine lakes or moats are common (*1*, *13*). The Antarctic Dry Valleys are home to one of the most intriguing and spectacular microbial ecosystems known (*2*): Blood Falls, where subglacial iron-rich seawater-derived brine episodically drains from Taylor Glacier (see the second figure, panel B). This brine contains a low diversity of microbes, mainly sulfur- and iron-using bacteria, including the Arctic species *Thiomicrospira arctica* (*14*).

Finally, deep, dark, and remote hypersaline habitats—such as mud volcanoes, brine lakes, and anoxic basins—occur at the bottom of the Black, Red, and Mediterranean seas and in the Gulf of Mexico (see the second figure, panel C). When subsurface fluids interact with ancient salt deposits, they can form warm brines, which migrate up through the sediments and are expelled at the sea floor or accumulate in brine pools. The microbial ecosystems associated with these brines vary with fluid composition and flow rate (*3*). Hypersaline anoxic basins in the eastern Mediterranean Sea result from the dissolution of Miocene salt deposits exposed to seawater after tectonic activity (*15*). Brine microbial ecosystems are associated with mud volcanoes along the tectonically active Mediterranean Ridge and on the passive Egyptian continental margin, where subsurface fluids interact with Messinian salt deposits as a result of gravitational transport (*16*).

The high density of hypersaline brine limits its mixing with overlying seawater, generating a chemocline up to a few meters thick (*3*). Viewing such habitats from a submersible is like seeing a lake in the ocean (see the second figure, panel C). These chemoclines host an elevated biomass and diversity of microorganisms relative to the overlying seawater and underlying brine, including novel bacterial and archaeal clades (*17*). Microorganisms profiting from the redox gradients, such as sulfide-oxidizing *Arcobacter*, leave visible sulfur precipitates floating on the brine (*16*). In Gulf of Mexico brines, which contain no sulfate, specific microbial functions—such as formation and consumption of acetate and subsequent methane production—have been observed for the first time at high salinity and were found to vary across the chemocline (*3*).

Saline habitats and their diverse halophilic inhabitants will remain an important focus for extremophile studies, furthering our knowledge of their unique adaptations and providing novel enzymes for biotechnological applications. In addition, remote and isolated briny

habitats such as those described in recent studies (*1*–*4*) are fascinating natural laboratories to study the persistence, energetics, and complexity of microbial life, with implications for the evolution of biogeochemical cycles on Earth and elsewhere.

References and Notes

1. W. J. Green, W. B. Lyons, *Aquat. Geochem.* **15**, 321 (2009).
2. J. A. Mikucki *et al.*, *Science* **324**, 397 (2009).
3. S. B. Joye *et al.*, *Nat. Geosci.* **2**, 349 (2009).
4. B. A. Biddanda *et al.*, *Eos* **90** (8), 61 (2009).
5. R. L. Mancinelli, T. F. Fahlen, R. Landheim, M. R. Klovstad, *Adv. Space Res.* **33**, 1244 (2004).
6. L. G. M. Baas-Becking, *J. Gen. Physiol.* **14**, 765 (1931).
7. A. Oren, *Saline Syst.* **4**, 2 (2008).
8. B. Wilkansky, *Nature* **138**, 467 (1936).
9. A. E. Walsby, *Nature* **283**, 69 (1980).
10. H. Bolhuis *et al.*, *BMC Genomics* **7**, 169 (2006).
11. D. R. Arahal *et al.*, *Appl. Environ. Microbiol.* **62**, 3779 (1996).
12. J. A. Mikucki, J. C. Priscu, *Appl. Environ. Microbiol.* **72**, 4029 (2007).
13. D. N. Thomas, G. S. Dieckmann, *Science* **295**, 641 (2002).
14. M. J. Siegert *et al.*, *Nature* **414**, 603 (2001).
15. P. W. J. J. van der Wielen *et al.*, *Science* **307**, 121 (2005).
16. E. O. Omoregie *et al.*, *Appl. Environ. Microbiol.* **74**, 3198 (2008).
17. W. Eder *et al.*, *Environ. Microbiol.* **4**, 758 (2002).

18. Supported by the NSF Microbial Observatories and Antarctic Organisms and Ecosystems programs, the European Union project HERMES, and the MARUM Center for Marine Environmental Sciences. We thank R. Jellison, M. Madigan, A. Oren, C. Pierre, and J. Sarrazin for providing images of brine organisms and/or habitats.

10.1126/science.1172979

IMMUNOLOGY

A Chronic Need for IL-21

A cytokine produced by helper T cells enables CD8$^+$ T cells to control viral infection.

Lisa D. S. Johnson and Stephen C. Jameson

Chronic viral infections provoke a war of attrition between cytotoxic T cells (the CD8$^+$ subclass) of the immune system and infected host cells. Although the CD8$^+$ T cell response gradually whittles away at the viral load, the cells progressively become "exhausted" and lose function during a chronic infection (*1*). This exhaustion becomes more severe in the absence of helper CD4$^+$ T cells, potentially leading to viral persistence and loss of virus-specific CD8$^+$ T cells (*1*, *2*). But how do CD4$^+$ cells help? Three reports in this issue, by Elsaesser *et al.* on page 1569 (*3*), Yi *et al.* on page 1572 (*4*), and Fröhlich *et al.* on page 1576 (*5*), suggest an unexpected role for a specific cytokine produced by CD4$^+$ T cells called interleukin-21 (IL-21) in controlling chronic viral infections.

IL-21 is produced by multiple CD4$^+$ T cell subsets, prominently T helper 17 (T_H17) cells, follicular helper T cells, and natural killer T cells (*6*, *7*). The cytokine enhances differentiation of some of these subsets, but other immune cells, including B, natural killer, and CD8$^+$ T cells, also respond to IL-21. The IL-21 receptor (IL-21R) belongs to the γC family of cytokine receptors (which includes receptors for IL-2, -7 and -15), and IL-21 can cooperate with other members of that group to enhance CD8$^+$ T cell responses (*8*, *9*). This lays the groundwork for considering whether CD4$^+$ cell "help" for CD8$^+$ T cell responses involves IL-21 as an intermediary.

The new reports show that in mice, IL-21 is produced by CD4$^+$ T cells responding to chronic lymphocytic choriomeningitis virus (LCMV) infection. As the infection persists, these T cells increase IL-21 production (while decreasing IL-2 production) (*3*, *4*) (see the figure). To test the relevance of this response, IL-21– or IL-21R–deficient mice were chronically infected with LCMV. Surprisingly, the studies found that both types of mice were more susceptible than normal mice to chronic infection, and had more dramatic exhaustion of LCMV-specific CD8$^+$ T cells. Furthermore, IL-21– and IL-21R–deficient mice could not overcome chronic infection compared to normal mice that were infected. By contrast, the magnitude of the CD4$^+$ T cell response was normal [or even enhanced (*3*)] in the IL-21– and IL-21R–deficient mice. Antibody production by B cells to LCMV was mildly impaired in IL-21– and IL-21R–deficient animals (IL-21 simulates B cell function) (*6*, *7*), but antibody is not thought critical for controlling chronic LCMV infection.

Because the sustained presence of viral antigen during chronic infection reinforces CD8$^+$ T cell exhaustion, IL-21 might enhance viral clearance by affecting other cells types (e.g., CD4$^+$ T cells). This might also relieve CD8$^+$ T cell exhaustion. The new studies addressed this issue by assessing the function of IL-21R–deficient CD8$^+$ T cells in normal recipient mice. CD8$^+$ T cells lacking IL-21R had impaired self-maintenance, suggesting an autonomous requirement for IL-21 sensitivity. Whether IL-21 also acts on other immune cell types to resolve chronic LCMV infection remains to be determined.

But is IL-21 the critical element that allows CD4$^+$ T cells to help CD8$^+$ T cells combat chronic viral infection? Yi *et al.* report that in response to injected IL-21, CD4$^+$-deficient mice with a chronic LCMV infection showed enhanced numbers and function of CD8$^+$ T cells and reduced viral titers. Although none of the new studies conclusively show that IL-21 produced by CD4$^+$ T cells is essential for helping CD8$^+$ T cells during chronic LCMV infection, the prominence of CD4$^+$ T cells as a source for IL-21 is highly suggestive. IL-21 shows promise in

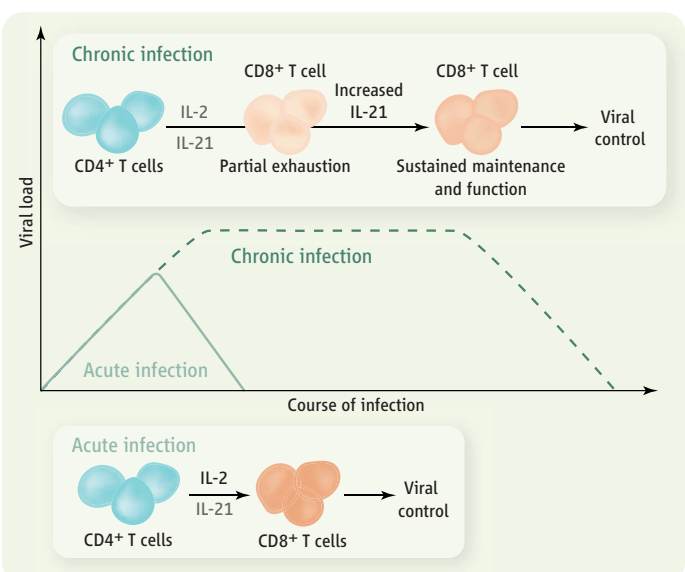

Help for the exhausted. During acute viral infection, IL-21 is produced by antigen-specific CD4$^+$ T cells, but is not required for the specific CD8$^+$ T cell response or control of the pathogen (solid curve). During chronic viral infection (dashed curve), the CD4$^+$ and CD8$^+$ T cell responses become partially "exhausted," but CD4$^+$ T cells eventually increase IL-21 production. This helps the CD8$^+$ T cell response, eventually leading to viral control.

CREDIT: N. KEVITIYAGALA/*SCIENCE*

Laboratory Medicine and Pathology, Center for Immunology, University of Minnesota, Minneapolis, MN 55455, USA. E-mail: james024@umn.edu

tumor treatments (another scenario in which the immune system is subject to chronic antigen exposure) (*6*, *10*), and its therapeutic potential is appealing. At the same time, the capacity of IL-21 to enhance the $CD8^+$ T cell response may come at a cost: Treating chronic LCMV-infected $CD4^+$-deficient animals with IL-21 led to severe sickness (*4*). Hence, prospective therapeutic use of IL-21 will need to be finely tuned.

$CD4^+$ T cell help is also important for the $CD8^+$ T cell response to various acute infections (*2*). In such responses, lack of $CD4^+$ help (or lack of IL-2 sensitivity) typically has minimal impact on $CD8^+$ T cell priming, but leads to a failure of memory $CD8^+$ T cells to mount a response to subsequent infection by the same pathogen (*2*). The current reports find no effect of IL-21 or IL-21R deficiency on the primary $CD8^+$ T cell responses to various acute infections (*3*–*5*), and in one study, memory $CD8^+$ T cell responses to LCMV were intact (*5*). Such data strongly suggest that IL-21 is a key element of $CD4^+$ T cell help in $CD8^+$ T cell responses to chronic but not acute infections. Furthermore, the elevated and sustained production of IL-21 (but not IL-2) in $CD4^+$ T cells from chronically infected animals contrasts with the sustained capacity for IL-2 (but not IL-21) synthesis by $CD4^+$ T cells following acute infection (*3*). Thus, the basis by which $CD4^+$ T cells help the $CD8^+$ T cell responses may change depending on the nature of the infection. IL-21 appears to induce a unique differentiation pathway in activated $CD8^+$ T cells (*6*, *10*, *11*), potentially equipping them to better clear virus during a chronic infection. Whether the IL-21–producing $CD4^+$ T cells also function as follicular helper T cells or T_H17 cells during chronic viral infection is unclear [although Fröhlich *et al*. argue against T_H17 involvement (*5*)]. Regardless, these studies suggest a key role for IL-21 in mediating $CD4^+$ help when it's needed most.

References

1. H. Shin, E. J. Wherry, *Curr. Opin. Immunol*. **19**, 408 (2007).
2. M. A. Williams, M. J. Bevan, *Annu. Rev. Immunol*. **25**, 171 (2007).
3. H. Elsaesser, K. Sauer, D. G. Brooks, *Science* **324**, 1569 (2009); published online 7 May 2009 (10.1126/science.1174182).
4. J. S. Yi, M. Du, A. J. Zajac, *Science* **324**, 1572 (2009); published online 14 May 2009 (10.1126/science.1175194).
5. A. Fröhlich *et al*., *Science* **324**, 1576 (2009); published online 28 May 2009 (10.1126/science.1172815).
6. R. Spolski, W. J. Leonard, *Annu. Rev. Immunol*. **26**, 57 (2008).
7. J. S. Silver, C. A. Hunter, *Immunity* **29**, 7 (2008).
8. R. Zeng *et al*., *J. Exp. Med*. **201**, 139 (2005).
9. M. T. Kasaian *et al*., *Immunity* **16**, 559 (2002).
10. C. S. Hinrichs *et al*., *Blood* **111**, 5326 (2008).
11. K. A. Casey, M. F. Mescher, *J. Immunol*. **178**, 7640 (2007).

10.1126/science.1176487

CHEMISTRY

Extracting Potentials from Spectra

An analysis of the spectra of the elusive beryllium dimer, aided by ab initio calculations, characterizes the molecule near its dissociation limit.

Peter F. Bernath

For most elements, we know whether they can form a diatomic molecule, especially for light atoms that have few electrons and can be treated readily by theory. But for one such light element, surprises are still in store. For most of the 20th century, experimental and theoretical studies agreed that the beryllium dimer (Be_2) did not exist. The Be atom has filled electron shells and—like the inert gases such as helium—was expected to form at most a weak van der Waals dimer at very large internuclear distances. Yet, as shown experimentally by Merritt *et al*. on page 1548 of this issue (*1*), Be_2 does exist and has a relatively short bond (2.45 Å), relative to the anticipated van der Waals complex with a bond length of about 5 Å. Its unusually flat potential curve limits the number of vibrational levels and provides the rare opportunity to study the highest vibrational state of a molecule just at its dissociation limit.

Experiments with beryllium are difficult because the metal is refractory (it has a low vapor pressure even at very high temperatures) and because beryllium-containing compounds are generally extremely toxic. However, Be vapor can be created through laser ablation of a Be metal target. Rapid cooling of the vapor during supersonic expansion through an orifice into vacuum allows preparation of the dimer. The rovibrational states of the dimer are then probed with a double-resonance method: One laser excites the molecule into an excited electronic state where the atoms are still bound; stimulated emission pumping (*2*) by a second laser returns the molecule back into each of the bound vibrational levels of the ground state.

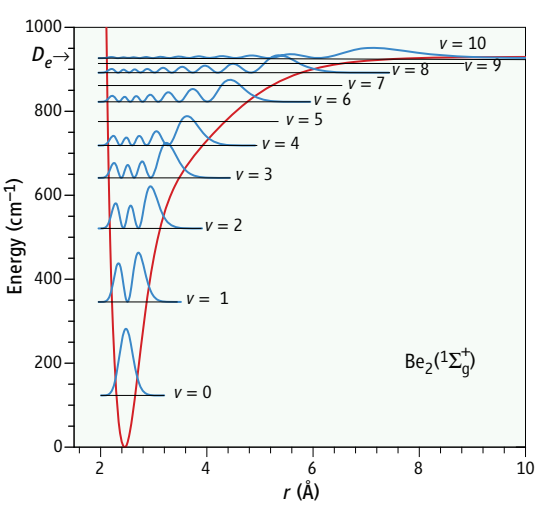

Shallow potentials with deeper implications. The potential energy function for Be_2 as a function of interatomic distance r was determined by Merritt *et al*. from a fit to the experimental observations. The levels become more congested as the energy nears the dissociation limit D_e. The bound vibrational energy levels and the square of the vibrational wave functions were calculated by LeRoy with his program LEVEL (*6*).

The data analysis performed by Merritt *et al*. is noteworthy because it allows a better connection to theory than standard methods. Vibration-rotation energy levels are usually reduced to spectroscopic constants that are parameters in a power series expansion that uses the relevant quantum numbers of the states (*3*, *4*). However, an excessively large number of expansion terms are needed, particularly for a potential with an unusual shape such as Be_2, and these fitting parameters have lost their physical meaning. In contrast, a parameterized potential function (see the figure) requires far fewer fitting parameters and makes a direct connection with ab initio quantum chemistry.

Merritt *et al*. adopted a more powerful analysis method that bypassed traditional constants in favor of a parameterized potential energy function obtained from a direct fit of the energy levels using the vibration-rotation Schrödinger

Department of Chemistry, University of York, Heslington, York, YO10 5DD, UK. E-mail: pfb500@york.ac.uk

equation. LeRoy has been one of the pioneers of this modern quantum mechanical approach, and the authors used his freely available computer code (*5*, *6*).

With only eight electrons, Be_2 has attracted and challenged quantum chemists for nearly 80 years. Ab initio quantum chemistry solves the electronic Schrödinger equation to obtain the interaction energy for a series of molecular geometries. Within the Born-Oppenheimer approximation, which separates fast electronic motion from slower vibration-rotation nuclear motion, these electronic energies are used to construct the potential energy function that is then used to solve the vibration-rotation Schrödinger equation. It is now even possible to deal with the breakdown of the Born-Oppenheimer approximation in both experiment (*7*) and ab initio theory (*8*).

Quantum chemistry attributes the formation of the Be–Be bond and the unusual potential shape to the inclusion of more and more p character in the valence orbitals as the atoms approach each other (*9*). The p orbitals are more directional than the s orbitals that describe the isolated atoms. The comparison between the experimentally derived potential of Merritt *et al*. and modern high-quality ab initio potentials such as those calculated in (*9*, *10*) is reasonable at the moment but definitely not perfect (*11*), with noticeable differences in the internuclear distance and in the dissociation energy.

It is experimentally challenging to measure the entire range of vibrational levels and locate the last bound level at $v = 10$, which has a binding energy of only a few wave numbers. Indeed it is even possible that there is another vibrational level with $v = 11$ that is bound by a tiny fraction of a wave number. As can be seen from the square of the wave function, which gives the probability distribution, the molecule spends nearly all of its time at a large internuclear separation of 7 Å for $v = 10$. The application of stimulated emission pumping and the availability of a suitable excited electronic state allowed Merritt *et al*. to map out the Be_2 levels.

Spectroscopic observations often focus on the lowest few vibrational levels of a potential because they are easier to observe and calculate, but modern computational and experimental methods—such as interactions seen in cold atom trapping (*12*)—can provide information on the last few levels near dissociation. In some cases [for example, MgH (*13*)], it is only the combination of modern potential fitting methods with high-quality observations that enables the last few bound levels to be located in the forest of stronger lines. The full characterization of all bound levels with experimental precision for small molecules such as water is still a distant goal, but the first steps with, for example, H_2 (*14*), MgH (*13*), and now Be_2, are important landmarks on the way.

References and Notes

1. J. M. Merritt, V. E. Bondybey, M. C. Heaven, *Science* **324**, 1548 (2009).
2. C. E. Hamilton, J. L. Kinsey, R. W. Field, *Annu. Rev. Phys. Chem*. **37**, 493 (1986).
3. J. L. Dunham, *Phys. Rev.* **41**, 721 (1932).
4. P. F. Bernath, *Spectra of Atoms and Molecules* (Oxford Univ. Press, Oxford, ed. 2, 2005).
5. R. J. LeRoy, J. Y. Seto, Y. Huang, "DPotFit; a computer program for fitting diatomic molecular spectral data to potential energy functions," University of Waterloo Chemical Physics Research Report CP-662R (2006).
6. See http://leroy.uwaterloo.ca/programs.html.
7. R. J. Le Roy *et al*., *J. Chem. Phys*. **123**, 204304 (2005).
8. D. W. Schwenke, *J. Chem. Phys*. **118**, 6898 (2003).
9. J. M. L. Martin, *Chem. Phys. Lett*. **303**, 399 (1999).
10. R. J. Gdanitz, *Chem. Phys. Lett.* **312**, 578 (1999).
11. V. Spirko, *J. Mol. Spectrosc.* **235**, 268 (2006).
12. J. M. Hutson, P. Soldán, *Int. Rev. Phys. Chem*. **25**, 497 (2006).
13. A. Shayesteh *et al*., *J. Phys. Chem.* A **111**, 12495 (2007).
14. I. Dabrowski, *Can. J. Phys*. **62**, 1639 (1984).

15. I thank R. J. LeRoy for making the figure and for his comments. Financial support was provided by the UK Engineering and Physical Sciences Research Council.

10.1126/science.1175751

NEUROSCIENCE

Bridging the Gap and Staying Local

Imaging with fluorescence reporters reveals the molecular nature of long-term memory storage at stimulated synapses.

Martin Korte

Long-term memory storage requires the transcription of specific genes in neurons (*1*). It also requires that the proteins encoded by these transcripts localize to regions in the neurons that forge the communicative neuronal connections, or synapses (*2*). Yet, how do gene products generated in the neuronal cell body (soma) "know" to which of all the neuron's synapses (up to 30,000) they have to be targeted? Two reports, by Wang *et al.* (*3*) on page 1536 of this issue and by Okada *et al.* (*4*), explore how long-lasting memory can be implemented at specific synapses.

One solution that has been debated is the tagging (or capture) hypothesis (*5*, *6*). The so-called synaptic tag serves as a molecular marker that targets synaptic plasticity-related proteins only to previously activated synapses. Generally available proteins would be transported into the activated synapses only after stimulation (*4*). Alternatively, the synaptic tag could spatially restrict new protein synthesis (local translation) at stimulated synapses (*7*, *8*). However, until now, there has been no direct evidence showing that specific messenger RNAs (mRNAs) undergo locally restricted translation at stimulated synapses only during long-lasting (transcription-dependent) synaptic plasticity.

To approach this problem, Wang *et al*. cultivated sensory and motor neurons of the sea slug *Aplysia californica* (a model system for studying synaptic plasticity) (*1*). This monosynaptic connection is a central part of the gill-withdrawal reflex in *Aplysia*. Multiple applications of the neurotransmitters serotonin or Phe-Met-Arg-Phe-NH_2 (FMRFamide) leads to long-term facilitation or depression of synaptic transmission, respectively, two effects that control memory storage. To monitor local translation of mRNA during long-lasting synaptic plasticity, Wang *et al*. generated an elegant molecular tool using mRNA that encodes sensorin, a sensory neuron–specific peptide neurotransmitter. Sensorin mRNA localizes to distal neuronal processes (neurites) and is abundant at synapses. Its translation to protein is necessary for serotonin-induced long-term facilitation. The authors fused the 5′ and 3′ untranslated regions of sensorin mRNA to the region of mRNA encoding dendra2, a fluorescent protein (*9*). Dendra2 switches its fluorescence irreversibly from green to red after illumination by ultraviolet light. The authors first converted dendra2 to red fluorescence by ultraviolet irradiation. Afterward, any green dendra2 detected represents newly produced protein via local translation (after the soma was cut off). Wang *et al.* show that green dendra2 became visible only at synapses that demonstrated long-term facilitation, but not at unstimulated synapses, nor when long-term depression was induced.

Zoological Institute, Division of Cellular Neurobiology, TU Braunschweig, D-38106 Germany. E-mail: m.korte@tu-bs.de

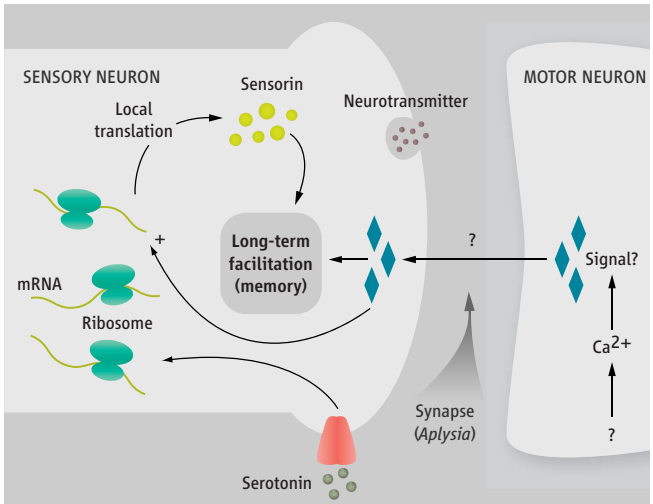

Restricted storage. The results of Wang *et al.* support a scenario for activity-dependent synaptic plasticity in which stimulation of a presynaptic neuron (for example, with the neurotransmitter serotonin), and a retrograde signal from a postsynaptic neuron, activate the local expression of specific mRNA. This, in part, underlies long-term facilitation memory storage.

One central finding of Wang *et al.* is that for local translation of mRNA to occur, the postsynaptic side (the motor neuron) is needed as well. Thus, without a chemical synapse (in which molecules relay signals across a synapse), local translation is not functional. Furthermore, the authors show that Ca^{2+} changes in the postsynaptic compartment are correlated to local protein translation in the presynaptic neuron. Therefore, a trans-synaptic retrograde signal is required for translational regulation in the presynaptic side (see the figure).

Local and precisely targeted protein synthesis is one solution to the specificity puzzle. Another solution would be to target ubiquitously available plasticity-related proteins into the stimulated synapse only. Okada *et al.* (*4*) showed that under resting conditions, Vesl-1S (also called Homer 1a), a late-phase plasticity-related protein required for long-term fear memory in mammals, was absent from the postsynaptic side of a stimulated synapse (in primary cultures of rat hippocampal neurons). Okada *et al.* used the fluorescence marker enhanced green fluorescent protein (fused to Vesl-1S) to detect the movement of the corresponding protein. Only after activation of the *N*-methyl-D-aspartate (NMDA) receptor (a glutamate receptor that induces synaptic plasticity) could Vesl-1S enter neuronal spines (small protrusions on dendrites that form the postsynaptic part of connections with other neurons). Localization of plasticity-related proteins into spines is thus tightly controlled by molecules that might function as synaptic tags. This finding invites speculation about the molecular nature of the gatekeeper in stimulated synapses and how it can "sense" the spatial and temporal strength of the incoming information from the presynaptic side. Perhaps molecules located at the neck of a dendritic spine, such as synaptopodin (*10*), could fulfill this function.

The studies of Wang *et al.* and Okada *et al.* demonstrate, in a reductionist cell culture system, that translation and transportation are indeed restricted to specific synapses. However, other data point out that in a more complex network system, there is additional cross-talk and interaction between individual synapses (*11, 12*). Also, the side of the synapse where synaptic strengthening takes place is not always restricted to the activated synapse itself, but rather to a consortium of synapses close to the stimulated side (*13*). Overall it will be exciting to see how processes of metaplasticity, in which the rules of synaptic plasticity are changed due to prior activity of the neuron, are implemented on a molecular basis (*14*). Nevertheless, the studies by Wang *et al.* and Okada *et al.* convincingly demonstrate how synapse specificity can be maintained during the implementation of long-lasting synaptic changes.

References

1. E. R. Kandel, *Science* **294**, 1030 (2001).
2. P. V. Nguyen, T. Abel, E. R. Kandel, *Science* **265**, 1104 (1994)
3. D. O. Wang *et al.*, *Science* **324**, 1536 (2009).
4. D. Okada, F. Ozawa, K. Inokuchi, *Science* **324**, 904 (2009).
5. U. Frey, R. G. M. Morris, *Nature* **385**, 533 (1997).
6. K. C. Martin *et al.*, *Cell* **91**, 927 (1997).
7. O. Steward, E. M. Schuman, *Annu. Rev. Neurosci.* **24**, 299 (2001).
8. A. Govindarajan, R. J. Kelleher, S. Tonegawa, *Nat. Rev. Neurosci.* **7**, 575 (2006).
9. N. G. Gurskaya *et al.*, *Nat. Biotechnol.* **24**, 461 (2006).
10. T. Deller *et al.*, *Proc. Natl. Acad. Sci. U.S.A.* **100**, 10494 (2003).
11. R. Fonseca, U. V. Nagerl, R. G. Morris, T. Bonhoeffer, *Neuron* **44**, 1011 (2004).
12. S. Sajikumar, S. Navakkode, T. C. Sacktor, J. U. Frey, *J. Neurosci.* **25**, 5750 (2005).
13. F. Engert, T. Bonhoeffer, *Nature* **388**, 279 (1997).
14. W. C. Abraham, *Nat. Rev. Neurosci.* **9**, 387 (2008).

10.1126/*Science*.1176484

EVOLUTION

Uniting Alignments and Trees

Ari Löytynoja and Nick Goldman

An iterative method that estimates both sequence alignments and phylogenies leads to improved phylogenetic trees for large data sets.

Phylogenetic trees depicting the evolutionary relatedness of different species or groups of species are often determined by analyzing the similarities and differences between genetic sequences. The problems involved—sequence alignment and phylogenetic inference—are among the oldest in bioinformatics (*1*, *2*) and are still much studied (*3*–*7*). As was noticed early on, however, alignment and phylogenetic inference are not separate problems but should be seen as two parts of one question: the detection of sequence homology (*8*). On page 1561 of this issue, Liu *et al.* (*9*) describe a new approach for the coestimation of phylogenetic trees and sequence alignments for very large data sets.

European Molecular Biology Laboratory European Bioinformatics Institute, Wellcome Trust Genome Campus, Hinxton CB10 1SD, UK. E-mail: ari@ebi.ac.uk, goldman@ebi.ac.uk

At its simplest, the evolution of sequences is a treelike forking process of speciations and sequence duplications (*10*). In this process, mutations—insertions, deletions, and substitutions—may occur in the branches that connect the nodes and leaves of the tree (see the figure, panel A). In evolutionary studies, an alignment—the placement of nucleotides or amino acids from a set of related sequences into the columns of a matrix (see the figure, panel C)—is an inference of homology: Each column contains the sequence characters (amino acids or nucleotides) believed to have evolved from a common ancestor through character substitutions only. This inference is complicated by the reduction of sequence similarity over evolutionary time because of substitutions and, more importantly, by insertions and deletions that cause breaks in the runs of consecutive homologous sites in each sequence. Errors in homology inference may lead

CREDIT: N. KEVITIYAGALA/*SCIENCE*

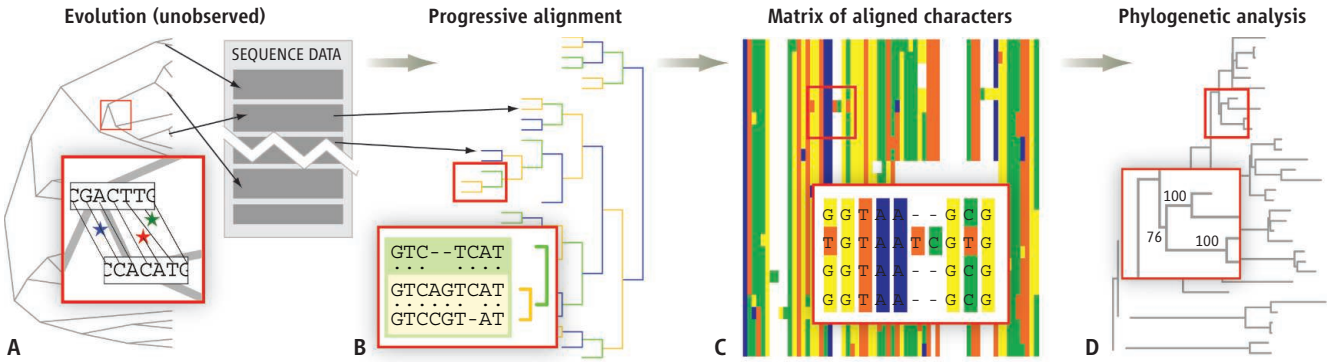

Interdependence of alignment and phylogeny. (**A**) Sequences are related through an unknown evolutionary tree; mutations occur along the branches that connect the sequences at the nodes. (**B**) Progressive alignment methods try to backtrack the evolutionary process and build the multiple alignment from sequential pairwise alignments performed according to a guide tree. (**C**) Sequence alignment is an inference of homology: each column represents the descendants of one ancestral character. (**D**) Phylogenetic inference is based on the alignment (C), which may be affected by the guide tree used to build it (B). The method of Liu *et al*. reduces this effect by alternating between steps (B) and (D) until their likelihood criterion no longer improves.

to erroneous conclusions in further analyses.

Phylogenetic sequence analyses are traditionally performed in two steps: Alignment is followed by reconstruction of a tree from the character patterns observed at each homologous site. However, this approach has an inherent problem of circularity. Widely used alignment algorithms require a guide tree (see the figure, panel B) before the sequences are aligned and a tree can be inferred (see the figure, panel D). Without a guide tree, alignment programs typically generate a tree using relatively unsophisticated methods. Errors in these starting trees may introduce errors in the resulting alignment that then affect the phylogenetic inference.

It is this vicious cycle of interdependence that Liu *et al.* attempt to break. Their solution is to apply existing alignment and phylogeny inference tools in a more efficient manner. By repeatedly breaking, reinferring, and merging the alignment around the center of a phylogenetic tree, which is itself reestimated after each cycle, they evade the errors in the starting guide tree and reduce the bias that those errors cause in phylogenetic inference.

Although the concept of iterating alignment and tree inference steps is not new (*11*), earlier implementations used relatively unsophisticated methods to infer trees, and were not efficient in exploring alternative solutions. Furthermore, Liu *et al*.'s approach is fast and can thus be used to analyze very large data sets, for which the initial guess of the tree is most likely to be seriously wrong. Liu *et al.* show that their method outperforms existing methods, recovering more correct homologies in sequence alignment and producing phylogenetic trees closer to the correct tree in large simulations of 500 and 1000 sequences. Their method is not better than the best existing methods on smaller data sets (where the initial tree may not be that wrong), but the authors point out that 1000 sequences are not that many if we are trying to resolve the evolutionary Tree of Life (*12*).

Liu *et al*.'s method is a good reminder that alignment and phylogeny should not be considered in isolation. It also raises some key questions and further challenges. The inference tools that Liu *et al.* use do not guarantee correct alignments, nor do they use all available information. Indeed, widely used alignment methods make systematic errors in the placement of insertions and deletions even when the correct tree is known (*13*).

Because Liu *et al*. evaluate alignment solutions with a traditional phylogenetic likelihood score that treats gapped sites (indicating insertions and deletion events) as missing data, these errors go largely undetected and alignments may even be biased toward certain types of errors. Neglecting insertions and deletions is also wasteful, because they are valuable phylogenetic markers that can be helpful in difficult problems such as determining the Tree of Life (*12*, *14*). Methodological complexity typically makes the inference slower, but future approaches to solving alignment and phylogeny problems will benefit from incorporating insertions and deletions in their optimization measures.

The central idea in Liu *et al*.'s approach, breaking and remerging the alignment, is general. Further improvements might be achieved by replacing the tools and measures they use with more advanced ones. Their method is not, however, a true simultaneous estimation based on a statistical model of evolutionary change by insertion, deletion, and substitution, and thus cannot address another obstacle in phylogenetic inference: the uncertainty of the alignment solution (*4*, *15*, *16*). For example, phylogenetic trees are commonly presented with statistical support values such as bootstrap proportions (*17*) (see the figure, panel D). Most studies ignore that these scores are based on a fixed sequence alignment that supports the tree in the first place; they may thus make us overly confident of its accuracy.

A key challenge will be to extend the evolutionary analysis methods—including Liu *et al.*'s approach—to assess the reliability of the overall solution and to consider the alignment uncertainty in the tree search and in downstream evolutionary analyses. And that is not all: Given that even the interpretation of bootstrap proportions is complicated (*18*), it will be a nightmare to visually portray the uncertainty of alignments.

References and Notes

1. S. B. Needleman, C. D. Wunsch, *J. Mol. Biol.* **48**, 443 (1970).
2. R. Eck, M. Dayhoff, *Atlas of Protein Sequence and Structure* (National Biomedical Research Foundation, Silver Spring, MD, 1966).
3. A. Stamatakis, *Bioinformatics* **22**, 2688 (2006).
4. B. D. Redelings, M. A. Suchard, *BMC Evol. Biol.* **7**, 40 (2007).
5. S. Whelan, *Syst. Biol.* **56**, 727 (2007).
6. J. Pei, N. Grishin, *Bioinformatics* **23**, 802 (2007).
7. B. D. Paten *et al.*, *Genome Res.* **18**, 1829 (2008).
8. D. Sankoff, *SIAM J. Appl. Math.* **28**, 35 (1975).
9. K. Liu *et al.*, *Science* **324**, 1561 (2009).
10. As well as speciation, a major form of genetic novelty comes about when a region of a genome (often containing a complete gene) is duplicated within the evolutionary lineage of one species. Typically, one copy retains the original function; the other takes on a new function.
11. P. Hogeweg, B. Hesper, *J. Mol. Evol.* **20**, 175 (1984).
12. D. R. Maddison, K.-S. Schulz, Eds., *The Tree of Life Web Project* (2007); see http://tolweb.org.
13. A. Löytynoja, N. Goldman, *Science* **320**, 1632 (2008).
14. A. Rokas, P. Holland, *Trends Ecol. Evol.* **15**, 454 (2000).
15. G. Lunter *et al.*, *BMC Bioinformatics* **6**, 83 (2005).
16. K. M. Wong, M. A. Suchard, J. P. Huelsenbeck, *Science* **319**, 473 (2008).
17. J. Felsenstein, *Evolution* **39**, 783 (1985).
18. M. E. Alfaro, S. Zoller, F. Lutzoni, *Mol. Biol. Evol.* **20**, 255 (2003).

19. A.L. is funded by the Wellcome Trust (Program grant GR078968), and N.G. is supported by the European Molecular Biology Laboratory.

10.1126/science.1175949

Graphene: Status and Prospects

A. K. Geim

Graphene is a wonder material with many superlatives to its name. It is the thinnest known material in the universe and the strongest ever measured. Its charge carriers exhibit giant intrinsic mobility, have zero effective mass, and can travel for micrometers without scattering at room temperature. Graphene can sustain current densities six orders of magnitude higher than that of copper, shows record thermal conductivity and stiffness, is impermeable to gases, and reconciles such conflicting qualities as brittleness and ductility. Electron transport in graphene is described by a Dirac-like equation, which allows the investigation of relativistic quantum phenomena in a benchtop experiment. This review analyzes recent trends in graphene research and applications, and attempts to identify future directions in which the field is likely to develop.

Graphene research has developed at a truly relentless pace. Several papers appear every day, and, if the bibliometrics predictions (*1*) are to be trusted, the amount of literature on graphene will keep rapidly increasing over the next few years. This makes it a real struggle to keep up with the developments. Newcomers are left without a broad perspective and are largely unaware of previous arguments and solved problems, whereas the community's doyens already show signs of forgetting their earlier papers. To combat this curse of success, many reviews have appeared in the last 2 years [e.g., (*2*)], and books on graphene are in the making. The electronic properties of graphene were recently discussed in an extensive theory review (*3*), and this basic information is unlikely to require any revision soon. More specialized papers discussing such topics as the quantum Hall effect in graphene, its Raman properties, and epitaxial growth on SiC are collected in (*4*). Despite, or perhaps because of, the vast amount of available literature, graphene research has now reached the stage where a strategic update is needed to cover the latest progress, emerging trends, and opening opportunities. This paper is intended to serve this purpose without repeating, whenever possible, the information available in the earlier reviews.

Growing Opportunities

Graphene is a single atomic plane of graphite, which—and this is essential—is sufficiently isolated from its environment to be considered freestanding. Atomic planes are, of course, familiar to everyone as constituents of bulk crystals, but one-atom-thick materials such as graphene remained unknown. The basic reason for this is that nature strictly forbids the growth of low-dimensional (low-D) crystals (*2*). Crystal growth implies high temperatures (T) and, therefore, thermal fluctuations that are detrimental for the stability of macroscopic 1D and 2D objects. One can grow flat molecules and nanometer-sized crystallites, but as their lateral size increases, the phonon density integrated over the 3D space available for thermal vibrations rapidly grows, diverging on a macroscopic scale. This forces 2D crystallites to morph into a variety of stable 3D structures.

The impossibility of growing 2D crystals does not actually mean that they cannot be made artificially. With hindsight, this seems trivial. Indeed, one can grow a monolayer inside or on top of another crystal (as an inherent part of a 3D system) and then remove the bulk at sufficiently low T such that thermal fluctuations are unable to break atomic bonds even in macroscopic 2D crystals and mold them into 3D shapes.

This consideration allows two principal routes for making 2D crystals (Fig. 1). One is to mechanically split strongly layered materials such as graphite into individual atomic planes (Fig. 1A). This is how graphene was first isolated and studied. Although delicate and time-consuming, the handcraft (often referred to as a scotch-tape technique) provides crystals of high structural and electronic quality, which can currently reach millimeter size. It is likely to remain the technique of choice for basic research and for making proof-of-concept devices in the foreseeable future. Instead of cleaving graphite manually, it is also possible to automate the process by using, for example, ultrasonic cleavage (*5*). This leads to stable suspensions of submicrometer graphene crystallites (Fig. 1B), which can then be used to make polycrystalline films and composite materials (*5*, *6*). Conceptually similar is the ultrasonic cleavage of chemically "loosened" graphite, in which atomic planes are partially detached first by intercalation, making the sonification more efficient (*6*). The sonification allows graphene production on an industrial scale.

The alternative route is to start with graphitic layers grown epitaxially on top of other crystals (*7*) (Fig. 1C). This is the 3D growth during which epitaxial layers remain bound to the underlying substrate and the bond-breaking fluctuations are suppressed. After the epitaxial structure is cooled down, one can remove the substrate by chemical etching. Technically, this is similar to making, for example, SiN membranes; however, the survival of one-atom-thick crystals was deemed impossible, and no one tried this route until recently (*8*–*10*). The isolation of epitaxial monolayers and their transfer onto weakly binding substrates (*2*) may

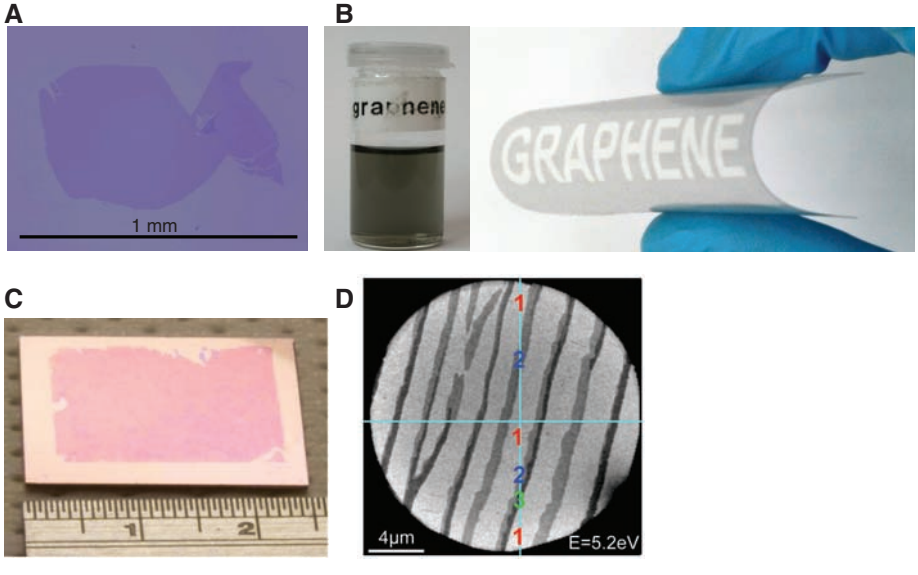

Fig. 1. Making graphene. (**A**) Large graphene crystal prepared on an oxidized Si wafer by the scotch-tape technique. [Courtesy of Graphene Industries Ltd.] (**B**) Left panel: Suspension of microcrystals obtained by ultrasound cleavage of graphite in chloroform. Right panel: Such suspensions can be printed on various substrates. The resulting films are robust and remain highly conductive even if folded. [Courtesy of R. Nair, University of Manchester] (**C**) The first graphene wafers are now available as polycrystalline one- to five-layer films grown on Ni and transferred onto a Si wafer. [Courtesy of A. Reina and J. Kong, MIT] (**D**) State-of-the-art SiC wafer with atomic terraces covered by a graphitic monolayer (indicated by "1"). Double and triple layers ("2" and "3") grow at the steps (*12*).

Manchester Centre for Mesoscience and Nanotechnology, University of Manchester, Oxford Road, Manchester M13 9PL, UK.

now seem obvious, but it was realized only last year (*9*, *10*).

With progress continuing apace, the production of graphene wafers looks like a done deal. Imagine the following technology: Let us start with a tungsten (011) wafer of many inches in diameter and epitaxially grow a thin Ni (111) film on top (*11*). This is to be followed by chemical vapor deposition of a carbon monolayer (the growth of graphene on Ni can be self-terminating with little lattice mismatch) (*7*, *11*). In this manner, wafer-scale single crystals of graphene (chemically bound to Ni) have been grown (*11*). A polymer or another film can then be deposited on top, and Ni is etched away as a sacrificial layer, leaving a graphene monolayer on an insulating substrate and the expensive W wafer ready for another round. The full cycle has not yet been demonstrated and will probably differ from the gedanken one outlined above (e.g., Cu can be used instead of Ni). Nonetheless, wafers of continuous few-layer graphene have already been grown on polycrystalline Ni films and transferred onto plastic and Si wafers (*9*, *10*) (Fig. 1C). These films exhibit carrier mobility μ of up to 4000 $cm^2\ V^{-1}\ s^{-1}$ (*10*)—close to that of cleaved graphene—even before the substrate material, growth, and transfer procedures have been optimized.

Where does this leave graphitic layers grown on SiC (*4*, *12*) (Fig. 1D)? These have been considered as a champion route to graphene wafers for electronics applications, mostly because SiC automatically provides an insulating substrate. First of all, one must distinguish between two principally different types of "graphene on SiC." One consists of single and double layers grown on the Si-terminated face, and the other is "multilayer epitaxial graphene" that rapidly grows on the carbon face (*4*, *12*). In the former case, carbon layers are bound to the substrate sufficiently weakly to retain graphene's linear spectrum away (>0.2 eV) from the charge neutrality point (NP) (*13*). However, interaction with the substrate induces strong doping (~10^{13} cm^{-2}) and spectral disorder at low energies [(*13*); see (*14*) for a possible model for the complex graphene-SiC interface]. The crystal quality and coverage homogeneity for the Si-face films have recently improved (*12*), and μ values start approaching those for graphene transferred from Ni. As for the carbon face, its epitaxial multilayers should probably be referred to as turbostratic graphene because they are rotationally disordered (no Bernal stacking) and separated by a distance slightly larger than that in graphite (*4*, *15*). Turbostratic graphene exhibits the Dirac-like spectrum of free-standing graphene, little doping, and exceptionally high electronic quality (μ ≈ 250,000 $cm^2\ V^{-1}\ s^{-1}$ at room temperature) (*15*). These features can be attributed to weak electronic coupling between inner layers; their protection from the environment by a few outer layers; and the absence of microscopic corrugations (*2*, *8*). Because an external electric field is screened within just a couple of near-surface layers, turbostratic graphene probably offers limited potential for electronics but is interesting from other perspectives, especially for fundamental studies close to NP.

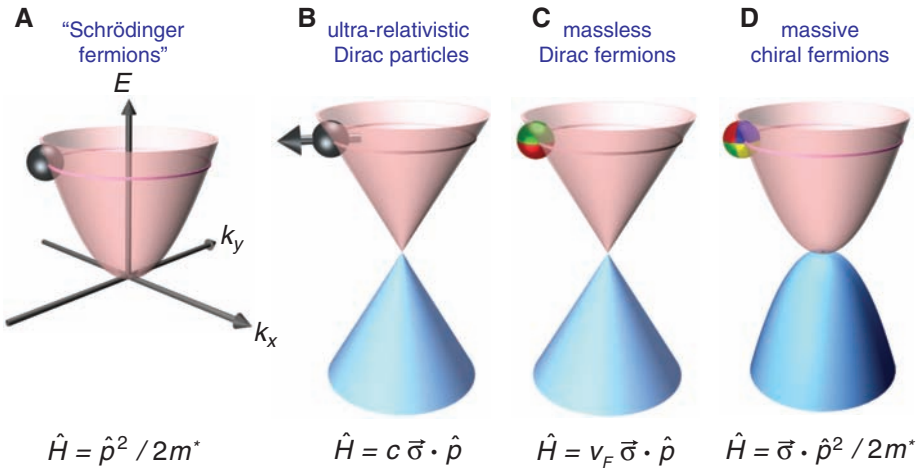

Fig. 2. Quasi-particle zoo. (**A**) Charge carriers in condensed matter physics are normally described by the Schrödinger equation with an effective mass m^* different from the free electron mass ($\hat{p}$ is the momentum operator). (**B**) Relativistic particles in the limit of zero rest mass follow the Dirac equation, where c is the speed of light and $\vec{\sigma}$ is the Pauli matrix. (**C**) Charge carriers in graphene are called massless Dirac fermions and are described by a 2D analog of the Dirac equation, with the Fermi velocity $v_F \approx 1 \times 10^6$ m/s playing the role of the speed of light and a 2D pseudospin matrix $\vec{\sigma}$ describing two sublattices of the honeycomb lattice (*3*). Similar to the real spin that can change its direction between, say, left and right, the pseudospin is an index that indicates on which of the two sublattices a quasi-particle is located. The pseudospin can be indicated by color (e.g., red and green). (**D**) Bilayer graphene provides us with yet another type of quasi-particles that have no analogies. They are massive Dirac fermions described by a rather bizarre Hamiltonian that combines features of both Dirac and Schrödinger equations. The pseudospin changes its color index four times as it moves among four carbon sublattices (*2*–*4*).

Whichever way one now looks at the prospects for graphene production in bulk and wafer-scale quantities, those challenges that looked so daunting just 2 years ago have suddenly shrunk, if not evaporated, thanks to the recent advances in growth, transfer, and cleavage techniques.

Quantum Update

The most explored aspect of graphene physics is its electronic properties. Despite being recently reviewed (*2*–*4*), this subarea is so important that it necessitates a short update. From the most general perspective, several features make graphene's electronic properties unique and different from those of any other known condensed matter system. The first and most discussed is, of course, graphene's electronic spectrum. Electrons propagating through the honeycomb lattice completely lose their effective mass, which results in quasiparticles that are described by a Dirac-like equation rather than the Schrödinger equation (*2*–*4*). The latter—so successful for the understanding of quantum properties of other materials—does not work for graphene's charge carriers with zero rest mass. Figure 2 provides a visual summary of how much our quantum playgrounds have expanded since the experimental discovery of graphene. Second, electron waves in graphene propagate within a layer that is only one atom thick, which makes them accessible and amenable to various scanning probes, as well as sensitive to the proximity of other materials such as high-κ dielectrics, superconductors, ferromagnetics, etc. This feature offers many enticing possibilities in comparison with the conventional 2D electronic systems (2DES). Third, graphene exhibits an astonishing electronic quality. Its electrons can cover submicrometer distances without scattering, even in samples placed on an atomically rough substrate, covered with adsorbates and at room temperature. Fourth, as a result of the massless carriers and little scattering, quantum effects in graphene are robust and can survive even at room temperature.

The initial studies of graphene's electronic properties were focused on the analysis of what new physics could be gained by using the Dirac equation within the standard condensed matter formalism (*2*–*4*). This "recycling" of quantum electrodynamics for the case of graphene has quickly led to the understanding of the half-integer quantum Hall effect and the predictions of such phenomena as Klein tunneling, zitterbewegung, the Schwinger production (*16*), supercritical atomic collapse (*3*, *17*), and Casimir-like interactions between adsorbates on graphene (*18*). As for experiment, only the Klein tunneling has been verified in sufficient detail (*19*, *20*). Furthermore, transport properties of real graphene devices have turned out to be much more complicated than theoretical quantum electrodynamics, and some basic questions about graphene's electronic properties still remain to be answered. For example, there is no consensus about the scattering mechanism that currently limits μ, little understanding of transport properties near NP [especially on zero Landau level (*21*)], and no evidence for many predicted interaction effects.

In the near term, much of this research will continue being driven by our knowledge about other low-D systems and by the "recycling" of the known issues and phenomena. Graphene-based quantum dots (*22*, *23*), p-n junctions (*19*, *20*), nanoribbons (*23*–*25*), quantum point contacts (*22*), and, especially, magnetotransport near NP have not received even a fraction of the attention they deserve. Also, it is easy to foresee the revisiting of lateral superlattices, magnetic focusing, electron optics, and many interference and ballistic effects studied previously in the conventional 2DES (*26*), which hopefully can either be more spectacular in graphene or clarify its physics. Among other usual suspects are electro- and magneto-optics, where graphene offers many unexplored opportunities.

Graphene is structurally malleable, and its electronic, optical, and phonon properties can be strongly modified by strain and deformation (*27*). For example, strain allows one to create local gauge fields (*3*) and even alter graphene's band structure. Research on bended, folded, and scrolled graphene is also gearing up. Furthermore, graphene and turbostratic graphene offer a dream playground for scanning probe microscopy, and many experiments can be constructed for observing supercritical screening, detecting local magnetic moments, mapping wave functions in quantizing fields, etc. Further down the line are interaction effects in split bilayers; observing such effects would be experimentally challenging but may bring up physics even more spectacular than that in the other 2DES (*28*). On the frontier of exploration is the fractional quantum Hall effect, whose possibility has already been tormenting graphene researchers who occasionally observe plateau-like features at fractional fillings, only to find them irreproducible for different devices.

The above sketchy agenda may take many years to complete, and the speed of developments will crucially depend on progress in growing wafers and improvements in sample quality. Inch-size wafers with μ values in the range of 1 million can no longer be dismissed as "graphene dreams," and when this happens, many-body phenomena and new physics that cannot even be envisaged at this stage are likely to emerge.

Chemistry Matters

Graphene is an ultimate incarnation of the surface: It has two faces with no bulk in between. Although this surface's physics is currently at the center of attention, its chemistry has remained largely unexplored. What we have so far learned about graphene chemistry is that, similar to the surface of graphite, graphene can adsorb and desorb various atoms and molecules (for example, NO_2, NH_3, K, and OH). Weakly attached adsorbates often act as donors or acceptors and lead to changes mostly in the carrier concentration, so that graphene remains highly conductive (*29*). Other adsorbates such as H^+ or OH^- give rise to localized ("mid-gap") states close to NP, which results in poorly conductive derivatives such as graphene oxide (*6*) and "single-sided graphane" (*30*). Despite the new names, these are not new chemical compounds but are the same graphene randomly decorated with adsorbates. Thermal annealing or chemical treatment allows the reduction of graphene to its original state with relatively few defects left behind (*30*). This reversible dressing up and down is possible because of the robust atomic scaffold that remains intact during chemical reactions.

Within this surface science perspective, graphene chemistry looks similar to that of graphite, and the latter can be used for guidance. There are principal differences too. First, chemically induced changes in graphene's properties are much more pronounced because of the absence of an obscuring contribution from the bulk (*29*). Second, unlike graphite's surface, graphene is not flat but typically exhibits nanometer-scale corrugations (*8*). The associated strain and curvature can markedly influence local reactivity. Third, reagents can attach to both graphene faces, and this alters the energetics, allowing chemical bonds that would be unstable if only one surface were exposed (*31*).

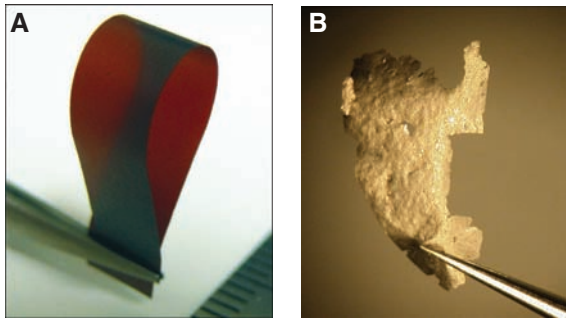

Fig. 3. Graphene derivatives. (**A**) Graphene oxide laminate is tough, flexible, transparent, and insulating (*6*). (**B**) Paper made in the same way as (A) but starting from graphene suspension (*5*) is porous, fragile, opaque, and metallic. [Courtesy of R. Nair, University of Manchester]

An alternative to the surface chemistry perspective is to consider graphene as a giant flat molecule (as first suggested by Linus Pauling). Like any other molecule, graphene can partake in chemical reactions. The important difference between the two viewpoints is that in the latter case, adsorbates are implicitly assumed to attach to the carbon scaffold in a stoichiometric manner—that is, periodically rather than randomly. This should result in new 2D crystals with distinct electronic structures and different electrical, optical, and chemical properties. The first known example is graphane, a 2D hydrocarbon with one hydrogen atom attached to every site of the honeycomb lattice (*30*, *31*). Many other graphene-based crystals should be possible because adsorbates are likely to self-organize into periodic structures, similar to the case of graphite, which is well known for its surface superstructures. Instead of doping with atomic hydrogen (as in graphane), F^-, OH^-, and many functional groups appear to be viable candidates in the search for novel graphene-based 2D crystals.

Graphene chemistry is likely to play an increasingly important role in future developments. For example, stoichiometric derivatives offer a way to control the electronic structure, which is of interest for many applications including electronics. Chemical changes can probably be induced even locally. Imagine, then, an all-graphene circuitry in which interconnects are made from pristine graphene, whereas other areas are modified to become semiconducting and allow transistors. Disordered graphene-based derivatives should not be overlooked either. They can probably be referred to as functionalized graphene, suitable for specific applications. "Graphene paper" is a spectacular example of how important such functionalization could be (Fig. 3). If it is made starting with a suspension of nonfunctionalized flakes (*5*), the resulting material is porous and extremely fragile. However, the same paper made of graphene oxide is dense, stiff, and strong (*6*, *32*). In the latter case, the functional groups bind individual sheets together, which results in a microscopic structure not dissimilar to that of nacre, known for its strength. Instead of aragonite bound in nacre by biopolymer glue, graphene oxide laminate, in particular its reduced version (*32*), makes use of atomic-scale stitching of the strongest known nanomaterial.

Despite a cornucopia of possible findings and applications, graphene chemistry has so far attracted little interest from professional chemists. One reason is that graphene is neither a standard surface nor a standard molecule. However, the main obstacle has probably been the lack of samples suitable for traditional chemistry. The recent progress in making graphene suspensions (*5*, *6*) has opened up a way to liquid-phase chemistry, and hopefully, the professional help that graphene researchers have long been waiting for is now coming.

Sleeping Beauty

It is customary these days to start reports on graphene by referring to it as a "unique electronic system." This statement belittles what graphene is actually about. 2DES and even Dirac-like quasi-particles were known before, but one-atom-thick materials were not. In this respect, graphene has founded a league of its own, but little is known about its non-electronic properties. The situation is now rapidly changing, and this brings beautiful new dimensions into graphene research.

Last year, the first measurements of graphene's mechanical and thermal properties were reported. It exhibits a breaking strength of ~40 N/m, reaching the theoretical limit (*33*). Record values for room-temperature thermal conductivity (~5000 W m^{-1} K^{-1}) (*34*) and Young's modulus (~1.0 TPa) (*33*) were also reported. Graphene can be stretched elastically

by as much as 20%, more than any other crystal (*27*, *33*). These observations were partially expected on the basis of previous studies of carbon nanotubes and graphite, which are structurally made of graphene sheets. Somewhat higher values observed in graphene can be attributed to the virtual absence of crystal defects in samples obtained by micromechanical cleavage. Even more intriguing are those findings that have no analogs. For example, unlike any other material, graphene shrinks with increasing T at all values of T because membrane phonons dominate in 2D (*35*). Also, graphene exhibits simultaneously high pliability (folds and pleats are commonly observed) and brittleness [it fractures like glass at high strains (*36*)]. The notions constitute an oxymoron, but graphene combines both properties. Equally unprecedented is the observation that the one-atom-thick film is impermeable to gases, including helium (*37*). When wafers become available, there should be an explosion of interest in (bio)molecular and ion transport through graphene and its membranes with designer pores.

Speaking of non-electronic properties, we do not even know such basic things about graphene as how it melts. Neither the melting temperature nor the order of the phase transition is known. Ultrathin films are known to exhibit melting temperatures that rapidly decrease with decreasing thickness. The thermodynamics of 2D crystals in a 3D space could be very different from that of thin films and may more closely resemble the physics of soft membranes. For example, melting can occur through generation of defect pairs and be dependent on the lateral size, similar to the Kosterlitz-Thouless transition. Experimental progress in studying graphene's thermodynamic properties has been hindered by the small sizes of available crystals, but the situation may change soon. On the other hand, theoretical progress is likely to remain slow because small sizes have also proven to be a problem in molecular dynamics and other numerical approaches, which struggle to grasp the underlying physics when studying crystals of only a few nanometers in size.

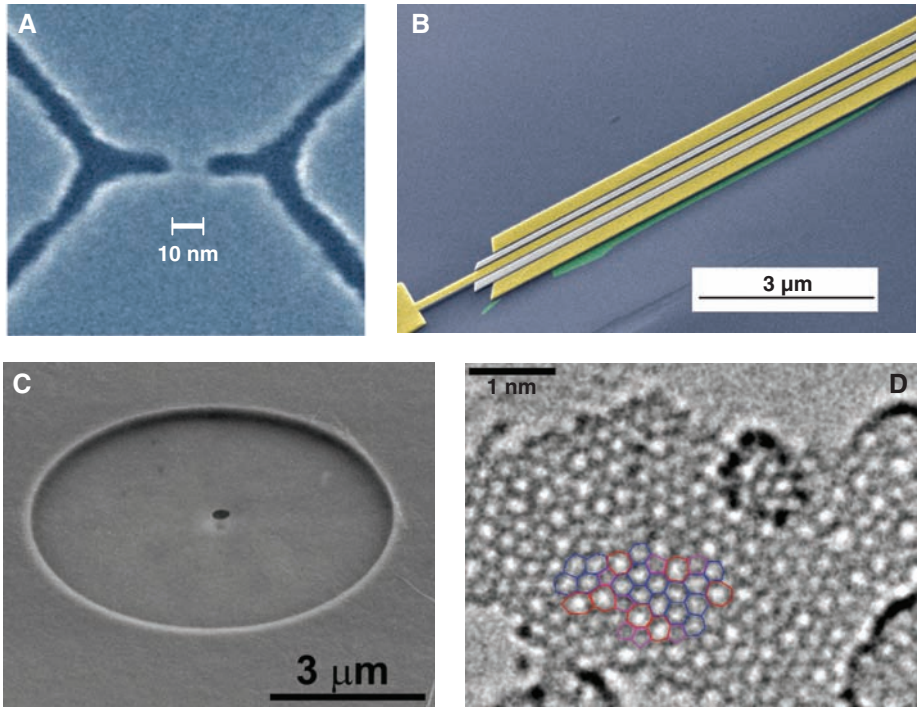

Fig. 4. From dreams to reality. (**A**) Graphene nanoribbons of sub-10-nm scale exhibit the transistor action with large on-off ratios (*22*, *25*). Scanning electron micrograph shows such a ribbon made by electron-beam lithography (*22*). Control of such a ribbon's width and its edge structure with atomic precision remains a daunting challenge on the way toward graphene-based electronics. (**B**) All the fundamentals are in place to make graphene-based HEMTs. This false-color micrograph shows the source and drain contacts in yellow, two top gates in light gray, and graphene underneath in green (*38*). [Courtesy of Y. Lin, IBM] (**C**) Graphene-based NEMS. Shown is a drum resonator made from a 10-nm-thick film of reduced graphene oxide, which covers a recess in a Si wafer (*32*). (**D**) Ready to use: Graphene membranes provide an ideal support for TEM. The central part is a monolayer of amorphous carbon. Graphene itself shows on this image only as a gray background (see the top part). Carbon atoms in the amorphous layer appear dark and make a random array of pentagons, hexagons, and heptagons, as indicated by color lines. Individual oxygen atoms clearly visible on graphene were also reported (*36*). [Courtesy of J. C. Meyer, A. Chuvilin, and U. Kaiser, University of Ulm]

Grandeur and Plainness

Potential applications of graphene were discussed in (*2*) and, during the past 2 years, substantial progress has been made along many lines. The major difference between now and then is the advent of mass production technologies for graphene. This has changed the whole landscape by making the subject of applications less speculative and allowing the development of new concepts unimaginable earlier.

Most of the current buzz surrounds graphene's long-term prospects in computer electronics. Immediate, but often mundane, applications are least discussed and remain unnoticed even within parts of the graphene community. An extreme example of popular speculations is an idea about graphene becoming the base electronic material "beyond the Si age." Although this possibility cannot be ruled out, it is so far beyond the horizon that it cannot be assessed accurately. At the very least, graphene-based integrated circuits require the conducting channel to be completely closed in the off state. Several schemes have been proposed to deal with graphene's gapless spectrum and, recently, nanoribbon transistors with large on-off current ratios at room temperature were demonstrated (*22*, *25*) (Fig. 4A). Nonetheless, the prospect of "graphenium inside" remains as distant as ever. This is not because of graphene shortfalls, but rather because experimental tools to define structures with atomic precision are lacking. More efforts in this direction are needed, but the progress is expected to be painstakingly slow and to depend on technological developments outside the research area.

An example to the contrary is the use of graphene in transmission electron microscopy (TEM). It is a tiny niche application, but it is real. Single-crystal membranes, one atom thick and with low atomic mass, provide the best imaginable support for atomic-resolution TEM. With micrometer-sized crystallites now available in solution (*5*) for their cheap and easy deposition on standard grids and with films transferable from metals (*9*, *10*) onto such grids, graphene membranes are destined to become a routine TEM accessory (Fig. 4D).

The space between graphene dreams and immediate reality is packed with applications. One such application is neither grand nor mundane: individual ultrahigh-frequency analog transistors (Fig. 4B). This area is currently dominated by GaAs-based devices known as high-electron-mobility transistors (HEMTs), which are widely used in communication technologies. Graphene offers a possibility to extend HEMTs' operational range into terahertz frequencies. The fundamentals allowing this are well known: Graphene exhibits room-temperature ballistic transport such that the charge transit between source and drain contacts takes only 0.1 ps for a typical channel length of 100 nm. Gate electrodes can be placed as close as several nanometers above graphene, which allows shorter channels and even quicker transit. Although graphene's gapless spectrum leads to low on-off ratios of 10 to 100, they are

considered sufficient for the analog electronics. The progress toward graphene HEMTs is hindered by experimental difficulties in accessing the microwave range. The first frequency tests of graphene transistors were reported only recently (*38*). Long channels and low mobility in these experiments limited the cutoff frequencies to less than 30 GHz (*38*), well below the operational range of GaAs-based HEMTs. However, the observed scaling of the operational frequency as a function of the channel length and μ indicates that the terahertz range is accessible (*38*). With graphene wafers in sight, these efforts are going to intensify, and HEMTs and other ultrahigh-frequency devices such as switches and rectifiers have a realistic chance to reach the market.

Sitting on a Graphene Mine

There has been an explosion of ideas that suggest graphene for virtually every feasible use. This is often led by analogies with carbon nanotubes that continue to serve as a guide in searching for new applications. For example, graphene powder is considered to be excellent filler for composite materials (*6*). Reports have also been made on graphene-based supercapacitors, batteries, interconnects, and field emitters, but it is too early to say whether graphene is able to compete with the other materials, including nanotubes. Less expectedly, graphene has emerged as a viable candidate for use in optoelectronics (*10*, *39*). Suspensions offer an inexpensive way to make graphene-based coatings by spinning or printing (Fig. 1B). An alternative is the transfer of films grown on Ni (*9*, *10*). These coatings are often suggested as a competitor for indium tin oxide (ITO), the industry standard in such products as solar cells, liquid crystal displays, etc. However, graphene films exhibit resistivity of several hundred ohms for the standard transparency of ~80% (*9*, *10*, *39*). Such resistivity is two orders of magnitude higher than for ITO and is unacceptable in many applications (e.g., solar cells). It remains to be seen whether the conductivity can be improved to the required extent. Having said that, graphene coatings also offer certain advantages over ITO. They are chemically stable, robust, and flexible and can even be folded, which gives them a good chance of beating the competition in touch screens and bendable applications.

There is also fast-growing interest in graphene as a base material for nanoelectromechanical systems (NEMS) (*32*, *40*), given that lightness and stiffness are the essential characteristics sought in NEMS for sensing applications. Graphene-based resonators offer low inertial masses, ultrahigh frequencies, and, in comparison with nanotubes, low-resistance contacts that are essential for matching the impedance of external circuits. Graphene membranes have so far shown quality factors of ~100 at 100-MHz frequencies (*40*). Even more encouraging are data for drum resonators made from reduced graphene oxide films (*32*). These nanometer-thick polycrystalline NEMS (Fig. 4C) exhibit high Young's moduli (comparable to those of graphene) and quality factors of ~4000 at room temperature. The films can be produced as wafers and then processed by standard microfabrication techniques. Further developments (increasing the frequency and improving quality factors) should allow graphene NEMS to assail such tantalizing challenges as inertial sensing of individual atoms and the detection of zero-point oscillations.

Among other applications that require mentioning are labs-on-chips (electronic noses) and various resistive memories. The high sensitivity of graphene to its chemical environment is well acknowledged, now that sensors capable of detecting individual gas molecules have been demonstrated (*29*). Imagine an array of graphene devices, each functionalized differently to be able to react to different chemicals or biomolecules. Such functionalization has been intensively researched for the case of carbon nanotubes, and graphene adds the possibility of mass-produced arrays of identical devices. Furthermore, there are several enticing reports on nonvolatile memories in which graphene-based wires undergo reversible resistance switching by, for example, applying a sequence of current pulses (*41*, *42*). The underlying mechanism remains largely unknown, but such nanometer-scale switches present an attractive alternative to phase-change memories and deserve further attention. Reports on graphene-ferroelectric memories (*43*) are also encouraging, given the basic simplicity of their operation.

More Room in the Flatland

Graphene has rapidly changed its status from being an unexpected and sometimes unwelcome newcomer to a rising star and to a reigning champion. The professional skepticism that initially dominated the attitude of many researchers with respect to graphene applications is gradually evaporating under the pressure of recent developments. Still, it is the wealth of new physics—observed, expected, and hoped for—that is driving the area for the moment. Research on graphene's electronic properties is now matured but is unlikely to start fading any time soon, especially because of the virtually unexplored opportunity to control quantum transport by strain engineering and various structural modifications. Even after that, graphene will continue to stand out in the arsenal of condensed matter physics. Research on graphene's non-electronic properties is just gearing up, and this should bring up new phenomena that may well sustain, if not expand, the graphene boom.

References and Notes

1. A. Barth, W. Marx, http://arxiv.org/abs/0808.3320 (2008).
2. A. K. Geim, K. S. Novoselov, *Nat. Mater.* **6**, 183 (2007).
3. A. H. Castro Neto, F. Guinea, N. M. R. Peres, K. S. Novoselov, A. K. Geim, *Rev. Mod. Phys.* **81**, 109 (2009).
4. Special edition: Exploring Graphene—Recent Research Advances, S. Das Sarma, A. K. Geim, P. Kim, A. H. MacDonald, Eds., *Solid State Commun.* **143**, issues 1–2 (2007).
5. Y. Hernandez *et al.*, *Nat. Nanotechnol.* **3**, 563 (2008).
6. D. A. Dikin *et al.*, *Nature* **448**, 457 (2007).
7. C. Oshima, A. Nagashima, *J. Phys. Condens. Matter* **9**, 1 (1997).
8. J. C. Meyer *et al.*, *Nature* **446**, 60 (2007).
9. A. Reina *et al.*, *Nano Lett.* **9**, 30 (2009).
10. K. S. Kim *et al.*, *Nature* **457**, 706 (2009).
11. A. Grüneis, D. V. Vyalikh, *Phys. Rev. B* **77**, 193401 (2008).
12. K. V. Emtsev *et al.*, *Nat. Mater.* **8**, 203 (2009).
13. S. Y. Zhou *et al.*, *Nat. Mater.* **6**, 770 (2007).
14. S. Kim, J. Ihm, H. J. Choi, Y. W. Son, *Phys. Rev. Lett.* **100**, 176802 (2008).
15. M. Orlita *et al.*, *Phys. Rev. Lett.* **101**, 267601 (2008).
16. D. Allor, T. D. Chen, D. A. McGady, *Phys. Rev. D* **78**, 096009 (2008).
17. A. V. Shytov, M. I. Katsnelson, L. S. Levitov, *Phys. Rev. Lett.* **99**, 246802 (2007).
18. A. Shytov, D. Abanin, L. Levitov, http://arxiv.org/abs/0812.4970 (2008).
19. A. F. Young, P. Kim, *Nat. Phys.* **5**, 222 (2009).
20. N. Stander, B. Huard, D. Goldhaber-Gordon, *Phys. Rev. Lett.* **102**, 026807 (2009).
21. J. G. Checkelsky, L. Li, N. P. Ong, *Phys. Rev. B* **79**, 115434 (2009).
22. L. A. Ponomarenko *et al.*, *Science* **320**, 356 (2008).
23. F. Molitor *et al.*, *Phys. Rev. B* **79**, 075426 (2009).
24. M. Y. Han, B. Ozyilmaz, Y. Zhang, P. Kim, *Phys. Rev. Lett.* **98**, 206805 (2007).
25. X. Li, X. Wang, L. Zhang, S. Lee, H. Dai, *Science* **319**, 1229 (2008); published online 23 January 2008 (10.1126/science.1150878).
26. C. W. J. Beenakker, H. van Houten, in *Semiconductor Heterostructures and Nanostructures*, H. Ehrenreich, D. Turnbull, Eds. (Academic, New York, 1991), pp. 1–228.
27. V. M. Pereira, A. H. Castro Neto, N. M. R. Peres, http://arxiv.org/abs/0811.4396 (2008).
28. H. Min, R. Bistritzer, J. J. Su, A. H. MacDonald, *Phys. Rev. B* **78**, 121401 (2008).
29. F. Schedin *et al.*, *Nat. Mater.* **6**, 652 (2007).
30. D. C. Elias *et al.*, *Science* **323**, 610 (2009).
31. J. O. Sofo, A. S. Chaudhari, G. D. Barber, *Phys. Rev. B* **75**, 153401 (2007).
32. J. T. Robinson *et al.*, *Nano Lett.* **8**, 3441 (2008).
33. C. Lee, X. Wei, J. W. Kysar, J. Hone, *Science* **321**, 385 (2008).
34. A. A. Balandin *et al.*, *Nano Lett.* **8**, 902 (2008).
35. W. Bao *et al.*, http://arxiv.org/abs/0903.0414 (2009).
36. T. J. Booth *et al.*, *Nano Lett.* **8**, 2442 (2008).
37. J. S. Bunch *et al.*, *Nano Lett.* **8**, 2458 (2008).
38. Y. M. Lin *et al.*, *Nano Lett.* **9**, 422 (2009).
39. X. Wang, L. Zhi, K. Müllen, *Nano Lett.* **8**, 323 (2008).
40. J. S. Bunch *et al.*, *Science* **315**, 490 (2007).
41. Y. Li, A. Sinitskii, J. M. Tour, *Nat. Mater.* **7**, 966 (2008).
42. B. Standley *et al.*, *Nano Lett.* **8**, 3345 (2008).
43. Y. Zheng *et al.*, *Appl. Phys. Lett.* **94**, 163505 (2009).

44. Supported by the Engineering and Physical Science Research Council (UK), U.S. Office of Naval Research, and U.S. Air Force Office of Scientific Research. I thank I. Grigorieva, A. Castro Neto, A. MacDonald, P. Kim, and K. Novoselov for many helpful comments, and the staff of the Max Planck Institute for Solid-State Research for their hospitality during my sabbatical when this review was partially written.

10.1126/science.1158877

Sexual Intercourse Involving Giant Sperm in Cretaceous Ostracode

R. Matzke-Karasz,[1]* R. J. Smith,[2] R. Symonova,[3] C. G. Miller,[4] P. Tafforeau[5]

The microcrustacean ostracodes are the most abundantly preserved arthropods in the fossil record dating from at least the Ordovician (450 million years ago) (*1*). However, their body and appendages are only rarely preserved. One example of high-quality soft parts preservation is *Harbinia micropapillosa* (Bate, 1972) (*2*) (Cyprididae, Cypridoidea) from the Cretaceous Santana Formation of Brazil. Because scanning electron microscopy (*3*) cannot view internal features, we performed holotomography of five *H. micropapillosa* specimens, three males and two females, revealing the morphology of their internal reproductive system.

We compared submicrometer inline quantitative phase x-ray synchrotron tomography (holotomography) (*4*) on the beamline ID19 of the ESRF (Grenoble, France) on specimens of *H. micropapillosa* and of the extant species *Eucypris virens* (Jurine, 1820) (*5*). Phase contrast–based microtomographic techniques have been applied to nondestructively image microfossils (*6*), but application of phase retrieval on dense and complex fossils is a recent and powerful approach in paleontology (*4*). Extant cypridoidean ostracodes possess an intricate reproductive system comprising about a third of the volume of the body. In both genders, the reproductive organs are divided into two separately functioning systems on both sides of the body. The males have two large sperm pumps (Zenker organs), modified from the posterior section of the vas deferens (fig. S1A). The females possess epithelial recipients (seminal receptacles) at the end of long ducts originating in the two vaginal openings. Empty seminal receptacles of virgin females are folded up; the volume of transferred sperm gives the receptacles their shape and size after mating. These specialized reproductive systems are required for maneuvering the giant sperm: aflagellate, but filiform sperm cells. Sperm lengths range across species from several hundred micrometers to millimeters and thus are often longer than the ostracodes themselves (fig. S1, B and C). Their resistant sheaths allow fossil sperm to be recovered from 5000-year-old ostracodes from Neolithic excavations (*7*).

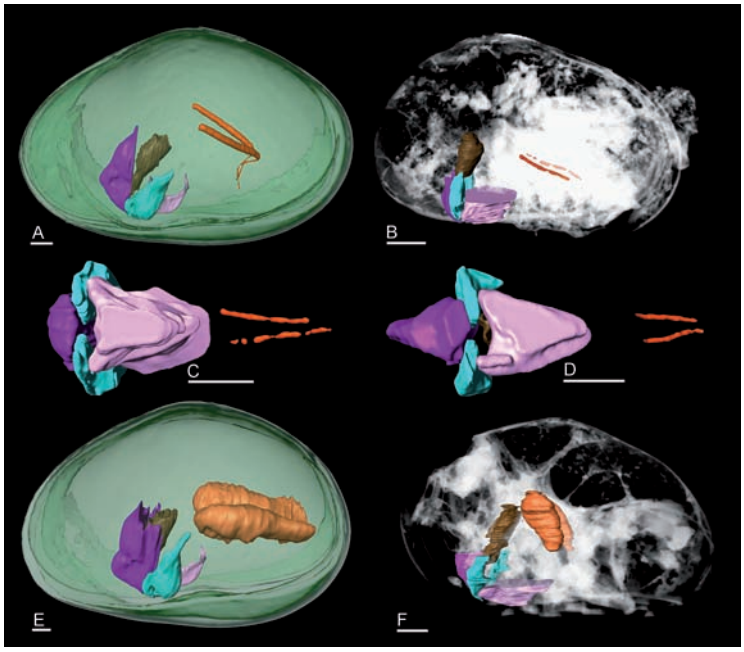

Fig. 1. Partial reconstruction of *E. virens* (extant) and *H. micropapillosa* (fossil). Anterior is to the left. Orange structures indicate central tubes of Zenker organs in males or seminal receptacles in females; brown, esophagus; turquoise, mandible; purple, upper lip; pink, lower lip; green, valves; and gray scales, whole-body reconstruction. All scale bars indicate 100 μm. (**A**) Lateral view of male *E. virens* with several organs included for comparison. (**B**) Male *H. micropapillosa* in lateral view with several organs in context of whole-body reconstruction. (**C** and **D**) Ventral views of several organs including tubes of Zenker organs of male *H. micropapillosa*. (**E**) Lateral view of female *E. virens* with several organs included for comparison. (**F**) Female *H. micropapillosa* in lateral view with several organs in context of whole-body reconstruction, including seminal receptacles.

Three-dimensional processing of holotomographic data (movies S1 to S3) revealed that three male specimens of *H. micropapillosa* contained paired hollow tubes in the posterior part of the body (Fig. 1, B to D) suggestive of Zenker organs. Two female specimens had paired cavities near the midpoint of the body (Fig. 1F), corresponding to the seminal receptacles in recent Cyprididae (Fig. 1E), which are only known from ostracodes reproducing with giant sperm. The receptacles must have been filled with sperm in order to be preserved as two cavities. Thus, giant sperm had developed in cypridoidean ostracodes by ~100 million years ago.

Reproduction with giant sperm, mainly studied in *Drosophila* species, occurs in distinct groups scattered over the animal kingdom. The influence of different selection pressures on this character has been examined, but its long-term stability was unknown. In spite of potential costs, this trait appears to be long-lived even in geological time scales. The wide occurrence of giant sperm in living members of suborder Cypridocopina, coupled with our fossil evidence, suggests that it evolved only once in the group, unlike in *Drosophila* (*8*). Given that sperm size provides an assay "for comparative analyses of the strength of sexual selection in … species without postmating parental investment" (*9*), the persistence of reproduction with giant sperm through geological time may add a criterion to test for the pressure of sexual selection with holotomography recovering data from the past through exceptionally preserved (micro)fossils.

[1]Department of Environmental and Geosciences, Palaeontology, and GeoBioCenter, Ludwig Maximilians University (LMU), 80333 Muenchen, Germany. [2]Lake Biwa Museum, Kusatsu, Shiga 525-0001, Japan. [3]Department of Zoology, Charles University, 12844 Prague, Czech Republic. [4]Department of Palaeontology, Natural History Museum, London SW7 5BD, UK. [5]European Synchrotron Radiation Facility (ESRF), 38043 Grenoble, France.

*To whom correspondence should be addressed. E-mail: r.matzke@lrz.uni-muenchen.de

References and Notes

1. M. Williams *et al.*, *Senckenb. Lethaea* **88**, 11 (2008).
2. D. A. Do Carmo, R. Whatley, J. Villar de Queiroz Neto, J. C. Coimbra, *J. Paleontol.* **82**, 790 (2008).
3. R. J. Smith, *Palaeontology* **43**, 63 (2000).
4. A. Pradel *et al.*, *Proc. Natl. Acad. Sci. U.S.A.* **106**, 5224 (2009).
5. Materials and methods are available as supporting material on *Science* Online.
6. P. Tafforeau *et al.*, *Appl. Phys. A* **83**, 195 (2006).
7. R. Matzke-Karasz, D. C. Horne, H. Janz, H. I. Griffiths, W. F. Hutchinson, *Naturwissenschaften* **88**, 268 (2001).
8. S. Pitnick, T. A. Markow, G. S. Spicer, *Proc. Natl. Acad. Sci. U.S.A.* **92**, 10614 (1995).
9. A. Bjork, S. Pitnick, *Nature* **441**, 742 (2006).
10. Supported by the ESRF (proposal ec-274), the European Union Marie Curie RTN *SexAsex* (FP6-512492), LMU Palaeontology, the Lake Biwa Museum (Japan), and the Natural History Museum (by loan of fossil specimens). Holotomographies are available online at http://paleo.esrf.eu.

Supporting Online Material

www.sciencemag.org/cgi/content/full/324/5934/1535/DC1
Materials and Methods
Fig. S1
Reference
Movies S1 to S3

23 March 2009; accepted 1 May 2009
10.1126/science.1173898

Synapse- and Stimulus-Specific Local Translation During Long-Term Neuronal Plasticity

Dan Ohtan Wang,[1] Sang Mok Kim,[1,2] Yali Zhao,[1] Hongik Hwang,[1] Satoru K. Miura,[3] Wayne S. Sossin,[6] Kelsey C. Martin[1,3,4,5]*

Long-term memory and synaptic plasticity require changes in gene expression and yet can occur in a synapse-specific manner. Messenger RNA localization and regulated translation at synapses are thus critical for establishing synapse specificity. Using live-cell microscopy of photoconvertible fluorescent protein translational reporters, we directly visualized local translation at synapses during long-term facilitation of *Aplysia* sensory-motor synapses. Translation of the reporter required multiple applications of serotonin, was spatially restricted to stimulated synapses, was transcript- and stimulus-specific, and occurred during long-term facilitation but not during long-term depression of sensory-motor synapses. Translational regulation only occurred in the presence of a chemical synapse and required calcium signaling in the postsynaptic motor neuron. Thus, highly regulated local translation occurs at synapses during long-term plasticity and requires trans-synaptic signals.

Long-lasting learning-related synaptic plasticity requires transcription for its persistence (*1*–*3*) and yet can occur in a synapse-specific manner (*4*–*7*). One mechanism that has been proposed to mediate this spatial restriction of gene expression during neuronal plasticity involves regulated translation of localized mRNAs at stimulated synapses (*8*–*10*). Many findings support the existence of local translation at synapses. First, all of the machinery required for translation is present in neuronal processes, including polyribosomes (*11*, *12*), translation factors (*13*), and a select population of mRNAs (*14*–*18*). Second, studies using protein synthesis inhibitors indicate a central role for local translation during long-lasting synaptic plasticity (*5*, *19*, *20*). Third, translation of specific transcripts has been visualized in dendrites of cultured neurons after stimulation with brain-derived neurotrophic factor (BDNF) (*21*) or KCl (*22*), or after inhibition of sodium channels, *N*-methyl-D-aspartate receptor, or the mammalian target of rapamycin (mTOR) signaling pathway (*9*, *23*, *24*). However, direct evidence that a specific mRNA undergoes spatially restricted translation at stimulated synapses during transcription-dependent synaptic plasticity has been lacking.

To directly visualize translation at the level of individual synapses during long-term, learning-related neuronal plasticity, we used the *Aplysia* sensory neuron (SN)–motor neuron (MN) culture system (*2*). The monosynaptic connection formed between SNs and MNs, a central component of the gill-withdrawal reflex in *Aplysia*, can be reconstituted in culture, where well-characterized stimuli elicit forms of plasticity that have direct correlates in the behavior of the animal. Specifically, five spaced applications of serotonin (5X5HT) induce a transcription-dependent long-term facilitation (LTF) of SN-MN synapses that parallels long-term sensitization of the gill-withdrawal reflex (*2*), whereas five spaced applications of the neuropeptide FMRFamide (5XFMRFamide) induce a transcription-dependent long-term depression (LTD) of SN-MN synapses that parallels long-term habituation of the gill-withdrawal reflex (*25*, *26*). Synapse-specific, transcription-dependent LTF of SN-MN synapses is blocked by perfusion of translational inhibitors to distal SN neurites (*5*). Furthermore, SNs only form chemical synapses with appropriate target MNs (*27*, *28*), allowing local translation to be studied in the presence or absence of synapses.

Sensorin translational reporter. To monitor translation at SN-MN synapses during neuronal plasticity, we generated translational reporters of sensorin, a SN-specific peptide neurotransmitter whose mRNA localizes to distal neuronal processes and concentrates at synapses in SNs paired with MNs (*15*, *27*, *29*). Sensorin translation is required for synapse stabilization between SNs and MNs (*27*, *30*), and both sensorin translation and secretion are required for 5HT-induced LTF of *Aplysia* SN-MN synapses (*31*). To generate sensorin translational reporters, we fused the 5′ and 3′ untranslated regions (UTRs) of sensorin to the coding region of the photoconvertible fluorescent protein dendra2 (*32*). Dendra2 switches fluorescence irreversibly from green to red after ultraviolet (UV) illumination, allowing newly synthesized proteins (green) to be differentiated from proteins synthesized before photoconversion (red). Addition of the 5′ and 3′UTRs of sensorin to the dendra2 coding sequence generated a reporter whose mRNA localization was indistinguishable from endogenous sensorin mRNA (Fig. 1A and figs. S1 and S2). Specifically, the reporter mRNA localized to neurites of isolated SNs and concentrated at SN-MN synapses as indicated by ectopic labeling of presynaptic terminals by expression of vesicle-associated membrane protein (VAMP)–mCherry and labeling of MNs with Alexa647 (Fig. 1B). Reporters containing either the 3′UTR or the 5′UTR alone revealed that the 3′UTR was sufficient for localization to neurites, whereas addition of the 5′UTR was required for targeting to synapses (fig. S2). Thus, distinct cis-acting elements mediate neuritic and synaptic mRNA localization.

To visualize local translation of the reporter during LTF induced by bath application of 5X5HT, we expressed the reporter in SNs paired with MNs, removed the SN soma, and photoconverted dendra2 (figs. S1 and S3) and (*33*). Newly synthesized protein (green) had to result from local translation in the neurite because the soma was no longer present. Although 5X5HT induces transcription-dependent LTF, 24 hours (but not 48 hours) facilitation occurs in a translation-dependent manner in the absence of a SN soma, indicating that the initial events involved in persistent LTF can be monitored in SNs lacking cell bodies (*34*). We imaged red and green channels before the first application and immediately after the fifth application of 5HT. Control cultures were stimulated with five applications of vehicle [5X artificial seawater (ASW)] or were untreated. Very little green signal, but robust red signal, was detected after UV illumination, indicating efficient photoconversion (Fig. 2A). After the fifth pulse of 5HT, green dendra2 signal increased at multiple sites within the neurite, and this was completely blocked by the translational inhibitor anisomycin (10 μM) (Fig. 2B and fig. S4). Modest increases in green dendra2 fluorescence were observed in control cultures after application of 5XASW, which were also blocked by anisomycin (10 μM) (Fig. 2B and fig. S4). This modest increase in green dendra2 fluorescence represents basal translation because it was also observed in untreated cultures (Fig. 2B and fig. S4). Immediately after imaging, we fixed the cells and performed fluorescence in situ hybridization (FISH) for the reporter mRNA. A total of 143 of 147 (97%) sites with new translation contained concentrated reporter mRNA. Thus, the subcellular localization of new translation

[1]Department of Psychiatry and Biobehavioral Sciences, University of California–Los Angeles (UCLA), BSRB 390B, 615 Charles E. Young Drive South, Los Angeles, CA 90095–1737, USA. [2]Interdepartmental Program in Neurosciences, UCLA, BSRB 390B, 615 Charles E. Young Drive South, Los Angeles, CA 90095–1737, USA. [3]Department of Biological Chemistry, UCLA, BSRB 310, 615 Charles E. Young Drive South, Los Angeles, CA 90095–1737, USA. [4]Semel Institute for Neuroscience and Human Behavior, UCLA, BSRB 390B, 615 Charles E. Young Drive South, Los Angeles, CA 90095–1737, USA. [5]Brain Research Institute, UCLA, BSRB 390B, 615 Charles E. Young Drive South, Los Angeles, CA 90095–1737, USA. [6]Montreal Neurological Institute, McGill University, 3801 University Street, Montreal, Quebec H3A-2B4, Canada.

*To whom correspondence should be addressed. E-mail: kcmartin@mednet.ucla.edu

correlated with the subcellular localization of reporter mRNA with remarkable accuracy. Because the reporter mRNA specifically concentrated in VAMP-positive synapses (Fig. 1 and fig. S2) (*27*), we conclude that the reporter was translated at synapses.

We quantified new translation as ΔF/F (× 100 = % change), normalized to the red dendra2 signal (which serves as a volume control) (*33*) (Fig. 2B). When stimuli were applied in the presence of anisomycin, there was no significant change in green signal, and thus no translation (2.3 ± 3.4% for Ani+5XASW; –8.9 ± 4.9% for Ani+5X5HT). In untreated or vehicle-treated cultures, we observed a 41.2 ± 3.7% and 43.5 ± 3.6% increase in translation. After stimulation with 5X5HT, we observed a 155.9 ± 18.7% increase in translation. Thus, a basal level of sensorin translation occurs in neurites, which is significantly increased after stimuli that induce LTF (***$P < 0.001$, ANOVA with Bonferroni's multiple comparison test).

Spatial specificity of translation. To determine the spatial specificity of stimulus-induced local translation, we perfused 5X5HT locally onto a subset of synapses (Fig. 3 and figs. S5 and S6). This protocol produces synapse-specific LTF of SN-MN synapses (*5*, *7*). Images were acquired from both stimulated (perfused) and unstimulated (nonperfused) sites within the same SN at the beginning and end of local perfusion. In vehicle-treated cultures, we detected modest increases in newly synthesized green dendra2 at both perfused and nonperfused synapses (27.4 ± 5.6% and 20.2 ± 8.2%, respectively). However, when 5X5HT was perfused onto a subset of synapses, robust increases in new green dendra2 signal were detected at stimulated sites (54.7 ± 10.9%), with only modest increases at nonperfused sites (16.6 ± 4.9%). For each neuron, we calculated the ratio of the ΔF/F at the perfused site to the average ΔF/F at nonperfused sites. In vehicle-treated cultures (Fig. 3D and fig. S7), this ratio was 1.0 ± 0.1, indicating no significant difference between perfused and nonperfused sites. In contrast, in cultures locally perfused with 5X5HT (Fig. 3A), the ratio was 1.3 ± 0.1, indicating a significant increase in new translation at perfused as compared with nonperfused sites (***$P < 0.001$, paired Student's *t* test). Thus, local serotoninergic stimulation induced spatially restricted translation within an individual neuron. FISH analysis revealed equivalent reporter mRNA at all synapses under all conditions (Fig. 3 and figs. S7 and S10). No significant difference in basal translation was observed at nonperfused synapses between 5XASW and 5X5HT groups (fig. S10). Finally, 5X5HT did not induce significant structural changes between the initial and final imaging times (fig. S6).

Stimulus specificity. Five spaced applications of the peptide neurotransmitter FMRFamide produce transcription-dependent LTD of *Aplysia* SN-MN synapses, and local perfusion of 5XFMRFamide has been shown to produce synapse-specific LTD (*35*). To ask whether the 5HT-induced translation of the reporter was stimulus-specific, we locally perfused 5XFMRFamide and monitored reporter translation. The ratio of translation between 5XFMRFamide perfused and nonperfused sites was 1.0 ± 0.1, indicating that FMRFamide did not stimulate sensorin translation (Fig. 3C), consistent with previous studies (*36*). In addition, one application of 5HT (1X5HT), which induces translation-independent STF (short-term facilitation), did not stimulate translation (Fig. 3D and figs. S8 and S10). Basal levels of translation at nonperfused synapses, and concentrations of reporter RNA were equivalent to those in cultures locally perfused with 5X5HT or 5XASW (Fig. 3 and figs. S7 and S10). Thus, translational regulation of the sensorin reporter is stimulus-specific.

Transcript specificity. Global translation in sensory neurites increases by a factor of 3 in response to 5HT (*5*). To determine whether 5HT stimulates global increases in translation in neurites, or whether it regulates translation of a specific subset of transcripts, we constructed a reporter containing the 3′UTR of sensorin (and 5′UTR of SV40), which localized to distal sensory neurites and is present but not concentrated in synapses (fig. S2). We expressed this reporter in SNs making synapses with MNs and asked whether local perfusion of 5X5HT stimulated its translation. We did not detect any increase in translation of this reporter at synapses stimulated with 5X5HT (ratio of ΔF/F at perfused versus nonperfused sites = 1.0 ± 0.1) (Fig. 3). The 3′UTR reporter was present in SN processes, and translation was quantified at sites containing equivalent amounts of 3′UTR or 5′3′UTR reporter (fig. S10). Thus, 5HT does not regulate the translation of all process-localized mRNAs.

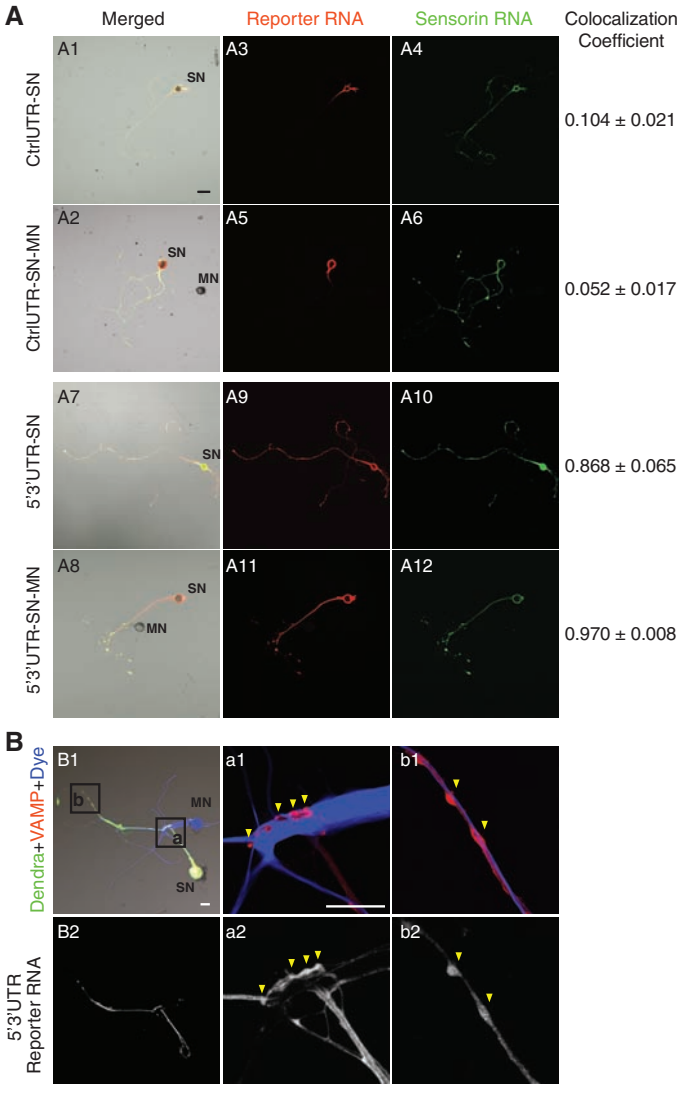

Fig. 1. Translation reporter mRNA colocalizes with endogenous sensorin mRNA at synapses. (**A**) Colocalization of 5′3′UTR sensorin reporter mRNA and endogenous sensorin mRNA. Expression vectors encoding the control (CtrlUTR) or sensorin (5′3′UTR) translational reporter were microinjected into DIV2 *Aplysia* SNs (isolated or paired with MNs). Cultures were fixed 48 hours later and processed for double-label FISH using digoxigenin (DIG)–labeled dendra2 riboprobes and biotin-labeled sensorin riboprobes. Representative confocal images of differential interference contrast (DIC)/merged (A1, 2, 7, and 8), dendra reporter mRNA in red (A3, 5, 9 and 11), and endogenous sensorin mRNA in green (A4, 6, 10, and 12). FISH signals are shown in isolated SNs (A1, 3, 4, 7, 9, and 10) and in SNs paired with MNs (A2, 5, 6, 8, 11, and 12). Scale bar, 50 μm. Colocalization was quantified as colocalization coefficient (0, no colocalization; 1, perfect colocalization). (**B**) VAMP-mCherry and reporter were coexpressed in SN; MN was labeled with Alexa647. Synapses are detected as VAMP-mCherry–positive varicosities contacting the MN. (B1) Low-magnification images of reporter protein (green), VAMP-mCherry (red), and MN (blue) with boxes of higher magnification images in a1 and b1. Cells were fixed after imaging and processed for reporter mRNA FISH in B2, a2, and b2. Scale bar, 50 μm.

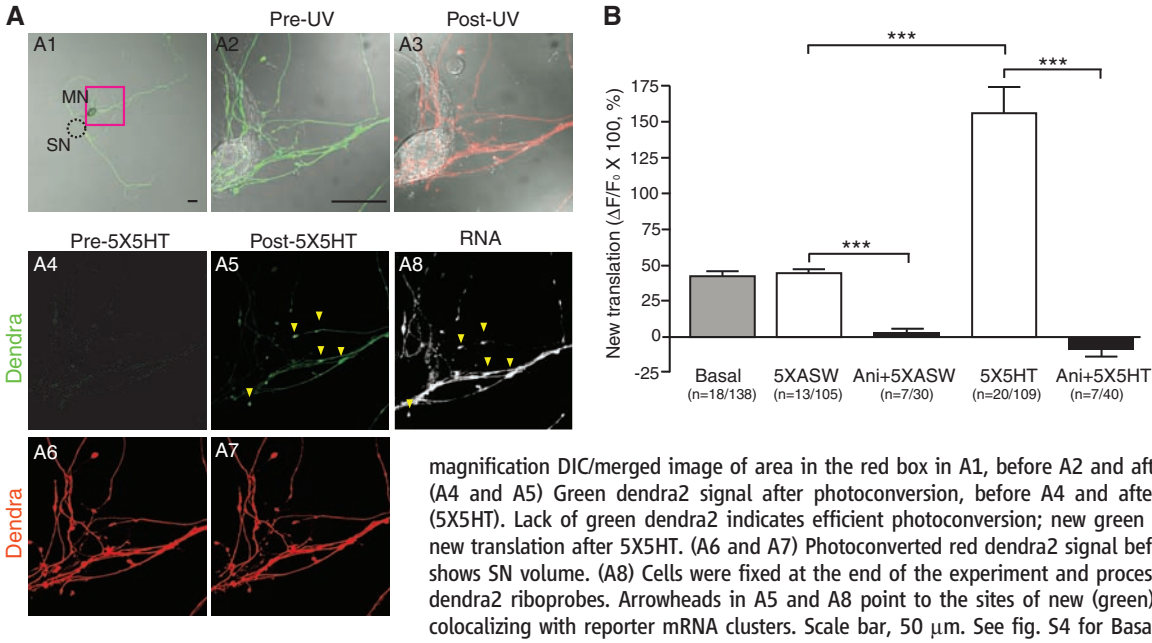

Fig. 2. Bath application of 5X5HT stimulates translation of reporter mRNA at synapses. Sensorin translational reporter was expressed in *Aplysia* SNs cocultured with MNs, the SN soma was removed, and dendra2 was UV photoconverted from green to red throughout the neuronal arbor. (**A**) (A1) Low-magnification image of dendra-reporter SN-MN coculture. The dashed circle outlines the removed soma. (A2 and A3) High-magnification DIC/merged image of area in the red box in A1, before A2 and after A3 UV photoconversion. (A4 and A5) Green dendra2 signal after photoconversion, before A4 and after A5 serotonin stimulation (5X5HT). Lack of green dendra2 indicates efficient photoconversion; new green dendra2 reveals significant new translation after 5X5HT. (A6 and A7) Photoconverted red dendra2 signal before A6 and after A7 5X5HT shows SN volume. (A8) Cells were fixed at the end of the experiment and processed for FISH with antisense dendra2 riboprobes. Arrowheads in A5 and A8 point to the sites of new (green) dendra2 protein synthesis colocalizing with reporter mRNA clusters. Scale bar, 50 μm. See fig. S4 for Basal, 5XASW, Ani+5X5HT, and Ani+5XASW results. (**B**) Quantification of new translation as ΔF/F, ***$P < 0.001$, ANOVA and Bonferroni multiple comparison test.

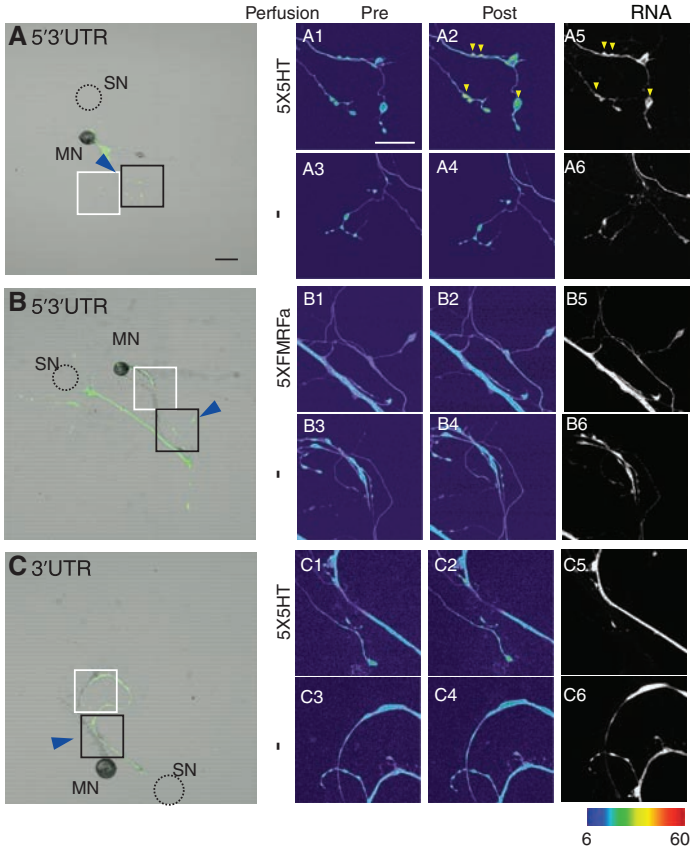

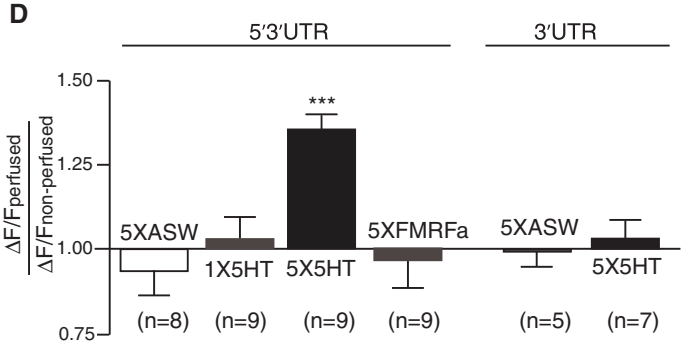

Fig. 3. Synapse-, stimulus- and transcript-specific translation. Sensorin translational reporter was expressed in SNs paired with MNs, SN soma was removed, and dendra2 was UV-photoconverted from green to red. Stimuli were locally applied to subsets of SN-MN synapses using perfusion electrodes (see fig. S3). (**A** to **C**) Low-magnification image of dendra2-reporter–expressing coculture. Dashed circle indicates removed SN soma; blue arrowheads indicate direction of perfusion; black squares denote regions imaged before and after local perfusion; white squares denote imaged nonperfused regions. (A to C, panels 1 to 4) Pseudocolored images of green dendra2 signal after photoconversion and before (pre) and after (post) local perfusion. (A to C, panels 5 and 6) Reporter mRNA FISH images. Arrowheads in A2 and A5 point to new translation colocalizing with reporter mRNA. (A) 5′3′UTR reporter, local perfusion of 5X5HT. (B) 5′3′UTR reporter, local perfusion of 5XFMRFamide. (C) 3′UTR, local perfusion of 5X5HT. See figs. S6 to S9 for images of pre-UV green and post-UV red photoconverted dendra2 signal, 5XASW controls, and 1X5HT stimulation. Scale bar, 50 μm. (**D**) Quantification of translational stimulation as ratio of ΔF/F at perfused compared with nonperfused sites reveals that translation occurs only with 5X5HT. ***$P < 0.0001$, Wilcoxon-Mann Whitney test (also see fig. S10 for group data).

Translational regulation requires a synapse. We next investigated the role of synaptic connectivity in translational regulation by 5HT. Specifically, we asked whether local perfusion of 5X5HT stimulated translation of the reporter in isolated SNs (which do not form chemical synapses) or in SNs paired with a nontarget MN, with which it does not form chemical synapses. Local perfusion of 5X5HT did not increase translation of the reporter in isolated SNs (ratio of perfused to nonperfused = 1.0 ± 0.1), despite abundant reporter mRNA (Fig. 4 and fig. S11). Notably, basal translation of the reporter in isolated SN was not significantly different from basal translation in SNs paired with MNs (figs. S12 and S13). To further test the requirement for chemical synapses, we cultured SNs with a nontarget MN, L11, with which SNs fasciculate but do not make chemical synapses (*27*, *28*). Local perfusion of 5X5HT did not increase reporter translation (ratio of perfused to nonperfused sites = 1.0 ± 0.1) (Fig. 4). Reporter mRNA was localized at perfused sites (Fig. 4 and fig. S13), and basal translation of the reporter did not differ from that in SNs paired with

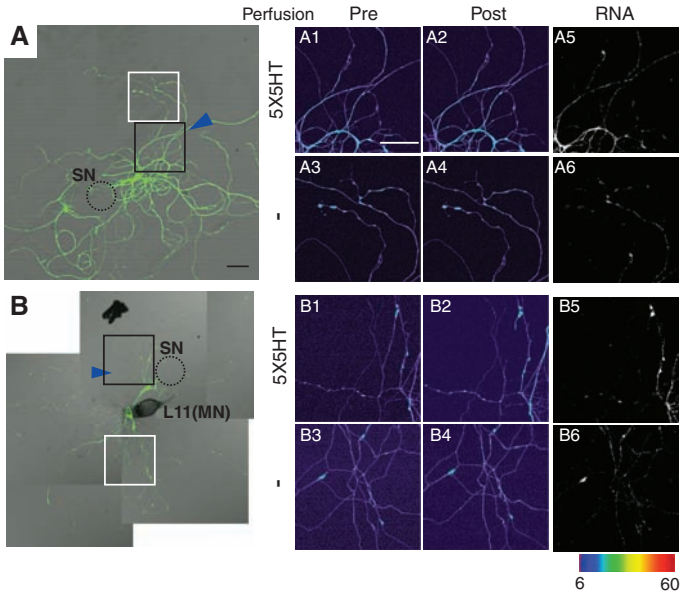

Fig. 4. Local stimulation with 5X5HT does not stimulate translation of sensorin reporter in isolated SNs or in SNs paired with nontarget MNs. Sensorin translational reporter was expressed in (A) isolated *Aplysia* SNs, or (B) SNs cocultured with nontarget L11 MNs. Local perfusion of 5X5HT was as described in Fig. 3. (**A** and **B**) Low-magnification image of dendra2-reporter expressing SNs. Dashed circle indicates removed soma; blue arrowheads indicate direction of perfusion; black squares denote regions imaged before and after local perfusion; white squares denote imaged nonperfused regions. (A and B, panels 1 to 4) Pseudocolored images of green dendra2 signal after photoconversion and before (pre) and after (post) local perfusion. (A and B, panels 5 and 6) Reporter mRNA FISH. See fig. S9 for images of red photoconverted dendra2 signal. Scale bar, 50 μm. (**C**) Quantification of translation as ratio of ΔF/F at perfused compared with nonperfused sites reveals no increase in translation with either 5X5HT or 5XASW (Wilcoxon-Mann-Whitney test; also see group data and RNA intensity quantification in fig. S13).

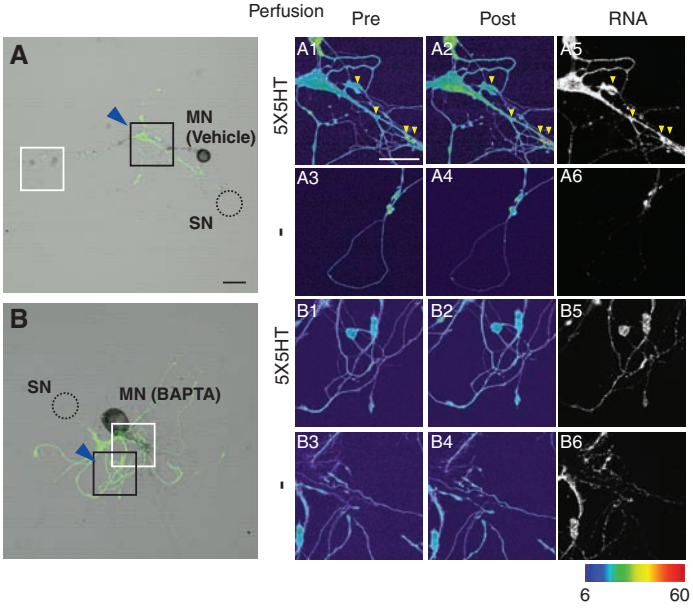

Fig. 5. Calcium signaling in motor neuron is required for 5HT-induced translation of reporter in sensory neuron. Sensorin translational reporter was expressed in *Aplysia* SNs cocultured with target LFS MNs. The SN soma was removed, either vehicle (A) or BAPTA (50 mM) (B) was microinjected into the MN, dendra2 was photoconverted, and 5X5HT was locally perfused. (**A** and **B**) Low-magnification image of dendra2-reporter expressing coculture. Dashed circle indicates removed soma; blue arrowheads indicate direction of perfusion; black squares denote regions imaged before and after local perfusion; white squares denote imaged nonperfused regions. (A and B, panels 1 to 4) Pseudocolored images of green dendra2 signal after photoconversion and before (pre) and after (post) local perfusion. (A and B, panels 5 and 6) Reporter mRNA FISH images. See fig. S13 for images of pre-UV and photoconverted dendra2 signal. Scale bar, 50 μm. (**C**) Quantification of translation as ratio of ΔF/F at perfused compared with nonperfused sites reveals that BAPTA injection into the MN blocks 5HT-induced translation in the SN (***$P < 0.0005$, *t* test).

target MNs (figs. S12 and S13). Thus, 5HT stimulates sensorin reporter translation only in the context of a chemical synapse.

Translational regulation requires postsynaptic calcium. To begin to explore the nature of the trans-synaptic signal provided by the MN, we asked whether it involved calcium signaling in the postsynaptic compartment. To do so, we microinjected the membrane-impermeable calcium chelator 1,2-Bis(2-aminophenoxy)ethane-N,N,N′,N′-tetraacetic acid tetrakis (BAPTA) (50 mM) into the MN and, 1 to 2 hours later, monitored reporter translation induced by 5X5HT in the SN. BAPTA injection blocks LTF of SN-MN synapses as well as increases in sensorin immunoreactivity in the SN, without affecting basal synaptic transmission (*37*). Calcium imaging (with Fluo-4) confirmed that BAPTA injection blocked depolarization-induced increases in intracellular calcium in the MN; FISH analysis revealed that it did not alter endogenous sensorin or reporter mRNA localization (fig. S14). BAPTA injection, however, completely blocked 5HT-induced translation of the reporter in the SN (ratio of ΔF/F at perfused versus nonperfused sites = 1.0 ± 0.0) (Fig. 5 and fig. S15). Vehicle injection into the MN did not inhibit translation in the SN (ratio of ΔF/F at perfused versus nonperfused sites = 1.2 ± 0.0) (Fig. 5 and fig. S16). Thus, a calcium-dependent trans-synaptic signal is required for translational regulation of the reporter in the presynaptic neuron by 5HT.

Our results provide direct evidence that local translation occurs at synapses in response to stimuli that induce transcription-dependent, learning-related synaptic plasticity. Spatially restricted translation and release of sensorin may function to spatially restrict the growth and/or stabilization of new synaptic growth and to thereby promote LTF precisely at the stimulated sites (*5*, *27*, *31*). Our results provide a number of additional insights into the regulation of local translation in neurons. First, translational regulation of the reporter is stimulus-specific, occurring during 5HT-induced LTF but not during FMRFamide-induced LTD. Second, 5HT does not regulate translation of all localized transcripts (because translation of the 3′UTR reporter is not stimulated), indicating that translational regulation is transcript-specific. Finally, stimulus-induced translation of the reporter requires calcium signaling in the postsynaptic MN, suggesting that a trans-synaptic retrograde signal is required for the regulation of local translation during neuronal plasticity.

References and Notes

1. C. M. Alberini, *J. Exp. Biol.* **202**, 2887 (1999).
2. E. R. Kandel, *Science* **294**, 1030 (2001).
3. P. L. Greer, M. E. Greenberg, *Neuron* **59**, 846 (2008).

4. P. V. Nguyen, T. Abel, E. R. Kandel, *Science* **265**, 1104 (1994).
5. K. C. Martin *et al*., *Cell* **91**, 927 (1997).
6. U. Frey, R. G. Morris, *Nature* **385**, 533 (1997).
7. A. Casadio *et al*., *Cell* **99**, 221 (1999).
8. K. C. Martin, *Curr. Opin. Neurobiol.* **14**, 305 (2004).
9. M. A. Sutton, E. M. Schuman, *Cell* **127**, 49 (2006).
10. A. Govindarajan, R. J. Kelleher, S. Tonegawa, *Nat. Rev. Neurosci.* **7**, 575 (2006).
11. O. Steward, W. B. Levy, *J. Neurosci.* **2**, 284 (1982).
12. L. E. Ostroff, J. C. Fiala, B. Allwardt, K. M. Harris, *Neuron* **35**, 535 (2002).
13. S. J. Tang *et al*., *Proc. Natl. Acad. Sci. U.S.A.* **99**, 467 (2002).
14. J. Eberwine, B. Belt, J. E. Kacharmina, K. Miyashiro, *Neurochem. Res.* **27**, 1065 (2002).
15. R. Moccia *et al*., *J. Neurosci.* **23**, 9409 (2003).
16. J. Zhong, T. Zhang, L. M. Bloch, *BMC Neurosci.* **7**, 17 (2006).
17. M. M. Poon, S. H. Choi, C. A. Jamieson, D. H. Geschwind, K. C. Martin, *J. Neurosci.* **26**, 13390 (2006).
18. T. Suzuki, Q. B. Tian, J. Kuromitsu, T. Kawai, S. Endo, *Neurosci. Res.* **57**, 61 (2007).
19. H. Kang, E. M. Schuman, *Science* **273**, 1402 (1996).
20. K. M. Huber, J. C. Roder, M. F. Bear, *J. Neurophysiol.* **86**, 321 (2001).
21. G. Aakalu, W. B. Smith, N. Nguyen, C. Jiang, E. M. Schuman, *Neuron* **30**, 489 (2001).
22. C. Job, J. Eberwine, *Nat. Rev. Neurosci.* **2**, 889 (2001).
23. W. Ju *et al*., *Nat. Neurosci.* **7**, 244 (2004).
24. K. F. Raab-Graham, P. C. Haddick, Y. N. Jan, L. Y. Jan, *Science* **314**, 144 (2006).
25. V. F. Castellucci, S. Schacher, *Prog. Brain Res.* **86**, 105 (1990).
26. S. L. Mackey *et al*., *Proc. Natl. Acad. Sci. U.S.A.* **84**, 8730 (1987).
27. V. Lyles, Y. Zhao, K. C. Martin, *Neuron* **49**, 349 (2006).
28. D. L. Glanzman, E. R. Kandel, S. Schacher, *Neuron* **3**, 441 (1989).
29. J. F. Brunet, E. Shapiro, S. A. Foster, E. R. Kandel, Y. Iino, *Science* **252**, 856 (1991).
30. J. Y. Hu, Y. Chen, S. Schacher, *J. Neurosci.* **27**, 11712 (2007).
31. J. Y. Hu, F. Wu, S. Schacher, *J. Neurosci.* **26**, 1026 (2006).
32. N. G. Gurskaya *et al*., *Nat. Biotechnol.* **24**, 461 (2006).
33. Materials and methods are available as supporting material on *Science* Online.
34. K. Liu, J. Y. Hu, D. Wang, S. Schacher, *J. Neurobiol.* **56**, 275 (2003).
35. Z. Guan *et al*., *Cell* **111**, 483 (2002).
36. L. Santarelli, P. Montarolo, S. Schacher, *J. Neurobiol.* **31**, 297 (1996).
37. D. Cai, S. Chen, D. L. Glanzman, *Curr. Biol.* **18**, 920 (2008).
38. We thank S. Braslow and K. Cadenas for assistance with image analysis; R. Grambo for assistance with figures; D. Black, C. Heusner, E. Meer, and L. Zipursky for critical reading of the manuscript; and G. Weinmaster and Martin laboratory members for helpful discussions. This work was supported by NIH grant NS045324, a W. M. Keck Foundation Young Scholar Award and Eleanor Leslie Term Chair from the UCLA Brain Research Institute (to K.C.M.), Canadian Institute of Health Research grant MT-15121 (to W.S.S.), and a fellowship from the Nakajima Foundation (to S.K.M.).

Supporting Online Material

www.sciencemag.org/cgi/content/full/1173205/DC1
Materials and Methods
Figs. S1 to S17
References

9 March 2009; accepted 5 May 2009
Published online 14 May 2009;
10.1126/science.1173205
Include this information when citing this paper.

REPORTS

Solar-Like Oscillations in a Massive Star

Kévin Belkacem,[1,2]* Réza Samadi,[1] Marie-Jo Goupil,[1] Laure Lefèvre,[1] Fréderic Baudin,[3] Sébastien Deheuvels,[1] Marc-Antoine Dupret,[1,2] Thierry Appourchaux,[3] Richard Scuflaire,[2] Michel Auvergne,[1] Claude Catala,[1] Eric Michel,[1] Andrea Miglio,[2] Josefina Montalban,[2] Anne Thoul,[2] Suzanne Talon,[4] Annie Baglin,[1] Arlette Noels[2]

Seismology of stars provides insight into the physical mechanisms taking place in their interior, with modes of oscillation probing different layers. Low-amplitude acoustic oscillations excited by turbulent convection were detected four decades ago in the Sun and more recently in low-mass main-sequence stars. Using data gathered by the Convection Rotation and Planetary Transits mission, we report here on the detection of solar-like oscillations in a massive star, V1449 Aql, which is a known large-amplitude (β Cephei) pulsator.

Stars burn hydrogen into helium through nuclear fusion during most of their life. Once the central hydrogen gets exhausted, the helium core starts contracting, and hydrogen-shell burning takes over as the main energy source. The subsequent evolution depends mostly on a star's mass at birth but also on the physical mechanisms occurring during the hydrogen-burning phase. For instance, transport of chemical elements determines the helium core size, which is crucial for the evolution of stars. Transport processes such as turbulence and those induced by rotation are not fully understood and are still poorly modeled, but stellar seismology can provide important constraints provided that the modes that probe the relevant regions are excited, detected, and identified. This will be the case for stars oscillating over a large range of oscillation modes probing different layers of the star.

Here, we report on the detection of solar-like oscillations (high-frequency acoustic modes that are damped but excited by turbulent convection and probe superficial convective regions) in a 10–solar mass star, V1449 Aql, already known to be a β Cephei (it oscillates on unstable low-frequency modes of high amplitude, also referred to as opacity-driven modes, which probe the deepest regions of stars) (*1*).

The largest-amplitude mode in the Fourier spectrum of V1449 Aql has been detected from the ground (*1*, *2*) at a frequency of 63.5 μHz. Those pulsations are excited by a thermal instability known as the κ-mechanism (*3*), which in the present case is related to the existence of an iron-opacity bump located in the upper layers of massive stars. The

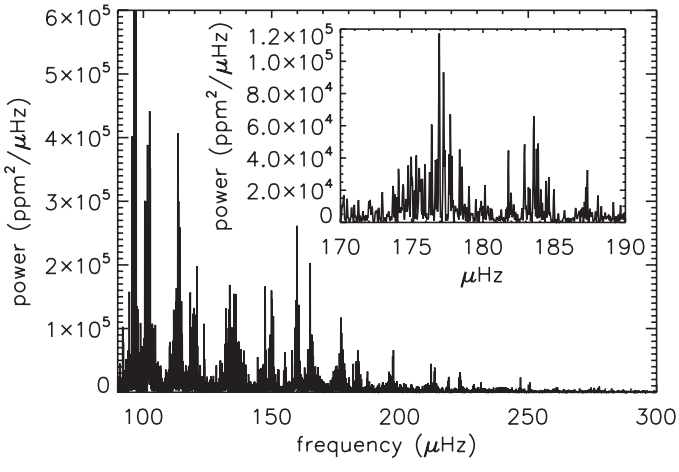

Fig. 1. Fourier spectrum of prewhitened light curve obtained from the quasi-uninterrupted 150 days of observations, with a duty cycle of 90%, of the star V1449 Aql by CoRoT, showing structures that are reproduced over the 100- to 250-μHz interval. (**Inset**) Enlarged part of the spectrum showing a typical solar-like structure. Below 100 μHz, we enter the bulk regime of unstable modes (fig. S1), and the possible existence of many such modes in this frequency domain then makes the deciphering of unstable versus stable modes quite delicate. Hence, to remain conservative we restrict the discussion to frequencies above 100 μHz.

[1]Laboratoire d'Études Spatiales et d'Instrumentation en Astrophysique, CNRS (UMR 8109), Observatoire de Paris, Place J. Janssen, F- 92195 Meudon, France; associated with Université Pierre et Marie Curie and Université Denis Diderot. [2]Institut d'Astrophysique et de Géophysique de l'Université de Liège, Allée du 6 Août 17–B 4000 Liège, Belgium. [3]Institut d'Astrophysique Spatiale, Université Paris-Sud 11 and CNRS (UMR 8617), Batiment 121, F-91405 Orsay, France. [4]Réseau Québécois de Calcul de Haute Performance, Université de Montréal, Casier Postal 6128, Succursale Centre-ville, Montréal, Québec H3C 3J8, Canada.

*To whom correspondence should be addressed. E-mail: kevin.belkacem@ulg.ac.be

iron-opacity bump in such a massive star induces the existence of a convective zone in the upper layers (*4*), which could be responsible for the excitation of the detected modes.

Our results are based on the quasi-uninterrupted (meaning, a duty cycle of 90%) light curve obtained over 150 days with the Convection Rotation and Planetary Transits (CoRoT) (*5*–*7*) Centre National d'Etudes Spatiales (CNES) space mission (Fig. 1). The dominant opacity-driven mode is located at 63.5 μHz with an amplitude of 3.9×10^4 parts per million (ppm). We looked for stochastically excited modes with frequencies above 100 μHz; below this limit, the existence of several opacity-driven modes makes the analysis more difficult. No signal is found above 250 μHz. In the frequency range 100 to 250 μHz, there are broad structures with a width of several μHz, with low amplitudes of hundreds of parts per million and well above the noise level, which is around 1 ppm.

These structures are not the result of instrumental effects [supporting online material (SOM) text]. To verify that they are not related to the existence of the opacity-driven modes, we carried out prewhitening (SOM text), which suppresses the influence of the dominant peaks and their harmonics in the relevant frequency domain as well as related aliases because of the observational interruptions. We validated our prewhitening method through numerical simulations (SOM text).

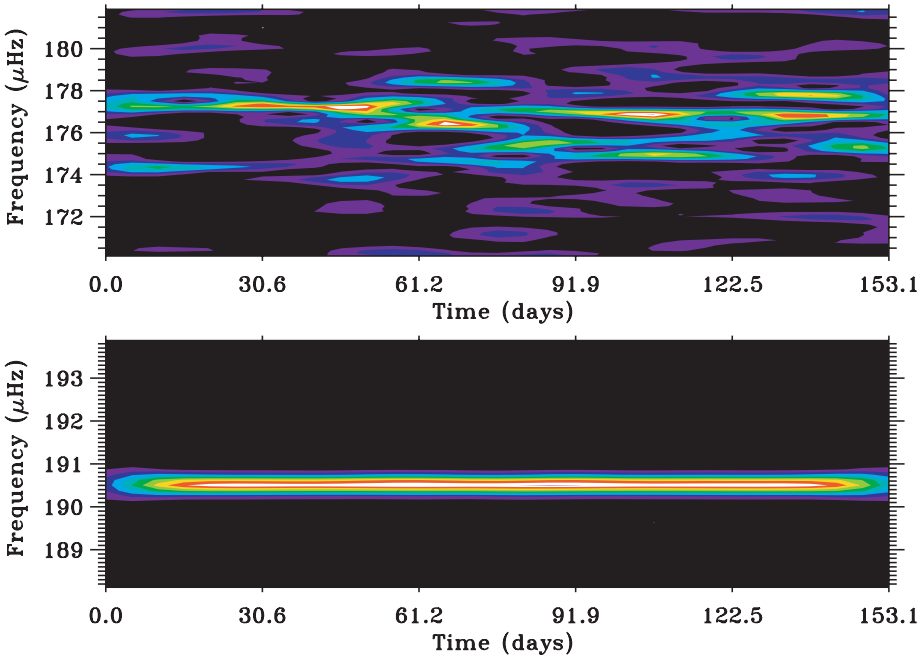

Fig. 2. Time-frequency diagram, using a Morlet wavelet with a 20-day width (*8*). (**Top**) Solar-like mode in the prewhitened light curve shown in the inset of Fig. 1, which exhibits a time-dependent behavior and a spreading over several μHz. (**Bottom**) For comparison, the second harmonic of the dominant peak, associated with the opacity-driven mode in the unprewhitened light curve.

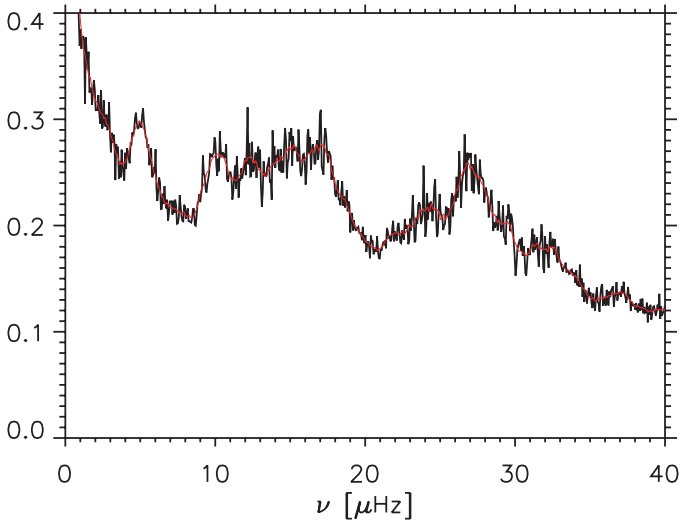

Fig. 3. Autocorrelation of the power-density spectrum associated with V1449 Aql. The red curve corresponds to the autocorrelation smoothed with a boxcar average width of 0.60 μHz. The autocorrelation has been computed between 130 and 300 μHz. The domain below 130 μHz is not considered to avoid the low-order modes, which in general depart from the regular spacing expected with the high-order p modes.

The modes associated with the broad structures have a finite lifetime, in contrast with opacity-driven modes, which are coherent oscillations and therefore appear as sinus cardinal functions in the Fourier spectrum. The amplitudes of these oscillations vary stochastically in time, again in contrast with the stationary property of the dominant opacity-driven mode and its harmonics. Their power is intermittent in time and dispersed in terms of frequency (Fig. 2). Such behavior, typical of solar-like modes (*8*), confirms the stochastic nature of the structures. In contrast, the temporal behavior of the second harmonic of the fundamental opacity-driven mode, which lies in the same frequency interval, is centered on a single frequency (Fig. 2, bottom). The widths of the detected high-frequency modes show that they are damped, which is a signature of modes excited by turbulent convection.

We looked for regularly spaced patterns in the Fourier spectrum, which are a characteristic signature of those modes. An autocorrelation of the Fourier spectrum shows periodicities centered around 5, 14, and 27 μHz (Fig. 3), indicating the existence of periodicities in the power spectrum.

Theoretical calculations show that these properties, interpreted as damped acoustic modes excited by turbulent convection, are compatible with solar-like oscillations of a massive main sequence star. We carried out numerical simulations using a 10–solar mass stellar model that is appropriate for V1449 Aql in that it corresponds to the observational constraints obtained from ground-based observations (*9*). A comparison between the theoretical and observational autocorrelations shows that the observed frequency spectrum is compatible with the presence of modes of angular degrees $l = 0$, 1, and 2, characterized by a large frequency separation around 27 μHz, with 1-μHz widths and a rotational splitting of 2.5 μHz related to a rotation with an axis inclined by 90° with respect to the line of sight (SOM text).

Mode amplitudes obtained from theoretical computations of the line width (*10*) and the energy supplied in the mode by turbulent convection (*11*) reach several tens of parts per million, which is well above the CoRoT detection threshold and in agreement with observations. Our calculations show that excitation by the turbulent convective motions associated with the iron-opacity bump in the upper layers of the star is efficient. This driving is operative when the convective time scale of energy-bearing eddies is close to the modal period, which explains why modes in the frequency range of 100 to 250 μHz are observed.

In summary, we showed that the broad structures at high frequencies detected in the CoRoT Fourier spectrum of the star V1449 Aql are not the result of instrumental effects, are independent of the opacity-driven modes, and present regularly spaced patterns that are characteristic of high-frequency acoustic modes. These structures have the theoretically expected properties of solar-like oscillations: modes excited by turbulent convection.

References and Notes

1. C. Waelkens *et al.*, *Astron. Astrophys.* **330**, 215 (1998).
2. K. Uytterhoeven *et al.*, *J. Phys. Conf. Ser.* **118**, 012077 (2008).
3. W. A. Dziembowski, A. A. Pamiatnykh, *Mon. Not. R. Astron. Soc.* **262**, 204 (1993).
4. M. Cantiello *et al.*, *Astron. Astrophys.* **499**, 279 (2009).
5. The CoRoT space mission, launched on 27 December 2006, has been developed and is operated by CNES, with the contribution of Austria, Belgium, Brazil, the European Space Agency (ESA) (Research and Scientific Support Department and Science Programme), Germany, and Spain.
6. M. Auvergne *et al.*, *Astron. Astrophys.*, http://arXiv.org/abs/0901.2206.
7. E. Michel *et al.*, *Science* **322**, 558 (2008).
8. F. Baudin, A. Gabriel, D. Gibert, *Astron. Astrophys.* **285L**, 29 (1994).
9. T. Morel, C. Aerts, *CoAst* **150**, 201 (2007).
10. M. A. Dupret, *Astron. Astrophys.* **366**, 166 (2001).
11. K. Belkacem *et al.*, *Astron. Astrophys.* **478**, 163 (2008).

12. K.B. acknowledges financial support from Liège University through the Subside Fédéral pour la Recherche. Part of this research was funded by the Belgian Prodex-ESA. L.L. has been partly supported by CNES. A.T. is Chercheur Qualifié at the Fonds National de la Recherche Scientifique (FNRS) and A.M. is Chargé de recherches FNRS.

Supporting Online Material

www.sciencemag.org/cgi/content/full/324/5934/1540/DC1
SOM Text
Figs. S1 to S5
References

5 February 2009; accepted 13 May 2009
10.1126/science.1171913

Colloidal Quantum-Dot Photodetectors Exploiting Multiexciton Generation

Vlad Sukhovatkin, Sean Hinds, Lukasz Brzozowski, Edward H. Sargent*

Multiexciton generation (MEG) has been indirectly observed in colloidal quantum dots, both in solution and the solid state, but has not yet been shown to enhance photocurrent in an optoelectronic device. Here, we report a class of solution-processed photoconductive detectors, sensitive in the ultraviolet, visible, and the infrared, in which the internal gain is dramatically enhanced for photon energies E_{photon} greater than 2.7 times the quantum-confined bandgap $E_{bandgap}$. Three thin-film devices with different quantum-confined bandgaps (set by the size of their constituent lead sulfide nanoparticles) show enhancement determined by the bandgap-normalized photon energy, $E_{photon}/E_{bandgap}$, which is a clear signature of MEG. The findings point to a valuable role for MEG in enhancing the photocurrent in a solid-state optoelectronic device. We compare the conditions on carrier excitation, recombination, and transport for photoconductive versus photovoltaic devices to benefit from MEG.

Multiexciton generation (MEG) refers to the creation of two or more electron-hole pairs per absorbed photon in a semiconductor (*1*). Colloidal quantum-dot materials in which MEG has been reported experimentally include PbS and PbSe (*2*), PbTe (*3*), CdSe (*4*), and Si (*5*). In bulk semiconductors, carrier multiplication has been observed repeatedly over the past five decades, both in elemental semiconductors such as germanium (*6*) and silicon (*7*) and also in lead chalcogenides (*8*), including the infrared-bandgap bulk semiconductor PbS (*9*). In the past year, experiments that carefully account for processes such as photoionization of nanoparticles during spectroscopic studies have evidenced the production of more than one exciton per photon (*10*) in colloidal quantum dots, with yields ranging from 1.1 to 2.4 excitons per photon (*10*) when the photon energy exceeds the MEG threshold near ~$E_{photon}/E_{bandgap} > 2.7$ (*11*), where E_{photon} is the photon energy and $E_{bandgap}$ is the quantum-confined bandgap.

MEG has been reported, based on all-optical spectroscopic data, not only in solution but also in thin solid films; however, in spite of numerous attempts with materials systems and photon energies reported to manifest MEG, neither the external quantum efficiency (EQE) nor the internal quantum efficiency (IQE) of the photocurrent in a device has been shown to exceed 100% (*12*–*20*). In particular, one careful and systematic study (*21*) recently explored whether a key signature of MEG—an IQE of greater than unity—was observable in the photocurrent of a low-bandgap PbSe colloidal quantum-dot photovoltaic device. Once reflection and absorption were carefully taken into account, IQEs approaching, but not exceeding, 100% were reported.

Recent reports (*22*) suggest that in some of the earlier spectroscopic studies, the apparent quantum yield of MEG was enhanced by photoionization in the presence of multiple excitons. The sequence of steps is depicted in Fig. 1. The generation of two excitons within one quantum dot (Fig. 1B) produces efficient Auger recombination; one exciton recombines, and one carrier associated with the other exciton is excited high within its band (Fig. 1C). Photoionization, in this instance known as Auger-assisted ionization (AAI), may occur when this excited charge carrier becomes trapped at or near the quantum dot's surface, resulting in a nanoparticle that possesses a long-lived net charge (Fig. 1D). The energetic Auger electron has a higher probability of being captured to a trap than does an already-thermalized electron (*23*) because it can more easily surmount the energetic barrier (such as a thin oxide on the nanoparticle surface), restricting access to a surface trap state.

Subsequent photogeneration of even a single exciton then results in the presence of a trion (an exciton plus a charge) that recombines rapidly, masquerading as MEG in recombination dynamics–based studies. Thus, MEG's time-resolved spectroscopic signatures are enhanced by photoionization. It should be emphasized that, at the low intensities of interest in MEG investigations, photoionization alone cannot masquerade as MEG and serves only to amplify the apparent quantum yield if MEG is already present.

Unfortunately, MEG combined with photoionization provides no advantages over MEG alone in the harvest of photovoltaic energy. Indeed, because trions resulting from photoionization accelerate recombination, they render even more challenging the extraction of MEG photocurrent from a photovoltaic device. To observe the benefits of MEG in the current extracted from a photovoltaic device, charge separation must occur before

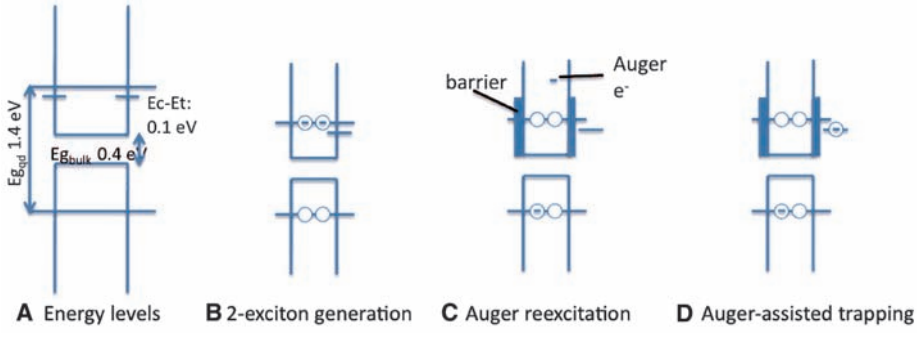

Fig. 1. MEG accompanied by photoionization. (**A**) Bands and trap levels for the quantum dots that were used. E_c is the quantum-confined conduction band edge, E_t is the trap energy, E_{gqd} is the quantum-confined bandgap, and E_{gbulk} is the constituent semiconductor's bulk bandgap. (**B**) Generation of a pair of excitons via photon absorption followed by carrier multiplication. (**C**) Auger-induced excitation of an electron to a higher-lying level concomitant with recombination of the other exciton. (**D**) Efficient trapping of the excited electron.

Department of Electrical and Computer Engineering, University of Toronto, Toronto, ON M5S 3G4, Canada.

*To whom correspondence should be addressed. E-mail: ted.sargent@utoronto.ca

Auger-accelerated multiexciton recombination. In PbS, for example, the biexciton lifetime is 50 ps and the triexciton lifetime is 30 ps (*24*). For a PbS photovoltaic device (*12*) with a typical built-in voltage of 0.35 V over a 100-nm-thick depletion region and for an electron and hole mobility of 1×10^{-3} cm^2/Vs measured in colloidal quantum-dot photovoltaic devices (*13*), the time for carriers to separate over ~5 nm (the interdot lengthscale) is on the order of 100 ps. Given the rapid rate of Auger recombination and the difficulty in dissociating excitons into distinct quantum dots, it is not surprising that the combination of materials parameters leading to greater-than-unity EQE or IQE in a photovoltaic device has yet to be conclusively observed.

We sought to identify a class of devices of applied interest in which telltale MEG signatures could be observed in the devices' photocurrents and in which photoionization would further improve, rather than detract from, performance. In photoconductive detectors (*25*), electron-hole pair generation is followed by the trapping of one type of carrier (such as electrons) and flow of the other (such as holes). If the flowing carrier can be recirculated (withdrawn from one contact and reinjected from the other) multiple times during the lifetime of the trapped carrier, then photoconductive gain results: Many charge carriers may be collected for every exciton generated.

In sum, photoconductors benefit from the capture of charge carriers to sensitizing centers, or traps, on the nanoparticle surface. We reasoned that they could therefore enjoy considerably enhanced electrical photocurrents when MEG and photoionization worked in concert. Thus, for $E_{photon} > \sim 2.7\ E_{bandgap}$, we expected that photoionization-enhanced MEG could considerably aid the trapping of charge carriers to sensitizing centers, leading to an improved signal-to-noise ratio that would be valuable in the sensitive detection of light. Because we worked with PbS nanoparticles that have quantum-confined bandgaps in the 750- to 1000-nm range, MEG enhancements were possible in the ultraviolet (UV).

Figure 1A depicts the bands of a typical set of PbS colloidal quantum dots that were used (*26*). PbS has a bulk bandgap of 0.4 eV; the effective bandgap rises to 1.4 eV through quantum confinement in the 2-nm-diameter dots investigated here. A shallow trap, resulting from $PbSO_3$ formed by surface oxidation of PbS (*27*), lies just below the first confined electron state. The use of devices (*28*) with a single trap-state lifetime facilitated the interpretation of the results presented.

The responsivity spectra are shown in Fig. 2B. By combining these data with careful measurements of the absorbance spectrum of the same film (Fig. 2A), we were able to determine the internal photoconductive gain of the device, which is plotted in Fig. 2C (*26*). Error analysis is presented in the figure caption.

Figure 2C reveals that the internal photoconductive gain is, as a function of wavelength, constant (spectrally flat) until 340 nm, a wavelength corresponding to a photon energy that is equal to 2.7 times the bandgap energy. At higher photon

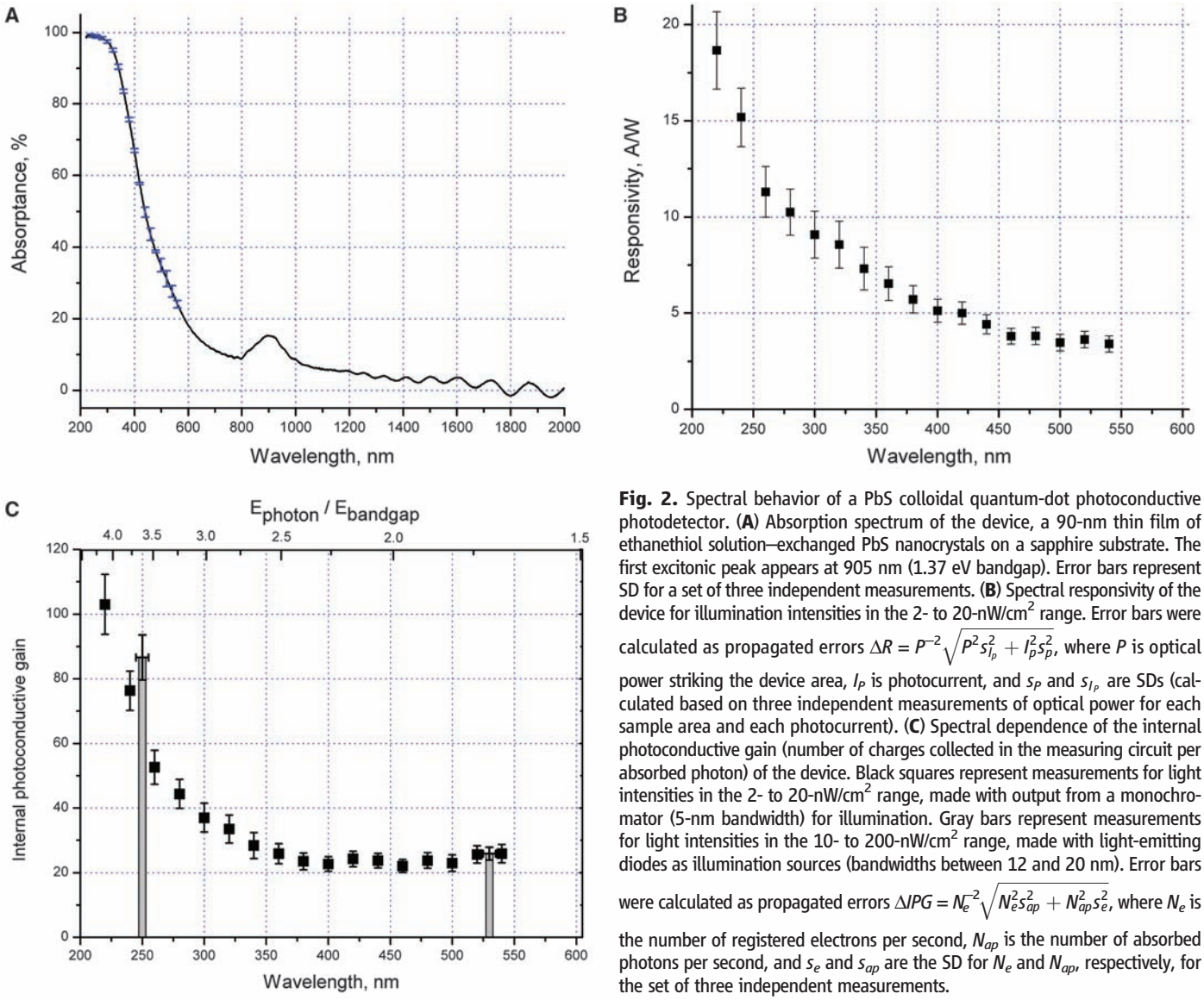

Fig. 2. Spectral behavior of a PbS colloidal quantum-dot photoconductive photodetector. (**A**) Absorption spectrum of the device, a 90-nm thin film of ethanethiol solution–exchanged PbS nanocrystals on a sapphire substrate. The first excitonic peak appears at 905 nm (1.37 eV bandgap). Error bars represent SD for a set of three independent measurements. (**B**) Spectral responsivity of the device for illumination intensities in the 2- to 20-nW/cm^2 range. Error bars were calculated as propagated errors $\Delta R = P^{-2}\sqrt{P^2 s_{I_p}^2 + I_p^2 s_P^2}$, where P is optical power striking the device area, I_P is photocurrent, and s_P and s_{I_p} are SDs (calculated based on three independent measurements of optical power for each sample area and each photocurrent). (**C**) Spectral dependence of the internal photoconductive gain (number of charges collected in the measuring circuit per absorbed photon) of the device. Black squares represent measurements for light intensities in the 2- to 20-nW/cm^2 range, made with output from a monochromator (5-nm bandwidth) for illumination. Gray bars represent measurements for light intensities in the 10- to 200-nW/cm^2 range, made with light-emitting diodes as illumination sources (bandwidths between 12 and 20 nm). Error bars were calculated as propagated errors $\Delta IPG = N_e^{-2}\sqrt{N_e^2 s_{ap}^2 + N_{ap}^2 s_e^2}$, where N_e is the number of registered electrons per second, N_{ap} is the number of absorbed photons per second, and s_e and s_{ap} are the SD for N_e and N_{ap}, respectively, for the set of three independent measurements.

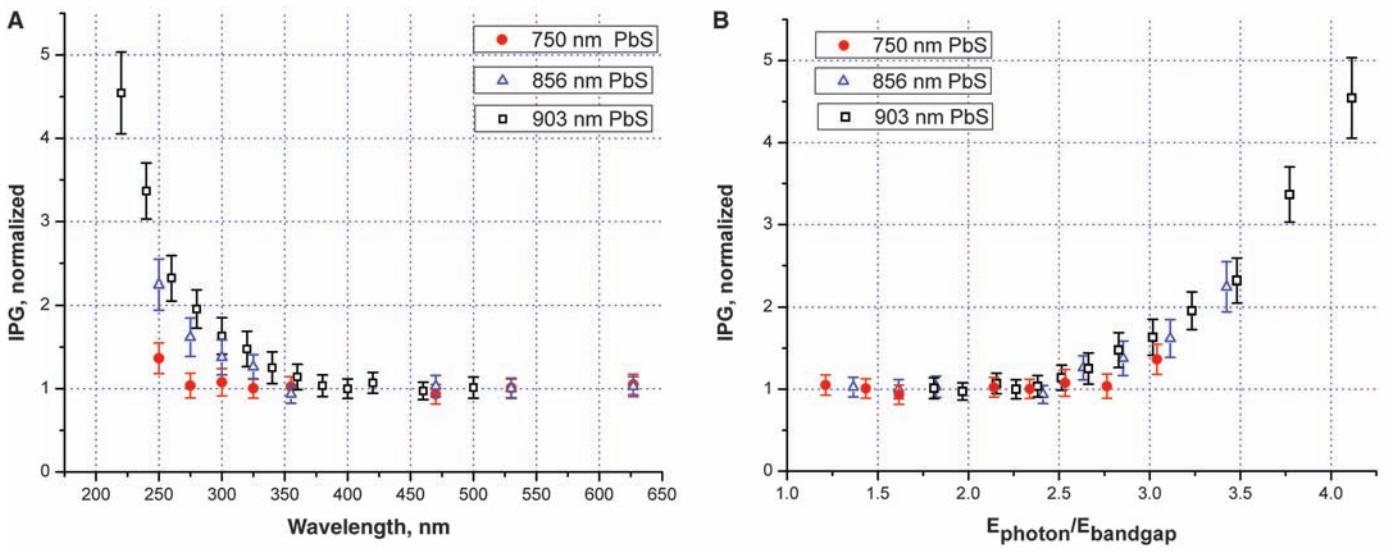

Fig. 3. Internal photoconductive gain spectra of three devices having different quantum-confined bandgaps. The left spectra (**A**) are plotted in absolute wavelength, whereas the right spectra (**B**) are plotted in (unitless) $E_{photon}/E_{bandgap}$. It is evident that $E_{photon}/E_{bandgap}$, and not absolute E_{photon}, is the quantity that drives the internal photoconductive gain spectral behavior. This finding is incompatible with direct ionization and compatible with MEG. Error bars were calculated as in Fig. 2.

energies, the internal gain rises sharply into the UV spectral range. The internal gain reaches a value of 100 ± 10 at 220-nm wavelength (~4.1 times the bandgap energy) as compared with its value of 25 ± 3 in the spectrally flat region below 2.7 times the bandgap energy.

Motivated by the fact that these results were consistent with, and even suggestive of, a role for MEG, we sought an experiment that could reveal MEG's unambiguous spectral signature: a universal quantum-yield curve dependent only on $E_{photon}/E_{bandgap}$. We built three devices using differently sized colloidal quantum dots having correspondingly different bandgaps (*26*). The devices' internal gain spectra, obtained exactly as in Fig. 2, are reported in Fig. 3.

We now discuss additional sets of controls that address potential artifactual explanations of these findings. One hypothesis is that trap states could be nonuniformly distributed throughout the film and perhaps clustered closer to the air-film interface; shorter-wavelength light would then be substantially absorbed in these denser and deeper trap regions. However, we compared internal-gain spectra for devices illuminated from the top versus the bottom and found no dependence in the curves of Figs. 2 and 3 on the side of optical incidence (fig. S3). A second hypothesis is that, in the case of short-wavelength illumination, excited carriers could be captured directly to traps during the subpicosecond time frame before relaxation to the quantum-confined band edge without need of MEG and AAI. This direct-ionization picture is incompatible with the observed universal normalized $E_{photon}/E_{bandgap}$ spectral dependence in Fig. 3; instead, it predicts that trapping efficiency should depend on E_{photon}, the barrier to electron escape, and the set of trap states available. To vary the trap states, we aged a series of devices in air to alter their trap-state densities and depths. We confirmed that the trap distribution had changed, observing an increase in dark current and the emergence of additional longer–time scale temporal components in the photoresponse that was consistent with the introduction of new and deeper traps. Despite these major changes in trap-state populations, we found that the spectral gain–dependence of Figs. 2 and 3 was preserved. Taken together, these observations suggest that carrier multiplication occurs more rapidly than either intersubband relaxation or the capture of excited carriers to traps.

We conclude with a brief discussion of the relevance to short-wavelength imaging of the devices we report here. A light sensor suited for imaging must simultaneously provide high responsivity combined with rapid temporal response (<1/15 s). Reports of UV-sensing elements based on solution-processed materials have, however, provided either promising sensitivity (61 A/W) but hundreds-of-seconds temporal response (*29*) or else fast response but few-milliamperes-per-Watt UV responsivity (*30*). The devices we report here are UV photodetectors with high responsivities of 18 A/W that at the same time offer an imaging-compatible 20-ms response time. The devices provide a 1000-fold improvement in gain-bandwidth product in solution-processed UV photodetection relative to previous reports. Compared with digital-imaging chips based on silicon photodiodes limited to at most one photoelectron per photon (thereby necessitating use of an extremely low-noise readout scheme), the devices we report here offer large gains that facilitate high-sensitivity low-light imaging.

References and Notes

1. A. J. Nozik, *Chem. Phys. Lett.* **457**, 3 (2008).
2. R. J. Ellingson *et al.*, *Nano Lett.* **5**, 865 (2005).
3. J. E. Murphy *et al.*, *J. Am. Chem. Soc.* **128**, 3241 (2006).
4. R. D. Schaller, M. Sykora, S. Jeong, V. I. Klimov, *J. Phys. Chem. B* **110**, 25332 (2006).
5. M. C. Beard *et al.*, *Nano Lett.* **7**, 2506 (2007).
6. J. Tauc, *J. Phys. Chem. Solids* **8**, 219 (1959).
7. S. Kolodinski, J. H. Werner, T. Wittchen, H. J. Queisser, *Appl. Phys. Lett.* **63**, 2405 (1993).
8. N. S. Baryshev, M. P. Shchetinin, S. P. Chashchin, Y. S. Kharionovskii, I. S. Aver'yanov, *Sov. Phys. Semicond.* **8**, 192 (1974).
9. A. Smith, D. Dutton, *J. Opt. Soc. Am.* **48**, 1007 (1958).
10. M. C. Beard *et al.*, *Nano Lett.* **9**, 836 (2009).
11. A. J. Nozik, *Chem. Phys. Lett.* **457**, 3 (2008).
12. K. W. Johnston *et al.*, *Appl. Phys. Lett.* **92**, 122111 (2008).
13. K. W. Johnston *et al.*, *Appl. Phys. Lett.* **92**, 151115 (2008).
14. G. I. Koleilat *et al.*, *ACS Nano* **2**, 833 (2008).
15. E. J. D. Klem, D. D. MacNeil, P. W. Cyr, L. Levina, E. H. Sargent, *Appl. Phys. Lett.* **90**, 183113 (2007).
16. M. Law *et al.*, *J. Am. Chem. Soc.* **130**, 5974 (2008).
17. J. M. Luther *et al.*, *ACS Nano* **2**, 271 (2008).
18. A. Luque, A. Martí, A. J. Nozik. *MRS Bull.* **32**, 236 (2007).
19. X. Jiang *et al.*, *J. Mater. Res.* **22**, 2204 (2007).
20. E. H. Sargent, *Nat. Photon.* **3**, 325 (2009).
21. M. Law *et al.*, *Nano Lett.* **8**, 3904 (2008).
22. J. A. Mcguire, J. Joo, J. M. Pietryga, R. D. Schaller, V. I. Klimov, *Acc. Chem. Res.* **41**, 1810 (2008).
23. V. Klimov *et al.*, *Conference on Quantum Electronics and Laser Science (QELS), Technical Digest Series* (IEEE, San Francisco, 2000).
24. E. Istrate *et al.*, *J. Phys. Chem. B* **112**, 2757 (2008).
25. G. Konstantatos *et al.*, *Nature* **442**, 180 (2006).
26. Materials and methods are available as supporting material on *Science* Online.
27. G. Konstantatos, L. Levina, A. Fischer, E. H. Sargent, *Nano Lett.* **8**, 1446 (2008).
28. S. Hinds *et al.*, *Adv. Mater.* **20**, 4398 (2008).
29. Y. Jin, J. Wang, B. Sun, J. C. Blakesley, N. C. Greenham, *Nano Lett.* **8**, 1649 (2008).
30. E. Mutlugun, I. M. Soganci, H. V. Demir, *Opt. Express* **16**, 3537 (2008).

31. This publication was based on work supported in part by an award from the King Abdullah University of Science and Technology, by the Natural Sciences and Engineering Research Council of Canada, by the Canada Research Chairs, and by the Canada Foundation for Innovation and the Ontario Innovation Trust.

Supporting Online Material

www.sciencemag.org/cgi/content/full/324/5934/1542/DC1
Materials and Methods
Figs. S1 to S3
References

19 March 2009; accepted 19 May 2009
10.1126/science.1173812

Aggregation-Induced Dissociation of $HCl(H_2O)_4$ Below 1 K: The Smallest Droplet of Acid

Anna Gutberlet,[1] Gerhard Schwaab,[1] Özgür Birer,[1]* Marco Masia,[2]† Anna Kaczmarek,[2]‡ Harald Forbert,[2] Martina Havenith,[1]§ Dominik Marx[2]

Acid dissociation and the subsequent solvation of the charged fragments at ultracold temperatures in nanoenvironments, as distinct from ambient bulk water, are relevant to atmospheric and interstellar chemistry but remain poorly understood. Here we report the experimental observation of a nanoscopic aqueous droplet of acid formed within a superfluid helium cluster at 0.37 kelvin. High-resolution mass-selective infrared laser spectroscopy reveals that successive aggregation of the acid HCl with water molecules, $HCl(H_2O)_n$, readily results in the formation of hydronium at $n = 4$. Accompanying ab initio simulations show that undissociated clusters assemble by stepwise water molecule addition in electrostatic steering arrangements up to $n = 3$. Adding a fourth water molecule to the ringlike undissociated $HCl(H_2O)_3$ then spontaneously yields the compact dissociated $H_3O^+(H_2O)_3Cl^-$ ion pair. This aggregation mechanism bypasses deep local energy minima on the $n = 4$ potential energy surface and offers a general paradigm for reactivity at ultracold temperatures.

Brønsted acid/base dissociation, leading to proton transfer and solvation (*1*, *2*) of the charged fragments in nanoenvironments (*3*–*13*), is one of the most fundamental chemical processes, at the root of myriad subsequent reactions. The process plays a central role not only in bulk aqueous chemistry but also in heterogeneous reactions in polar stratospheric clouds (*14*, *15*), the spontaneous synthesis of molecules in interstellar space at ultracold temperatures (*16*), and dissociative adsorption and ionization at surfaces (*17*–*22*). In particular, the dissociation mechanism of the strong acid HCl has been the focus of recent studies in ambient bulk water (*1*, *2*, *23*, *24*), as well as at low temperatures in confined geometries; for example, on amorphous ice surfaces, on ice nanocrystals, and in microsolvation environments most relevant to atmospheric or interstellar environments (*15*, *18*, *19*, *25*). In view of Arrhenius' activation law, however, a persistent puzzle has been the means whereby reactants at ultracold temperatures surmount energetic barriers that far exceed the available thermal energy. Traditionally it is assumed that photochemical excitations or tunneling are the major triggers enabling such reactions.

Despite impressive progress on the fundamental steps of HCl dissociation on ice (*18*, *25*), infrared (IR) spectra of microsolvated HCl remain underanalyzed. Suhm and co-workers (*26*, *27*) observed several IR bands in a $HCl/H_2O/He$ expansion and were able to assign two IR bands between 3000 and 2000 cm^{-1} to undissociated $HCl(H_2O)_n$, with $n = 1$ and 2. A prominent and unusually broad absorption band centered at ≈2570 cm^{-1} was attributed to dissociated structures of unknown cluster sizes. Multiple theoretical studies (*28*–*32*) lend support to the conjecture that four H_2O molecules might provide the smallest possible H-bonded water network, in which the most stable structure incorporating HCl is the charge-separated solvent-shared ion pair (SIP) $H_3O^+(H_2O)_3Cl^-$, as depicted in Fig. 1 (this species is sometimes termed a solvent-separated ion pair in the cluster literature). Still, experimental spectroscopic evidence is so far lacking and, in addition, the pathway to dissociation at low temperatures remains elusive.

Here we report the full dissociation of a single HCl molecule as a result of molecular aggregation with exactly four water molecules in superfluid He nanodroplets at 0.37 K. These droplets provide a gentle matrix for step-by-step aggregation of molecular clusters, via a controllable pickup process governed by Poisson's statistics, and they allow for concurrent high-resolution spectroscopy (*33*–*35*). IR and mass-spectroscopic evidence, in conjunction with theory, shows the formation of a SIP within a minimal H-bonded network in which three water molecules solvate both H_3O^+ and Cl^- as shown in Fig. 1, thus producing what we believe is the smallest droplet of dissociated acid. We find that stepwise aggregation can induce reactions in an energetically downhill fashion, preventing the system from being trapped in deep local minima out of which it would need substantial activation to escape. At the same time, sufficiently small energy barriers can be overcome by using kinetic energy gained upon lowering the potential energy during aggregation. Transcending the specific system here, such aggregation-induced reactions are expected to play a pivotal role in explaining chemical reactivity under cryogenic conditions.

Ab initio molecular dynamics simulations (*36*), as well as frequency calculations, were performed in the framework of density functional theory using the BLYP functional (*37*). In addition, Helmholtz free-energy calculations were carried out with ab initio metadynamics (*37*) in the extended Lagrangian formulation, using two collective variables (CVs) to drive the isomerization reaction of the $HCl(H_2O)_4$ system from the undissociated (UD) initial state to the most stable global minimum; that is, the dissociated SIP species. One CV is defined to be the coordination number CN_{Cl-O} of Cl with respect to all O's, and the other CV, ϕ, is the dihedral angle formed by the four O atoms and thus measures the two-dimensional (2D) versus 3D character of the aggregate. Aggregation simulations (*37*) probing the effects of electrostatic steering were carried out with both fragments dipole-aligned in their initial configuration, while keeping the nearest heavy atoms separated in equilibrating canonical simulations at 0.5 K. Subsequent release of the constraint and microcanonical ab initio molecular dynamics propagation yield the product complexes within a few picoseconds at

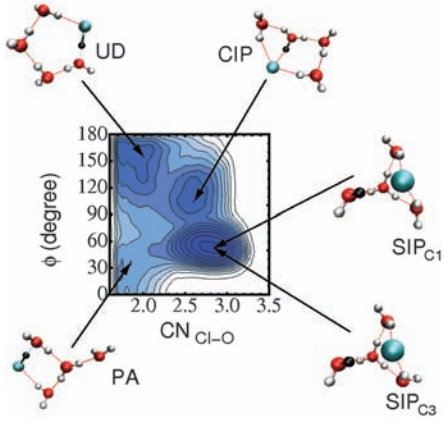

Fig. 1. Free-energy surface (*37*) of $HCl(H_2O)_4$ spanned by two collective reaction coordinates: the Cl to O coordination number CN_{Cl-O} and the dihedral angle ϕ given by the four O atoms; the contour lines are 3 kJ/mol apart. The relevant free-energy minima were found to be associated with the following fully optimized structures as marked by arrows: UD, CIP, PA, and SIP_{C1} and SIP_{C3}, with C_1 and C_3 symmetry, respectively, as determined by the orientation of the water molecule in the lower right corner. The proton derived from HCl is marked in black in all structures. The free-energy barriers are as follows: from UD to CIP, ≈930 K; from CIP to SIP, ≈650 K; and from PA to SIP, ≈100 K; the reaction coordinates used do not distinguish between the conformations (i.e., C_3 versus C_1) that characterize the SIP_{C3} and SIP_{C1} species, the latter being only ≈2.7 kJ/mol higher in potential energy.

[1]Lehrstuhl für Physikalische Chemie II, Ruhr-Universität Bochum, 44780 Bochum, Germany. [2]Lehrstuhl für Theoretische Chemie, Ruhr-Universität Bochum, 44780 Bochum, Germany.

*Present address: Department of Chemistry, Koc University, Rumelifeneri Yolu Sariyer, 34450 Istanbul, Turkey.

†Present address: Dipartimento di Chimica, Università degli Studi di Sassari, CNR-INFM SLACS and INSTM, Via Vienna 2, 07100 Sassari, Italy.

‡Present address: Faculty of Chemistry, Nicolaus Copernicus University, Gagarina 7, 87-100 Toruń, Poland.

§To whom correspondence should be addressed. E-mail: martina.havenith@rub.de

most, which is much faster than the expected He cooling rate.

Comprehensive mapping of the free-energy surface for the $n = 4$ species $HCl(H_2O)_4$ clearly demonstrates that the UD species reaches the SIP global minimum via a partially dissociated contact ion pair (CIP) as a locally stable intermediate (Fig. 1). The SIP structure $H_3O^+(H_2O)_3Cl^-$ is the most compact network wherein a hydronium core, H_3O^+, forms an Eigen complex (*1*, *2*); i.e., $H_3O^+(H_2O)_3$, by donating three H bonds to the three remaining water molecules, which in turn can nicely microsolvate Cl^- by creating an anionic solvation shell. The network structures of pure protonated water clusters $H_3O^+(H_2O)_n$ have been thoroughly characterized by IR spectroscopy (*9*–*13*) as a function of n including the bare Eigen cation $n = 3$. Frequency analyses of $HCl(H_2O)_n$ species predict a prominent IR active mode around 2708 cm^{-1} corresponding to a symmetric O-H stretching motion in the H_3O^+ core that specifically characterizes the lowest-energy SIP minimum. Both UD and CIP structures do not show any calculated signal in this spectral regime for $n = 4$. For the UD structure, the closest vibrations are the water O-H stretches (>2900 cm^{-1}) and the H-Cl stretch (<1700 cm^{-1}), whereas the nearest frequencies in the CIP structure are predicted to be more than 200 cm^{-1} and ≈150 cm^{-1} higher and lower in frequency, respectively.

We have studied microsolvation of HCl in He nanodroplets via high-resolution IR spectroscopy, using the Bochum He-nanodroplet apparatus in combination with a home-built continuous wave optical parametric oscillator with full frequency coverage in the range from 2600 to 3400 cm^{-1}, high output power (up to 2.7 W), and high resolution (0.0001 cm^{-1}). Briefly (*37*), He droplets with an average size of 8500 He were formed in a supersonic expansion of precooled (16 K) gaseous He through a 5-μm-diameter nozzle. In a partitioned second chamber, the He droplets were doped with HCl or DCl as the first dopant and H_2O as the second dopant. They were detected in a quadrupole mass spectrometer after passing through a 0.9-m spectroscopic interaction region. Absorption of an IR photon and subsequent cooling to the ground state result in the evaporation of several hundred He atoms, yielding a depletion of the mass spectrometer signal due to a reduced droplet ionization cross section. We used two different scanning modes: Frequency scans yield spectroscopic information on all complexes in the investigated frequency range, using the high-pass mode of the mass spectrometer [mass-to-charge ratio (m/z) > 8], whereas optically selective mass spectroscopy (OSMS) (*38*) returns information on a single species and its fragments. In He nanodroplets, soft ionization often allows detection of the parent as well as large fragments. Electron bombardment of a He cluster results in the ionization of a He atom, subsequent charge migration, and excitation of either a He cluster state $(He_n)^+$* or the dopant molecule.

We experimentally searched the frequency range from 2645 to 2915 cm^{-1} for IR absorption bands of HCl/water and DCl/water complexes aggregated in He droplets that might indicate dissociation. Bands of HCl monomer, HCl homodimer, and the undissociated HCl-H_2O heterodimer in He droplets have been observed and assigned previously by us (*39*). In addition to those, we found two strong absorption bands centered at 2669.854(1) and 2667.804(2) cm^{-1}, subject to an intensity ratio of about 3:1 (Fig. 2A) upon sequential pickup of HCl and H_2O. These signals disappeared when pure HCl or H_2O was added alone to the He droplets.

In order to assign the observed bands to a specific cluster, we measured the dependence of the depletion signal on the partial pressure of both dopants and used OSMS (*38*). The variation with pressure supported our assignment to a cluster aggregated from one HCl and four H_2O molecules (*37*). A comparison of mass spectra (Fig. 3) acquired at the HCl/water resonances (at 2667.8 and 2669.8 cm^{-1}) to the off-resonance mass spectrum (at 2673.8 cm^{-1}) shows a clear increase in depletion at the masses corresponding to pure hydronium and to hydronium/water clusters $H_3O^+(H_2O)_n$, with $n = 0, 1, 2, 3$ (m/z = 19, 37, 55, and 73). No increase is observed at the undissociated HCl mass (m/z = 36), the undissociated parent cluster mass [m/z = 108 for $HCl(H_2O)_4$], and larger dissociated cluster masses with $n > 3$ (m/z = 91, 109, ...). In the case of a DCl/H_2O mixture (Fig. 3), comparing an on-resonance spectrum at 2671.3 cm^{-1} to an off-resonance spectrum at 2666.4 cm^{-1} reveals an increase for masses corresponding to H_3O^+, $H_3O^+H_2O$, H_3O^+HDO, and $H_3O^+HDO(H_2O)_n$, with $n = 1, 2$ (m/z = 19, 37, 38, 56, and 74).

For a dissociated charge-separated cluster, we expect to detect the positively charged ion and its ionized fragments; negative ions such as Cl^- are deflected or neutralized after electron impact ionization and charge transfer, and thus are not detected by the mass spectrometer. The highest mass affected by the change from on- to off-resonance is attributed to the parent ion, which has $m/z = 73$ in the case of HCl/water and $m/z = 74$ for DCl/water. All observations are fully consistent with an assignment to the solvent-shared ion pair $H_3O^+(H_2O)_3Cl^-$. An undissociated cluster would, in contrast, have been expected to give rise to OSMS signals at the HCl and $HCl(H_2O)_4$ parent cluster masses, as observed for undissociated $HCl/(H_2O)_1$. No signal at the mass (m/z = 20) of deuterated hydronium, H_2DO^+, was detected, indicating that D replaces one of the H atoms in the solvent layer (in agreement with our simulations) and not one of the H atoms in the hydronium core.

The two peaks separated by ≈2 cm^{-1} may then be explained in two ways: either as an isotopic splitting due to the ^{35}Cl:^{37}Cl natural abundance ratio (close to 3:1) within one SIP structure, or as a symmetry splitting due to the presence of different SIP conformers for $n = 4$. The calculations predict a negligible Cl isotopic shift (less than 0.0002 cm^{-1}). This prediction was confirmed experimentally: Substitution of the natural isotopic mixture with isotopically pure $H^{35}Cl$ (Fig. 2B) yielded a nearly identical spectrum. Thus,

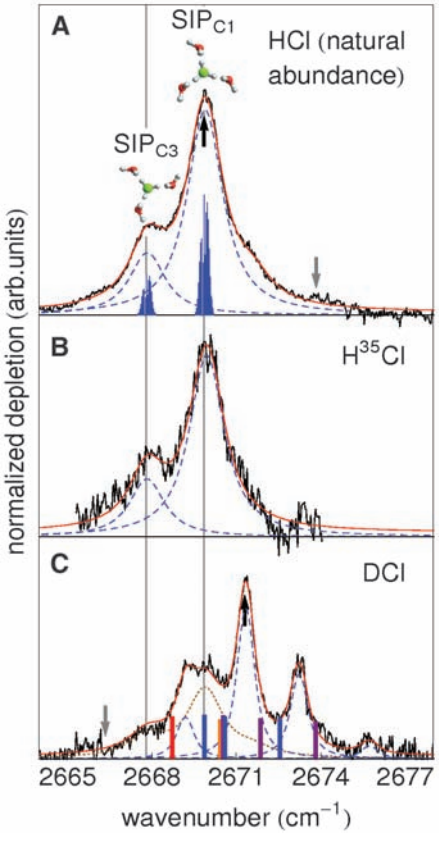

Fig. 2. IR depletion spectra (arbitrary units) of the symmetric hydronium stretch of $H_3O^+(H_2O)_3Cl^-$ in He nanodroplets. (**A**) H_2O and HCl in a natural abundance isotopic mixture. (**B**) H_2O and isotopically pure $H^{35}Cl$. (**C**) H_2O and DCl in a $^{35}Cl/^{37}Cl$ natural abundance mixture. Measured spectra are shown in black and overall fits in red; dashed blue lines show Lorentzian line profiles fitted to asymmetric top stick spectra. The H_2O/HCl spectrum in (A) shows two absorption bands, which are assigned to two different structures of $H_3O^+(H_2O_3)Cl^-$: SIP_{C3} and SIP_{C1}, as shown. Four absorption bands contribute to the $DCl(H_2O)_4$ absorption in (C). The stick spectra in (C) show the calculated frequencies (*37*) for the symmetric O-H stretching motion in the H_3O^+ core of $H_3O^+(H_2O)_2(HDO)Cl^-$, with the length of the bars being proportional to the IR intensities. The predicted frequencies of the symmetric O-H stretching mode in the H_3O^+ core of the SIP_{C3} conformer are marked, respectively, by red and orange vertical bars when D (stemming from DCl) is substituted for H in the H bond between an intact water molecule and Cl^- (HB OH), or substituted for H in the free OH group of such a water molecule (free OH); blue (HB OH) and purple (free OH) bars correspond to the same scenarios for SIP_{C1}. The brown dashed line corresponds to residual signals caused by H/D exchange in the gas feeding system.

the three water molecules in the Eigen-type SIP network are arranged in either C_3 or C_1 conformation with respect to their free OH bonds (see SIP_{C3} and SIP_{C1} in Fig. 1). The C_1 conformer is statistically sixfold degenerate, whereas there are only two SIP_{C3} structures, a relationship in agreement with the observed 3:1 intensity ratio by combinatorics. In accord with experimental results, the calculated symmetric hydronium O-H stretching frequency is slightly blue-shifted in SIP_{C1} as compared to SIP_{C3}. We therefore assign the two observed peaks to the SIP_{C1} and SIP_{C3} species. Given the 2.7 kJ/mol (≈320 K) energy gap separating the SIP_{C1} structure from the SIP_{C3} global minimum, Boltzmann weighting at 0.37 K would fully suppress the blue peak due to SIP_{C1}, thus suggesting the observation of a nonequilibrium distribution.

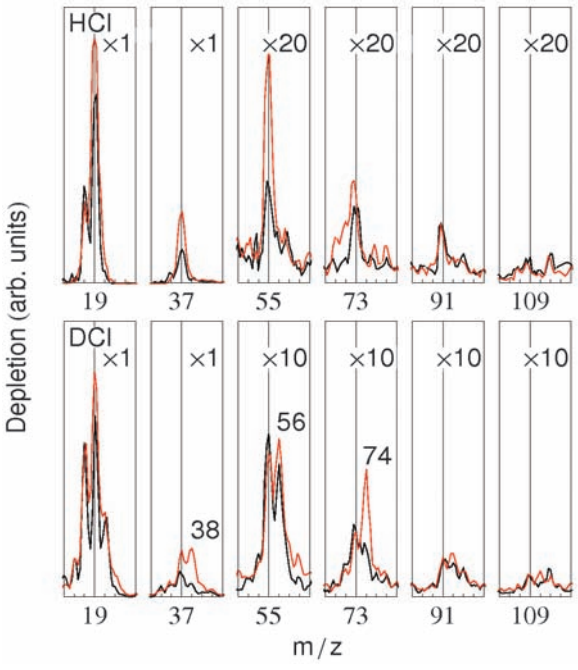

Fig. 3. The top and bottom panels show a comparison of on-resonance (red) and off-resonance (black) optically selective mass spectra for HCl and DCl water clusters, respectively. The corresponding frequencies are shown in Fig. 2 as black and gray arrows for the on- and off-resonance measurements, respectively. The masses correspond to the parents $H_3O^+(H_2O)_3$ and $H_3O^+(H_2O)_2(HDO)$ and their fragments. Tick marks represent integer *m/z* values.

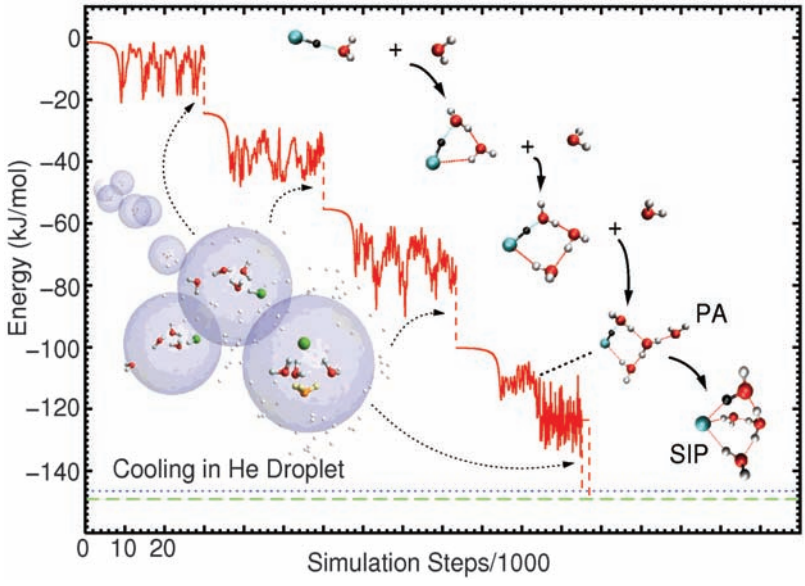

Fig. 4. Simulation of a stepwise aggregation process leading to aggregation-induced dissociation of $HCl(H_2O)_n$ from $n = 3$ to $n = 4$ according to the sequence $HCl + 4\ H_2O \rightarrow HCl(H_2O) + 3\ H_2O \rightarrow HCl(H_2O)_2 + 2\ H_2O \rightarrow HCl(H_2O)_3 + H_2O \rightarrow H_3O^+(H_2O)_3Cl^-$. The optimized structures for the $n = 4$ PA and SIP are explicitly labeled; only the global minimum (the SIP_{C3} conformation) is shown here but using a different perspective from that in Fig. 1. The proton derived from HCl is marked in black in all structures. The solid red lines show the evolution of the potential energy on the scale given by the binding energy {that is, $E[HCl(H_2O)_n] - E[HCl] - nE[H_2O]$} obtained from representative aggregation simulations (*37*) as a function of the ab initio molecular dynamics step. Vertical dashed red lines symbolize cooling of the aggregation product (obtained via full structure optimization) inside the He droplet (schematically represented at left) before the next aggregation simulation commences. Horizontal dashed green and dotted blue lines mark the binding energies of SIP_{C3} and SIP_{C1}, respectively.

Substitution of HCl by DCl leads to a substantial spectral shift and further splitting (Fig. 2C). Strong absorption peaks are now found at frequencies of 2669.152(6), 2671.300(1), and 2673.198(2) cm^{-1}; a further transition is just evident at the detection limit at 2675.70(3) cm^{-1}. The observed H/D shift is consistent with a predicted blue shift of up to at most 4 cm^{-1} for the various possible D positions in the H_2O molecules of the SIP structures. In contrast, substitution in the H_3O^+ core would result in major red shifts in the range of 70 to 120 cm^{-1}, in disagreement with the experiment (*37*). The predicted transitions (also in Fig. 2C) compare favorably to the observed spectrum.

Given this experimental evidence that the fully dissociated SIP_{C1} and SIP_{C3} complexes form in He droplets, the puzzle remains how the huge barriers of ≈930 and ≈650 K along the two-step dissociation mechanism following the UD → CIP → SIP pathway on the $n = 4$ free-energy surface (Fig. 1) can be surmounted at only 0.37 K. Such high barriers are indeed expected in view of the required fundamental rearrangement of the H-bonded network from a 2D to a 3D topology: The original UD complex is a flat five-membered ring, whereas the SIP dissociation product is compact, with three water molecules sandwiched between the hydronium core and Cl^- anion.

To account for our observations, we first note that within the He droplets, the dopants are cooled down to 0.37 K at typical rates of 10^{10} K/s (*35*). The associated cooling times are shorter than the time scales (*35*) for migration of the dopants within the droplet (≈10 μs), as well as the time scale between single pickup processes (≈0.1 ms). Thus, precooled monomers aggregate sequentially, a process that may yield nonequilibrium structures not found at higher temperatures (*40*, *41*). We then consider that the $n = 4$ free-energy surface possesses an extremely shallow minimum, corresponding to the partially aggregated (PA) species in Fig. 1: an undissociated cyclic $HCl(H_2O)_3$ structure wherein the added fourth H_2O molecule accepts a H bond from the free OH of the central H_2O in the ring. Thus, the solution to the puzzle is provided by a process of aggregation-induced dissociation. A sequence of aggregation simulations (*37*) using electrostatic steering initial conditions (Fig. 4) yields cluster growth around undissociated HCl up to the ringlike $n = 3$ structure; adding the fourth H_2O then leads to the open PA structure, which readily dissociates into either SIP_{C1} or SIP_{C3} according to combinatorial statistics without ever transiting through the much-discussed UD or CIP trap states. According to this $HCl(H_2O)_3 + H_2O \rightarrow$

PA → SIP mechanism, the acid's proton is transferred to one of the three solvent H_2O molecules, in full agreement with the OSMS HCl/DCl data. This mechanism would translate into an indirect, solvent-mediated proton transfer from HCl to H_3O^+ in bulk solvation environments (*1*, *2*).

References and Notes

1. D. Marx, *Chem. Phys. Chem.* **7**, 1848 (2006).
2. D. Marx, *Chem. Phys. Chem.* **8**, 209 (2007) [addendum to (*1*)].
3. A. Stace, *Science* **294**, 1292 (2001).
4. W. H. Robertson, M. A. Johnson, *Science* **298**, 69 (2002).
5. S. M. Hurley, T. E. Dermota, D. P. Hydutsky, A. W. Castleman Jr., *Science* **298**, 202 (2002).
6. W. H. Robertson, E. G. Diken, E. A. Price, J.-W. Shin, M. A. Johnson, *Science* **299**, 1367 (2003).
7. A. F. Voegele, K. R. Liedl, *Angew. Chem. Int. Ed.* **42**, 2114 (2003).
8. W. Domcke, A. L. Sobolewski, *Science* **302**, 1693 (2003).
9. M. Miyazaki, A. Fujii, T. Ebata, N. Mikami, *Science* **304**, 1134 (2004).
10. J. Shin *et al*., *Science* **304**, 1137 (2004).
11. T. S. Zwier, *Science* **304**, 1119 (2004).
12. J. M. Headrick *et al*., *Science* **308**, 1765 (2005).
13. J. M. Headrick *et al*., *Science* **309**, 1326 (2005) [erratum to (*12*)].
14. B. Gertner, J. Hynes, *Science* **271**, 1563 (1996).
15. T. Huthwelker, M. Ammann, T. Peter, *Chem. Rev.* **106**, 1375 (2006).
16. I. W. M. Smith, B. R. Rowe, *Acc. Chem. Res.* **33**, 261 (2000).
17. D. C. Clary, *Science* **271**, 1509 (1996).
18. J. P. Devlin, N. Uras, J. Sadlej, V. Buch, *Nature* **417**, 269 (2002).
19. R. Bianco, J. T. Hynes, *Acc. Chem. Res.* **39**, 159 (2006).
20. L. M. Pegram, M. T. Record Jr., *Proc. Natl. Acad. Sci. U.S.A.* **103**, 14278 (2006).
21. C. J. Mundy, I. F. W. Kuo, *Chem. Rev.* **106**, 1282 (2006).
22. C.-W. Lee, P.-R. Lee, H. Kang, *Angew. Chem. Int. Ed.* **45**, 5529 (2006).
23. K. Laasonen, M. Klein, *J. Am. Chem. Soc.* **116**, 11620 (1994).
24. K. Ando, J. T. Hynes, *Adv. Chem. Phys.* **110**, 381 (1999).
25. V. F. McNeill, T. Loerting, F. M. Geiger, B. L. Trout, M. J. Molina, *Proc. Natl. Acad. Sci. U.S.A.* **103**, 9422 (2006).
26. M. Weimann, M. Fárník, M. A. Suhm, *Phys. Chem. Chem. Phys.* **4**, 3933 (2002).
27. M. Fárník, M. Weimann, M. A. Suhm, *J. Chem. Phys.* **118**, 10120 (2003).
28. C. T. Lee, C. Sosa, M. Planas, J. J. Novoa, *J. Chem. Phys.* **104**, 7081 (1996).
29. D. E. Bacelo, R. C. Binning, Y. Ishikawa, *J. Phys. Chem. A* **103**, 4631 (1999).
30. A. Milet, C. Struniewicz, R. Moszynski, P. E. S. Wormer, *J. Chem. Phys.* **115**, 349 (2001).
31. S. Odde, B. J. Mhin, S. Lee, H. M. Lee, K. S. Kim, *J. Chem. Phys.* **120**, 9524 (2004).
32. M. Masia, H. Forbert, D. Marx, *J. Phys. Chem. A* **111**, 12181 (2007).
33. S. Goyal, D. L. Schutt, G. Scoles, *Phys. Rev. Lett.* **69**, 933 (1992).
34. G. Scoles, K. K. Lehmann, *Science* **287**, 2429 (2000).
35. J. P. Toennies, A. F. Vilesov, *Angew. Chem. Int. Ed.* **43**, 2622 (2004).
36. D. Marx, J. Hutter, *Ab Initio Molecular Dynamics: Basic Theory and Advanced Methods* (Cambridge University Press, Cambridge, 2009).
37. Materials and methods are detailed and references are given in the supporting material available on *Science* Online.
38. W. K. Lewis, C. M. Lindsay, R. J. Bemish, R. E. Miller, *J. Am. Chem. Soc.* **127**, 7235 (2005).
39. M. Ortlieb, O. Birer, M. Letzner, G. W. Schwaab, M. Havenith, *J. Phys. Chem. A* **111**, 12192 (2007).
40. K. Nauta, R. E. Miller, *Science* **287**, 293 (2000).
41. F. Madeja *et al*., *J. Chem. Phys.* **120**, 10554 (2004).

42. The authors are grateful to W. Sander for helpful discussions and K. Merz for support in the synthesis of isotopically pure HCl. We thank D. Habig, S. Henkel, M. Ortlieb, and T. Poerschke for help with the experiment and data evaluation. Support by the Deutsche Forschungsgemeinschaft (grants HA 2394/13 and MA 1547/8 within FOR 618 "Molecular Aggregation") and Fonds der Chemischen Industrie is gratefully acknowledged, as well as computer resources from Bovilab@RUB and Rechnerverbund-Nordrhein-Westfalen (LiDO).

Supporting Online Material

www.sciencemag.org/cgi/content/full/324/5934/1545/DC1
Materials and Methods
Figs. S1 to S3
Table S1
References

2 February 2009; accepted 12 May 2009
10.1126/science.1171753

Beryllium Dimer—Caught in the Act of Bonding

Jeremy M. Merritt,[1] Vladimir E. Bondybey,[2] Michael C. Heaven[1]*

The beryllium dimer is a deceptively simple molecule that, in spite of having only eight electrons, poses difficult challenges for ab initio quantum chemical methods. More than 100 theoretical investigations of the beryllium dimer have been published, reporting a wide range of bond lengths and dissociation energies. In contrast, there have been only a handful of experimental studies that provide data against which these models could be tested. Ultimately, the uncertain extrapolation behavior associated with the available data has prevented quantitative comparisons with theory. In our experiment, we resolve this issue by recording and analyzing spectra that sample all the bound vibrational levels of the beryllium dimer molecule's electronic ground state. After more than 70 years of research on this problem, the experimental data and theoretical models for the dimer are finally reconciled.

During the last few decades, there has been tremendous progress in the development of theoretical methods for ab initio prediction of molecular structures and properties. This progress, combined with the rapid advances in computational hardware, has reached the point where high-level theoretical models can be applied to reasonably large systems (molecules containing tens of atoms). There are, however, certain classes of problems where simple molecules can pose a considerable challenge for quantum chemistry calculations. The beryllium dimer, with just eight electrons, is a celebrated example.

[1]Department of Chemistry, Emory University, Atlanta, GA 30322, USA. [2]Technical University Munich, Garching, Germany.

*To whom correspondence should be addressed. E-mail: mheaven@emory.edu

The story of the beryllium dimer extends to the early days of molecular spectroscopy. Spectra for the simplest metal dimer, Li_2, were observed and analyzed by 1930. The first attempts to study the next simplest dimer, carried out around the same time in the laboratory of Herzberg (*1*), failed to produce Be_2 and resulted only in observations of the oxide BeO (*2*). The authors concluded (*1*, *2*) that the interaction between two ground-state Be atoms is repulsive, and the vapor of beryllium should be strictly monatomic.

Around the same time, theoretical models of molecular bonding were being developed, with the simplest molecular orbital theory predicting a bond order of zero for Be_2. An early valence bond study by Bartlett and Furry (*3*) in 1931 found Be_2 to be repulsive, and starting with the development of computers and computational techniques, dozens of theoretical studies appeared with vastly divergent results. The self-consistent field (SCF) computations of Fraga and Ransil (*4*, *5*) predicted an unstable ground state, as did the study of Bender and Davidson (*6*), who concluded that their configuration interaction (CI) results were just as repulsive as those from an SCF calculation. They noted that a minimum in the potential was possible only if the effects of electron correlation increase faster with decreasing internuclear separation than the SCF repulsion increases. Several subsequent studies concluded that the Be_2 potential has only a shallow van der Waals minimum at a large internuclear distance (4.5 to 5.1 Å), whereas another group of investigations found deeper minima at considerably shorter bond lengths of 2.3 to 2.9 Å. There were also calculations that yielded double minimum potential energy curves where the long-range minimum was attributed to van der Waals attraction. By the early 1980s, the extensive multi-reference CI (MRCI) computations of Lengsfield *et al*. (*7*) and the full CI (FCI) studies by Harrison and Handy (*8*) appeared to tilt the controversy in favor of a short bond length and a single minimum potential.

Despite the growing theoretical interest, experimental data for Be_2 has remained elusive. The fact that beryllium has high melting and boiling points, and at these temperatures the vapor is almost purely monatomic, introduces a technical challenge for experimental studies. Adding to the problem, beryllium is very easily oxidized, and the oxide particles are extremely toxic. Electronic absorption spectra for Be_2 iso-

lated in cryogenic Ne and Ar matrices were reported by Brom *et al*. (*9*), but these measurements did not provide information concerning the ground state. Gas phase spectra were finally obtained with the advent of pulsed laser ablation techniques. With this method, minute quantities of the metal could be vaporized, cooled by collisions with an inert buffer gas, and investigated spectroscopically using tunable dye lasers. Bondybey and English (*10*) reported the first gas-phase spectrum in 1984, followed by two additional studies by Bondybey (*11*, *12*). Rotationally resolved data showed that the molecule does have a short bond length (2.45 Å). Helium buffer gas cooling was used to stabilize the dimer, and the effective temperature of the measurements was near 90 K. Under these conditions, only bands involving the lowest $v'' = 0$ and 1 vibrational levels of the ground state could be observed, yielding a vibrational frequency ($\Delta G_{1/2}$) of 223.4 cm^{-1}. At a much lower resolution, vibrational levels up to $v'' = 3$ were observed in dispersed fluorescence spectra. Assuming a Morse-like potential energy curve, extrapolation of the low-resolution vibrational data indicated a well depth (D_e) of 790 ± 30 cm^{-1} (9.45 ± 0.36 kJ mol^{-1}).

The definitive demonstration that ground-state Be_2 is bound motivated another wave of theoretical studies. Calculations before 1995 were reviewed by Røeggen and Almlöf (*13*). Part of the difficulty in describing the dimer derives from the small energy separation between the 2s and 2p orbitals of beryllium atoms, which results in a multi-configurational ground state. Theory has shown that the detailed shape of the dimer potential energy curve results from a delicate balance of many attractive and repulsive forces (*13*–*17*). The main attractive force at long range is the van der Waals dispersion interaction. At shorter range, where orbital overlap becomes substantial, mixing of excited determinants becomes important, signaling the onset of orbital hybridization. The early controversy over a short or long bond length reflected the competition between these two interactions. The sensitivity of the Be_2 potential energy curve to the level of theory has made analysis of this molecule a benchmark problem for quantum mechanics and a critical test for new theoretical models and procedures. At present, more than 100 papers devoted to beryllium dimers and clusters have appeared, making the dimer one of the most extensively theoretically studied molecules. The highest-level studies suggest that the D_e value obtained in the original experimental study was too low, and the theoretical estimates have gradually increased with time. Here we mention just a sampling of those studies.

Petersson and Shirley (*18*) carried out a series of ab initio computations with extrapolation to the complete basis set limit. The dissociation energy they obtained (D_e = 827 cm^{-1}) was higher than that of Bondybey (*11*), but they proposed that the discrepancy could be resolved through reinterpretation of the experimental data. They noted that the Morse potential energy function originally used to extrapolate the experimental data does not have the correct behavior at larger internuclear distances. To impose the correct asymptotic behavior, they added a $-C_6/r^6$ term (where C_6 is a constant and r is the internuclear separation) to the potential energy function, obtaining a revised experimental estimate for the dissociation energy of D_e = 839 cm^{-1}. Gdanitz (*15*) reported a very high quality (r_{12})MRCI calculation, yielding D_e = 898 cm^{-1}. Martin (*16*) obtained a FCI result of D_e = 844 cm^{-1}, whereas the valence electron–only FCI computation of Evangelisti *et al*. (*14*) predicted a binding energy lower than the experimental value, clearly demonstrating the need for correlation of the inner-shell electrons. In a separate study, Evangelisti *et al*. (*19*) carried out an all-electron FCI calculation that involved more than a billion D_{2h} symmetry-adapted determinants. Spirko (*20*) corrected the FCI potential of Martin (*16*), which yielded almost precisely the observed $\Delta G_{1/2}$ = 223.4 cm^{-1}, for its clearly incorrect asymptotic behavior. This was done by first converting the (r_{12})MRCI curve of Gdanitz (*15*) into a reduced potential energy curve form and then adjusting the potential parameters to reproduce the experimentally observed ro-vibrational energies and the shape of the FCI potential near the minimum (*16*). A D_e value of 922.9 cm^{-1} was derived from this procedure. Patkowski *et al*. (*21*) carried out large-scale calculations for the dimer series Be_2, Mg_2, and Ca_2. Extrapolation to the complete basis set limit was examined for coupled cluster methods, and additional frozen core FCI calculations were performed for Be_2, leading to a predicted dissociation energy of D_e = 938 ± 15 cm^{-1}.

Evaluation of the current generation of theoretical calculations for Be_2 is hampered by the uncertainties of the existing experimental data, particularly the details of the extrapolation to the dissociation limit. A recent experimental study (*22*) has advanced our understanding of the excited states of Be_2, but it provided little in the way of new information for the ground state. Our objective was to obtain accurate experimental data for

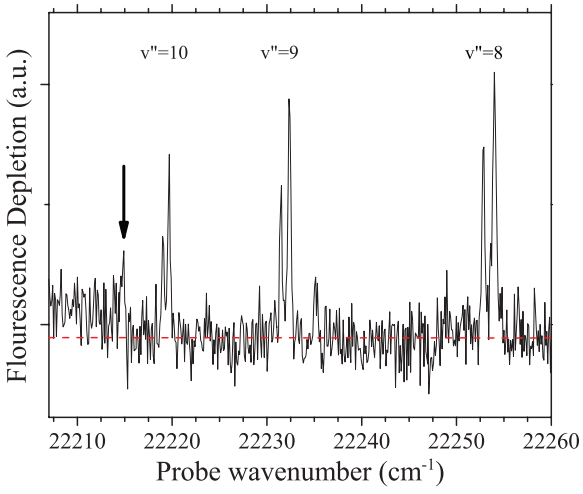

Fig. 1. Experimental SEP spectrum recorded with the pump laser exciting the R(0) line of the $A^1\Pi_u(v' = 2) \leftarrow X^1\Sigma_g^+$ ($v'' = 0$) transition of Be_2. The progression of R(0)/P(2) doublets shown are assigned to the $v'' = 8$, 9, and 10 levels. Continuous SEP signal was observed beyond $v'' = 10$, signaling the onset of dissociation (denoted by the arrow). The red dashed line indicates the baseline of the SEP spectrum. a.u., arbitrary units.

Table 1. Measured and calculated properties of $Be_2(X^1\Sigma_g^+)$. All parameters have units of inverse centimeters unless otherwise indicated. ϕ has units of inverse angstroms. Estimated experimental uncertainties (SDs) in the vibrational band origins (E_{rel}) and rotational constants (B_v) are ±0.5 cm^{-1} and ±0.005 cm^{-1}, respectively. Predicted energies and rotational constants from (*20*) are also given. Potential parameters are as follows: D_e = 929.742348; r_e = 2.453603 Å; ϕ_0 = 2.173585, ϕ_1 = 1.190734, ϕ_2 = −0.974995, ϕ_3 = −9.377098, ϕ_4 = 11.556851, and ϕ_5 = −3.401979. Dashes indicate data not determined.

v''	E_{rel} (exp.)	B_v (exp.)	E_{rel} (calc.)	B_v (calc.)	E_{rel} (*20*)	B_v (*20*)
0	0.0	0.609	0.0	0.607	0.0	0.609
1	222.6	0.562	222.7	0.567	223.3	0.562
2	397.1	0.509	397.8	0.505	396.4	0.500
3	518.1	0.424	518.2	0.425	515.9	0.422
4	594.8	0.355	595.4	0.355	592.4	0.353
5	651.5	0.306	652.4	0.309	649.1	–
6	698.8	0.272	699.4	0.273	695.6	–
7	737.7	0.237	738.2	0.237	733.5	–
8	768.2	0.196	768.8	0.200	762.9	–
9	789.9	0.153	790.7	0.157	783.1	–
10	802.6	0.102	803.4	0.102	793.7	–
D_0	807.4	–	806.5	–	–	–

all bound vibrational levels of the ground state, $Be_2(X)$. We succeeded by applying stimulated emission pumping (SEP) to record rotationally resolved spectra (*23*). The basic principles of this experiment are described here. A pulsed laser (designated as the "pump") is used to populate a single ro-vibrational level of the electronically excited $A^1\Pi_u$ state. The fluorescence resulting from the radiative relaxation of this level is detected along an axis that is perpendicular to the laser beam. A second laser ("dump"), which is counter-propagated along the axis of the pump beam, is used to drive population down from the excited level via stimulated emission. When the dump laser is tuned to a resonant transition, the resonance is detected as a drop in the intensity of the pump laser–induced fluorescence. The $A^1\Pi_u$ state was chosen for these measurements, as it has a shorter equilibrium internuclear distance than the $X^1\Sigma_g^+$ ground state. Because of this difference, transitions from the low vibrational levels of $A^1\Pi_u$ to the vibrationally excited levels of the ground state are favored. A second advantage of using the $A^1\Pi_u$ state is that it has a relatively long fluorescence decay lifetime (~200 ns) that facilitates detection of the SEP effect (*24*).

Be_2 was formed in the gas phase by pulsed laser vaporization and cooled by pulsed supersonic expansion of the helium carrier gas into vacuum (*22*). Laser excitation spectra for Be_2 were consistent with a rotational temperature of 1.5 to 2.0 K. Each vibronic band exhibited just three strong rotational lines, corresponding to R(0), R(1), and Q(1) (see fig. S1). The selection rules for the A-to-X transition are such that excitation of a Q-branch line allows only Q lines to appear in the SEP spectrum. Alternatively, pump laser excitation of a P or R line yields progressions of P/R doublets. For example, Fig. 1 shows a SEP spectrum recorded with the use of pump laser excitation of the 2-to-0 band R(0) line. The expected progression of R(0)/P(2) doublets is evident. To determine the ground-state rotational constants, we recorded SEP spectra using R(0), R(1), and Q(1) excitations of the 2-to-0 and 3-to-0 vibronic transitions. We observed all ground-state vibrational levels in the range $v'' = 0$ to 10, with the latter clearly identified as the last bound vibrational state. We observed the $Be(^1S) + Be(^1S)$ dissociation limit in the spectrum as a continuum SEP signal with a sharp onset. The vibrational energies, dissociation energy (D_0), and rotational constants derived from the spectra are listed in Table 1.

The fact that the potential energy curve for $Be_2(X)$ has an unusual shape was immediately apparent from the measured vibrational energies. Figure 2 shows the vibrational interval ($E_{v''+1} - E_{v''}$) as a function of the vibrational quantum number (Birge-Sponer plot). This plot would be linear for a Morse potential or gently curved for a Morse-like potential that transitions to a van der Waals potential at long range. However, the present results show a pronounced deviation from the slope of the initial line above $v'' = 3$. This behavior accounts for the original underestimation of the dissociation energy from a Birge-Sponer extrapolation of the $v'' = 0$ to 3 data, and it supports the reanalysis proposed by Petersson and Shirley (*18*).

The full potential energy curve was recovered from the data presented in Table 1 by least-squares fitting of an analytical potential energy function to reproduce the observed vibrational and rotational energies. The eigenvalues of the potential were obtained by numerical integration of the Schrödinger equation. Le Roy's DPotFit computer code (*25*, *26*) was used for these calculations. A satisfactory fit, within two SDs for the experimental uncertainties, was obtained with the use of the expanded Morse oscillator (EMO) function to represent the potential. This function was defined by the expressions

$$V(r) = D_e[1 - e^{-\phi(r)\cdot(r-r_e)}]^2 \qquad (1)$$

$$\phi(r) = \sum_{i=0}^{5} \phi_i \left(\frac{r^p - r_{ref}^p}{r^p - r_{ref}^p}\right)^i \qquad (2)$$

with $p = 4$ and $r_{ref} = 2.45$ Å. Fitted parameters for this potential (D_e, ϕ_i, and r_e) are given in Table 1, along with the calculated vibrational energies and rotational constants. The dissociation energy obtained from this analysis was $D_e = 929.7 \pm 2.0$ cm^{-1}.

The fitted potential function and associated vibrational levels are shown in Fig. 3. The $v'' = 10$ level has its outer turning point near 7.9 Å, so the long-range segment of the potential is well defined by the range of vibrational states characterized. For comparison, Fig. 3 also depicts a Morse potential energy function that was constructed to reproduce the measured dissociation energy and the harmonic vibrational constant. The marked difference between the attractive limbs of these curves highlights the anomalous long-range behavior of $Be_2(X)$. Petersson and Shirley (*18*) made the reasonable assumption that the long-range potential could be represented by $-C_6/r^6$, but the present results show that this is a poor approximation for $r < 8$ Å. Attempts to fit the data with the use of a hybrid Morse Oscillator/Lennard-Jones potential (*25*) yielded results that were inferior to those obtained with the EMO function. Petersson and Shirley's (*18*) extrapolated value for D_e was an improvement over the Birge-Sponer analysis, but, because of the deviation from the $-C_6/r^6$ form, still too low. Comparison

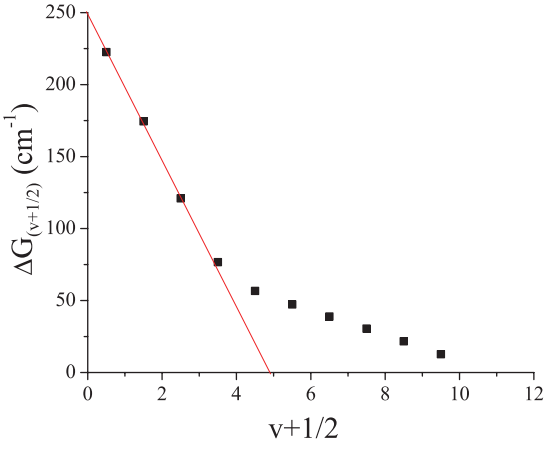

Fig. 2. Birge-Sponer plot of the vibrational intervals $E_{v''+1} - E_{v''}$. The red straight line is a linear fit to the first four points, representing the expected behavior for a Morse potential energy curve. The deviation from Morse-like behavior resulted in the underestimation of the dissociation energy in previous experimental studies.

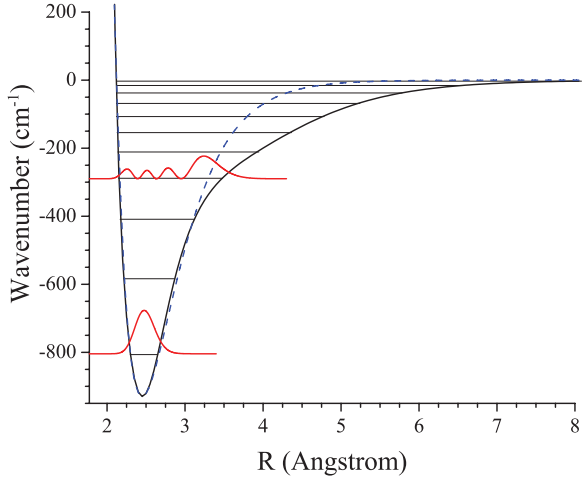

Fig. 3. Ground electronic state potential energy curve of the beryllium dimer derived by fitting to the SEP data. The vibrational wave functions for $v'' = 0$ and 3 are also shown for reference. The dashed curve is a Morse potential constructed to reproduce the experimental dissociation energy and harmonic vibrational constant.

with the (r_{12})MRCI curve of Gdanitz (*15*) indicates that this ab initio method, combined with a large basis set, recovered the true shape of the potential. The differences between Spirko's (*20*) potential energy curve and the fitted potential are too small to be seen as the scale of the plot shown in Fig. 3. To illustrate the differences, the vibrational energies and rotational constants generated from Spirko's (*20*) potential can be compared with the present results in Table 1. The close agreement shows that the reduced potential curve model is capable of achieving near spectroscopic accuracy.

The shape of the Be_2 potential energy curve is quite different from that of a standard Morse-like potential, and it is equally far away from a simple physical potential such as the Lennard-Jones model. Be_2 is unique in this respect as the related dimers of closed-shell metal atoms Mg_2 (*27*), Ca_2 (*28*), Zn_2 (*21*, *29*), and Hg_2 (*29*) exhibit typical Morse–van der Waals type potentials.

The measurements reported here resolve the question of the dissociation energy for $Be_2(X)$ and define the potential energy curve for internuclear distances less than 8.5 Å. The unusual shape of the attractive limb of the ground-state potential reflects the evolution of the configurational mixing that occurs as the atoms approach. Hence, Be_2 shows atoms passing through stages of orbital hybridization as they form an incipient chemical bond. Theoretical analyses indicate that chemical and physical interactions are finely balanced at the equilibrium distance (*14*, *17*, *30*). As a result, the Be_2 molecule has a weak bond, but a bond length that is more characteristic of a conventional covalent interaction. Our experimentally determined potential energy curve establishes a benchmark for tests of high-level theoretical methods for treatment of configurational mixing and electron correlation. Given that such interactions are also especially important in the treatment of excited electronic states and transition state regions of the potential energy surface, one can hope to assess the reliability of quantum chemical methods in situations where they are applied to regions of the potential energy surface that are not easily probed by experiment.

References and Notes

1. G. Herzberg, *Z. Phys.* **57**, 601 (1929).
2. L. Herzberg, *Z. Phys.* **84**, 571 (1933).
3. J. H. Bartlett Jr., W. H. Furry, *Phys. Rev.* **38**, 1615 (1931).
4. S. Fraga, B. J. Ransil, *J. Chem. Phys.* **35**, 669 (1961).
5. S. Fraga, B. J. Ransil, *J. Chem. Phys.* **36**, 1127 (1962).
6. C. F. Bender, E. R. Davidson, *J. Chem. Phys.* **47**, 4972 (1967).
7. B. H. Lengsfield III, A. D. McLean, M. Yoshimine, B. Liu, *J. Chem. Phys.* **79**, 1891 (1983).
8. R. J. Harrison, N. C. Handy, *Chem. Phys. Lett.* **98**, 97 (1983).
9. J. M. Brom Jr., W. D. Hewett Jr., W. Weltner Jr., *J. Chem. Phys.* **62**, 3122 (1975).
10. V. E. Bondybey, J. H. English, *J. Chem. Phys.* **80**, 568 (1984).
11. V. E. Bondybey, *Chem. Phys. Lett.* **109**, 436 (1984).
12. V. E. Bondybey, *Science* **227**, 125 (1985).
13. I. Røeggen, J. Almlöf, *Int. J. Quantum Chem.* **60**, 453 (1996).
14. S. Evangelisti, G. L. Bendazzoli, L. Gagliardi, *Chem. Phys.* **185**, 47 (1994).
15. R. J. Gdanitz, *Chem. Phys. Lett.* **312**, 578 (1999).
16. J. M. L. Martin, *Chem. Phys. Lett.* **303**, 399 (1999).
17. A. Krapp, F. M. Bickelhaupt, G. Frenking, *Chem. Eur. J.* **12**, 9196 (2006).
18. G. A. Petersson, W. A. Shirley, *Chem. Phys. Lett.* **160**, 494 (1989).
19. S. Evangelisti, G. L. Bendazzoli, R. Ansaloni, F. Duri, E. Rossi, *Chem. Phys. Lett.* **252**, 437 (1996).
20. V. Spirko, *J. Mol. Spectrosc.* **235**, 268 (2006).
21. K. Patkowski, R. Podeszwa, K. Szalewicz, *J. Phys. Chem. A* **111**, 12822 (2007).
22. J. M. Merritt, A. L. Kaledin, V. E. Bondybey, M. C. Heaven, *Phys. Chem. Chem. Phys.* **10**, 4006 (2008).
23. Materials and methods are available as supporting material on *Science* Online.
24. F. J. Northrup, T. J. Sears, *Annu. Rev. Phys. Chem.* **43**, 127 (1992).
25. R. J. LeRoy, J. Y. Seto, Y. Huang, *DPotFit; A Computer Program for Fitting Diatomic Molecular Spectral Data to Potential Energy Functions* (University of Waterloo Chemical Physics Research Report CP-662R, Waterloo, Ontario, Canada, 2006).
26. R. J. Le Roy *et al.*, *J. Chem. Phys.* **123**, 204304 (2005).
27. E. Czuchaj, M. Krosnicki, H. Stoll, *Theor. Chem. Acc.* **107**, 27 (2001).
28. E. Czuchaj, M. Krosnicki, H. Stoll, *Theor. Chem. Acc.* **110**, 28 (2003).
29. L. Bucinsky, S. Biskupic, M. Ilcin, V. Lukes, V. Laurinc, *J. Comput. Chem.* **30**, 65 (2008).
30. I. Røeggen, K. Morokuma, K. Yamashita, *Chem. Phys. Lett.* **140**, 349 (1987).

31. We are grateful for the financial support of this work provided by NSF (grant CHE-0518094). V.E.B. thanks Die Deutsche Forschungsgemeinschaft for partial support of his visit to Emory University.

Supporting Online Material

www.sciencemag.org/cgi/content/full/1174326/DC1
Materials and Methods
Fig. S1
References

31 March 2009; accepted 6 May 2009
Published online 21 May 2009;
10.1126/science.1174326
Include this information when citing this paper.

Atmospheric Carbon Dioxide Concentration Across the Mid-Pleistocene Transition

Bärbel Hönisch,[1] N. Gary Hemming,[1,2] David Archer,[3] Mark Siddall,[4] Jerry F. McManus[1]

The dominant period of Pleistocene glacial cycles changed during the mid-Pleistocene from 40,000 years to 100,000 years, for as yet unknown reasons. Here we present a 2.1-million-year record of sea surface partial pressure of CO_2 (Pco_2), based on boron isotopes in planktic foraminifer shells, which suggests that the atmospheric partial pressure of CO_2 (pco_2) was relatively stable before the mid-Pleistocene climate transition. Glacial Pco_2 was ~31 microatmospheres higher before the transition (more than 1 million years ago), but interglacial Pco_2 was similar to that of late Pleistocene interglacial cycles (<450,000 years ago). These estimates are consistent with a close linkage between atmospheric CO_2 concentration and global climate, but the lack of a gradual decrease in interglacial Pco_2 does not support the suggestion that a long-term drawdown of atmospheric CO_2 was the main cause of the climate transition.

The mid-Pleistocene transition (MPT) is the period around 1250 to 700 thousand years ago (ka), when global climate variability changed from the dominant 40-thousand-year (ky) orbital period of the Pliocene/early Pleistocene to the 100-ky ice-age cycles of the past 700 ky (*1*–*3*). Orbital variation does exert some forcing on the 100-ky time scale, but it is relatively weak and seems a feeble explanation for the 100-ky ice ages. The change in periodicity was accompanied by a gradual increase in value and amplitude of the oxygen isotopic composition of benthic foraminifer shells, suggesting that total ice volume increased and/or deep-water temperatures probably decreased over the MPT (*3*, *4*). It has been suggested the MPT was caused by global cooling, possibly due to a long-term decrease in atmospheric CO_2 concentrations (*5*), but the evidence is inconclusive. Sea surface temperature (SST) estimates from eastern basin upwelling areas (*6*–*9*) are consistent with substantial cooling, but estimates from the western Pacific warm pool (WPWP) indicate relatively stable temperatures across the transition (*10*, *11*). Because the WPWP is an area particularly sensitive to changes in radiative forcing, that temperature stability has been used to argue that a secular decrease in atmospheric partial pressure of CO_2 (pco_2) did not occur (*10*). In contrast, another study observed higher glacial SSTs before the MPT and ascribed these to changes in greenhouse forcing (*11*). Thus, there currently is no direct evidence substantiating any long-tem trend in pco_2.

The most accurate archive for atmospheric pco_2 comes from ancient air trapped in polar ice. Ice core records reveal that pco_2 varied between

[1]Department of Earth and Environmental Sciences, Lamont-Doherty Earth Observatory of Columbia University, NY 10964–8000, USA. [2]School of Earth and Environmental Sciences, Queens College, New York, NY, 11367–1597, USA. [3]Department of Geophysical Sciences, University of Chicago, Chicago, IL 60637, USA. [4]Department of Earth Sciences, University of Bristol, Bristol, UK.

180 and 300 parts per million by volume (ppmv) during the last four glacial cycles (*12*) and between 172 and 260 ppmv for the period from 800 to 450 ka (*13*, *14*). Contrary to the suggestion that pCO_2 decreased toward the late Pleistocene, the earlier pCO_2 amplitude and average were lower than in the more recent past. However, existing ice core records are limited to the past 800 ky, and no ice core data are available for the full duration of the MPT.

Because CO_2 is well mixed in the atmosphere over the time scale of a few years, and because CO_2 is exchanged rapidly between the surface ocean and atmosphere, marine proxy records of past sea surface carbonate chemistry can place constraints on past atmospheric pCO_2. The boron isotopic composition of planktic foraminifer shells is a proxy for past seawater pH. This proxy is based on the equilibrium reaction between the two dominant species of dissolved boron in seawater and the isotope fractionation between the two species [supporting online material (SOM)]. Atmospheric pCO_2 can be estimated from the boron isotopic composition of those shells if (i) aqueous partial pressure of CO_2 (PCO_2) at the core site is in equilibrium with atmospheric pCO_2, and (ii) another carbon parameter of the water in which the foraminifers grew is known. Using reasonable assumptions about seawater alkalinity, quantitative replication of select intervals of the Vostok pCO_2 record from boron isotopes in the planktic foraminifer *Globigerinoides sacculifer* (*15*) has demonstrated the validity of this method.

Here, we extend the existing 400-ky boron isotope record from Ocean Drilling Program (ODP) site 668B beyond the MPT to 2.1 million years ago. ODP site 668B is located on the Sierra Leone Rise in the eastern equatorial Atlantic (4°46′N, 20°55′W) at a water depth of 2693 m. Nearby oceanographic data (from World Ocean Circulation Experiment cruise A15, station 34) indicate that in the modern ocean, aqueous PCO_2 and atmospheric pCO_2 are in equilibrium. Reconstruction of the local marine carbonate chemistry thus allows us to estimate PCO_2 and infer pCO_2.

From this sediment core, we constructed a high-resolution oxygen isotope ($\delta^{18}O$) record from shells of the surface-dwelling *G. ruber*. The record allows us to establish an age model, which is simultaneously tied (*16*) to the stack of 57 globally distributed benthic $\delta^{18}O$ records [the LR04 stack (*4*)] and the planktic $\delta^{18}O$ record of ODP site 677 (*17*). Large *G. sacculifer* shells were selected from extreme glacial and interglacial samples and transitional periods for boron isotope analysis (fig. S1 and SOM). Boron isotopes were measured by negative thermal ionization mass spectrometry and complemented by Mg/Ca analyses on small shells of *G. ruber* for temperature reconstruction (see SOM for further details). Boron isotope data were then converted into pH estimates, using the empirical calibration for *G. sacculifer* (*18*) and following the procedure outlined in (*15*). Mg/Ca-based SSTs were estimated according to the method of (*19*). The salinity effect on Mg/Ca temperature estimates discovered by (*20*) has been considered but found to be of negligible importance for PCO_2 estimates (SOM).

In order to translate the pH estimates into PCO_2, a second parameter of the carbonate system is required, such as $[CO_3^{=}]$ or alkalinity. An evaluation of methods to estimate this second param-

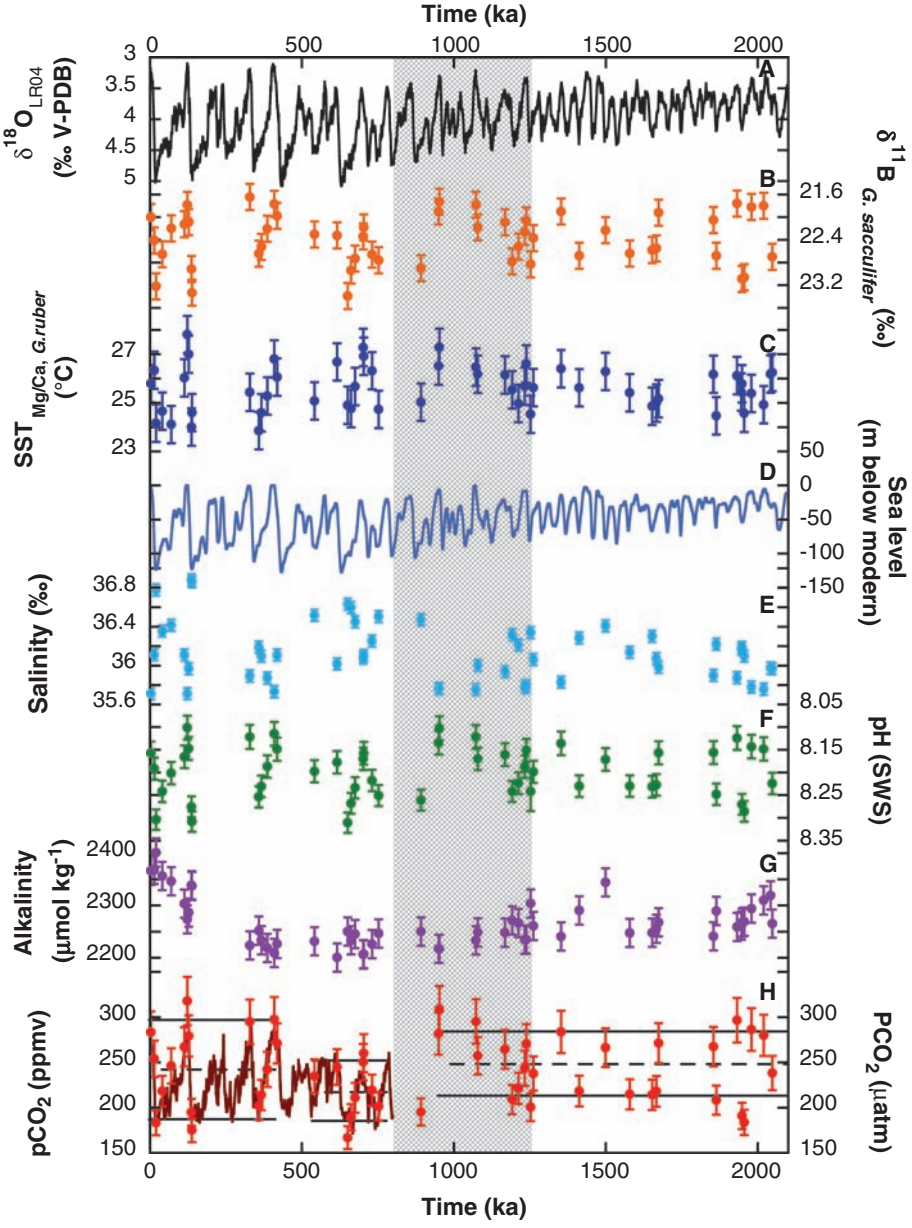

Fig. 1. 2.1-million-year estimation of atmospheric pCO_2 from marine proxies recorded at ODP site 668B in the eastern equatorial Atlantic. (**A**) The LR04 benthic oxygen isotope stack (*4*) reflects the change from the dominant 40-ky periodicity of glacial cycles before 1200 ka to the 100-ky ice-age cycles of the past 700 ky. The MPT is indicated by the horizontal gray bar and describes the transition period. (**B**) Planktic $\delta^{11}B$ data reflect extreme glacial and interglacial times and few transitional periods, selected from the $\delta^{18}O$ record, and are complemented by (**C**) Mg/Ca SST estimates and (**E**) local salinity estimates computed from (**D**) modeled global sea level (*21*). (**F**) Surface seawater pH on the seawater scale (SWS) was calculated as a function of $\delta^{11}B$, SST, and salinity. (**G**) Alkalinity estimates are based on a modeled global ocean estimate (*3*), adjusted to modern local alkalinity at the core site and varying sea level. (**H**) Surface ocean aqueous PCO_2 was then calculated as a function of pH, alkalinity, SST, and salinity. Comparison with the ice core record of atmospheric pCO_2 [dark red line in (H)] reveals a remarkable match for the period from 800 ka to the present. Average glacial and interglacial PCO_2 is indicated by solid horizontal black lines for different intervals in (H). Dashed lines indicate G/I averages. Error bars indicate the propagated error of the individual pH, SST, salinity, and alkalinity uncertainties on the PCO_2 estimate (see SOM for details).

eter is given in the SOM. We followed a similar procedure to that outlined in (*15*), bracketing the potential variations in whole-ocean inventory of alkalinity between two possibilities: (i) Alkalinity remained constant in the past (constant alkalinity scenario); and (ii) alkalinity varied as a function of past terrestrial weathering, ocean $CaCO_3$ production, and sediment dissolution rates [varying alkalinity scenario, after (*3*)]. The degree to which local salinity and alkalinity were increased during glacial periods, when sea level was lower, was approximated with the global sea-level estimate determined by (*21*) relative to average ocean depth (see the SOM for further details and additional validation of this approach).

The pH, temperature, and Pco_2 estimates are shown in Fig. 1. The pre-MPT ocean chemistry revealed from $\delta^{11}B$ is characterized by less basic glacials (pH 8.24 ± 0.03, 1 SD) relative to the post-MPT (pH 8.29 ± 0.02), whereas interglacial pH is comparable between the two intervals (pH 8.14 ± 0.02 and 8.14 ± 0.03, respectively). Several uncertainties were considered for the Pco_2 calculation (SOM) but were found to be of minor importance. The only significant Pco_2 difference stems from the choice of alkalinity, where a total difference in alkalinity of up to 221 μmol kg^{-1} between scenarios results in a maximum Pco_2 difference of 27 microatmospheres (μatm) and an average difference of 17.7 μatm (fig. S1 and SOM). The Pco_2 estimates presented here are based on the varying alkalinity scenario [after (*3*)], in which weathering of the Canadian Shield modulates 4% of global weathering rates. Although all Pco_2 estimates are very similar, this one yields the best match with the measured atmospheric pco_2 over the past 800 ky (fig. S1 and SOM). According to this scenario, our proxy estimates translate into pre-MPT interglacial Pco_2 similar to that of the most recent interglacials (283 μatm) but relatively higher pre-MPT glacial Pco_2 (213 μatm). In comparison, the constant alkalinity scenario yields Pco_2 ~ 10 to 20 μatm higher for the entire record (fig. S1 and SOM). The large uncertainty in alkalinity thus results in only a small difference in the Pco_2 estimate and indicates that seawater pH is a a sensitive parameter for calculating Pco_2. Because changes in ocean alkalinity were probably accompanied by similar changes in total dissolved inorganic carbon, they appear to exert only a small impact.

Considering only extreme glacial/interglacial (G/I) samples, as determined by the oxygen isotope stratigraphy, the values and amplitudes of our reconstructed Pco_2 cycles show good agreement with ice core measurements (Table 1). The ice core pco_2 data for the intervals 0 to 418 ka (180 to 300 ppmv range, 239 ppmv average) and 540 to 800 ka (172 to 260 ppmv range, 221 ppmv average) (*12*–*14*) are remarkably consistent with our marine proxy estimates for those intervals (184 to 297 μatm range, 241 μatm average; and 181 to 252 atm range, 217 μatm average, respectively). In addition, the exceptionally low pco_2 (172 ppmv) measured in ice cores during marine isotope stage (MIS) 16 is reflected in a similarly low boron isotope estimate of 167 ± 13 μatm.

Our reconstructed pH and Pco_2 changes also agree well with the climate signal recorded in the LR04 stack (*4*): Extreme interglacial benthic $\delta^{18}O$ was relatively constant over the course of our 2.1-million-year record [3.2 to 3.5 per mil (‰)], but extreme glacial benthic $\delta^{18}O$ increased from 4.3‰ at 2.1 Ma to 5.1‰ for the post-MPT glacials (Fig. 1). The relatively less extreme glacials of the pre-MPT are thus reflected in a smaller land ice extent and/or warmer deep-sea temperatures and correlate well with higher glacial pco_2. Our data are also consistent with SST reconstructions from the WPWP indicating warmer glacial SSTs pre-MPT as compared to post-MPT, but similar interglacial SSTs (*11*). Strong correlations also exist between sub-Antarctic alkenone SST and ice core change in temperature and between the abundance of alkenones in ODP site 1090 and pco_2 measured in ice cores (*22*). The record covers only 1.1 million years but agrees well throughout with our boron isotope reconstruction. In particular, the alkenone record shows exceptionally high SST and exceptionally low alkenone abundance for MIS 25 (950 ka), suggesting high pco_2 of ≥300 ppm. This observation agrees well with the warmest interglacial SSTs observed in the WPWP for MIS 25 (*11*) and is consistent with our boron isotope estimate, which indicates higher than average Pco_2 (308 μatm) for MIS 25. Comparison with independent climate records of polar ice extent and deep ocean temperature (*4*), sub-Antarctic SST (*22*), and WPWP SSTs (*11*) thus corroborates the validity of our estimates and supports the notion that interglacial atmospheric pco_2 before the MPT was similar to that in the preindustrial period, but that pre-MPT glacial pco_2 was ~31 μatm higher than during post-MPT glacials.

In order to estimate climate sensitivity from the observed CO_2 changes, we focus on the pre-MPT glacials, because pre- and post-MPT interglacial Pco_2 are statistically indistinguishable (Table 1). We use a logarithmic climate sensitivity equation (*23*) with an average equilibrium temperature change of 5 K for doubling CO_2. This temperature change is at the high end of CO_2 sensitivity estimates on short time scales but is more appropriate for the longer time scales considered here, which include slow feedbacks such as ice-sheet albedo effects (*24*). Based on this sensitivity, the global average surface air temperature during pre-MPT glacials was 1.06 K warmer than during post-MPT glacials. In comparison, the mean global temperature change from the Last Glacial Maximum to the preindustrial period is 3.3 to 5.1 K [as estimated by the Paleoclimate Model Intercomparison Project (*25*)]. Consequently, the average pre-MPT G/I global temperature change was ~30% smaller than during the past 400 ky. However, the smaller temperature range does not imply a gradual decline in greenhouse forcing over the MPT. Although the average G/I pco_2 was ~7 μatm higher before the transition (Table 1), this difference is entirely a result of higher glacial pco_2. The higher glacial pco_2 is consistent with the warmer glacial SSTs, ice extent, and/or deep-sea temperatures, but interglacial pco_2 was similar before and after the transition. We therefore conclude that CO_2 was unlikely to have been the main driver of the MPT. We also conclude that present-day atmospheric pco_2 is the highest it has been for the past 2.1 million years, requiring a search for an analog for present-day conditions, possibly during the time before the acceleration of Northern Hemisphere glaciation before 2.7 million years ago.

Table 1. Comparison of glacial and interglacial pco_2 extremes as measured from ice cores (*12*–*14*) and estimated from boron isotopes in planktic foraminifers (see fig. S1 for the selection and number of data included in each average). Cumulative uncertainties have been calculated for the G/I boron isotope Pco_2 estimates, assuming that the propagated errors of individual data are normally distributed.

Interval (ka)	Ice core pco_2 (ppmv)			Boron isotope Pco_2 (μatm)		
	Minimum	Maximum	Average	Minimum	Maximum	G/I average
0–418	180	300	239	184^{+17}_{-14}	297^{+29}_{-21}	241
450–800	172	260	221	181^{+15}_{-20}	252^{+17}_{-14}	217
892–2048	–	–	–	213^{+30}_{-28}	283^{+30}_{-37}	248

References and Notes

1. J. Hays, J. Imbrie, N. Shackleton, *Science* **194**, 1121 (1976).
2. N. G. Pisias, T. C. Moore Jr., *Earth Planet. Sci. Lett.* **52**, 450 (1981).
3. P. U. Clark *et al.*, *Quat. Sci. Rev.* **25**, 3150 (2006).
4. L. E. Lisiecki, M. E. Raymo, *Paleoceanography* **20**, 10.1029/2004PA001071 (2005).
5. M. E. Raymo, W. F. Ruddiman, P. N. Froelich, *Geology* **16**, 649 (1988).
6. J. R. Marlow, C. B. Lange, G. Wefer, A. Rosell-Mele, *Science* **290**, 2288 (2000).
7. M. W. Wara, A. C. Ravelo, M. L. Delaney, *Science* **309**, 758 (2005).
8. E. L. McClymont, A. Rosell-Melé, *Geology* **33**, 389 (2005).
9. K. T. Lawrence, Z. Liu, T. D. Herbert, *Science* **312**, 79 (2006).
10. T. de Garidel-Thoron, Y. Rosenthal, F. Bassinot, L. Beaufort, *Nature* **433**, 294 (2005).
11. M. Medina-Elizalde, D. W. Lea, *Science* **310**, 1009 (2005).
12. J. R. Petit *et al.*, *Nature* **399**, 429 (1999).
13. U. Siegenthaler *et al.*, *Science* **310**, 1313 (2005).
14. D. Lüthi *et al.*, *Nature* **453**, 379 (2008).
15. B. Hönisch, N. G. Hemming, *Earth Planet. Sci. Lett.* **236**, 305 (2005).
16. D. Paillard, L. Labeyrie, P. Yiou, *Eos* **77**, 379 (1996).
17. N. J. Shackleton, A. Berger, W. A. Peltier, *Trans. R. Soc. Edinb. Earth Sci.* **81**, 251 (1990).
18. A. Sanyal, J. Bijma, H. J. Spero, D. W. Lea, *Paleoceanography* **16**, 515 (2001).
19. P. S. Dekens, D. W. Lea, D. K. Pak, H. J. Spero, *Geochem. Geophys. Geosyst.* **3**, 10.1029/2001GC000200 (2002).
20. B. Kisakürek, A. Eisenhauer, F. Böhm, D. Garbe-Schönberg, J. Erez, *Earth Planet. Sci. Lett.* **273**, 260 (2008).

21. R. Bintanja, R. S. W. van de Wal, *Nature* **454**, 869 (2008).
22. A. Martínez-Garcia *et al.*, *Paleoceanography* **24**, 10.1029/2008PA001657 (2009).
23. D. Archer, *Global Warming—Understanding the Forecast* (Blackwell Publishing, Malden, MA, 2006).
24. J. Hansen *et al.*, *Open Atm. Sci. J.* **2**, 217 (2008).
25. E. Jansen *et al.*, in *Climate Change 2007: The Physical Science Basis. Contribution of Working Group I to the Fourth Assessment Report of the Intergovernmental Panel on Climate Change,* S. Solomon *et al.*, Eds. (Cambridge Univ. Press, Cambridge, 2007).

26. We thank ODP for sediment samples and NSF (grant OCE 06-23621) for financial support. The idea for this study was seeded through conversations with S. Hemming. L. Leon is gratefully acknowledged for laboratory assistance, P. deMenocal for Mg/Ca analyses at the Lamont-Doherty Earth Observatory (LDEO), and M. Segl for isotope analyses at Bremen University. We also thank C. Pelejero and two anonymous reviewers for valuable comments. Discussions with P. Köhler and R. Bintanja improved the manuscript. The oxygen isotope data are available in the National Oceanic and Atmospheric Administration Paleoclimatology database (www.ngdc.noaa.gov/paleo/data.html). This is LDEO contribution number 7261.

Supporting Online Material
www.sciencemag.org/cgi/content/full/324/5934/1551/DC1
Materials and Methods
Figs. S1 and S2
Table S1
References

27 January 2009; accepted 6 May 2009
10.1126/science.1171477

Fossil Plant Relative Abundances Indicate Sudden Loss of Late Triassic Biodiversity in East Greenland

Jennifer C. McElwain,[1]* Peter J. Wagner,[2] Stephen P. Hesselbo[3]

The pace of Late Triassic (LT) biodiversity loss is uncertain, yet it could help to decipher causal mechanisms of mass extinction. We investigated relative abundance distributions (RADs) of six LT plant assemblages from the Kap Stewart Group, East Greenland, to determine the pace of collapse of LT primary productivity. RADs displayed not simply decreases in the number of taxa, but decreases in the number of common taxa. Likelihood tests rejected a hypothesis of continuously declining diversity. Instead, the RAD shift occurred over the upper two-to-four fossil plant assemblages and most likely over the last three (final 13 meters), coinciding with increased atmospheric carbon dioxide concentration and global warming. Thus, although the LT event did not induce mass extinction of plant families, it accompanied major and abrupt change in their ecology and diversity.

Ecological theory shows that relative abundance distributions (RADs) provide important information on the ecological assembly rules for communities in both the present (*1*, *2*) and past (*3*). The general ecological rules that underpin community assembly are also independent of species composition, thus providing a metric of past diversity that is applicable to communities of disparate composition, phylogenetic history, and age (*1*, *2*). Differences among RADs reflect differences in dominance and rarity as well as richness. RADs describe dominance and rarity more exactly than does evenness (i.e., uniformity of abundances) alone (*4*). Hypotheses of ecological deterioration make predictions about changes in RADs over time without necessarily predicting extinction (*5*, *6*). Therefore, if prolonged ecological deterioration precedes a mass extinction, then RADs could reveal ecological deterioration better than richness or evenness alone.

We use RADs to examine the pace of diversity loss leading to the Triassic-Jurassic boundary (TJB). The TJB extinction is one of the five greatest in Earth history (*7*), but the pace of biodiversity loss remains uncertain (*8*–*12*). This hampers our ability to distinguish between competing hypotheses on the causal mechanisms of the TJB mass extinction. Gradual extinction patterns have been reported. RADs offer an opportunity to reexamine the pace of LT biodiversity change in greater detail than provided by either changes in richness or evenness.

We assessed trends in RADs over six taphonomically similar Rhaetian aged fossil plant beds from Astartekløft, East Greenland (*10*). First, we determined the most likely RAD model for each bed based on the expected number of taxa with x specimens given the observed sample size (*3*). We considered four RAD models: geometric and the zero-sum multinomial, which are governed largely by ecological succession (*1*, *2*); and lognormal and Zipf, which are governed by increasing ecospace due to facilitation or niche construction (*1*). Because the different RADs do not represent special cases of each other, we use Akaike's modified information criterion to choose the best model (*3*, *13*).

Second, we assessed a series of increasingly complicated temporal models of LT plant diversity change. We did this by assessing the likelihood of a range of models, and thus the joint likelihood that 2+ assemblages shared the same RAD. Because not all beds fit the same RAD model, we labeled each model with a more general aspect of diversity: the hypothesized number of genera (S) with frequency greater than 10^{-6} ($S_{f>10^{-6}}$). In order of increasing complexity, we considered (i) uniform diversity over the whole Rhaetian-aged portion of the Astartekløft section ($\Delta S_{f>10^{-6}} = 0$); (ii) linear diversity decrease over the same interval ($\Delta S_{f>10^{-6}} < 0$); (iii) static diversity followed by linear decrease in the later Rhaetian portion of the section; (iv) static diversity followed by curvilinear decrease in the later Rhaetian portion of the section.

The simpler temporal models are special cases of the more complicated temporal models. Thus, we can use log-likelihood ratios to test whether a more complicated temporal model is significantly better than a simpler one (*14*). We tested hypothesized RAD shifts by how well those hypotheses predict observed abundances given the best general RAD model and the hypothesized shift in $S_{f>10^{-6}}$, not by how well they predict the best exact model. Second, we reach identical conclusions using $S_{f>10^{-5}}$ or $S_{f>10^{-4}}$.

Table 1. Modified Akaike's information criteria (AICc) for best examples of each general RAD model. AICc = $-2 \times \ln L[H|data] \times n/(n - k - 1)$, where H is the best hypothesis from each model, n is the number of specimens, and k is the number of parameters ($k = 1$ for geometric; otherwise $k = 2$). The lowest AICc value (bold) gives the best fit (*13*).

			RAD model AICc			
Bed	Taxa	n	Geometric	Zero sum	Lognormal	Zipf
1	13	224	**91.6**	96.9	97.2	123.3
1.5	9	62	**50.8**	54.4	52.6	52.4
2	12	258	**96.8**	99.0	98.9	107.6
3	9	525	68.0	124.3	**62.3**	62.6
4	11	876	**96.1**	97.5	124.3	162.5
5A	7	275	**52.4**	60.9	63.4	76.1

[1]UCD School of Biology and Environmental Science, University College Dublin, National University of Ireland, Belfield, Dublin 4, Ireland. [2]Department of Paleobiology, National Museum of Natural History, Smithsonian Institution, Washington, DC 20560, USA. [3]Department of Earth Sciences, University of Oxford, Oxford OX1 3PR, UK.

*To whom correspondence should be addressed. E-mail: jennifer.mcelwain@ucd.ie

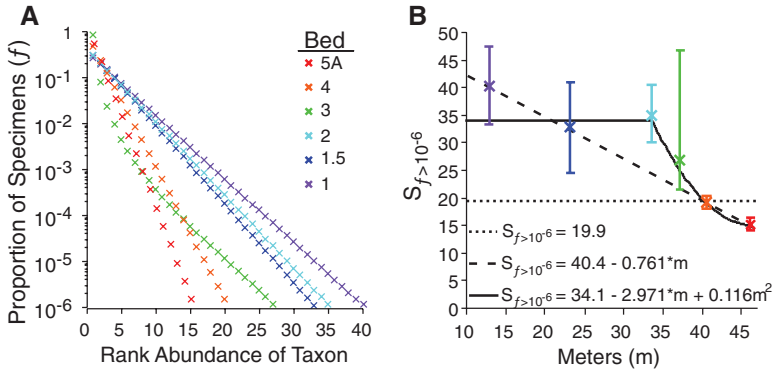

Fig. 1. Trends in Late Triassic plant community relative abundance distributions (RADs) and diversity for Astartekløft, East Greenland. (**A**) Best-fit RAD hypotheses for each bed. (**B**) Most likely richness of genera with $f > 10^{-6}$ for each bed ($S_{f>10^{-6}}$). Bars give 1-unit support (i.e., lnL ≤ 1 less than maximum); bar width decreases both with increasing sample size and increased fit of general model to the data (*14*). Lines give predicted diversity given the best hypothesis from three different models of diversity change over meters of sediment. *m* in the equations gives meters beyond 13 m and 37 m (the heights of apparent shifts). The final hypothesis has one more parameter, as S_f is static until bed 3.

Table 2. Hypotheses of changing diversity going up-section, given here as the changing numbers of taxa (*S*) with relative abundance >10^{-6}. *k* gives the number of varying parameters for each hypothesis. lnL gives the log-probability of all observed abundances given the hypothesis and the best model from Table 1. *P* gives the probability of the difference in log-likelihoods if the simpler hypothesis is correct. Because simple hypotheses are special cases of the complex hypotheses, we assess *P* using log-likelihood ratio tests. The best 3*k* hypothesis, linear decrease in diversity over the last 13 m, is omitted as it is worse than the best 2*k* hypothesis.

Hypothesis	*k*	lnL	*P*
$S_{f>10^{-6}}$ = 19.9	1	−232.7	–
$S_{f>10^{-6}}$ = 40.4→15.1	2	−224.8	7.0×10^{-5}
$S_{f>10^{-6}}$ = 34.1→15.1 in last 13 m	4	−220.7	0.018

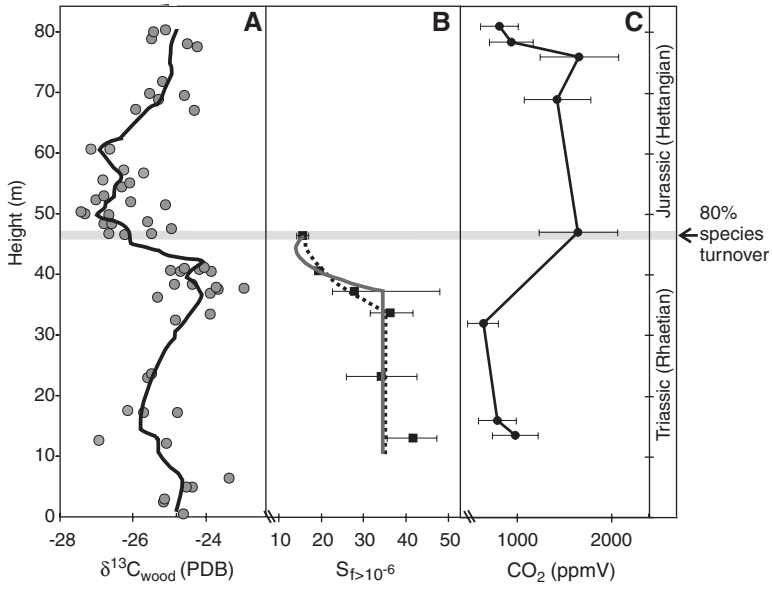

Fig. 2. Trends in fossil wood stable carbon isotopic composition ($\delta^{13}C_{wood}$), plant diversity, and atmospheric CO_2 concentration. (**A**) Compilation of published (*9*) $\delta^{13}C_{wood}$ data from Astartekløft, East Greenland, showing LOESS smoothed trends (using Gaussian kernel function (*20*). (**B**) Best hypothesis of plant diversity change (dotted line) plus the best hypothesis postponing that shift (gray line). $S_{f>10^{-6}}$ is the hypothesized number of genera with $f > 10^{-6}$; the same results are achieved with $f > 10^{-5}$ or $f > 10^{-4}$. (**C**) Record of atmospheric CO_2 concentration in ppmv derived from stomatal analysis of fossil Ginkgoales leaves from Astartekløft and other localities within Jameson Land (*8*). $\delta^{13}C_{wood}$ from the same section show a marked decrease, and atmospheric CO_2 concentration increases within the stratigraphic range of the plant diversity decrease.

Like confidence-interval studies [e.g., (*15*)], RADs account for unsampled taxa, with lower sample sizes leading to best-fit RADs positing greater numbers of unsampled taxa (*3*). Although samples from the same RAD over time will show gradual last occurrences of taxa [the Signor-Lipps effect (*16*)], our likelihood tests will show indistinguishable RADs and thus suggest constant diversity (*17*). Thus, the Signor-Lipps effect cannot create trends in RADs, even if sampling decreases up-section. The RAD approach has the two additional advantages of implying changes in rarity among (unspecified) unsampled taxa and requiring fewer fossiliferous horizons, as the statistical power comes from the number of sampled fossils rather than the number of occurrences.

We analyze genera rather than species. Because 95% of fossil plant genera in Kap Stewart Group strata have monospecific occurrences within plant beds (*10*), species-level patterns cannot differ too greatly from genus-level patterns. Moreover, most species determinations for the Kap Stewart flora reflect leaf surface micromorphological traits (*18*), which might not be taxonomically reliable (*10*). Genera also add a conservative bias, as the greater taxon numbers provided by species would increase our ability to recognize different RADs.

Taphonomic studies demonstrate that despite some general biases [see (*10*) for further discussion], leaf litter from temperate and relatively low diversity subtropical floodplain forests provides a relatively accurate indication of both the richness and the dominance-diversity relationship of the live forest community (*19*). We assume that similar processes affected leaf litter on and preservation from LT floodplain forests of East Greenland (*10*). RADs of census-collected fossil leaf collections from Greenland should therefore elucidate patterns of changes in LT plant community assembly and diversity for this region. All six LT fossil plants beds at Astartekløft [with the exception of bed 5 (*17*)] likely represent a geologically instantaneous sample of the standing plant community preserved during river flooding on one or several occasions. RADs from these beds are therefore unlikely to be subjected to any significant time averaging, which can result in lognormal RADs by mixing of different exponential distributions (*3*).

All beds except bed 3 best fit geometric RADs; bed 3 best fits a lognormal RAD (Table 1 and Fig. 1A). This suggests that LT plant communities were predominantly assembled by simple niche-partitioning rather than more complex assembly rules (*3*). More important, the best RADs for each bed show a distinct trend toward increasing slope moving up-section and thus decreasing diversity through time (Fig. 1A), especially above 35 m (Fig. 1B). The best hypothesis of continuously decreasing plant diversity (where $S_{f>10^{-6}}$ declines by 0.777 per meter; Fig. 1B) is significantly more likely than

is the best hypothesis of static diversity (Table 2). The likelihood improves significantly more given a hypothesis of an identical geometric RAD for the first three beds (the first 24 m) and decreasing diversity decreasing markedly over the last three beds [the final 13 m (*17*)]. Variations on the final model show that we cannot reject the idea that the plant diversity shift is concentrated in the upper 9 m of the Rhaetian aged Astartekløft sedimentary rocks (beds 3 to 5A; Fig. 2), although we can reject the ideas that the shift was distributed over the upper 23 m (beds 1.5 to 5A) or the upper 6 m (beds 4 and 5A). Regardless of the exact timing, a hypothesis of continuous, gradual plant diversity loss suggested by richness decrease alone (*10*) is not tenable (*20*).

Environmental degradation on ecologic time scales decreases community diversity and complexity and increases RAD slopes (*5*, *6*). We see the same pattern here, but on an evolutionary time scale. If sedimentation for the section was fairly constant and if the Rhaetian is completely represented, then the shift in RADs most likely begins approximately 300,000 to 500,000 years before the TJB. Extraordinarily high sedimentation rates would be required for beds 3 to 5 to represent a snapshot of ecologic time-scale processes. Conversely, large decreases in sedimentation rates over beds 3 to 5 relative to beds 1 to 2 are required to salvage the hypothesis that diversity decreased continuously through the section. There is no sedimentological or taphonomic support for either proposition.

Within uncertainties, the abrupt diversity loss coincides with a moderate +0.95‰ positive excursion in organic matter carbon-isotope composition (Fig. 2) just before the onset of the main TJB negative carbon isotopic excursion (*9*). These results suggest that the decline in plant diversity at Astartekløft coincided with a major transition between different states in the global carbon cycle from predominantly ^{12}C-sink to ^{12}C-source processes. Available low-resolution CO_2 records indicate that the diversity loss occurred between minimum CO_2 values reported for the interval [480 ± 160 parts per million by volume (ppmv)] at 32 m and maximum values (1240 ± 400 ppmv) at 47 m (*8*) and coincided with a major sea-level fall across Europe (*11*, *21*). Concurrently, the inferred global mean surface temperature difference from present (ΔGMST) changed from 2 ± 1.0°C to 7 ± 1.0°C ΔGMST (*8*). Interpolating between available CO_2 estimates indicates that the sudden diversity drop between 33 and 37 m coincided with a mere ~100 to ~350 ppmv rise in CO_2 concentration. This was followed by a more protracted diversity decline with a lessening slope approaching the TJB, as atmospheric CO_2 (*8*) and estimated ΔGMST increased to their respective maximum values (*21*). Therefore, although CO_2-induced global warming was likely an important contributory factor to plant species turnover at the TJB (46 m), an alternative or additional triggering mechanism for the abrupt loss of plant diversity between 33 and 37 m at Astartekløft may be possible.

We cannot extrapolate the vegetation responses from one locality globally. However, global hypotheses for the end-Triassic extinctions must predict local patterns; thus, hypotheses failing to predict the Kap Stewart patterns are unlikely as global explanations. Moreover, the most parsimonious explanation for the trends we observe is that they represent regional responses to global environmental change. This argument is supported by the observation that the highest occurrences of plant species at Astartekløft at ~46 m are contemporaneous with those from 12 other Kap Stewart Group localities (*18*) and that high turnover of fossil plant taxa within the TJB interval has been recorded in North America (*22*), UK (*21*), Sweden (*18*), Spain (*23*), Austria (*24*), and Italy (*25*). Cross-correlation of the stable carbon isotopic profiles from across the globe (*9*, *21*, *24*, *25*) suggests that the abrupt loss in plant diversity at Astartekløft began at the onset, not the zenith, of the main global carbon isotopic excursion and before turnover of 90% of macrofossil plant species in the Jameson Land region (*10*, *18*). Palynology further supports this temporal correlation as the first appearance of the morphospecies *Cerebropollenites thiergartii* coincides with the turn to more negative $\delta^{13}C$ values in TJB sections at Astartekløft (*26*), St Audries Bay (UK), and Tiefengraben (Austria) (*24*). The abrupt loss in Astartekløft plant diversity also coincides with several patterns indicating severe environmental disturbance to the marine environment, including turnover (*27*) and extinction of shallow marine shelly invertebrates (*25*), a shallow-water carbonate production crisis (*21*), and at least localized proliferation of green algal phytoplankton (*21*, *24*).

The abrupt plant diversity loss between 33 and 37 m is consistent with expected plant responses to a catastrophically rapid rather than gradual environmental change and argues against the currently favored extinction mechanisms invoking gradual CO_2-induced global warming due to slow release of CO_2 from the mantle associated with extrusion of basalt over an area of >10 million km^2 (CAMP; Central Atlantic Magmatic Province) (*9*, *10*). Proposed mechanisms of rapid environmental change include a meteorite impact (*12*), exhalation of thermogenic methane or other gases generated by intrusion of CAMP sill magma (*11*), sulfur dioxide aerosol release during CAMP eruptions (*28*), or biogenic methane release from gas hydrates (*29*). An alternative explanation for the abrupt diversity loss is that it represents a threshold response of LT vegetation to relatively minor increases in CO_2 concentration and/or global temperature. High-resolution proxy CO_2 and SO_2 records, coupled with controlled environment experiments, are required to test further the primary drivers of abrupt LT biodiversity loss.

References and Notes

1. J. S. Gray, in *Organization of Communities Past and Present*, J. H. R. Gee, P. S. Gillier, Eds. (Blackwell, Oxford, 1987), pp. 53–67.
2. S. P. Hubbell, *The Unified Neutral Theory of Biodiversity and Biogeography*, S. A. Levin, H. S. Horn, Eds., Monographs in Population Biology (Princeton Univ. Press, Princeton, NJ, 2001).
3. P. J. Wagner, M. A. Kosnik, S. Lidgard, *Science* **314**, 1289 (2006).
4. M. A. Kosnik, P. J. Wagner, *Evol. Ecol. Res.* **8**, 195 (2006).
5. R. A. Kempton, *Biometrics* **35**, 307 (1979).
6. R. M. May, M. J. Crawley, G. Sugihara, in *Theoretical Ecology Principles and Applications* M. R. May, A. R. McLean, Eds. (Oxford Univ. Press, Oxford, 2007), pp. 111–131.
7. D. M. Raup, J. J. Sepkoski Jr., *Science* **215**, 1501 (1982).
8. J. C. McElwain, D. J. Beerling, F. I. Woodward, *Science* **285**, 1386 (1999).
9. S. P. Hesselbo, S. A. Robinson, F. Surlyk, S. Piasecki, *Geology* **30**, 251 (2002).
10. J. C. McElwain, M. E. Popa, S. P. Hesselbo, M. Haworth, F. Surlyk, *Paleobiology* **33**, 547 (2007).
11. S. P. Hesselbo, C. A. McRoberts, J. Pálfy, *Palaeogeogr. Palaeoclimatol. Palaeoecol.* **244**, 1 (2007).
12. P. E. Olsen *et al*., *Science* **296**, 1305 (2002).
13. K. P. Burnham, D. R. Anderson, *Model Selection and Inference: A Practical Information-Theoretic Approach* (Springer, New York, ed. 2, 2002).
14. A. W. F. Edwards, *Likelihood—Expanded Edition* (Johns Hopkins Univ. Press, Baltimore, 1992).
15. S. C. Wang, P. J. Everson, *Paleobiology* **33**, 324 (2007).
16. P. W. Signor III, J. H. Lipps, *Geological Society of America Special Paper* 190, 291 (1982).
17. Supporting material is available on *Science* Online.
18. T. M. Harris, *Medd. Gronl.* **112**, 82 (1937).
19. R. J. Burnham, *Rev. Palaeobot. Palynol.* **58**, 5 (1989).
20. W. S. Cleveland, S. J. Devlin, *J. Am. Stat. Assoc.* **83**, 596 (1988).
21. B. van de Schootbrugge *et al*., *Palaeogeogr. Palaeoclimatol. Palaeoecol.* **244**, 126 (2007).
22. J. H. Whiteside, P. E. Olsen, D. V. Kent, S. J. Fowell, M. Et-Touhami, *Palaeogeogr. Palaeoclimatol. Palaeoecol.* **244**, 345 (2007).
23. J. J. Gomez, A. Goy, E. Barron, *Palaeogeogr. Palaeoclimatol. Palaeoecol.* **244**, 89 (2007).
24. W. M. Kuerschner, N. R. Bonis, L. Krystyn, *Palaeogeogr. Palaeoclimatol. Palaeoecol.* **244**, 257 (2007).
25. M. T. Galli, F. Jadoul, S. M. Bernasconi, S. Cirilli, H. Weissert, *Palaeogeogr. Palaeoclimatol. Palaeoecol.* **244**, 52 (2007).
26. L. Mander, personal communication (2008).
27. L. Mander, R. J. Twitchett, M. J. Benton, *J. Geol. Soc. London* **165**, 319 (2008).
28. J. G. McHone, in *The Central Atlantic Magmatic Province*, W. E. Hames *et al*., Eds., American Geophysical Union Monograph 136 (American Geophysical Union, Washington, DC, 2002), pp. 241–254.
29. D. J. Beerling, R. A. Berner, *Global Biogeochem. Cycles* **16**, 1036 (2002).

30. J.C.M. collected plant paleoecological data, S.P.H collected isotopic and stratigraphic data, and P.J.W. undertook data analyses. J.C.M and P.J.W cowrote the paper, and all authors contributed equally to interpretation. We gratefully acknowledge funding from a Marie Curie Excellence Grant (MEXT-CT- 2006-042531) to J.C.M. and NSF-EAR-0207874 to P.J.W. This is Paleobiology Database contribution 95.

Supporting Online Material

www.sciencemag.org/cgi/content/full/324/5934/1554/DC1
Methods
Figs. S1 to S3
Table S1
References

2 February 2009; accepted 7 May 2009
10.1126/science.1171706

Pandemic Potential of a Strain of Influenza A (H1N1): Early Findings

Christophe Fraser,[1]* Christl A. Donnelly,[1]* Simon Cauchemez,[1] William P. Hanage,[1] Maria D. Van Kerkhove,[1] T. Déirdre Hollingsworth,[1] Jamie Griffin,[1] Rebecca F. Baggaley,[1] Helen E. Jenkins,[1] Emily J. Lyons,[1] Thibaut Jombart,[1] Wes R. Hinsley,[1] Nicholas C. Grassly,[1] Francois Balloux,[1] Azra C. Ghani,[1] Neil M. Ferguson[1]†;

Andrew Rambaut,[2] Oliver G. Pybus[3];

Hugo Lopez-Gatell,[4] Celia M. Alpuche-Aranda,[5] Ietza Bojorquez Chapela,[4] Ethel Palacios Zavala[4];

Dulce Ma. Espejo Guevara[6];

Francesco Checchi,[7] Erika Garcia,[7] Stephane Hugonnet,[7] Cathy Roth[7]

The WHO Rapid Pandemic Assessment Collaboration‡

A novel influenza A (H1N1) virus has spread rapidly across the globe. Judging its pandemic potential is difficult with limited data, but nevertheless essential to inform appropriate health responses. By analyzing the outbreak in Mexico, early data on international spread, and viral genetic diversity, we make an early assessment of transmissibility and severity. Our estimates suggest that 23,000 (range 6000 to 32,000) individuals had been infected in Mexico by late April, giving an estimated case fatality ratio (CFR) of 0.4% (range: 0.3 to 1.8%) based on confirmed and suspected deaths reported to that time. In a community outbreak in the small community of La Gloria, Veracruz, no deaths were attributed to infection, giving an upper 95% bound on CFR of 0.6%. Thus, although substantial uncertainty remains, clinical severity appears less than that seen in the 1918 influenza pandemic but comparable with that seen in the 1957 pandemic. Clinical attack rates in children in La Gloria were twice that in adults (<15 years of age: 61%; ≥15 years: 29%). Three different epidemiological analyses gave basic reproduction number (R_0) estimates in the range of 1.4 to 1.6, whereas a genetic analysis gave a central estimate of 1.2. This range of values is consistent with 14 to 73 generations of human-to-human transmission having occurred in Mexico to late April. Transmissibility is therefore substantially higher than that of seasonal flu, and comparable with lower estimates of R_0 obtained from previous influenza pandemics.

On 29 April 2009, the World Health Organization (WHO) announced that the rapid global spread of a strain of influenza A (H1N1) virus detected in the previous week warranted moving the global pandemic alert level to phase 5 (www.who.int/csr/disease/swineflu/). Phase 5 indicates sustained human-to-human transmission of a novel influenza strain of animal origin in one WHO region of the world, and exported cases detected in other regions. In this outbreak, the earliest affected country may have been Mexico, with many cases in other nations associated with travels from that country. There are uncertainties about all aspects of this outbreak, including the virulence, transmissibility, and origin of the virus, and this in turn results in uncertainty in judging the pandemic potential of the virus and when reactive public health responses, such as recommendations to stay at home or to close schools, should be implemented in individual countries. Here we report findings of key early investigations into the outbreak that could aid such policy decisions.

The presence of fatalities [29 confirmed plus 88 suspected deaths in Mexico as of 4 May 2009 (*1*), 1 confirmed in the United States as of 5 May 2009 (*2*)] is not necessarily indicative of the virulence of the infection. The interpretation of these statistics depends on the total number of infections, including those with mild infection or who are asymptomatic, which is currently unknown, given the absence of a specific serological test for the new H1N1 influenza strain and associated population-level screening. As of 4 May 2009, 11,356 suspected and 822 laboratory-confirmed cases have been reported in Mexico (*1*), but these may represent an underestimate of true case numbers as surveillance has understandably focused on severe cases. Furthermore, severe cases in older individuals will be more difficult to identify because of the higher rate of respiratory illness in those over 60 years of age (*3*), and this could result in an underestimate of overall morbidity. Right censoring of mortality data, which occurs when additional deaths subsequently arise among cases already included in surveillance data, can also bias estimates of the true case fatality ratio (*4*). Finally, suspected deaths may not all have been caused by infection with the novel virus. These uncertainties necessarily affect any estimate of the case fatality ratio (CFR).

On the basis of international travel patterns, we would expect a proportion of cases of any infection spreading widely in Mexico to be exported by travelers (*5*). Owing to intense surveillance for influenza-like illness in those returning from Mexico, ascertainment of early cases in newly affected countries was almost certainly more complete and rapid than local surveillance of mild cases in Mexico. Airline passenger flow out of Mexico shows a significant correlation with the frequency of detected confirmed cases worldwide (Spearman correlation coefficient: 0.56, $P = 0.004$) (Fig. 1, A and B). We thus use data on cases among travelers and backcalculation methods to estimate the total number of people infected in Mexico. Key underlying assumptions in this analysis are that population mixing in Mexico is equally likely between Mexican residents and tourists, and tourists and Mexican residents are at equal risk of infection (despite demographic and other differences). If infections are concentrated away from traveler destinations (Fig. 1E presents the spatial distribution, by state, of cases within Mexico by 5 May), the number of people infected in Mexico will be underestimated, and conversely will be overestimated if the epidemic has disproportionately affected geographical zones visited by travelers. Under the assumption that reporting of infections in travelers was complete, we estimated the number of infections that occurred in Mexico by late April from a model of the interval-censored country case counts, which varied between 18,000 and 32,000 (Table 1), depending on the mean duration of stay of tourists assumed, with perhaps the most credible single value (based on journey duration data) being 23,000. An alternative model that assumed at least one case had been confirmed in every country affected by late April gave lower estimates of the number infected in Mexico, in the range of 6000 to 11,000. However, this model may be viewed as a worst case (from the perspective of resulting CFR estimates), and it fitted the observed number of exported cases in key countries (such as the United States and Canada) substantially worse than did the first model. We used 30 April 2009 as the cut-off date for the data analyzed, but the case data analyzed are subject to delays (clinical onset, testing, and reporting) of up to 1 week, so these estimates may be more representative of infections up to 23 April. The epidemic has subsequently spread further, although the impact of the nonpharmaceutical interventions introduced in Mexico is not yet known.

On the basis of the 9 confirmed and 92 suspected deaths that were reported by 30 April 2009

[1]MRC Centre for Outbreak Analysis and Modelling, Department of Infectious Disease Epidemiology, Imperial College London, Faculty of Medicine, Norfolk Place, London W2 1PG, UK. [2]Institute of Evolutionary Biology, University of Edinburgh, Ashworth Laboratories, Edinburgh EH9 3JT, UK. [3]Department of Zoology, University of Oxford, South Parks Road, Oxford OX1 3PS, UK. [4]Directorate General of Epidemiology, FCO. De P. Miranda, 177 5th Floor, Mexico City, 01480, Mexico. [5]National Institute of Epidemiological Diagnosis and Reference, Prolongación Carpio No. 470 (3° piso), Col Santo Tomás, México City, C.P. 11340, Mexico. [6]Secretaría de Salud - Servicios de Salud de Veracruz Soconusco No. 36, Colonia Aguacatal, C.P. 910 Xalapa, Veracruz, México State. [7]World Health Organization.

*These authors contributed equally to this work.
†To whom correspondence should be addressed. E-mail: neil.ferguson@imperial.ac.uk
‡All authors are members of this collaboration.

(*6*) and assuming similar times from infection to confirmation and from infection to death, we estimated CFRs in the range of 0.3 to 0.6% from the interval-censored case count model, based on confirmed and suspected deaths combined, or 0.03 to 0.05% for confirmed deaths only. Using the alternative, more pessimistic, country presence/absence model, we estimated CFRs of 0.9 to 1.8% based on suspected and confirmed deaths, and 0.08 to 0.16% from the confirmed deaths alone. These estimates have already changed somewhat as a result of data available after 30 April, but we deliberately report the earlier analysis because it formed part of the evidence base used by WHO to move to phase 5.

Another source of information on severity comes from the large outbreak of respiratory disease seen in the small, isolated community of La Gloria in Veracruz province, one case of which has been confirmed to have been caused by the novel H1N1 strain. It is possible that other viruses were circulating at the same time as the outbreak, but the overall attack rate is substantially larger than would be expected for a seasonal influenza outbreak. No fatalities among 616 cases have been attributed to infection during the full period of surveillance of that outbreak (Fig. 3A), giving a 95% confidence interval (CI) of 0 to 0.60%.

Data on the magnitude of the current outbreak in Mexico can also be used to estimate the transmissibility of the virus if the start date of the outbreak is known or can be estimated. Epidemiological investigations into the emergence of the virus in Mexico have focused on the La Gloria outbreak, where the first case in that outbreak is thought to have occurred around 15 February 2009 (Fig. 3A).

An alternative approach to estimating the start date of the outbreak is to look at the diversity in the genetic sequences of viral samples collected from confirmed cases, assuming that diversity accumulates according to a molecular clock model. Twenty-three complete publicly available hemagglutinin (HA) gene sequences from cases not linked in epidemiological clusters were analyzed with a Bayesian coalescent method that assumes exponential growth of the viral population (*7*). This yielded an estimate of the time of most recent common ancestor (TMRCA) of 12 January 2009 [95% credible interval (CrI): 3 November 2008 to 2 March 2009]. The genetic model also gave an estimate of the doubling time of the epidemic of 10 days (95% CrI: 4.5 to 37.5 days) (Fig. 2). Assuming exponential growth, the TMRCA is a reasonable estimate of the start of the outbreak, although it is formally an upper bound due to incomplete sampling of the epidemic and the effects of the exponential model prior to distribution. These findings from a population genetic analysis are consistent with the epidemiological investigation of both the start and magnitude of the current epidemic in Mexico. Figure 2 also shows a preliminary version of this analysis based on the first 11 sequences, which gave similar estimates highlighting the power of these methods. [See (*8*) for further sensitivity analysis and methods.]

The reproduction number, defined as the number of cases one case generates on average over the course of their infectious period, is a key measure of transmissibility and can be estimated in a number of ways from the data currently available.

First, by assuming exponential growth, the growth rate of the epidemic (r) can be inferred from estimates of the current cumulative number of infections (Y_f) and estimated start date and size for the outbreak (t_0 and Y_0, respectively). The basic reproduction number (R_0) can be estimated from the exponential growth rate if one also assumes that the generation time distribution for the new H1N1 strain is similar to that of other strains of seasonal and pandemic viruses (*9*, *10*) [Table 1 and (*8*)]. Using the date of 15 February as the first case of the La Gloria outbreak (*8*) gives reproduction number estimates of between 1.31 and 1.42, depending on which variant of the geographical backcalculation model is used. Extending a more sophisticated Bayesian estimation method (*11*) that allows for stochastic variability intrinsic to epidemic dynamics and parameter uncertainty gave similar but slightly higher estimates for R_0 with wider ranges: posterior median = 1.40; 95% CrI: 1.15 to 1.90 (Fig. 1C).

Second, by assuming a prior distribution on the generation time distribution informed by previous estimates of influenza, the Bayesian coa-

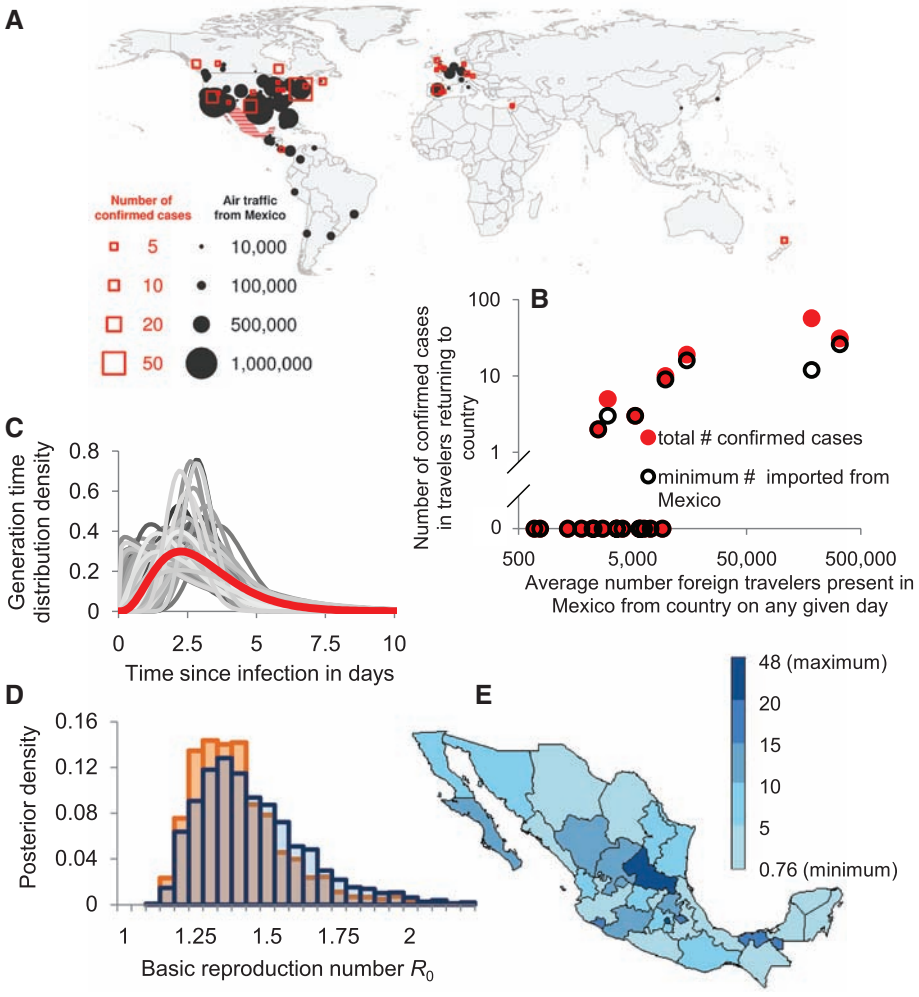

Fig. 1. (**A**). The number of passengers flying out of Mexico by actual destination and the number of confirmed cases as reported on 30 April 2009. (**B**) The number of cases exported to country j as reported on 30 April 2009 as a function of the estimated average number of foreign travelers in Mexico from country j on any given day in March or April. Black circles: minimal number based on one exposure per epidemiological cluster; filled red circles, total number of confirmed cases. (**C**) Mean assumed generation time distribution (red) and 100 illustrative draws from the prior distribution, and (**D**) corresponding posterior distribution of R_0 estimates for a stochastic model of an epidemic within Mexico with travelers infected at a rate proportional to the estimated density of travelers per local resident. The two bar charts correspond to a 7-day delay between infection and confirmation (blue) and no delay (orange) in cases among travelers. (**E**) Number of acute respiratory infection cases per 100,000 inhabitants by state as reported on 5 May 2009 (*1*), demonstrating spatial distribution of disease within Mexico.

lescent population genetic analysis yielded a second set of estimates for R_0: posterior median = 1.22; 95% CrI: 1.05 to 1.60 (Fig. 2C).

Third, R_0 can also be estimated from analysis of the dynamics of the epidemic within defined settings. Detailed data collected by the Mexican authorities investigating the La Gloria outbreak indicate that 616 individuals from a resident population of 1575 had acute respiratory infection between 15 February and 14 April 2009 (Fig. 3A). Data on the age distribution of cases and the dates of disease onset were used in our analysis. Figure 3B shows that the clinical attack rate varied markedly as a function of age, with 61% of individuals under 15 years old affected, dropping to 29% of people over that age. The corresponding relative risk is 2.13, with a 95% CI of 1.89 to 2.39. Based on all confirmed cases in Mexico as reported on 5 May 2009 (*1*), the corresponding relative risk is 1.52 (95% C I: 1.33 to 1.73). The overall community attack rates seen in La Gloria are comparable to (or higher than) those seen in previous pandemics (*12*).

Fitting alternative epidemic models to the La Gloria data (*8*) demonstrated that a model with heterogeneous mixing by age plus age-dependent susceptibility to infection was required to adequately fit the data with plausible parameter estimates. The resulting maximum-likelihood estimate of R_0 was 1.58 with a 95% CI of 1.34 to 2.04 (Table 2). This analysis also provided the only independent estimate of the mean generation time, T_g (1.91 days; 95% CI: 1.30 to 2.71 days) (Table 2), shorter than earlier estimates for influenza (*9*, *10*), though not significantly so. It is biologically plausible that R_0 and T_g could be correlated, because both are linked to the underlying replicative fitness of the virus. More data are needed. Owing to parameter identifiability issues, it was not possible to estimate age-dependent infectiousness, as well as age-dependent mixing, from these data. Although these estimates are informative, it should be emphasized that some uncertainties remain regarding the denominator population and that a range of other models may fit the data as well as the model choice shown here. Household data would be particularly useful in reducing remaining uncertainty.

Fourth, the time-dependent reproduction number (R_t) can be estimated from the time series of reported disease onsets among confirmed cases in Mexico (Fig. 4). These data are subject to much uncertainty because of marked changes in surveillance over the reporting interval, plus the nonspecificity of symptoms that are similar to existing and perhaps simultaneously circulating strains of influenza. However, we developed methods for analyzing such data (*8*) that account for substantial underreporting, with a change in the underreporting rate from 17 April when surveillance within Mexico was intensified. The average value of R_t estimated for Mexico up until the end of April was 1.37 (95% CrI: 1.24 to 1.59) for a model with Poisson case counts, and 1.47 (95% CrI: 1.21 to 1.88) for a perhaps more plausible negative binomial model allowing daily case counts to be overdispersed (*8*).

Given estimates of R_0 and the current epidemic size x, we can estimate the number of generations N_t of transmission of the virus among humans that is necessary to explain the current epidemic. Assuming a simple branching process with reproduction number R_0, the mean number of generations of transmission is given by $N_t = \ln(x/x_0)/\ln(R_0)$, assuming the epidemic was started by x_0 humans being infected from animal sources. Assuming $x_0 = 1$ gives estimates of N_t between 14 and 73. But even if we assume that 5% of cases were infected directly from animal sources, we obtain an estimated 5 to 22 generations of transmission, indicating sustained human-to-human transmission in Mexico.

All of the R_0 estimates are comparable with, but perhaps on the low end of, R_0 estimates

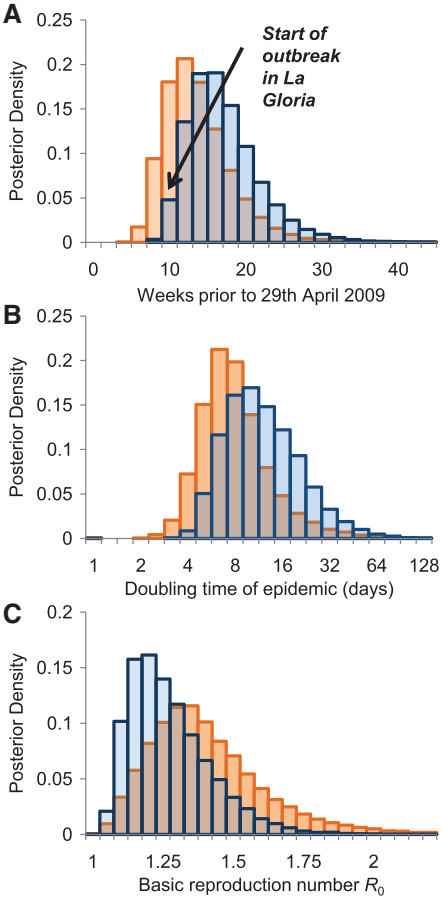

Fig. 2. (**A**) Starting from publicly available HA viral sequences, a posterior distribution of the estimated TMRCA was derived using a Bayesian coalescent model, which assumes exponential population growth (coded in BEAST 1.4), with the date of the first known human case highlighted. Details of the BEAST analysis and parameter estimates are presented in (*8*). Posterior distribution of the doubling time of the epidemic (**B**) and of R_0 (**C**). The bar charts show the results obtained from the first 11 sequences available on 2 May 2009 (orange) and from an updated analysis with 23 epidemiologically unlinked sequences available on 7 May 2009 (blue). The differences in estimates arise due to some sequences in the smaller sample being from epidemiological clusters, highlighting the importance of careful sampling.

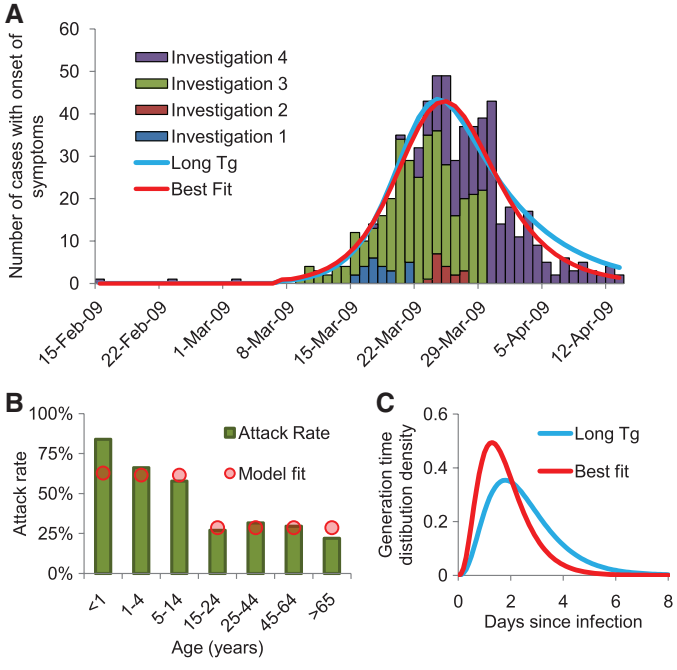

Fig. 3. Results of a detailed investigation into an outbreak in the village of La Gloria. (**A**) The time series of cases based on repeat rounds of investigation into the outbreak, and the best fit of an age-stratified transmission model (see Table 2 for estimates). The graph also shows the best fit of a model where the generation time is constrained to be consistent with earlier estimates for influenza (2.6 days), which does not fit significantly worse than the unconstrained best fit (see Table 2 legend). (**B**) Observed (bars) and fitted (using best fit, circles) age-specific attack rates; (**C**) best fit and constrained estimate of the generation time distribution.

Table 1. Parameter estimates (and 95% confidence intervals) for the cumulative number of influenza A (H1N1) infections in Mexico among Mexican residents by late April 2009, along with corresponding estimates for the case fatality ratio (CFR), the basic reproduction number, and the exponential growth rate, assuming that infections in travelers occurred in Mexico.

Assumed average duration of stay for visitors arriving by flights	Estimated number of infections among Mexican residents	Case fatality ratio*		Estimated reproduction number R_0‡	Estimated exponential growth rate‡ (doubling time in days‡)
		Assuming 9 deaths§	Assuming 101 deaths§		
Based on analysis of interval-censored country counts					
6 days	32,000 (26,000, 39,000)	0.03% (0.02%, 0.03%)	0.32% (0.26%, 0.39%)	1.42	0.123 (5.6)
9 days (*23*)	23,000 (20,000, 280,00)	0.04% (0.03%, 0.05%)	0.44% (0.37%, 0.52%)	1.40	0.118 (5.9)
12 days	180,00 (150,00, 220,00)	0.05% (0.04%, 0.06%)	0.55% (0.46%, 0.66%)	1.39	0.114 (6.1)
Based on analysis of presence or absence of confirmed disease in countries					
6 days	11,000 (5,000, 27,000)	0.08% (0.03%, 0.20%)	0.90% (0.37%, 2.20%)	1.36	0.106 (6.6)
9 days (*23*)	7,000 (3,000, 18,000)	0.12% (0.05%, 0.29%)	1.36% (0.56%, 3.30%)	1.33	0.098 (7.0)
12 days	6,000 (2,000, 14,000)	0.16% (0.07%, 0.39%)	1.81% (0.74%, 4.40%)	1.31	0.093 (7.4)

*This is a simple estimate of the CFR (*4*). The numbers of deaths and the data on cases in countries were both obtained as reported on 30 April. Although censoring is important to consider when estimating the CFR (due to the time interval between case report and death), in these data we have both the time between clinical onset and death within Mexico and the time between clinical onset and case confirmation in other countries to consider. Given uncertainty surrounding both of these distributions, we have made the simplifying assumption that these time intervals are similar and thus that the CFR can be estimated by the deaths within Mexico attributed to the novel influenza A (H1N1) divided by the estimated number of infections among Mexican residents based on data reported up to 30 April. §Based on 9 confirmed and 92 suspected deaths (101 total) that were reported by 30 April 2009 (*6*). ‡These estimates assume that the estimated cumulative number of influenza A (H1N1) infections in Mexico among Mexican residents relates to the cumulative number of infections up to 23 April 2009 (i.e., 1 week before the data were reported).

Table 2. Epidemiological parameters estimated by fitting an age-stratified mathematical model to the outbreak in the village of La Gloria (Fig. 3). For sensitivity analysis and model selection, we tested several reduced model variants. None fitted significantly worse, but several produced implausible estimates of the generation time. The respective best-fit values are as follows: 1. No asymptomatics and no misreporting, no assortative mixing: $p_{symp} \equiv 1$, $\theta \equiv 0$, $R_0 = 1.37$, $T_g = 1.39$, and $\rho_{child} = 2.80$. 2. No asymptomatics and no misreporting: $p_{symp} \equiv 1$, $R_0 = 1.41$, $T_g = 1.53$ days, $\theta = 0.31$, and $\rho_{child} = 2.22$. 3. No assortative mixing: same as variant 1. 4, model with long generation time consistent with previous estimates from influenza (also shown in Fig. 3), $T_g \equiv 2.60$ days, $R_0 = 1.97$, $\rho_{child} = 2.52$, $\theta = 0.51$, and $p_{symp} = 0.72$. (The symbol "$\equiv$" denotes parameters defined to take fixed values.)

	Best estimate	95% confidence interval	Description
R_0	1.58	1.34–2.04	Basic reproduction number
T_g	1.91	1.30–2.71	Mean generation time (days)
p_{symp}	86%	69–100%	Proportion of cases that are symptomatic and ascertained
ρ_{child}	2.06	1.60–3.31	Susceptibility of children relative to adults
θ	0.50	0.00–0.72	Assortativity of mixing between children and adults (0 = random, 1 = fully assortative)
	Assumed value		
f_L	1/3	Assumed	Fraction of the generation time that is latent (uninfectious)
ϕ_{child}	1	Assumed	Infectiousness of children relative to adults

obtained from analysis of previous pandemics [1.4 to 2.0 for 1918, 1957, and 1968 (*9*, *13*–*15*)].

Overall, our transmissibility estimates are consistent with the lowest values used in earlier detailed computer simulations used to study scenarios in pandemic mitigation (*16*, *17*), indicating that the conclusions regarding control policy effectiveness reached by those analyses could be relevant to the current epidemic. However, the key trade-off remains the balancing of the economic and societal cost of interventions, such as school closure, against the numbers of lives saved through use of such measures. Where substantial antiviral stockpiles are available, a secondary trade-off is the extent to which large-scale prophylaxis is justified, given the potential risks of high-level resistance developing (*18*–*21*). At present, estimates of disease severity are insufficiently robust to allow these trade-offs to be properly evaluated, but that uncertainty should diminish rapidly in coming weeks as more data on severe cases in the United States and other countries become available.

As the situation develops, a key issue is to optimize study designs and surveillance protocols to be most informative in estimating some of these unknown factors, thus potentially informing and refining the public health response. Clearly, detailed investigations of transmission in households and schools will be useful, as would be the consistent collection and dissemination of electronic patient records, which could be used to detect cofactors in the severity of infection.

In conclusion, while the emerging data from Mexico and other countries have enabled important insights into the origin, extent, transmissibility, and severity of the unfolding pandemic [including detailed epidemiological analysis of data from the U.S. outbreak recently published (*22*)], many uncertainties remain and should not be underestimated. The incubation and infectious periods have not yet been reliably ascertained, leaving uncertainty in estimates of the generation time. Much remains to be done to estimate clinical severity of infection, to understand regional variations seen so far (or indeed, whether they exist). As the epidemic spreads further, it is likely that severity will vary from country to country depending on health care resources and the public health measures adopted to mitigate impact. The existence of any cross-immunity (perhaps not mediated via HA-specific antibodies) from past exposure to prior influenza A subtypes is unknown, but the strong age dependence in clinical attack rates seen in La Gloria is intriguing. Cross-immunity would imply that R_0 could be higher in fully susceptible populations than estimated here.

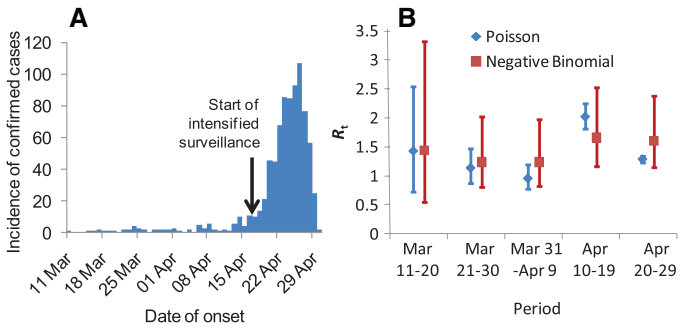

Fig. 4. (**A**) Time course of the Mexican epidemic with (**B**) the posterior estimates (median and 95% CrI) of the reproduction number over time obtained under Poisson and negative binomial models from the analysis of confirmed cases. The estimate of the negative binomial dispersion parameter k is for a low-to-moderate overdispersion, but this is enough to greatly increase the uncertainty in $R(t)$.

The future evolution of the transmissibility, antigenicity, virulence, and antiviral resistance profile of this or any influenza virus is difficult to predict. It is also unclear whether this strain will displace existing influenza A subtypes from the human population, as occurred in the past three pandemics. The extent to which seasonal damping of transmission in North America and Europe is responsible for the moderate transmissibility seen to date is uncertain; the progress of transmission in the Southern Hemisphere (which is just entering its influenza season) needs to be carefully monitored in the next few months. To reduce all these uncertainties, it is essential that public health agencies around the world continue to collect high-quality epidemiological data in a focused, resource-efficient manner despite the expected increases in case numbers in coming weeks. Epidemiological analysis and modeling are useful tools for guiding such efforts and interpreting the resulting data.

Note added in proof: We cited two sources (*1*, *6*) for confirmed and suspected deaths in Mexico, reported by 4 May 2009 and 30 April 2009, respectively. These sources are not publicly available at present. However, similar reports are publicly available: The Mexican government Web site (*24*) gives some data on the 5 May situation report (*25*) documenting 26 confirmed deaths and 114 suspected deaths (77 without samples for analysis), and *Morbidity and Mortality Weekly Report* (*26*) lists 7 confirmed and 77 suspected deaths posted on 30 April. Since this article appeared online, the number of deaths in Mexico up to 23 April has been determined to be 21, resulting in a revised estimate of the CFR of 0.091% (range: 0.066 to 0.35%) (*24*).

References and Notes

1. México Dirección General Adjunta de Epidemiología, *Brote de influenza humana A H1N1 México* (4 and 5 May 2009).
2. WHO, *Swine Influenza—Update 15* (www.who.int/csr/don/2009_05_05/en/index.html; accessed 5 May 2009).
3. W. P. Glezen, A. A. Payne, D. N. Snyder, T. D. Downs, *J. Infect. Dis.* **146**, 313 (1982).
4. A. C. Ghani *et al.*, *Am. J. Epidemiol.* **162**, 479 (2005).
5. T. D. Hollingsworth, N. M. Ferguson, R. M. Anderson, *Nat. Med.* **12**, 497 (2006).
6. Mexico Dirección General Adjunta de Epidemiología, *Brote de influenza porcina México* (30 April 2009).
7. A. J. Drummond, A. Rambaut, *BMC Evol. Biol.* **7**, 214 (2007).
8. Additional details on methods, data, and results are in the Supporting Online Material.
9. N. M. Ferguson *et al.*, *Nature* **437**, 209 (2005).
10. J. Wallinga, M. Lipsitch, *Proc. Biol. Sci.* **274**, 599 (2007).
11. M. Lipsitch *et al.*, *Science* **300**, 1966 (2003).
12. W. H. Frost, E. Sydenstricker, *Public Health Rep.* **34**, 491 (1919).
13. C. E. Mills, J. M. Robins, M. Lipsitch, *Nature* **432**, 904 (2004).
14. R. Gani *et al.*, *Emerg. Infect. Dis.* **11**, 1355 (2005).
15. C. Viboud *et al.*, *Vaccine* **24**, 6701 (2006).
16. N. M. Ferguson *et al.*, *Nature* **442**, 448 (2006).
17. T. C. Germann, K. Kadau, I. M. Longini Jr., C. A. Macken, *Proc. Natl. Acad. Sci. U.S.A.* **103**, 5935 (2006).
18. M. D. de Jong *et al.*, *N. Engl. J. Med.* **353**, 2667 (2005).
19. A. Lackenby *et al.*, *Euro Surveill.* **13** (2008); available at www.eurosurveillance.org/images/dynamic/EE/V13N05/art8026.pdf.
20. A. Moscona, *N. Engl. J. Med.* **353**, 2633 (2005).
21. S. H. Hauge, S. Dudman, K. Borgen, A. Lackenby, O. Hungnes, *Emerg. Infect. Dis.* **15**, 155 (2009).
22. Novel Swine-Origin Influenza A Virus Investigation Team, *N. Engl. J. Med.* 10.1056/NEJMoa0903810 (2009).
23. L. E. Hudman, R. H. Jackson, *Geography of Travel and Tourism* (Cengage Learning, Thomson Learning, Clifton Park, NY, ed. 4, 2002).
24. http://portal.salud.gob.mx/contenidos/noticias/influenza/estadisticas.html.
25. http://portal.salud.gob.mx/sites/salud/descargas/pdf/influenza/presentacion20090505.pdf.
26. www.cdc.gov/mmwr/preview/mmwrhtml/mm5817a5.htm.

27. We thank all those in Mexico and WHO (in particular J. Fitzner, K. Vandemaele and A. Merianos) who helped to collate the data used in this analysis. We also thank A. Borquez for help with translation and data collection and R. Eggo for data collation. We thank R. Anderson, K. Fukada, R. Hatchett, M. Lipsitch, D. Shay and L. Wolfson for useful discussions and comments. We thank the U.S. Centers for Disease Control; the Instituto de Salud Carlos III, Spain; Statens Erum Institut, Denmark; Erasmus MC Rotterdam, Netherlands; University of Regensburg, Germany; and the WHO collaborating centre for Reference and Research on Influenza, Australia, for posting viral sequences on GenBank. The work at Imperial College was funded by the Medical Research Council UK Centre grant. We also acknowledge additional support for individual staff members from the National Institute of General Medical Sciences (NIH) Models of Infectious Disease Agent Study (MIDAS) programme, The Royal Society (C.F., W.P.H., N.C.G., A.R., O.G.P.), Research Councils UK (S.C.), Bill and Melinda Gates Foundation (M.V.K., T.D.H., J.G.), The Wellcome Trust (R.F.B., grant GR082623MA), Biotechnology and Biological Sciences Research Council UK (T.J.), Microsoft Research (W.R.H.), and a studentship from the Medical Research Council (H.E.J.). GenBank accession numbers: GQ117067, FJ973557, FJ966082, FJ966952, FJ966960, FJ966974, FJ966971, FJ969511, GQ117040, FJ985753, GQ117119, FJ982430, GQ117097, GQ117059, GQ117103, GQ117112, CY039527, FJ984364, FJ984397, FJ985763, FJ974021, GQ117056, and FJ966982 for the main analysis and CY039527, FJ966082, FJ966959, FJ966960, FJ966974, FJ969509, FJ969511, FJ966952, FJ966982, FJ971076, and FJ973557 for the preliminary analysis.

Supporting Online Material

www.sciencemag.org/cgi/content/full/1176062/DC1
Methods
Figs. S1 to S3
Tables S1 to S12
References
Epidemiological data

5 May 2009; accepted 11 May 2009
Published online 11 May 2009;
10.1126/science.1176062
Include this information when citing this paper.

Rapid and Accurate Large-Scale Coestimation of Sequence Alignments and Phylogenetic Trees

Kevin Liu,[1] Sindhu Raghavan,[1] Serita Nelesen,[1] C. Randal Linder,[2] Tandy Warnow[1]*

Inferring an accurate evolutionary tree of life requires high-quality alignments of molecular sequence data sets from large numbers of species. However, this task is often difficult, slow, and idiosyncratic, especially when the sequences are highly diverged or include high rates of insertions and deletions (collectively known as indels). We present SATé (simultaneous alignment and tree estimation), an automated method to quickly and accurately estimate both DNA alignments and trees with the maximum likelihood criterion. In our study, it improved tree and alignment accuracy compared to the best two-phase methods currently available for data sets of up to 1000 sequences, showing that coestimation can be both rapid and accurate in phylogenetic studies.

Phylogeny estimation from molecular sequences typically has two phases: An alignment is estimated, and then a tree is produced for the alignment. Alignment methods like MAFFT (*1*), Probcons (*2*), Probtree (*3*), Prank (*4*), and Muscle (*5*) provide more accurate alignments than earlier methods (*3*, *4*, *6*), and maximum likelihood (ML) methods of phylogeny estimation [e.g., RAxML (*7*, *8*), GARLI (*9*), and Phyml (*10*)] produce more accurate trees for large data sets than other

phylogeny estimation methods (*10*). Still, estimation of phylogenies and alignments for large data sets is difficult and highly inaccurate when the sequences examined for phylogenetic reconstruction have evolved with many substitutions and insertions and deletions (indels).

Alignment estimation methods typically estimate guide trees on which an alignment is then produced. The methods can be highly sensitive to the guide tree (*3*), and automated alignments often require manual realignment, sometimes necessitating months of intensive analysis of the sequences and taxa (*11*, *12*). Manual realignment can be error prone due to limitations in alignment editors; the inability of an individual to view all the sequences simultaneously; or idiosyncratic, unstated realignment criteria. Also, hard-to-align DNA regions that might contain phylogenetically useful information may be rejected due to a lack of confidence in the alignments. Finally, regions that are hard to align are typically aligned differently by different programs, and phylogenies estimated on these different alignments can differ substantially (*13*). Consequently, molecular phylogenies often are produced using slowly evolving DNA regions that can be aligned relatively easily. Restriction to such regions likely has resulted in less fully resolved evolutionary histories for many groups due to underutilization of data.

Current methods for estimating trees directly from unaligned sequences include POY (*14*), POY* (*15*), ALIFRITZ (*16*), BAli-Phy (*17*), and the method of Lunter *et al*. (*18*), while SATCHMO (*19*) can be used for estimating trees directly from amino acid sequences. These methods potentially circumvent some of the aforementioned issues, but have limitations of their own. POY and POY* can be run on large data sets but have not produced trees more accurate than those of the best two-phase methods (*15*, *20*). The other methods are based on parametric statistical models of sequence evolution including substitutions and indels. ALIFRITZ and BAli-Phy use models that allow multinucleotide indel events, engendering large computational burdens. A study assessing their performance (*21*) found that ALIFRITZ could analyze ~30 sequences, and BAli-Phy was limited to 10. Our studies of these methods on 100 taxon data sets (tables S28 and S29) showed that after 2 weeks of analysis, although BAli-Phy and ALIFRITZ were able to produce trees and alignments on some data sets, their trees were not as accurate as those produced by the best two-phase methods. A method that includes only single-nucleotide indel events (*18*) was reported to analyze data sets with 50 sequences (*21*); however, our attempts to test this method (fig. S4) revealed that the current implementation is not operational.

We present SATé (simultaneous alignment and tree estimation), a program designed to address current speed and accuracy limitations in phylogenetic analysis (available at www.cs.utexas.edu/users/tandy/science-paper.html). To make large-scale coestimation of trees and alignments feasible, we used a maximum likelihood rather than a Bayesian approach, with gaps treated as missing data. These choices improved scalability over ALIFRITZ and BAli-Phy, while improving accuracy over two-phase methods on large, hard-to-align data sets.

SATé searches for a tree/alignment pair with an optimal ML score by performing hill-climbing searches from a collection of starting tree/alignment pairs. For each starting alignment, SATé estimates

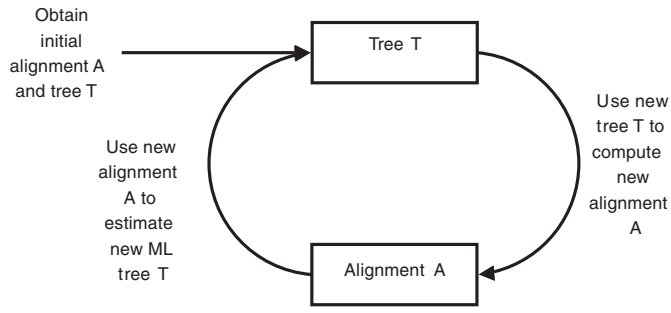

Fig. 1. SATé's second stage. Beginning with the current best tree/alignment pair, SATé iterates between realigning on the current tree and estimating a RAxML tree for each new alignment. At the end of each iteration, the tree/alignment pair optimizing ML under the GTR+Gamma model of evolution is saved.

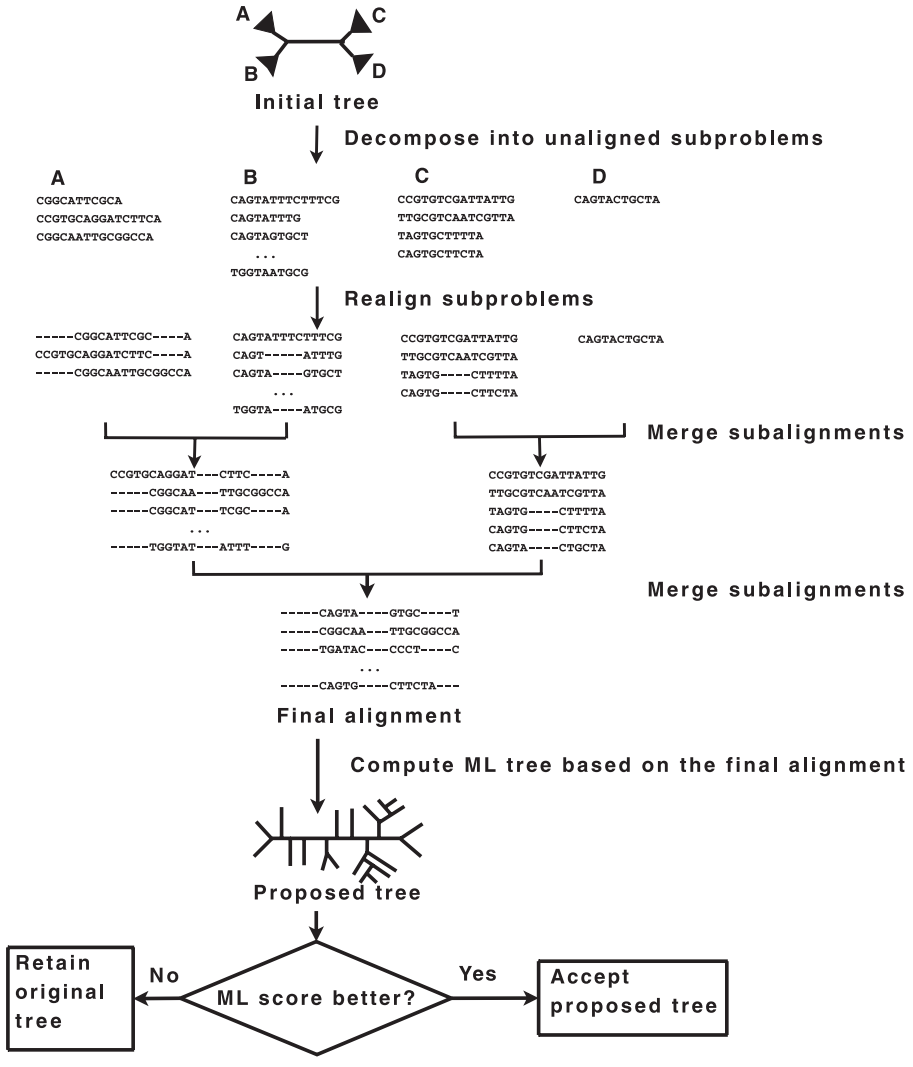

Fig. 2. SATé's divide-and-conquer strategy, illustrated with a CT-2 decomposition. A branch in the initial tree is selected, and the subtrees—A, B, C, D—around the branch are determined. The sequences for each of the four subtrees are realigned by MAFFT. These realigned subproblems are then aligned with one another, two at a time, using Muscle, until an alignment on the full data set is obtained. RAxML then computes a tree on the alignment. SATé iterates this process, as shown in Fig. 1.

[1]Department of Computer Sciences, The University of Texas at Austin, One University Station C0500, Austin, TX 78712, USA. [2]Section of Integrative Biology, School of Biological Sciences, The University of Texas at Austin, One University Station C0930, Austin, TX 78712, USA.

*To whom correspondence should be addressed. E-mail: tandy@cs.utexas.edu

an ML tree (general time reversible + gamma model) with RAxML. The "second stage" then uses an iterative, greedy search heuristic to find tree/alignment pairs with better ML scores (Fig. 1). In each iteration, a new alignment is proposed by our divide-and-conquer method: Center-Tree-*i* (CT-*i*) decomposition (Fig. 2). The default setting runs stage 2 for 24 hours, allowing the final iteration begun before the 24-hour limit to complete. The user can specify the stopping criterion, e.g., time limits or until no improvement in the ML score has occurred for 24 hours. If two or more starting tree/alignment pairs are used, the final tree/alignment pairs from each run are compared, and the one with the best ML score is returned.

For a CT-*i* decomposition, SATé computes a bifurcating tree with maximum diameter $2i - 1$ around a branch selected in the current best tree. The branch is typically either a midpoint branch (the middle branch on a longest path in the tree) or a centroid branch, which splits the tree into two subtrees with roughly equal numbers of taxa. A CT-*i* decomposition produces at most 2^i subsets, which are clades in the current tree (see Fig. 2 and Supporting Online Material for examples), where i is user-specified (default: $i = 5$), allowing the number and size of subproblems to be tuned for the number of taxa in the full data set. Sequences in each subset are realigned (default = MAFFT), and the alignments are progressively merged (default = Muscle), using the current tree as a guide tree, into an alignment on the full data set. An ML tree is estimated on the new alignment with RAxML. The tree/alignment pair with the better ML score (either the original pair or the new pair) is then used for the next iteration.

To determine the best defaults and options for SATé, we explored multiple combinations of the algorithmic parameters (*22*). We observed that CT-5 decompositions performed reliably well, and that starting with a tree/alignment pair having a good ML score improved SATé's convergence rate, but that SATé was robust to the choice of starting alignment/tree pairs (figs. S7 to S10 and tables S20, S21, and S28).

Two variants of SATé performed particularly well. The first, SATé^{24}, was fast and produced highly accurate alignments and trees. For its starting alignment/tree pair, SATé^{24} selects among four tree/alignment pairs by running RAxML on four alignments [ClustalW (*23*), Muscle, MAFFT, and Prank+GT, which is Prank provided with a RAxML-on-MAFFT guide tree] and picks the pair with the best ML score on its tree. SATé^{24} then uses its hill-climbing strategy for 24 hours to search for better solutions. The second variant, SATé^{BML}, was slower but produced more accurate alignments and trees than the first. It uses two starting alignment/tree pairs (the ClustalW alignment and its RAxML tree, and the pair used by SATé^{24}), lets each of the hill-climbing SATé analyses run until no change has occurred for 24 hours, and returns the solution with the best ML score.

We tested these SATé variants on both simulated and biological data sets, relative to the alignment methods ClustalW, MAFFT, Muscle, and Prank+GT, and to RAxML, run to completion.

For the simulation studies, we compared SATé^{24} to the two-phase methods, using ROSE (*24*) to simulate sequence evolution under 30 models (20 replicates per model, root sequences of 1000 base pairs, trees of 500 and 1000 taxa) representing a wide range of conditions (tables S1 to S3). We used ROSE's output to determine the true alignment for each data set and the model-tree branches on which no changes occurred (zero-event branches). We used the true alignment to calculate SP-FN alignment error rates. SP-FN is the sum of pairs for the false-negative error rate: the percentage of evolutionarily homologous pairs of nucleotides missing in the estimated alignment and the complement of the SP accuracy measure (*25*). We contracted zero-event branches of the model trees—because reconstruction of these branches is effectively random (*26*)—producing potentially inferable model trees (PIMTs). We used the PIMTs to quantify the percentage of branches missing from an estimated tree but present in the PIMT (the missing branch rate).

RAxML runs on the true alignment consistently produced a low proportion of missing branches

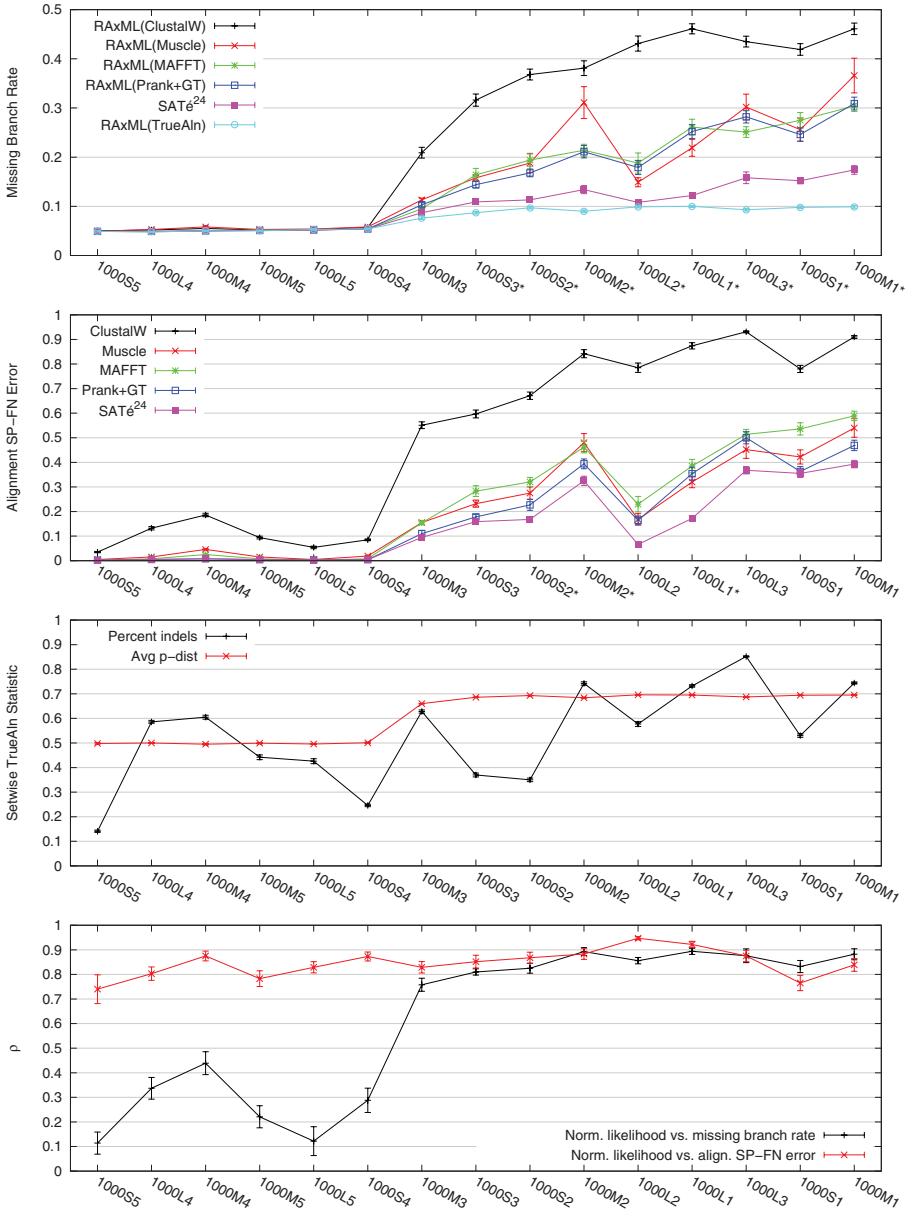

Fig. 3. The 1000-taxon model results. All *x* axes show the 15 1000-taxon models, from easy to hard, based on missing branch rates. From top-to-bottom panels, the *y* axes are missing branch rate, alignment SP-FN error, true alignment setwise statistics, and Spearman rank correlation coefficients (ρ). All data points include SE bars. For the top two panels, models on the *x* axis followed by an asterisk indicate that SATé's performance was significantly better than the nearest two-phase method (paired *t* tests, setwise $\alpha = 0.05$, $n = 40$ for each test).

(averaging 7.4% overall), even when run on models whose true alignments contained high proportions of indels and high substitution rates (Fig. 3 and fig. S6), indicating that treating indels as missing data introduced minimal error in tree estimation, even for data sets containing many indels. SATé[24]'s missing branch rates (averaging 9.1% overall) were only somewhat higher than those obtained by RAxML on the true alignment (Table 1). By comparison, the overall average missing branch rates for RAxML trees produced on estimated alignments were 12.6% for MAFFT, 13.0% for Prank+GT, 15.3% for Muscle, and 21.6% for ClustalW (Table 1). On these data sets, runtimes for SATé[24]'s second stage were at most 28 hours for 500 taxa and 34 hours for 1000 taxa (table S9).

We labeled some models "easy" because all methods produced trees with accuracy close to that of RAxML on the true alignment (Fig. 3 and fig. S6). For the remaining "moderate-to-difficult" models (Table 1, Fig. 3, and fig. S6), SATé[24] produced the most accurate trees and alignments, ClustalW produced the least, and the other methods were intermediate. SATé[24]'s missing branch rates on the moderate-to-difficult models were significantly better than those produced by the closest two-phase method in all cases ($P \leq 0.004$; paired t test) except that of model 1000M3, whose performance was similar to that obtained by running RAxML on a MAFFT alignment (Fig. 3 and table S13). For all methods, missing branch rates and alignment error rates tended to increase as the number of taxa (Table 1) or rate of evolution increased (Fig. 3); however, SATé[24]'s error rates generally increased much less than those of the other methods. Thus, SATé[24] provided the largest advantage on the hardest data sets. SATé[24]'s worst average missing branch rate (17.4%) was on model 1000M1, on which all other methods had error rates >30% (Fig. 3). Furthermore, SATé[24] achieved these performance gains on standard desktop computers with 4 GB of RAM.

Because tree error may increase when unreliable sites are included, we estimated ML trees on data sets from which sites were eliminated using four techniques [including two variants of Gblocks (*27*)]. These techniques either had little impact on tree estimation accuracy or made the estimations worse (tables S31 to S34).

SATé[24]'s improved tree/alignment accuracy arose from its divide-and-conquer strategy and use of the ML criterion. The CT-5 decomposition improved starting alignments and trees on the moderate-to-difficult models (table S11) and modified (without necessarily improving) them on the easy models (table S12). The ML score was positively correlated with alignment and tree accuracy across all models, especially the moderate-to-difficult models (Fig. 3, fig. S6, and tables S14 and S15). Furthermore, even when SATé[24] proposed alignments that were accepted but resulted in trees of reduced accuracy, the average reduction in alignment or tree accuracy was at most 0.5% (table S11).

SATé sometimes found better trees and alignments with different starting tree/alignment pairs (figs. S7 and S9 and table S28). Therefore, we recommend multiple runs of SATé using more than one starting pair, e.g., using SATé[BML] if time permits.

We compared SATé[BML] to the two-phase methods on six biological ribosomal RNA data sets (117 to 1028 taxa; table S7) for which highly reliable, curated alignments are available. SATé[BML] and MAFFT alignments were of comparable accuracy and better than the other alignments (table S18), and SATé[BML] trees were more accurate than those produced by any two-phase method (table S19).

Thus, SATé is a fast, effective, and fully automated method for simultaneous estimation of trees and alignments for nucleotide sequences on large numbers of taxa. For rapidly evolving sequences, it dramatically speeds and improves tree and alignment estimations compared to the best current two-phase methods, and it removes or significantly reduces the need for hand realignment of data sets. Finally, it makes possible the use of DNA regions previously rejected for alignment difficulty, potentially leading to significantly improved resolution of species' relationships.

Table 1. Missing branch rates and alignment SP-FN error rates. For each statistic and model, the best-performing methods (within 1%) are in boldface. The best overall is indicated with an asterisk (*). For each "All models" entry, $n = 600$; for each easy entry, $n = 120$; for each moderate-to-difficult entry, $n = 180$.

Method	All models	Moderate to difficult		Easy	
		1000	500	1000	500
	% (SE)	% (SE)	% (SE)	% (SE)	% (SE)
Missing branch rate					
RAxML(TrueAln)	7.4 (0.1)	9.3 (0.1)	8.4 (0.1)	5.1 (0.1)	5.3 (0.1)
SATé	***9.1** (0.2)	***13.1** (0.3)	***10.4** (0.2)	***5.1** (0.1)	**5.4** (0.1)
RAxML(Prank+GT)	13.0 (0.3)	21.0 (0.6)	15.2 (0.4)	***5.1** (0.1)	***5.3** (0.1)
RAxML(MAFFT)	12.6 (0.4)	21.6 (0.6)	13.5 (0.3)	***5.1** (0.1)	***5.3** (0.1)
RAxML(Muscle)	15.3 (0.5)	22.9 (1.0)	20.5 (0.9)	**5.4** (0.1)	**5.8** (0.1)
RAxML(ClustalW)	21.6 (0.6)	38.7 (0.7)	21.6 (0.6)	**5.3** (0.1)	**5.7** (0.1)
Alignment SP-FN error rate					
SATé	***14.2** (0.6)	***25.0** (1.3)	***21.3** (0.7)	***0.4** (0.02)	***1.0** (0.1)
Prank+GT	18.5 (0.8)	30.6 (1.2)	29.9 (1.1)	***0.4** (0.02)	**1.1** (0.1)
MAFFT	20.6 (0.8)	38.6 (1.3)	28.5 (1.0)	**0.9** (0.1)	**1.7** (0.1)
Muscle	22.7 (0.9)	34.0 (1.4)	38.5 (1.5)	1.8 (0.1)	2.9 (0.2)
ClustalW	46.9 (1.3)	77.1 (1.1)	64.1 (1.2)	9.8 (0.5)	12.9 (0.6)

References and Notes

1. K. Katoh, K. Kuma, H. Toh, T. Miyata, *Nucleic Acids Res.* **33**, 511 (2005).
2. C. B. Do, M. Mahabhashyam, M. Brudno, S. Batzoglou, *Genome Res.* **15**, 330 (2005).
3. S. Nelesen, K. Liu, D. Zhao, C. R. Linder, T. Warnow, *Pac. Symp. Biocomput.* **13**, 25 (2008).
4. A. Loytynoja, N. Goldman, *Proc. Natl. Acad. Sci. U.S.A.* **102**, 10557 (2005).
5. R. C. Edgar, *BMC Bioinformatics* **5**, 113 (2004).
6. R. C. Edgar, S. Batzoglou, *Curr. Opin. Struct. Biol.* **16**, 368 (2006).
7. A. Stamatakis, *Bioinformatics* **22**, 2688 (2006).
8. A. Stamatakis, in *Proc. 20th IEEE International Parallel and Distributed Processing Symposium*, Rhodes Island, Greece, 25 to 29 April 2006 (IEEE Computer Society, Los Alamitos, CA, 2006), pp. 278–285.
9. D. Zwickl, GARLI download page (2006); project Web site at www.zo.utexas.edu/faculty/antisense/Garli.html.
10. S. Guindon, O. Gascuel, *Syst. Biol.* **52**, 696 (2003).
11. L. Goertzen, J. Cannone, R. Gutell, R. Jansen, *Mol. Phylogenet. Evol.* **29**, 216 (2003).
12. Early Bird ATOL Project, (2007); project Web site at www.fieldmuseum.org/research_collections/zoology/zoo_sites/early_bird/.
13. K. M. Wong, M. A. Suchard, J. P. Huelsenbeck, *Science* **319**, 473 (2008).
14. A. Varón, L. S. Vinh, I. Bomash, W. C. Wheeler, POY Software (2007). Documentation by A. Varón *et al*. Available for download at research.amnh.org/scicomp/projects/poy.php.
15. K. Liu, S. Nelesen, S. Raghavan, C. Linder, T. Warnow, *IEEE/ACM Trans. Comput. Biol. Bioinform.* **6**, 7 (2009).
16. R. Fleissner, D. Metzler, A. von Haeseler, *Syst. Biol.* **54**, 548 (2005).
17. B. D. Redelings, M. Suchard, *Syst. Biol.* **54**, 401 (2005).
18. G. Lunter, I. Miklós, A. Drummond, J. L. Jensen, J. Hein, *BMC Bioinformatics* **6**, 83 (2005).
19. R. C. Edgar, K. Sjolander, *Bioinformatics* **19**, 1404 (2003).
20. T. Heath Ogden, M. S. Rosenberg, *Syst. Biol.* **55**, 314 (2006).
21. G. Lunter, A. Drummond, I. Miklós, J. Hein, in *Statistical Methods in Molecular Evolution (Statistics for Biology and Health)*, R. Nielsen, Ed. (Springer, Berlin, 2005), pp. 375–406.
22. Materials and methods are available as supporting materials on *Science* Online.
23. J. D. Thompson, D. Higgins, T. Gibson, *Nucleic Acids Res.* **22**, 4673 (1994).
24. J. Stoye, D. Evers, F. Meyer, *Bioinformatics* **14**, 157 (1998).
25. J. D. Thompson, F. Plewniak, O. Poch, *Bioinformatics* **15**, 87 (1999).
26. R. Desper, O. Gascuel, *Mol. Biol. Evol.* **21**, 587 (2004).
27. G. Talavera, J. Castresana, *Syst. Biol.* **56**, 564 (2007).

28. This research was supported by the U.S. NSF under grants DEB 0733029, ITR 0331453, ITR 0121680, EIA 0303609, and IGERT 0114387. The simulated and biological data sets, true and curated alignments, PIMTs, and all software are available at www.cs.utexas.edu/users/tandy/science-paper.html.

Supporting Online Material

www.sciencemag.org/cgi/content/full/324/5934/1561/DC1
Materials and Methods
SOM Text
Figs. S1 to S10
Tables S1 to S34
References

22 January 2009; accepted 30 April 2009
10.1126/science.1171243

Structure and Mechanism of an Amino Acid Antiporter

Xiang Gao,[1,2]* Feiran Lu,[1,2]* Lijun Zhou,[1,2]* Shangyu Dang,[1,2] Linfeng Sun,[1,2] Xiaochun Li,[1,2] Jiawei Wang,[1,2] Yigong Shi[2,3]†

Virulent enteric pathogens such as *Escherichia coli* strain O157:H7 rely on acid-resistance (AR) systems to survive the acidic environment in the stomach. A major component of AR is an arginine-dependent arginine:agmatine antiporter that expels intracellular protons. Here, we report the crystal structure of AdiC, the arginine:agmatine antiporter from *E. coli* O157:H7 and a member of the amino acid/polyamine/organocation (APC) superfamily of transporters at 3.6 Å resolution. The overall fold is similar to that of several Na^+-coupled symporters. AdiC contains 12 transmembrane segments, forms a homodimer, and exists in an outward-facing, open conformation in the crystals. A conserved, acidic pocket opens to the periplasm. Structural and biochemical analysis reveals the essential ligand-binding residues, defines the transport route, and suggests a conserved mechanism for the antiporter activity.

Enteric bacteria, including *Shigella*, *Salmonella*, *Yersinia*, and *Escherichia coli* strain O157:H7, are among the most virulent pathogens (*1*). To survive the extremely acidic environment (pH 2 to 3) of the stomach, these bacteria have acquired elaborate systems to maintain a higher intracellular pH (*2*). In *E. coli*, the acid-resistance systems 2 (AR2) and 3 (AR3) expel intracellular protons through two coupled processes: intracellular decarboxylation of glutamate (Glu) and arginine (Arg) by AR2 and AR3, respectively, and the exchange of the reaction products, γ-aminobutyric acid (GABA) and agmatine (Agm), with extracellular Glu and Arg (*2*). The Glu:GABA antiporter GadC (*3*, *4*) and the Arg:Agm antiporter AdiC (*5*, *6*) are at the center of the systems.

AdiC and GadC are members of the amino acid/polyamine/organocation (APC) superfamily [transporter class (TC) no. 2.A.3] of membrane transporters, which has at least 250 members in diverse organisms (*7*, *8*). AdiC shares considerable sequence similarity with GadC; the lysine:cadaverine antiporter, CadB (*9*, *10*); and the ornithine:putrescine antiporter, PotE (*11*–*13*). AdiC couples the influx of Arg with the efflux of Agm, resulting in net expulsion of one proton for each transport cycle (*5*, *14*). Recombinant AdiC is a homodimer in both detergent micelles and lipid mem-

[1]State Key Laboratory of Bio-membrane and Membrane Biotechnology, Tsinghua University, Beijing 100084, China. [2]Center for Structural Biology, Department of Biological Sciences and Biotechnology, Tsinghua University, Beijing 100084, China. [3]School of Medicine, Tsinghua University, Beijing 100084, China.

*These authors contributed equally to this work.
†To whom correspondence should be addressed. E-mail: shi-lab@tsinghua.edu.cn

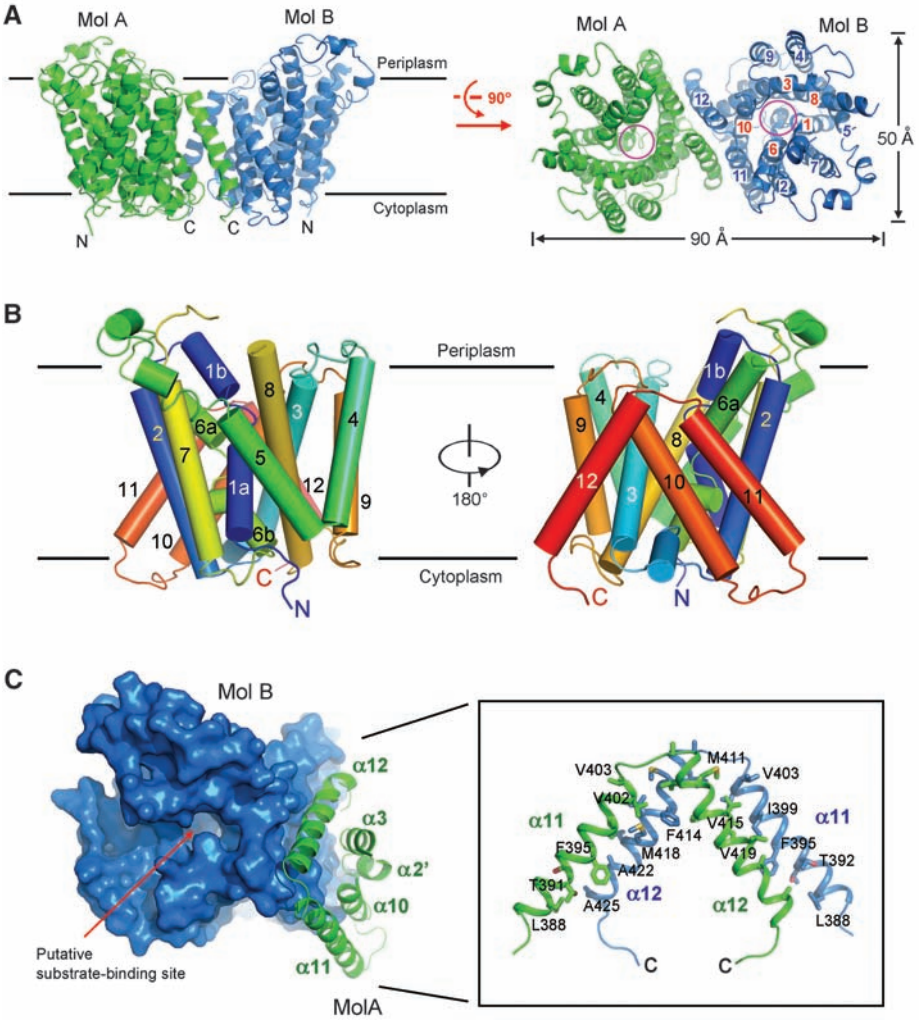

Fig. 1. Structure of AdiC, an amino acid antiporter of the APC superfamily. (**A**) Structure of the AdiC homodimer in an asymmetric unit in the $P2_12_12_1$ space group. Two perpendicular views are shown. Each molecule of AdiC consists of an inner layer of five TMs (red labels) and an outer layer of seven TMs (blue labels). The magenta circles indicate the location of the central cavity in AdiC. (**B**) A close-up view of an AdiC protomer. Note that TM1 and TM6 each consists of two α-helical segments that are connected by short, conserved sequence loops. (**C**) Dimerization interface of AdiC. Homodimerization is mediated mainly by TM11 and TM12. Specific amino acids that contribute to homodimerization are labeled in the right-hand image (*30*). The central cavity is thought to be the substrate-binding site. [Figures 1 to 3 were prepared with use of PyMol (*31*)]

branes and facilitates Arg:Agm exchange between pH 4 and 8 (*8*, *15*). The available structural information on the APC superfamily is limited to low-resolution structures of AdiC (*8*) and another protein (*16*), which were derived from electron crystallography and electron microscopy, respectively.

We purified recombinant AdiC as described (*15*, *17*). After screening more than 800 crystals in several space groups, we achieved a diffraction limit of 3.6 Å resolution for crystals grown in the $P2_12_12_1$ space group. The structure was determined by osmium-based, single-wavelength anomalous dispersion (SAD) (table S1 and fig. S1). Sequence assignment was facilitated by difference Fourier analysis of SeMet-labeled (where Met indicates methionine) protein (fig. S2). Each asymmetric unit contains two molecules of AdiC, which form a homodimer, with a pseudo-twofold symmetry axis perpendicular to the lipid membrane (Fig. 1A). We also solved the structure of AdiC in the *P*1 space group, which contains four molecules in an asymmetric unit (table S1 and fig. S3). These four molecules are organized into two homodimers, each with the same structure as that in the $P2_12_12_1$ space group (fig. S3). For simplicity, we only discuss one AdiC homodimer.

Despite lack of sequence similarity, AdiC exhibits the same fold as that of the Na^+-coupled symporters, including $LeuT_{Aa}$ of the neurotransmitter sodium symporter (NSS) family (*18*), BetP of the betaine/chlorine/carnitine transporters (BCCT) family (*19*), vSGLT of the sodium solute symporter (SSS) family (*20*), and Mhp1 of the nucleobase-cation-symport-1 (NCS1) family (*21*). This finding confirms an earlier prediction (*22*). Each molecule of AdiC has 12 transmembrane segments (TMs), arranged in two layers (Fig. 1 and fig. S4). The inner layer, containing TM1, TM3, TM6, TM8, and TM10, is surrounded by the outer layer, consisting of TM2, TM4, TM5, TM7, TM9, TM11, and TM12 (Fig. 1, A and B). Similar to the Na^+-coupled symporters (*18*–*21*), TM1 to TM5 are structurally related to TM6 to TM10 (fig. S5), with a root mean square deviation of 3.7 Å over 116 Cα atoms. Each AdiC molecule contains a centrally located cavity, which opens to the periplasmic side (Fig. 1, A and C).

As in the Na^+-coupled symporters (*18*–*21*), TM1 and TM6 are disrupted by short, nonhelical, Gly-containing loops (Fig. 1B). Amino acids in these loops are highly conserved within distinct families of the APC superfamily. For example, AdiC, CadB, and PotE, which all belong to the basic amino acid:polyamine antiporter (APA) family (*7*), share two signature loop sequences, the GSG motif (Gly^{25}-Ser^{26}-Gly^{27}) in TM1 and the GVESA motif (Gly^{206}-Val-Glu-Ser-Ala^{210}) in TM6 (fig. S4). The discontinuity of transmembrane helices has also been observed in other classes of transporters (*23*), including the Ca^{2+}–adenosine triphosphatase (ATPase) (*24*), the H^+/Cl^- exchanger CLC (*25*), the Na^+/H^+ exchanger NhaA (*26*), and the glutamate and aspartate transporter Glt_{Ph} (*27*, *28*). The unwound helices expose ordered carbonyl and amide groups, which may facilitate interactions with the substrate (*23*) and aid conformational switches required for substrate transport (*29*).

The homodimeric interface of AdiC involves four TMs from each molecule. Hydrophobic amino acids from TM11 of one AdiC molecule interdigitate with nonpolar residues from TM12 of the adjacent molecule (Fig. 1C). Additional interactions are mediated by the N-terminal portion of TM3 and the C-terminal portion of TM10. Comparison with the Na^+-coupled symporters (*18*–*21*) suggests that dimerization mediated by TM11 and TM12 may be unique to the APC superfamily.

Among TMs of the inner layer, TM6 appears to exhibit the largest degree of conformational difference among AdiC and the four Na^+-coupled symporters (fig. S6). The N-terminal backbone of TM6 in AdiC is shifted by 5, 9, and 14 Å, respectively, relative to the corresponding structural elements in $LeuT_{Aa}$, BetP, and vSGLT. TM10 also displays marked conformational variations among these transporters (fig. S6). This analysis suggests that TM6 and TM10 might play an important role in the transport process. Supporting this analysis, TM6 contributes to substrate binding in all four Na^+-coupled symporters (*18*–*21*), and TM10 was proposed to control substrate access to the periplasm (*21*).

Amino acids that are invariant among AdiC, CadB, and PotE, three APA family antiporters (*7*), were mapped onto the structure of AdiC (Fig. 2A). About a third of the conserved, polar or charged amino acids are clustered in the central cavity and its vicinity, making the central cavity the most conserved area in the entire molecule (Fig. 2B) and suggesting that it may be the substrate-binding site. The central cavity measures about 20 Å in depth and 5 to 10 Å in diameter. The bottom of the cavity is defined by four polar or charged amino acids: Asn^{22} at the C-terminal end of TM1a, Tyr^{93} in the middle of TM3, Glu^{208} at the breakage point of TM6, and Tyr^{365} in the middle of TM10 (Fig. 2B). The surface of the

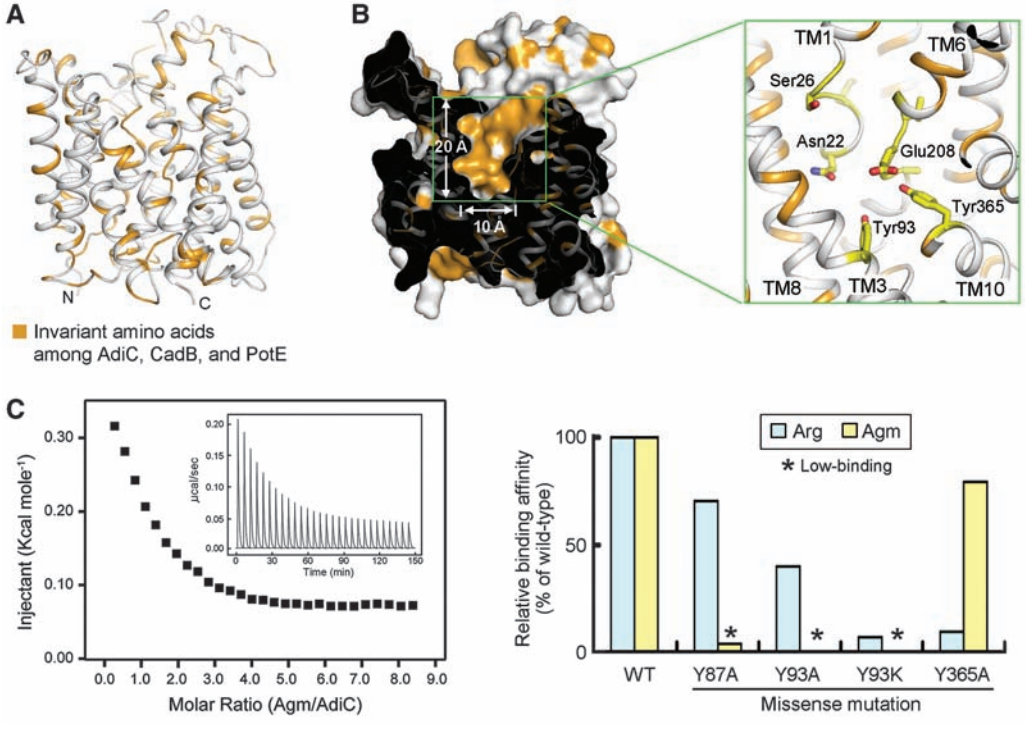

Fig. 2. Identification and features of the substrate-binding site. (**A**) Mapping conserved amino acids onto the structure of AdiC. Amino acids that are invariant among AdiC, CadB, and PotE are colored orange. (**B**) Identification of a putative substrate-binding site. The central cavity of AdiC is enriched with conserved amino acids, opens to the periplasm, and is likely the binding site for substrate (left). A close-up view shows a number of polar and charged amino acids, including Asn^{22} and Ser^{26} from TM1, Tyr^{93} from TM3, Glu^{208} from TM6, and Tyr^{365} from TM10. (**C**) Substrate binding by AdiC as measured by ITC. (Left) A representative ITC experiment, in which Agm was titrated into a solution of AdiC. (Inset) The original titration traces. (Right) The relative binding affinities for four AdiC mutants (*30*) compared with that of the WT protein. The association constant for the WT protein was standardized as 100%. Asterisks indicate three cases of low-affinity binding for Agm, where, despite readily detectable binding, curve fitting was difficult.

cavity is lined by a number of invariant residues, including the GSG motif from TM1; Tyr[87] and Tyr[101] from TM3; Val[217], Asn[219], and the GVESA motif from TM6; Cys[286], Ser[289], Leu[290], and Trp[293] from TM8; and Val[358] from TM10 (fig. S4). The negative electrostatic potential of the central cavity may contribute to binding of the positively charged substrate molecules such as Arg and Agm (fig. S7).

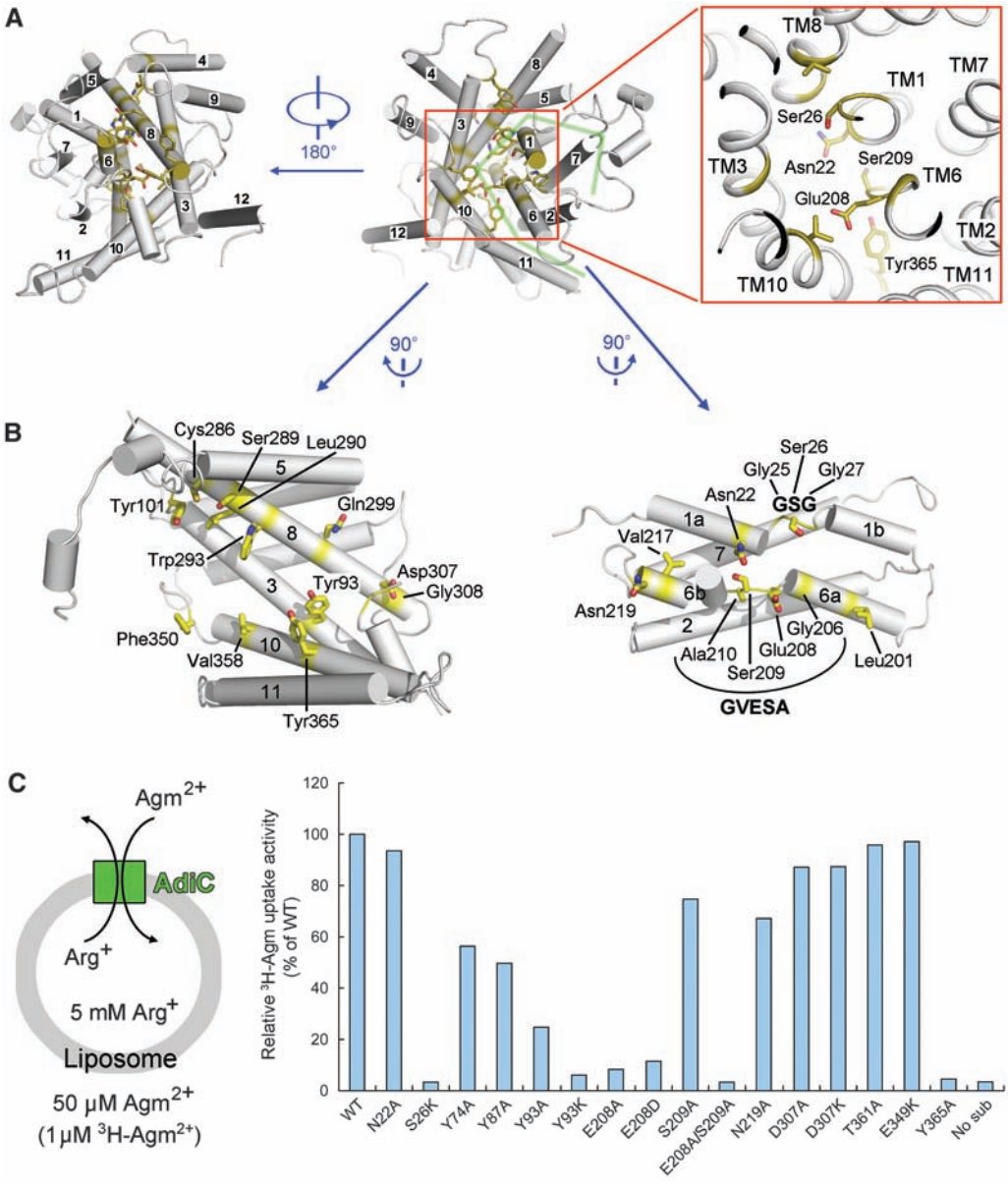

Fig. 3. Identification and features of the transport route. (**A**) Substrate transport route along the central axis. The putative transport route is identified by residues (colored yellow) that are invariant among AdiC, CadB, and PotE. The cytoplasmic and periplasmic sides of the route are depicted in the left and middle images, respectively. The right image highlights a few key residues. (**B**) Composition of the amino acids along the transport route. The structure of AdiC is separated into two portions to show all 25 highly conserved amino acids along the transport route, of which 60% are polar or charged. (**C**) Characterization of the antiport activity for WT and mutant AdiC. The left image depicts the assay. Uptake of ^{3}H-labeled Agm into the AdiC-incorporated liposome was monitored. The right graph summarizes the result. The values shown represent the average of three independent experiments. The standard deviations were estimated to be 10 to 15% of the values shown.

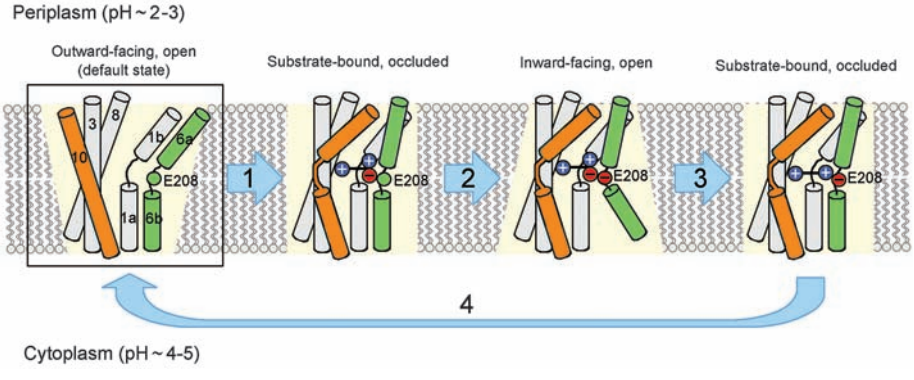

Fig. 4. A working model for AdiC and the APA family of antiporters. The antiport activity of AdiC may involve four sequential steps. The default state is likely to be the current structure, in an open, outward-facing conformation. Step 1, substrate binding to the antiporter results in occlusion of primary substrate to the periplasm. Step 2, the antiporter switches to an open, inward-facing conformation, where Arg is competitively displaced by Agm. Step 3, the antiporter bound to the secondary substrate closes down and occludes the substrate from the cytoplasm. Step 4, the antiporter opens up to the periplasm, allowing the release of the secondary substrate, completing the antiport cycle. Under extremely acidic conditions such as the stomach, Glu[208] is proposed to be the sensor amino acid in AdiC, which remains protonated at periplasmic pH but undergoes deprotonation at cytoplasmic pH. Differences in protonation states are proposed to contribute to differential binding of primary and secondary substrates. TM6 and TM10 are thought to undergo conformational changes in response to substrate binding.

To characterize the role of the conserved amino acids, we generated a number of missense mutations and evaluated their impacts on substrate binding by using isothermal titration calorimetry (ITC). As previously reported (*8*, *15*), substrate binding by AdiC is endothermic (Fig. 2C, left). The association constant (K_a) was estimated by curve fitting, and AdiC interacts with Agm with a K_a value that is about eight times higher than that for Arg (*8*, *15*). To facilitate comparison, we represented K_a values of the mutant proteins as a percentage of that for the wild-type (WT) AdiC (Fig. 2C, right). The mutation Y93K (*30*), at the bottom of the cavity, nearly crippled binding to both Arg and Agm. Y87A, on the cytoplasmic side, markedly reduced binding affinity for Agm but not for Arg. This observation is consistent with the antiporter function of AdiC: transporting Arg into, while expelling Agm out of, the cytoplasm. In contrast, Y365A, at the bottom of the cavity, markedly weakened binding to Arg but not to Agm (Fig. 2C). This analysis confirms the central cavity as the substrate-binding site and identifies key residues that are involved in binding to Arg and Agm. The observation that binding to Arg and Agm was simultaneously affected by mutations of Tyr^{93} suggests that the binding site for Arg may at least partially overlap with that for Agm.

A number of conserved, polar amino acids are located below the substrate-binding cavity and along the central axis (Fig. 3, A and B), which likely constitute the route of transport. We generated a number of missense mutations in the putative transport route and evaluated their impacts on the antiporter activity of AdiC by monitoring the uptake of ^{3}H-labeled Agm in an in vitro proteoliposome-based transport assay (*8*, *15*) (Fig. 3C, left). In the absence of substrate (Arg) in the liposome, the uptake of ^{3}H-labeled Agm was at background level (Fig. 3C, right). The WT AdiC showed robust antiport activity, with a transport rate of about 60 μmoles per mg of AdiC within the first 5 min. This transport rate is very similar to that reported previously (*15*). Four mutations, S26K, Y93K, E208A, and Y365A (*30*), which affect amino acids at the bottom of the substrate-binding site, led to abrogation of antiport activity (Fig. 3C). Consistent with this finding, Y93K exhibited crippled binding to Arg and Agm, and Y365A had markedly reduced binding affinity for Arg (Fig. 3D). Y87A and Y93A, each exhibiting severely compromised binding to Agm and weakened binding to Arg (Fig. 2C), also displayed reduced levels of antiporter activity (Fig. 3C). By contrast, a number of other mutations had little impact on the uptake of ^{3}H-labeled Agm. This analysis identifies amino acids that directly contribute to the antiport activity.

The antiport activity of AdiC may involve four sequential steps. The default state is likely to be the current structure, in an open, outward-facing conformation (Fig. 4). First, substrate binding leads to the occlusion of the bound, primary substrate (Arg) to the periplasm. Second, the antiporter switches to an open, inward-facing conformation, where Arg is competitively displaced by Agm, the secondary substrate. Third, the antiporter bound to the secondary substrate closes down and occludes the bound substrate from the cytoplasm. In the fourth and final step, the antiporter opens up to the periplasm, releasing the secondary substrate. Although the general folds of AdiC and the Na^+-coupled symporters are similar, their modes of substrate binding markedly deviate from each other (fig. S8). The conformation of the TMs surrounding the putative substrate-binding site in AdiC closely resembles that of $LeuT_{Aa}$. It remains to be seen how AdiC interacts with substrate molecules and carries out its antiport activity.

On the basis of our structural and biochemical analysis, we propose that Glu^{208}, invariant among AdiC, CadB, and PotE (fig. S4), is a pH sensor and plays a major role in the antiport activity. In the stomach (pH 2 to 3), Glu^{208}, with $pK_a \sim 4.25$, is predominantly protonated. The majority of the extracellular substrate amino acids are deprotonated in their α-carboxylate groups ($pK_a \sim 2$). Thus, the majority of these amino acids carry no net charge on their head groups, with the positively charged α-amino group offsetting the negatively charged α-carboxyl group. Protonated Glu^{208} likely binds to the neutral head groups of the substrate amino acid (Fig. 4). Once facing the intracellular environment (pH 4 to 5), the sensor residue Glu^{208} is likely to deprotonate, thus developing a net negative charge in the substrate-binding cavity. The negative charge may favor binding by the positively charged head group of the α-decarboxylated amino acid (Fig. 4). Consequently, the secondary substrate (Agm) displaces the primary substrate (Arg) on the antiporter.

What structural elements undergo the proposed conformational changes during transport? Gouaux and colleagues proposed that TM1 and TM6 might be the toggle switches (*18*). This model gained additional support from a recent structural study on BetP (*19*). By contrast, Weyand *et al*. argued that TM3 and TM8 may adopt alternating conformations to allow the switches from outward-open to inward-open (*21*). These conjectures have their bases mostly in structural comparison of different molecules in different transport states: $LeuT_{Aa}$ (*18*) and Mhp1 (*21*) in outward-facing states, vSGLT in inward-facing conformation (*20*), and BetP in between (*19*). The backbone of TM1 in AdiC appears to maintain a very similar conformation compared to that of the Na^+-coupled symporters (fig. S6). In contrast, TM6, and to a lesser extent, TM10, exhibit pronounced conformational shifts. Hence, we propose that TM6 may serve as the primary switch to allow different substrate-binding states and TM10 may facilitate the occlusion of substrate (Fig. 4).

References and Notes

1. M. S. Donnenberg, *Nature* **406**, 768 (2000).
2. J. W. Foster, *Nat. Rev. Microbiol.* **2**, 898 (2004).
3. B. M. Hersh, F. T. Farooq, D. N. Barstad, D. L. Blankenhorn, J. L. Slonczewski, *J. Bacteriol.* **178**, 3978 (1996).
4. M. P. Castanie-Cornet, T. A. Penfound, D. Smith, J. F. Elliott, J. W. Foster, *J. Bacteriol.* **181**, 3525 (1999).
5. R. Iyer, C. Williams, C. Miller, *J. Bacteriol.* **185**, 6556 (2003).
6. S. Gong, H. Richard, J. W. Foster, *J. Bacteriol.* **185**, 4402 (2003).
7. D. L. Jack, I. T. Paulsen, M. H. Saier, *Microbiology* **146**, 1797 (2000).
8. F. Casagrande *et al*., *J. Biol. Chem.* **283**, 33240 (2008).
9. W. Soksawatmaekhin, A. Kuraishi, K. Sakata, K. Kashiwagi, K. Igarashi, *Mol. Microbiol.* **51**, 1401 (2004).
10. W. Soksawatmaekhin, T. Uemura, N. Fukiwake, K. Kashiwagi, K. Igarashi, *J. Biol. Chem.* **281**, 29213 (2006).
11. K. Kashiwagi *et al*., *J. Biol. Chem.* **275**, 36007 (2000).
12. K. Kashiwagi, S. Miyamoto, F. Suzuki, H. Kobayashi, K. Igarashi, *Proc. Natl. Acad. Sci. U.S.A.* **89**, 4529 (1992).
13. K. Kashiwagi, S. Shibuya, H. Tomitori, A. Kuraishi, K. Igarashi, *J. Biol. Chem.* **272**, 6318 (1997).
14. A. Accardi, C. Miller, *Nature* **427**, 803 (2004).
15. Y. Fang, L. Kolmakova-Partensky, C. Miller, *J. Biol. Chem.* **282**, 176 (2007).
16. N. Reig *et al*., *J. Biol. Chem.* **282**, 13270 (2007).
17. Materials and methods are available as supporting material on *Science* Online.
18. A. Yamashita, S. K. Singh, T. Kawate, Y. Jin, E. Gouaux, *Nature* **437**, 215 (2005).
19. S. Ressl, A. C. Terwisscha van Scheltinga, C. Vonrhein, V. Ott, C. Ziegler, *Nature* **458**, 47 (2009).
20. S. Faham *et al*., *Science* **321**, 810 (2008).
21. S. Weyand *et al*., *Science* **322**, 709 (2008).
22. J. S. Lolkema, D. J. Slotboom, *Mol. Membr. Biol.* **25**, 567 (2008).
23. E. Screpanti, C. Hunte, *J. Struct. Biol.* **159**, 261 (2007).
24. C. Toyoshima, M. Nakasako, H. Nomura, H. Ogawa, *Nature* **405**, 647 (2000).
25. R. Dutzler, E. B. Campbell, M. Cadene, B. T. Chait, R. MacKinnon, *Nature* **415**, 287 (2002).
26. C. Hunte *et al*., *Nature* **435**, 1197 (2005).
27. D. Yernool, O. Boudker, Y. Jin, E. Gouaux, *Nature* **431**, 811 (2004).
28. O. Boudker, R. M. Ryan, D. Yernool, K. Shimamoto, E. Gouaux, *Nature* **445**, 387 (2007).
29. O. Jardetzky, *Nature* **211**, 969 (1966).
30. Single-letter abbreviations for the amino acid residues are as follows: A, Ala; C, Cys; D, Asp; E, Glu; F, Phe; G, Gly; H, His; I, Ile; K, Lys; L, Leu; M, Met; N, Asn; P, Pro; Q, Gln; R, Arg; S, Ser; T, Thr; V, Val; W, Trp; and Y, Tyr.
31. W. L. DeLano, www.pymol.org (2002).

32. We thank N. Shimizu at the Spring-8 beamline BL41XU and T. Kumasaka and S. Baba at beamline BL38XU for on-site assistance, Q. Liu for screening crystals at MacCHESS (Macromolecular Diffraction at the Cornell High Energy Synchrotron Source), and N. Yan for discussion and comments on the manuscript. This work was supported by funds from the Ministry of Science and Technology (grant no. 2009CB918801), Tsinghua University 985 Phase II funds, National Natural Science Foundation, and Beijing Municipal Commissions of Education and Science and Technology. The atomic coordinates have been deposited in the Protein Data Bank with the accession codes 3H5M and 3H6B.

Supporting Online Material

www.sciencemag.org/cgi/content/full/1173654/DC1
Materials and Methods
Figs. S1 to S8
Tables S1
References

17 March 2009; accepted 30 April 2009
Published online 28 May 2009;
10.1126/science.1173654
Include this information when citing this paper.

IL-21 Is Required to Control Chronic Viral Infection

Heidi Elsaesser,[1] Karsten Sauer,[2] David G. Brooks[1]*

CD4+ and CD8+ T cell functions are rapidly aborted during chronic infection, preventing viral clearance. CD4+ T cell help is required throughout chronic infection so as to sustain CD8+ T cell responses; however, the necessary factor(s) provided by CD4+ T cells are currently unknown. Using a mouse model of chronic viral infection, we demonstrated that interleukin-21 (IL-21) is an essential component of CD4+ T cell help. In the absence of IL-21 signaling, despite elevated CD4+ T cell responses, CD8+ T cell responses are severely impaired. CD8+ T cells directly require IL-21 to avoid deletion, maintain immunity, and resolve persistent infection. Thus, IL-21 specifically sustains CD8+ T cell effector activity and provides a mechanism of CD4+ T cell help during chronic viral infection.

During chronic viral infections, antiviral $CD4^+$ and $CD8^+$ T cells become nonresponsive to viral antigens and are either physically deleted or persist in a nonfunctional "exhausted" state, unable to produce important antiviral and immunostimulatory cytokines such as interleukin-2 (IL-2), tumor necrosis factor–α (TNF-α), and interferon-γ (IFN-γ); lyse virally infected cells; or proliferate (*1*–*4*). To date, the majority of work analyzing T cell exhaustion during chronic viral infection has focused on $CD8^+$ T cells; however, $CD4^+$ T cells also exhibit reduced function, thus further exacerbating viral persistence. $CD4^+$ T cells are required throughout chronic viral infection in order to sustain $CD8^+$ T cell function and control infection, prevent deletion of high-affinity antiviral $CD8^+$ T cells, and eventually resolve the infection (*5*–*7*). The loss of $CD4^+$ and $CD8^+$ T cell function is associated with viruses that establish chronic viral infections in their hosts: HIV and hepatitis B and hepatitis C virus (HCV) in humans and lymphocytic choriomeningitis virus (LCMV) in rodents (*8*–*12*). Chronic LCMV infection is eventually controlled in the periphery 60 to 80 days after infection in a $CD4^+$ T cell–dependent manner, suggesting that exhausted $CD4^+$ T cells retain helper activity. Expression of the key $CD4^+$ T cell helper cytokine IL-2, however, is rapidly extinguished during viral persistence (*4*, *13*), indicating that an alternative helper mechanism is being implemented.

To determine how $CD4^+$ T cells help $CD8^+$ T cells to clear a viral infection, we infected mice with the Armstrong strain of LCMV (Arm) that induces a robust T cell response, resulting in viral clearance within 8 to 10 days or with the Clone 13 strain of LCMV (Cl 13) that generates a chronic infection due to the up-regulation of immunosuppressive factors that induce a dramatic depletion and inactivation of virus-specific T cells (*14*–*18*). LCMV-Arm and –Cl 13 share identical $CD4^+$ and $CD8^+$ T cell epitopes, enabling direct comparison of virus-specific T cell responses during acute and persistent infection (*15*, *17*). In initial experiments, we observed high amounts of IL-21 mRNA expression in the spleen during LCMV–Cl 13 infection (Fig. 1A). On the basis of the known immunomodulatory effects of IL-21 on T cells (*19*), we further investigated the function of IL-21 during viral persistence.

IL-21 is primarily produced by activated $CD4^+$ T cells (*20*–*22*); however, the cells that produce IL-21 during chronic viral infection are unknown. Natural killer T cells, B cells, macrophages, and dendritic cells expressed low amounts of IL-21 mRNA during both acute and chronic LCMV infection (Fig. 1B and fig. S1). In contrast, IL-21 was highly expressed by total $CD4^+$ T cells after either acute or chronic LCMV infection (Fig. 1B). To determine whether IL-21 production by virus-specific $CD4^+$ T cells was elevated during chronic infection, we transferred LCMV-specific $CD4^+$ T cell receptor (TCR) transgenic T cells (SMARTA), which recognize LCMV-derived peptide $GP_{61\text{-}80}$ in the context of $I\text{-}A^b$, into C57BL/6 mice and then infected the mice with LCMV-Arm or LCMV–Cl 13. Virus-specific $CD4^+$ T cells from LCMV–Cl 13–infected mice exhibited a greater than 11-fold increase in IL-21 mRNA expression as compared with that in $CD4^+$ T cells from LCMV-Arm–infected mice, and the increase was sustained through chronic infection (Fig. 1B). Depletion of $CD4^+$ T cells reduced IL-21 mRNA expression to that observed in uninfected mice (Fig. 1A), indicating that $CD4^+$ T cells are probably the main source of IL-21 during chronic LCMV infection. The modest increase in IL-21 mRNA by total $CD4^+$ T cells during chronic infection as compared with the substantial increase in IL-21 by virus-specific $CD4^+$ T cells is probably due to the decreased frequency of virus-specific $CD4^+$ T cells during chronic infection (*4*). Whereas the ability of virus-specific $CD4^+$ T cells to produce IL-2 was rapidly extinguished after LCMV–Cl 13 infection, many virus-specific $CD4^+$ T cells produced IL-21 throughout persistent infection, resulting in an inversion from a predominantly IL-2–producing to an IL-21–producing cell population (Fig. 1C and fig. S2). Thus, although the expression of many cytokines by virus-specific $CD4^+$ T cells is decreased during chronic infection, IL-21 is maintained.

To determine the effect of IL-21 on antiviral $CD8^+$ T cell immunity, we infected wild-type (WT) C57BL/6 mice and IL-21 receptor knockout ($Il21r^{-/-}$) mice (*23*) with LCMV-Arm or –Cl 13. In both WT and $Il21r^{-/-}$ mice, LCMV-Arm infection stimulated robust virus-specific $CD8^+$ T cell expansion and production of IFN-γ and TNF-α (fig. S3). Early after LCMV–Cl 13 infection (day 9), the extent of $CD8^+$ T cell exhaustion was similar in WT and $Il21r^{-/-}$ mice (fig. S3). The lack of IL-21 signaling during the chronic phase of Cl 13 infection (day 30), however, resulted in a dramatic decrease of IFN-γ and IFN-γ/TNF-α dual-producing CD8 T cells (fig. S3). To determine whether the reduction in cytokine-producing $CD8^+$ T cells during chronic infection was due to enhanced functional exhaustion or physical deletion, we used LCMV-$GP_{33\text{-}41}$ major histocompatability complex (MHC) class I tetramers to directly enumerate virus-specific T cells. Both the frequency and number of $Il21r^{-/-}$ $tetramer^+$ $CD8^+$ T cells were increased relative to WT mice early (day 9) after LCMV–Cl 13 infection; however, they were significantly diminished in $Il21r^{-/-}$ mice as compared with WT mice as chronic infection progressed (day 30) (Fig. 2, A and B). These results suggested that IL-21 is required to sustain virus-specific $CD8^+$ T cells as chronic infection progressed.

Using two approaches, we next assessed whether IL-21–mediated help was directly acting on virus-specific $CD8^+$ T cells. We performed the first approach by transferring WT or $Il21r^{-/-}$ LCMV-specific $CD8^+$ TCR transgenic P14 cells, which recognize LCMV-peptide $GP_{33\text{-}41}$ in the context of $H\text{-}2K^b$, into separate $Il21r^{+/+}$ mice. We observed comparable functional and numerical responses after LCMV-Arm infection and in the early phase (day 8) of LCMV–Cl 13 infection (Fig. 2C and fig. S4) similar to that in $Il21r^{-/-}$ mice. In contrast, $Il21r^{-/-}$ P14 T cells exhibited enhanced functional exhaustion and deletion as compared with WT P14 T cells as chronic infection progressed (day 30) (Fig. 2C and fig. S4). In the second approach, irradiated WT mice were reconstituted with a mixture of WT ($Ly5.1^+$) and $Il21r^{-/-}$ ($Ly5.2^+$) bone marrow, allowing for both WT and $Il21r^{-/-}$ virus-specific $CD8^+$ T cells to be exposed to identical inflammatory signals and cell interactions. We observed a similar frequency of LCMV-$GP_{33\text{-}41}$–specific $tetramer^+$ $CD8^+$ T cells on day 8 after LCMV–Cl 13 infection; however, although the frequency of WT bone marrow–derived $tetramer^+$ cells was maintained as the infection progressed, $Il21r^{-/-}$ bone marrow–derived virus-specific $CD8^+$ T cells were deleted (Fig. 2D). We did not observe deletion of $Il21r^{-/-}$ bone marrow–derived $tetramer^+$ $CD8^+$ T cells after LCMV-Arm infection (fig. S5). After LCMV-Arm or LCMV–Cl 13 infection of the bone-marrow chimeric mice, the ratio of WT to $Il21r^{-/-}$ $CD8^+$ T cells rapidly decreased from 60:40 before infection to 80:20 by day 8 after infection that was then stably main-

[1]Department of Microbiology, Immunology, and Molecular Genetics and University of California, Los Angeles (UCLA) AIDS Institute, David Geffen School of Medicine, UCLA, Los Angeles, CA 90095, USA. [2]Department of Immunology and Microbial Sciences, The Scripps Research Institute, La Jolla, CA 92037, USA.

*To whom correspondence should be addressed. E-mail: dbrooks@em.ucla.edu

tained (fig. S5), suggesting a growth advantage for IL-21R–expressing total CD8$^+$ T cells during viral infection. Any growth advantage of total IL-21R–expressing CD8$^+$ T cells did not affect the frequency of tetramer$^+$ CD8$^+$ T cells in response to LCMV-Arm infection (fig. S5) and occurred before the loss of *Il21r*$^{-/-}$ bone marrow–derived tetramer$^+$ cells during LCMV–Cl 13 infection (Fig. 2D and fig. S4). Thus, IL-21 directly sustains virus-specific CD8$^+$ T cells during chronic infection.

Although IL-21 is produced by CD4$^+$ T cells, how it regulates CD4$^+$ T cell function in the context of an in vivo viral infection is unclear. We observed increased amounts of IFN-γ–producing and LCMV-GP$_{61-80}$–specific MHC class II tetramer$^+$ CD4$^+$ T cells in *Il21r*$^{-/-}$ as compared with WT mice at days 9 and 30 after LCMV-Arm or –Cl 13 infection (Fig. 3, A to C). Furthermore, we observed rapid suppression of IL-2 and TNF-α after LCMV–Cl 13 infection in WT mice (Fig. 3, A and B, and fig. S5). TNF-α expression was also rapidly diminished in *Il21r*$^{-/-}$ mice after LCMV–Cl 13 infection (fig. S6); however, unlike WT mice, virus-specific CD4$^+$ T cells continued to produce IL-2 in LCMV–Cl 13–infected *Il21r*$^{-/-}$ mice in quantities similar to those observed at day 9 after LCMV-Arm infection (Fig. 3, A and B). These findings indicate that IL-21 signaling results in decreased IL-2 production by virus-specific CD4$^+$ T cells. The elevated frequencies of virus-specific CD4$^+$ T cells producing IL-2 observed early during LCMV–Cl 13 infection in *Il21r*$^{-/-}$ mice declined as the infection progressed and by 30 days after infection was similar to frequencies observed in WT mice (Fig. 3, A and B). The total number of IL-2–expressing virus-specific CD4$^+$ T cells, however, remained significantly increased in *Il21r*$^{-/-}$ mice after LCMV-Arm and particularly LCMV–Cl 13 infection, as compared with that in WT mice (Fig. 3B). Thus, IL-21 suppresses distinct facets of CD4$^+$ T cell function during viral persistence, such as early IL-2 expression, whereas other facets, such as TNF-α expression, are not affected.

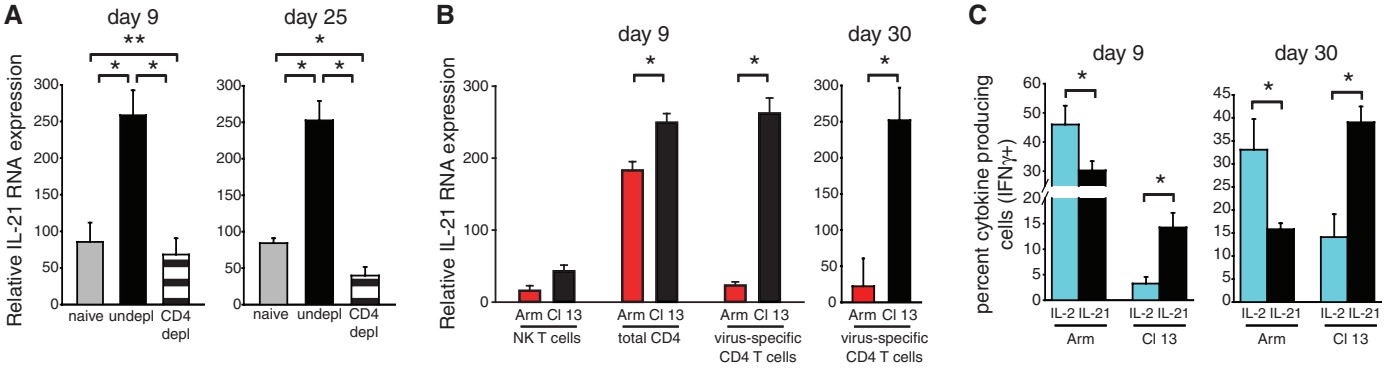

Fig. 1. IL-21 mRNA expression during viral infection. IL-21 mRNA expression was quantified by real-time reverse transcription polymerase chain reaction after LCMV-Arm or LCMV–Cl 13 infection in (**A**) uninfected (gray bar), LCMV–Cl 13 infected (black bar), or LCMV–Cl 13 infected and CD4$^+$ T cell–depleted (striped bar) splenocytes or in (**B**) the indicated sorted cell population. Red Bars indicate cells sorted from LCMV-Arm–infected animals; black bars indicate cells sorted from LCMV–Cl 13–infected animals. (**C**) Frequency of IFN-γ$^+$ SMARTA T cells that simultaneously produced IL-2 or IL-21 on day 9 and day 30 after infection. Error bars represent the average ± SD of 3 to 5 mice per group and 2 to 4 independent experiments. *$P < 0.05$, **$P = 0.4$.

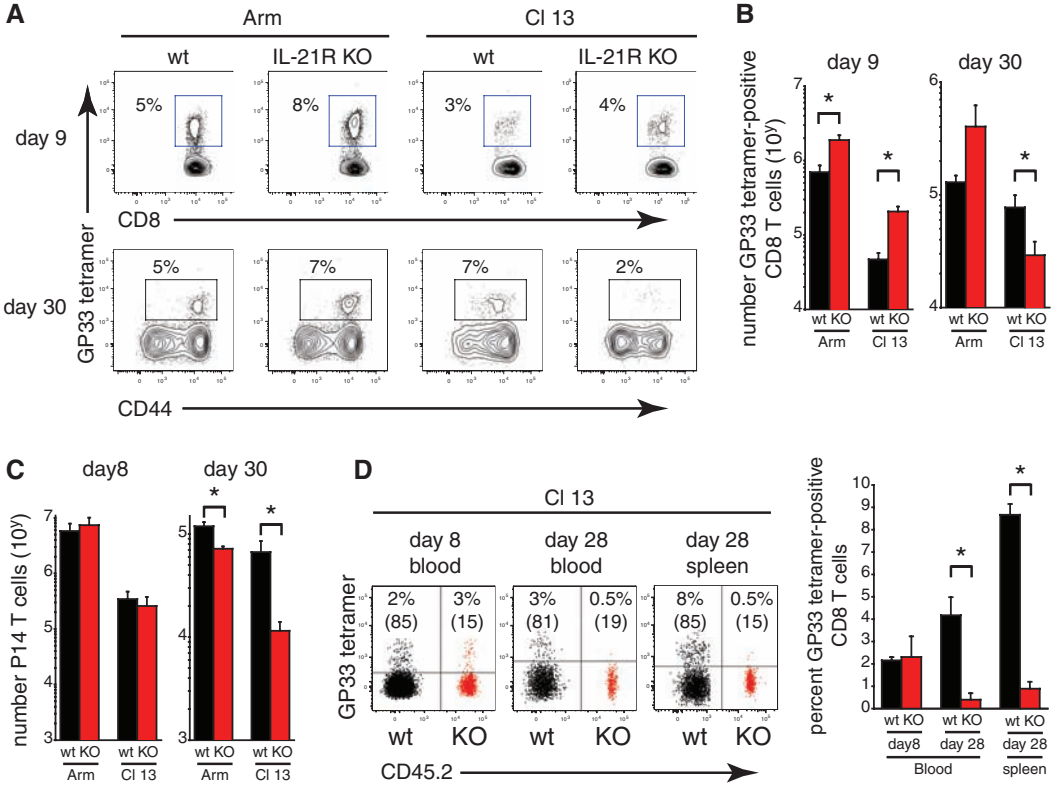

Fig. 2. IL-21 sustains virus-specific CD8$^+$ T cells during viral persistence. (**A**) LCMV-GP$_{33-41}$ MHC class I tetramer staining on days 9 or 30 after LCMV-Arm or LCMV–Cl 13 infection. Numbers indicate the frequency of tetramer$^+$ CD8$^+$ T cells in WT and *Il21r*$^{-/-}$ (KO) mice. (**B**) Number of tetramer$^+$ CD8$^+$ T cells on days 9 and 30 after LCMV-Arm or LCMV–Cl 13 infection of WT and *Il21r*$^{-/-}$ mice. (**C**) Number of WT or *Il21r*$^{-/-}$ P14 T cells after infection of *Il21r*$^{+/+}$ mice. (**D**) Frequency of WT and *Il21r*$^{-/-}$ LCMV-GP$_{33-41}$ tetramer$^+$ CD8$^+$ T cells in bone-marrow chimeric mice on days 8 and 28 in the blood and on day 28 in the spleen after LCMV–Cl 13 infection. Numbers in parentheses indicate the total proportion of WT and *Il21r*$^{-/-}$ CD8$^+$ T cells. Bar graphs represent the average ± SD of 3 to 5 mice per group and represent 2 to 4 independent experiments. *$P < 0.05$.

$CD8\ T^+$ cells are required to resolve LCMV–Cl 13 infection (*5*), thus the reduced numbers of virus-specific $CD8^+$ T cells in *Il21r*$^{-/-}$ mice suggested that they may be insufficient to resolve the infection. The initial generation of productive T cell responses led to acute clearance of LCMV-Arm infection in WT and *Il21r*$^{-/-}$ mice (Fig. 4A). In contrast, the rapid T cell exhaustion after LCMV–Cl 13 infection led to chronic infection in WT and *Il21r*$^{-/-}$ mice (Fig. 4A). Consistent with the similar generation of virus-specific $CD8^+$ T cell responses after infection, LCMV–Cl 13 titers were initially equal in WT and *Il21r*$^{-/-}$ mice; however, whereas infection in WT mice resolved after two months, *Il21r*$^{-/-}$ mice did not resolve the infection (Fig. 4A). In the presence of chronic infection, virus-specific *Il21r*$^{-/-}$ $CD8^+$ T cell responses continued to decline as compared with that in WT mice,

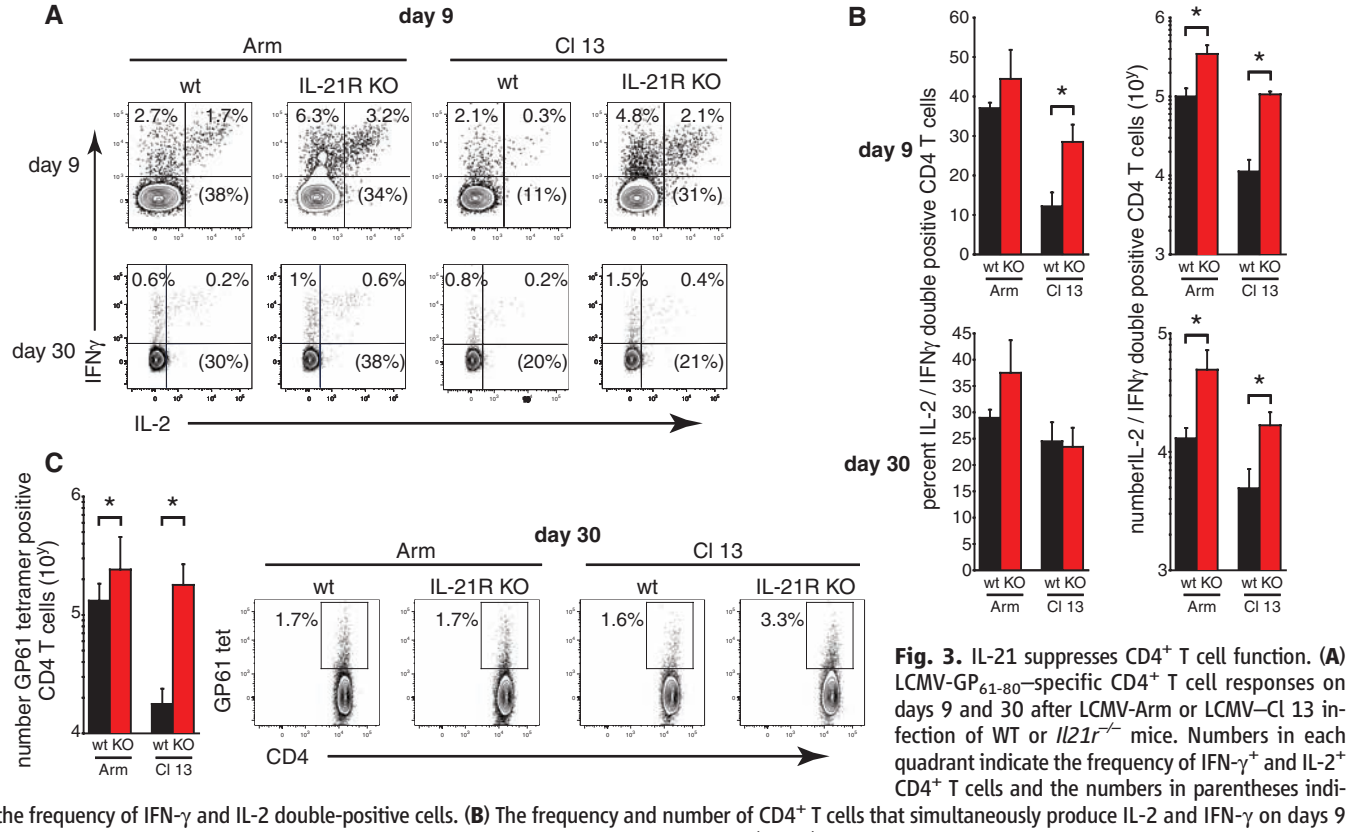

Fig. 3. IL-21 suppresses $CD4^+$ T cell function. (**A**) LCMV-$GP_{61\text{-}80}$–specific $CD4^+$ T cell responses on days 9 and 30 after LCMV-Arm or LCMV–Cl 13 infection of WT or *Il21r*$^{-/-}$ mice. Numbers in each quadrant indicate the frequency of IFN-γ^+ and IL-2^+ $CD4^+$ T cells and the numbers in parentheses indicate the frequency of IFN-γ and IL-2 double-positive cells. (**B**) The frequency and number of $CD4^+$ T cells that simultaneously produce IL-2 and IFN-γ on days 9 or 30 after LCMV-Arm or LCMV–Cl 13 infection. (**C**) Frequency of LCMV-$GP_{61\text{-}80}$ tetramer$^+$ $CD4^+$ T on day 30 after LCMV-Arm or LCMV–Cl 13 infection. The bar graph represents the number of tetramer$^+$ $CD4^+$ T cells. Bar graphs summarize the average ± SD of 3 to 4 mice per group and 3 to 4 independent experiments. *$P < 0.05$.

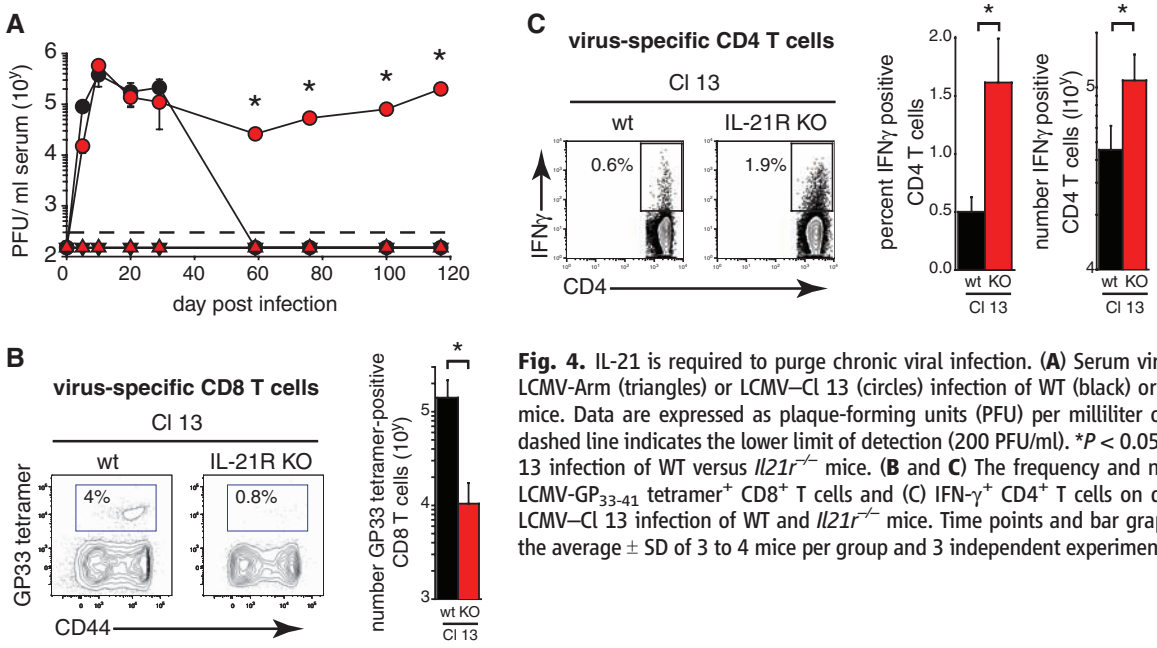

Fig. 4. IL-21 is required to purge chronic viral infection. (**A**) Serum viral titers after LCMV-Arm (triangles) or LCMV–Cl 13 (circles) infection of WT (black) or *Il21r*$^{-/-}$ (red) mice. Data are expressed as plaque-forming units (PFU) per milliliter of serum. The dashed line indicates the lower limit of detection (200 PFU/ml). *$P < 0.05$ for LCMV–Cl 13 infection of WT versus *Il21r*$^{-/-}$ mice. (**B** and **C**) The frequency and number of (B) LCMV-$GP_{33\text{-}41}$ tetramer$^+$ $CD8^+$ T cells and (C) IFN-γ^+ $CD4^+$ T cells on day 100 after LCMV–Cl 13 infection of WT and *Il21r*$^{-/-}$ mice. Time points and bar graphs represent the average ± SD of 3 to 4 mice per group and 3 independent experiments. *$P < 0.05$.

whereas no further decrease was observed in WT mice over this same time period (Figs. 2D and 4B). Conversely, the number of IFN-γ^+ (virus-specific) $CD4^+$ T cells remained elevated 100 days after LCMV-Arm (fig. S7) and –Cl 13 infection in *Il21r*$^{-/-}$ mice (Fig. 4C). Thus, despite the increased presence of virus-specific $CD4^+$ T cells in *Il21r*$^{-/-}$ mice, $CD8^+$ T cell responses are not sustained and the infection is not resolved.

IL-21 signaling also affects antibody production by B cells and antigen-presenting cell responses (*19*), which in addition to $CD8^+$ T cell deletion could contribute to the failure to resolve infection. Compared with that in WT mice, antigen-presenting cell maturation was not differentially affected in *Il21r*$^{-/-}$ mice after LCMV-Arm or –Cl 13 infection and by some measurements was increased in the absence of IL-21 signaling (fig. S8). Furthermore, the total number of B cells was similar in WT and *Il21r*$^{-/-}$ mice during chronic infection (fig. S9). We observed a 1.9-fold decrease in LCMV-specific immunoglobulin G antibody titers in *Il21r*$^{-/-}$ mice, although substantial antibody titers were observed in both WT and *Il21r*$^{-/-}$ mice (fig. S9). LCMV-neutralizing antibody titers were undetectable in both WT and *Il21r*$^{-/-}$ mice at day 30 after LCMV-Cl 13 infection. Together, these data suggest that antigen-presenting cells impairment or impaired humoral immunity are unlikely to underlie the reduced control of chronic infection in *Il21r*$^{-/-}$ mice.

The requirement for $CD4^+$ T cell help to control chronic viral infection has long been established (*5*, *6*); however, because $CD4^+$ T cells rapidly lose the ability to produce traditional helper cytokines such as IL-2, the specific mechanisms and factors that comprise $CD4^+$ T cell help have remained elusive. Our results suggest that $CD4^+$ T cells do not necessarily "exhaust" or "lose" function during chronic viral infection. Instead, we propose that $CD4^+$ T cell function is diverted toward the production of factors such as IL-21 that sustain effector activity to control infection. Multiple effector mechanisms probably contribute to the long-term development of $CD8^+$ T cell responses. In combination with (or in the absence of) other yet unidentified helper factors, IL-21 maintains the $CD8^+$ T cell effector activity required to control infection and thus provides a mechanism for $CD4^+$ T cell help in response to chronic viral infection. Failure of $CD4^+$ T cell help is associated with the inability to acutely clear HCV infection and with the progression to AIDS after HIV infection (*8*–*12*). Thus, loss of IL-21 as $CD4^+$ T cell responses decline may hinder control of these human chronic viral infections. Further identification of helper factors and how they regulate precise immune outcomes will provide valuable insight into the generation and maintenance of antiviral immunity to prevent and treat chronic viral infections.

References and Notes

1. A. J. Zajac *et al.*, *J. Exp. Med.* **188**, 2205 (1998).
2. A. Gallimore *et al.*, *J. Exp. Med.* **187**, 1383 (1998).
3. E. J. Wherry, J. N. Blattman, K. Murali-Krishna, R. van der Most, R. Ahmed, *J. Virol.* **77**, 4911 (2003).
4. D. G. Brooks, L. Teyton, M. B. Oldstone, D. B. McGavern, *J. Virol.* **79**, 10514 (2005).
5. M. Battegay *et al.*, *J. Virol.* **68**, 4700 (1994).
6. M. Matloubian, R. J. Concepcion, R. Ahmed, *J. Virol.* **68**, 8056 (1994).
7. R. Ou, S. Zhou, L. Huang, D. Moskophidis, *J. Virol.* **75**, 8407 (2001).
8. J. T. Gerlach *et al.*, *Gastroenterology* **117**, 933 (1999).
9. R. Thimme *et al.*, *J. Exp. Med.* **194**, 1395 (2001).
10. A. Grakoui *et al.*, *Science* **302**, 659 (2003).
11. S. Smyk-Pearson *et al.*, *J. Virol.* **82**, 1827 (2008).
12. P. Klenerman, A. Hill, *Nat. Immunol.* **6**, 873 (2005).
13. M. J. Fuller, A. J. Zajac, *J. Immunol.* **170**, 477 (2003).
14. Materials and methods are available as supporting material on *Science* Online.
15. R. Ahmed, A. Salmi, L. D. Butler, J. M. Chiller, M. B. Oldstone, *J. Exp. Med.* **160**, 521 (1984).
16. D. L. Barber *et al.*, *Nature* **439**, 682 (2006).
17. D. G. Brooks *et al.*, *Nat. Med.* **12**, 1301 (2006).
18. M. Ejrnaes *et al.*, *J. Exp. Med.* **203**, 2461 (2006).
19. R. Spolski, W. J. Leonard, *Annu. Rev. Immunol.* **26**, 57 (2008).
20. J. Parrish-Novak *et al.*, *Nature* **408**, 57 (2000).
21. C. Holm, C. G. Nyvold, S. R. Paludan, A. R. Thomsen, M. Hokland, *Cytokine* **33**, 41 (2006).
22. J. M. Coquet *et al.*, *J. Immunol.* **178**, 2827 (2007).
23. K. Ozaki *et al.*, *Science* **298**, 1630 (2002).

24. We thank M. Oldstone for his generous support (AI09484). Our work was supported by the UCLA Center for AIDS Research, the Eli and Edythe Broad Center of Regenerative Medicine and Stem Cell Research at UCLA, and NIH grants AI077012, AI082975 (to D.G.B.), and AI070845 (to K.S.).

Supporting Online Material

www.sciencemag.org/cgi/content/full/1174182/DC1
Materials and Methods
Figs. S1 to S9
References

22 October 2008; accepted 28 April 2009
Published online 7 May 2009;
10.1126/science.1174182
Include this information when citing this paper.

A Vital Role for Interleukin-21 in the Control of a Chronic Viral Infection

John S. Yi, Ming Du, Allan J. Zajac*

Understanding the factors that regulate the induction, quality, and longevity of antiviral T cell responses is essential for devising rational strategies to prevent or combat infections. In this study, we show that interleukin-21 (IL-21), likely produced by $CD4^+$ T cells, directly influences the generation of polyfunctional $CD8^+$ T cells and that the number of $CD4^+$ T cells that produce IL-21 differs markedly between acute and chronic infections. IL-21 regulates the development of $CD8^+$ T cell exhaustion and the ability to contain chronic lymphocytic choriomeningitis virus infection. Thus, IL-21 serves as a critical helper factor that shapes the functional quality of antiviral $CD8^+$ T cells and is required for viral control.

A hallmark of robust antiviral immunity is the induction of $CD4^+$ and $CD8^+$ T cell responses, which act cooperatively and in conjunction with other immune system components, to control infection. The consequences of an ineffective immune response can be catastrophic, favoring viral persistence or the erosion of long-lived immunological memory. During the initial phases of many chronic infections, including hepatitis C virus (HCV) and human immunodeficiency virus (HIV) infections, $CD8^+$ T cell responses are induced but can fail to attain or lose the ability to elaborate key effector functions (*1*–*9*). Although the cellular and molecular cues that dictate the development of robust $CD8^+$ T cells are not fully elucidated, in the absence of $CD4^+$ T cell help, $CD8^+$ T cell responses are compromised (*2*, *5*, *6*, *10*–*18*). $CD4^+$ T cells are the primary producers of interleukin-21 (IL-21), a member of the common-γ chain family of cytokines (*19*–*21*). Functions of IL-21 are wide-ranging and include promoting B cell and antibody responses and inducing the development of Th17 and follicular helper $CD4^+$ (Tfh) lineages (*19*–*24*). Given that $CD4^+$ T cells are necessary for optimal antiviral $CD8^+$ T cell responses, we investigated the role of IL-21 in $CD8^+$ T cell responses to viral infections.

A comparative analysis of lymphocytic choriomeningitis virus (LCMV)–specific $CD4^+$ T cells revealed marked differences in the induction of IL-21^+ $CD4^+$ T cells after acute LCMV-Armstrong (Arm) and chronic LCMV–clone 13 (Cl 13) infections of C57BL/6 (B6) mice (Fig. 1) (*25*). By 8 days, both infections elicited polyclonal virus-specific IL-21^+ $CD4^+$ T cells; however, this response was 7.8 times lower in the LCMV–Cl 13–infected cohort (Fig. 1B; $P < 0.001$). Because $CD4^+$ T cells are obligatory for the control of LCMV–Cl 13, these results suggest that the $CD4^+$ T cell response to this infection, albeit weak, is capable of providing some help (*2*, *5*, *6*, *10*).

Department of Microbiology, University of Alabama at Birmingham, Birmingham, AL 35294–2170, USA.

*To whom correspondence should be addressed. E-mail: azajac@uab.edu

The pronounced IL-21$^+$ CD4$^+$ T cell response after acute LCMV-Arm infection prompted us to analyze whether IL-21 influenced the generation of germinal center (GC) B cells, Tfh cells, and antibody responses (fig. S1). The percentage and number of GC B cells and Tfh (ICOS$^+$, CXCR5$^+$) T cells as well as LCMV-specific antibody titers were similar between 8 to 9 days after LCMV-Arm infection of *Il21*$^{+/+}$ and $^{-/-}$ mice. Thus, acute LCMV infection can trigger the development of these responses even in the absence of IL-21. Moreover, all cohorts successfully controlled LCMV-Arm infection because serum viral titers were below the limits of detection [<50 plaque-forming units (PFU)/ml] by this time point. Although appreciable antibody levels were detectable between days 44 to 120 after infection, endpoint titers were three times lower in *Il21*$^{-/-}$ mice.

To further analyze the role of IL-21 in promoting antiviral immunity, we evaluated the responses of *Il21*$^{+/+}$, $^{+/-}$, and $^{-/-}$ mice to LCMV–Cl 13 infection. Mice infected with LCMV–Cl 13 typically exhibit high-grade viremia and progressive reductions in the functional capacity of antiviral CD8$^+$ T cells, termed exhaustion (*1*, *2*, *5*, *6*, *9*, *26*). Eight days after LCMV–Cl 13 infection, during the effector phase, the magnitudes of the antiviral CD4$^+$ and CD8$^+$ T cell responses and the frequency of interferon-γ (IFN-γ)–producing antiviral CD8$^+$ T cells were similar among *Il21*$^{+/+}$, $^{+/-}$, and $^{-/-}$ cohorts (figs. S2 and S3, A and B); however, we observed differences in their functional quality (Fig. 2, A and B, and fig. S3B). Both the percentages and absolute numbers of polyfunctional, IL-2–producing CD8$^+$ T cells were reduced in *Il21*$^{-/-}$ mice, with *Il21*$^{+/-}$ mice exhibiting an intermediate phenotype (Fig. 2, A and B, and fig. S3B). We observed similar trends for tumor necrosis factor–α (TNF-α) production (fig. S4A). Thus, IL-21 deficiency results in impaired polyfunctional effector CD8$^+$ T cell responses during the initial phases of LCMV infection.

Given the altered cytokine responses by antiviral CD8$^+$ T cells after LCMV–Cl 13 infection of *IL21*$^{-/-}$ mice, we next tracked viral loads over time to determine whether the absence of IL-21 compromised the containment of the infection (Fig. 2C and fig. S5). As expected, *Il21*$^{+/+}$ hosts slowly controlled LCMV–Cl 13 infection (*1*, *2*, *5*, *9*, *26*). By contrast, viral titers in the serum, livers, and lungs of *Il21*$^{-/-}$ mice remained high, a phenotype similar to that observed in mice lacking CD4$^+$ T cells (Fig. 2C and fig. S5). *Il21*$^{+/-}$ mice showed an intermediate pattern of clearance, with viral loads decreasing more slowly than in *Il21*$^{+/+}$ mice and the infection persisting at high levels or breaking through in three of the five *Il21*$^{+/-}$ mice tested between days 136 and 148 after infection. These data suggest that IL-21 is critical for control of chronic viral infection.

Evaluation of antiviral CD8$^+$ T cell responses at later stages after LCMV–Cl 13 infection revealed severe functional exhaustion in *Il21*$^{-/-}$ mice (Fig. 2D and figs. S3, C and D, and S4). By 136 days, *Il21*$^{+/+}$ mice had brought the infection under control, and IFN-γ, IL-2 (Fig. 2D), and TNF-α (fig. S4B) production was detectable by antiviral, primarily glycoprotein (GP)–specific, CD8$^+$ T cells. Moreover, these antiviral CD8$^+$ T cells expressed intermediate levels of CD43 (CD43^{int}) and low levels of programmed death–1 (PD-1^{low}), a phenotype more similar to resting memory T cells (Fig. 2, E and F). In *Il21*$^{+/-}$ mice, the phenotypic and functional properties of the antiviral CD8$^+$ T cells diverged depending on their virological status. CD8$^+$ T cells from mice able to contain the infection resembled antiviral CD8$^+$ T cells from *Il21*$^{+/+}$; however, in mice with high viral titers, CD8$^+$ T cell responses were more similar to those observed in *Il21*$^{-/-}$ hosts (fig. S4B). IL-2, IFN-γ, and TNF-α production by *Il21*$^{-/-}$ virus-specific CD8$^+$ T cells were greatly reduced or absent (Fig. 2D and figs. S3D and S4B), but these T cells were CD43^{high}, PD-1^{high} (Fig. 2, E and F), a hallmark of the exhaustion that develops in chronically infected hosts (*6*, *9*). Interestingly, the emergence of exhausted virus-specific CD8$^+$ T cells in *Il21*$^{-/-}$ mice parallels what is observed after LCMV–Cl 13 infection of CD4-deficent hosts (*2*, *5*, *6*, *10*). Thus, the absence of IL-21 production results in a failure to contain the infection and a silencing of antiviral CD8$^+$ T cell functions.

We next examined whether IL-21 was acting directly to promote and sustain CD8$^+$ T cell responses. To directly compare, within the same host, the responses and fates of cells of the immune system that can and cannot perceive IL-21–derived signals, we generated bone-marrow chimeras with use of a mixture of allelically marked *Il21r*$^{+/+}$ (CD45.1) and *Il21r*$^{-/-}$ (CD45.2) donor cells. As a control, we also generated mixed bone-marrow chimeric mice that were reconstituted with *Il21r*$^{+/+}$ (CD45.1) bone marrow and *Il21r*$^{+/+}$ (CD45.2) bone marrow prepared from the littermates of *Il21r*$^{-/-}$ mice. Before infection, the ratio of CD45.1:CD45.2 CD8$^+$ T cells was 52:48 and 70:30 in the control and experimental cohorts, respectively. Nevertheless, both *Il21r*$^{+/+}$ and *Il21r*$^{-/-}$ virus-specific CD8$^+$ T cells were detectable in the circulation by 8 days after LCMV–Cl 13 infection (Fig. 3). Thus, the elaboration of primary virus-specific CD8$^+$ T cell responses can occur independently of IL-21. Further tracking of virus-specific CD8$^+$ T cells in the circulation at 16 days after infection revealed a preferential and rapid loss of *Il21r*$^{-/-}$ antiviral CD8$^+$ T cells. This was confirmed by enumeration of splenic responses 3 weeks after infection, which revealed a 40 times fewer number of *Il21r*$^{-/-}$ virus-specific CD8$^+$ T cells by comparison with *Il21r*$^{+/+}$ counterparts in the same host (Fig. 3, C and D). These data illustrate the direct requirement of IL-21 for supporting and maintaining antiviral CD8$^+$ T cells during chronic viral infections.

We next evaluated whether the addition of IL-21 enhanced antiviral CD8$^+$ T cells because the absence of IL-21–dependent signaling impaired these responses. We investigated whether administration of IL-21 could improve responses and viral control in *Cd4*$^{-/-}$ mice because CD4$^+$ T cells are a principal source of this cytokine. These "helpless" mice do not usually control

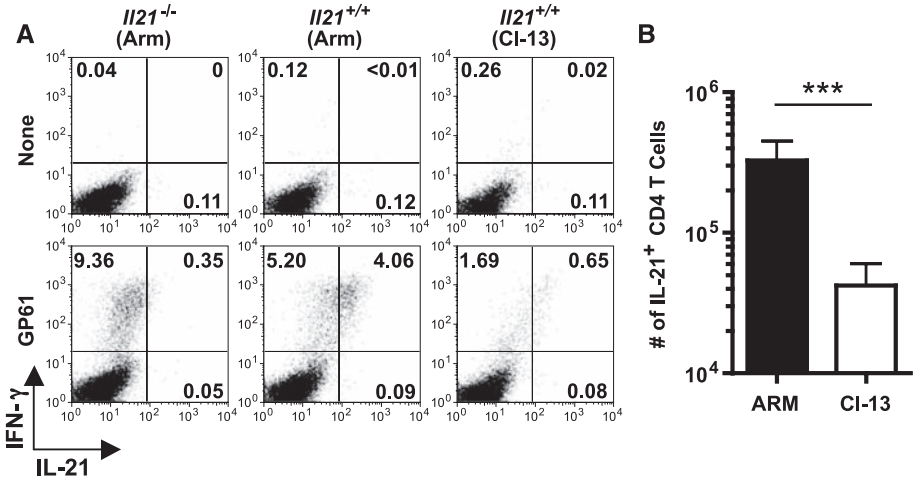

Fig. 1. Diminished IL-21$^+$ CD4$^+$ T cell responses during the initial phase of LCMV–Cl 13 infection. IL-21 and IFN-γ production by LCMV GP$_{61-80}$ CD4$^+$ T cells was determined 8 days after LCMV-Arm or –Cl 13 infections of B6 mice. (**A**) Flow cytometric analysis of intracellular staining for IL-21 and IFN-γ in splenocytes from LCMV-infected *Il21*$^{-/-}$ and *Il21*$^{+/+}$ mice after stimulation with GP$_{61-80}$ peptide. Gated total CD4$^+$ T cells are shown. (**B**) Enumeration of IL-21–producing CD4$^+$ T cells at 8 days after LCMV-Arm or –Cl 13 infection. Graphs represent mean ± SD; ***P < 0.001. Representative results are shown from two independent experiments (n = 8 to 9 for *Il21*$^{+/+}$ cohorts and n = 2 for *Il21*$^{-/-}$ mice).

LCMV–Cl 13 infection and develop severe $CD8^+$ T cell exhaustion (*2*, *5*, *6*, *10*). Daily injections of recombinant IL-21 to LCMV–Cl 13–infected $Cd4^{-/-}$ mice enhanced the functional quality of virus-specific $CD8^+$ T cells, particularly the nucleoprotein $(NP)_{396}$ epitope-specific population, which usually rapidly succumbs to exhaustion (Fig. 4). Importantly, IL-21 treatment resulted in lower viral titers (Fig. 4C). The delicate balance between the quality and size of the antiviral immune response and the hosts' viral burden became apparent as 70% of the treated mice became moribund, reaching experimental endpoints requiring euthanasia. Illness and death after LCMV infection is classically associated with immunopathology (*27*). Thus, although IL-21 administration can improve antiviral $CD8^+$ T cell responses and viral clearance and has been safely used in the context of tumor immunotherapy in mice and humans, care will need to be taken before applying this treatment strategy to chronic viral infections (*21*, *28*, *29*).

Collectively, our findings provide insights into the determinants of the functional quality of $CD8^+$ T cell responses and the role of IL-21 in ensuring the successful control of infection. The results implicate IL-21 as a critical helper factor that couples the requirement for $CD4^+$ T cells, which produce this cytokine, to the elaboration and maintenance of polyfunctional $CD8^+$ T cells capable of clearing virus-infected cells. We observed that induction of IL-21–producing $CD4^+$ T cells is markedly reduced during the ini-

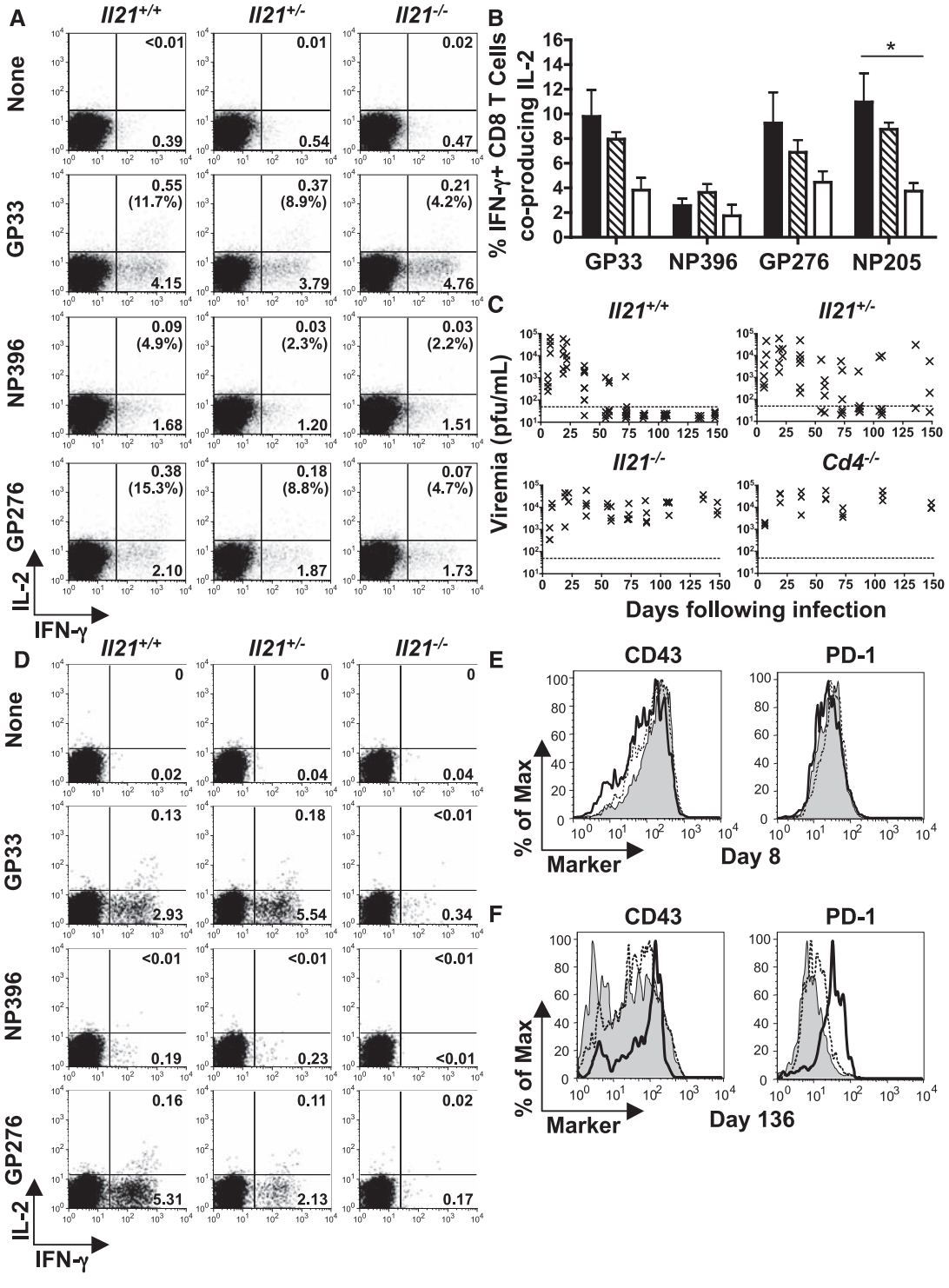

Fig. 2. Severe $CD8^+$ T cell exhaustion and viral persistence in the absence of IL-21. Splenic $CD8^+$ T cell responses and viral titers were evaluated after LCMV–Cl 13 infection of $Il21^{+/+}$, $^{+/-}$, and $^{-/-}$ mice. (**A**) Flow cytometric analysis of intracellular cytokine staining for IFN-γ and IL-2 production by $CD8^+$ T cells at 8 days after infection after restimulation without or with the indicated peptide epitopes. Gated $CD8^+$ T cells are shown, and the percentages of $CD8^+$, IFN-γ^+ cells that co-produce IL-2 are reported in parentheses. (**B**) Percentages of epitope-specific $CD8^+$, IFN-γ^+ cells that co-produce IL-2 at 8 days after infection. Error bars are SEM; $^*P < 0.05$ by comparison with $Il21^{+/+}$ group. (**C**) Serum viral titers over time after LCMV–Cl 13 infection of $Il21^{+/+}$, $^{+/-}$, $^{-/-}$, and $Cd4^{-/-}$ mice. Results from individual mice are shown; the dotted line represents the limit of detection. (**D**) IFN-γ and IL-2 production by LCMV-specific $CD8^+$ T cells at 136 days after infection. Gated $CD8^+$ T cells are shown. (**E** and **F**) CD43 and PD-1 expression by GP33 tetramer$^+$ $CD8^+$ T cells from $Il21^{+/+}$ (shaded), $^{+/-}$ (dashed line), and $^{-/-}$ (bold line) mice at 8 (E) and 136 (F) days postinfection. The $Il21^{+/-}$ data shown in (D) and (F) are from mice that were aviremic at the time of analysis. Representative or composite data are shown from two independent experiments (n = 3 to 6).

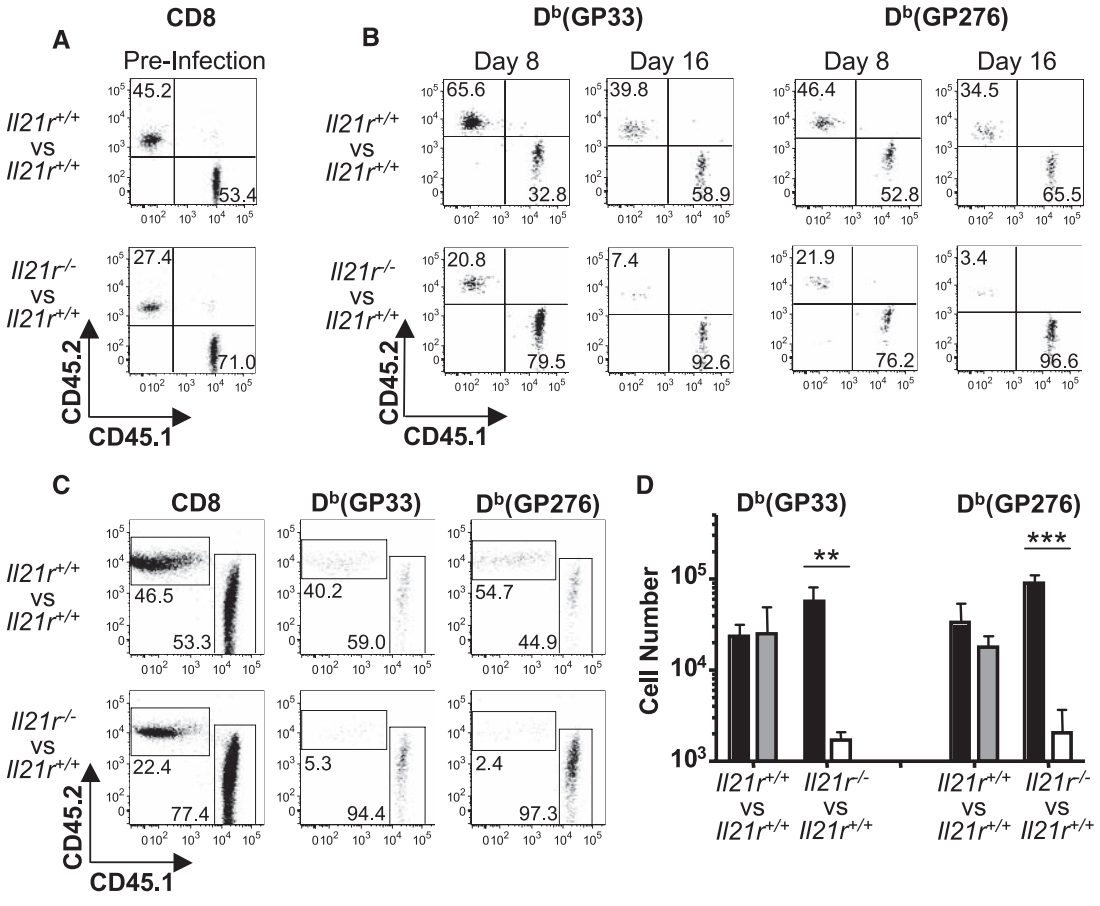

Fig. 3. IL-21 acts directly to sustain virus-specific CD8$^+$ T cells during an ongoing infection. Cohorts of control *Il21r*$^{+/+}$/*Il21r*$^{+/+}$ (CD45.1/CD45.2) and experimental *Il21r*$^{+/+}$/*Il21r*$^{-/-}$ (CD45.1/CD45.2) mixed bone-marrow chimeras were infected with LCMV-Cl 13 and CD8$^+$ T cell responses evaluated over time. (**A**) Peripheral blood mononuclear cells were evaluated by flow cytometry to check reconstitution of CD8$^+$ T cells in *Il21r*$^{+/+}$/*Il21r*$^{+/+}$ or *Il21r*$^{+/+}$/*Il21r*$^{-/-}$ mixed bone-marrow chimeras before infection. Gated CD8$^+$ T cells are shown. (**B**) Flow cytometric analysis of GP_{33}- and GP_{276}-specific CD8$^+$ T cell responses in the circulation at days 8 and 16 after infection. Gated tetramer$^+$ CD8$^+$ T cells are shown. (**C**) Flow cytometric analysis of splenic CD8$^+$ T cells and GP_{33}- and GP_{276}-specific responses at 3 weeks after infection. Gated CD8$^+$ (left) or CD8$^+$ tetramer$^+$ (right) cells are shown. (**D**) Absolute numbers of GP_{33}- and GP_{276}-specific CD8$^+$ T cells in mixed bone-marrow chimeras 3 weeks after infection. Graphs represent average + SD of *Il21r*$^{+/+}$ CD45.1 CD8$^+$ T cells (black), *Il21r*$^{+/+}$ CD45.2 CD8$^+$ T cells (gray), and *Il21r*$^{-/-}$ CD45.2 CD8 T cells (white). $^{**}P < 0.01$, $^{***}P < 0.001$. Representative results are shown from one of two similar experiments ($n = 7$ and 8 for *Il21r*$^{+/+}$/*Il21r*$^{+/+}$ and *Il21r*$^{+/+}$/*Il21r*$^{-/-}$ cohorts, respectively).

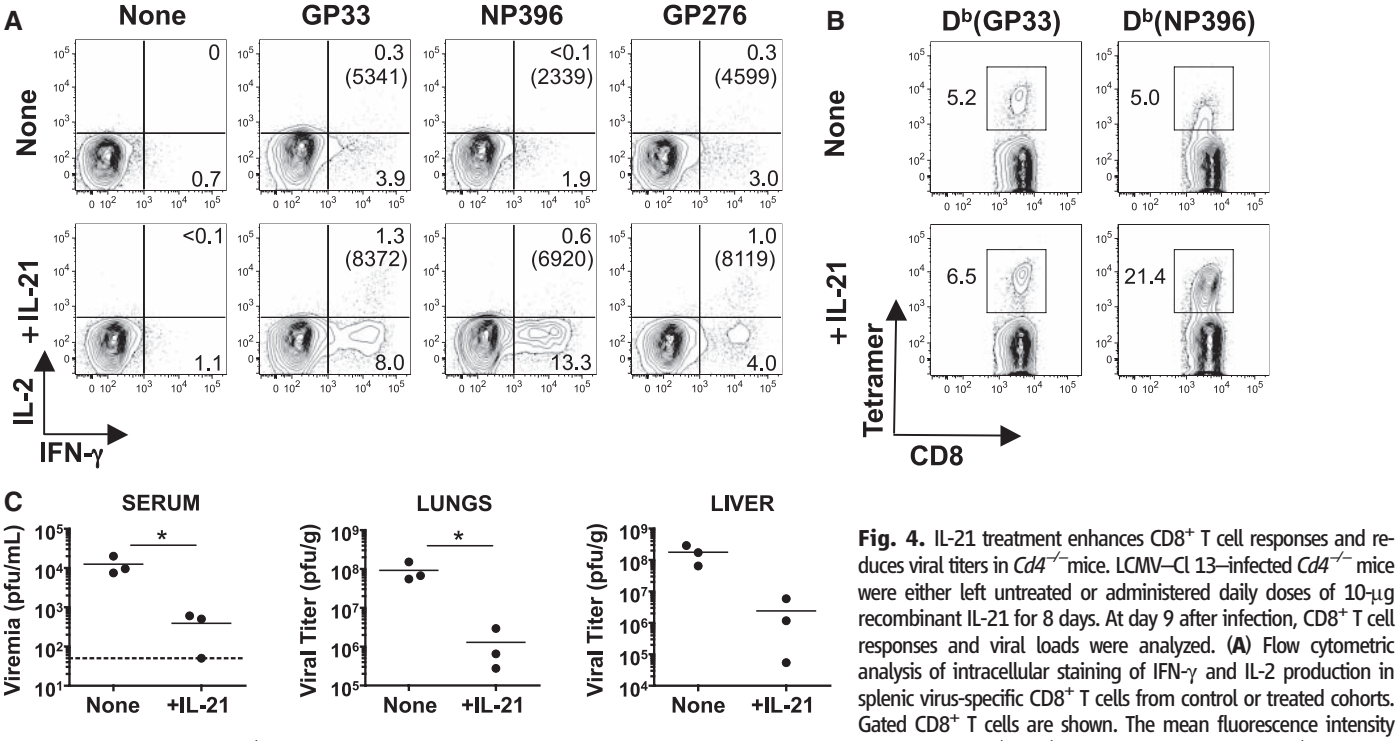

Fig. 4. IL-21 treatment enhances CD8$^+$ T cell responses and reduces viral titers in *Cd4*$^{-/-}$ mice. LCMV–Cl 13–infected *Cd4*$^{-/-}$ mice were either left untreated or administered daily doses of 10-μg recombinant IL-21 for 8 days. At day 9 after infection, CD8$^+$ T cell responses and viral loads were analyzed. (**A**) Flow cytometric analysis of intracellular staining of IFN-γ and IL-2 production in splenic virus-specific CD8$^+$ T cells from control or treated cohorts. Gated CD8$^+$ T cells are shown. The mean fluorescence intensity (MFI) of IFN-γ–producing CD8$^+$ T cells is reported in parentheses. (**B**) Flow cytometric analysis of GP_{33} and NP_{396} tetramer$^+$ CD8$^+$ T cells. Plots show gated CD8$^+$ T cells. (**C**) Viral titers were assessed in the serum, lungs, and liver of control and IL-21–treated mice. Dotted line indicates the limit of detection (50 PFU/ml) for serum samples. $^*P < 0.05$. Representative results from one of two independent experiments are shown ($n = 7$ and 6 for control and treated groups, respectively).

tial phase of chronic viral infection, suggesting that this could be a general feature of infections that elicit nonprotective adaptive immune responses, such as hepatitis B virus, HCV, and HIV (*8*, *30*). This poor induction of IL-21 may result from the failure to initiate robust $CD4^+$ T cell responses as well as the exhaustion or the viral-induced depletion of these cells that may occur during certain chronic infections. Therefore, we anticipate that the cautious development of approaches to modulate the levels of IL-21, or regulate the induction of cellular subsets that generate IL-21, will provide new therapeutic opportunities to improve immunity to diseases that require $CD8^+$ T cell responses to be controlled, such as chronic viral infection and tumors.

References and Notes

1. D. Moskophidis, F. Lechner, H. Pircher, R. M. Zinkernagel, *Nature* **362**, 758 (1993).
2. M. Matloubian, R. J. Concepcion, R. Ahmed, *J. Virol.* **68**, 8056 (1994).
3. A. Oxenius, R. M. Zinkernagel, H. Hengartner, *Immunity* **9**, 449 (1998).
4. A. Gallimore *et al.*, *J. Exp. Med.* **187**, 1383 (1998).
5. A. J. Zajac *et al.*, *J. Exp. Med.* **188**, 2205 (1998).
6. M. J. Fuller, A. Khanolkar, A. E. Tebo, A. J. Zajac, *J. Immunol.* **172**, 4204 (2004).
7. D. G. Brooks, L. Teyton, M. B. Oldstone, D. B. McGavern, *J. Virol.* **79**, 10514 (2005).
8. N. L. Letvin, B. D. Walker, *Nat. Med.* **9**, 861 (2003).
9. E. J. Wherry, J. N. Blattman, K. Murali-Krishna, R. van der Most, R. Ahmed, *J. Virol.* **77**, 4911 (2003).
10. M. Battegay *et al.*, *J. Virol.* **68**, 4700 (1994).
11. M. G. von Herrath, M. Yokoyama, J. Dockter, M. B. Oldstone, J. L. Whitton, *J. Virol.* **70**, 1072 (1996).
12. G. T. Belz, D. Wodarz, G. Diaz, M. A. Nowak, P. C. Doherty, *J. Virol.* **76**, 12388 (2002).
13. C. Bourgeois, H. Veiga-Fernandes, A. M. Joret, B. Rocha, C. Tanchot, *Eur. J. Immunol.* **32**, 2199 (2002).
14. E. M. Janssen *et al.*, *Nature* **421**, 852 (2003).
15. D. J. Shedlock, H. Shen, *Science* **300**, 337 (2003).
16. J. C. Sun, M. J. Bevan, *Science* **300**, 339 (2003).
17. C. M. Smith *et al.*, *Nat. Immunol.* **5**, 1143 (2004).
18. A. Khanolkar, M. J. Fuller, A. J. Zajac, *J. Immunol.* **172**, 2834 (2004).
19. J. Parrish-Novak *et al.*, *Nature* **408**, 57 (2000).
20. K. Brandt, P. B. Singh, S. Bulfone-Paus, R. Ruckert, *Cytokine Growth Factor Rev.* **18**, 223 (2007).
21. R. Spolski, W. J. Leonard, *Annu. Rev. Immunol.* **26**, 57 (2008).
22. K. Ozaki *et al.*, *Science* **298**, 1630 (2002).
23. T. Korn *et al.*, *Nature* **448**, 484 (2007).
24. N. Fazilleau, L. Mark, L. J. McHeyzer-Williams, M. G. McHeyzer-Williams, *Immunity* **30**, 324 (2009).
25. Materials and methods are available as supporting material on *Science* Online.
26. R. Ahmed, A. Salmi, L. D. Butler, J. M. Chiller, M. B. Oldstone, *J. Exp. Med.* **160**, 521 (1984).
27. M. J. Buchmeier, A. J. Zajac, in *Persistent Viral Infections*, R. Ahmed, I. S. Y. Chen, Eds. (Wiley, West Sussex, UK, 1999), pp. 575–605.
28. R. Zeng *et al.*, *J. Exp. Med.* **201**, 139 (2005).
29. M. G. Dodds *et al.*, *Cancer Immunol. Immunother.* **58**, 843 (2009).
30. C. Boni *et al.*, *J. Virol.* **81**, 4215 (2007).

31. We thank L. Harrington, P. Goepfert, B. Hahn, G. Shaw, and the members of the Zajac laboratory for discussions and assistance. This work was supported by grants AI049360 and AI067993 (to A.J.Z.) and T32 AI007051 (to J.S.Y.) from the NIH.

Supporting Online Material

www.sciencemag.org/cgi/content/full/1175194/DC1
Materials and Methods
Figs. S1 to S5
References

23 October 2008; accepted 6 May 2009
Published online 14 May 2009;
10.1126/science.1175194
Include this information when citing this paper.

IL-21R on T Cells Is Critical for Sustained Functionality and Control of Chronic Viral Infection

Anja Fröhlich,[1] Jan Kisielow,[1] Iwana Schmitz,[1] Stefan Freigang,[1] Abdijapar T. Shamshiev,[1] Jacqueline Weber,[1] Benjamin J. Marsland,[1] Annette Oxenius,[2] Manfred Kopf[1]*

Chronic viral infection is often associated with the dysfunction of virus-specific T cells. Our studies using *Il21r*-deficient (*Il21r*$^{-/-}$) mice now suggest that interleukin-21 (IL-21) is critical for the long-term maintenance and functionality of $CD8^+$ T cells and the control of chronic lymphocytic choriomeningitis virus infection in mice. Cell-autonomous IL-21 receptor (IL-21R)–dependent signaling by $CD8^+$ T cells was required for sustained cell proliferation and cytokine production during chronic infection. *Il21r*$^{-/-}$ mice showed normal $CD8^+$ T cell expansion, effector function, memory homeostasis, and recall responses during acute and after resolved infection with several other nonpersistent viruses. These data suggest that IL-21R signaling is required for the maintenance of polyfunctional T cells during chronic viral infections and have implications for understanding the immune response to other persisting antigens, such as tumors.

Chronic viral infections, including HIV and hepatitis B and C viruses (HBV and HCV), afflict >0.5 billion people worldwide. Although the reasons for ineffective antiviral immunity remain poorly defined, studies of chronic infection with lymphocytic choriomeningitis virus (LCMV) in mice and HIV, HCV, and HBV in humans show that the loss of T cell functionality, termed exhaustion, is a hallmark of chronic infection (*1*). Long-term maintenance of potent virus-specific $CD8^+$ T cell responses requires help from $CD4^+$ T cells and cytokines produced by T and non-T cells (*2*, *3*). Specifically, members of a cytokine subfamily with receptors sharing the common gamma (γ_c) chain such as interleukin-2 (IL-2), IL-7, and IL-15 have distinct activities on the development and maintenance of antiviral effector and memory T cells (*4*–*8*). IL-21, an additional family member, has pleiotropic activities on $CD4^+$ T cells (*9*), although its role in antiviral $CD8^+$ T cell responses is unknown.

LCMV can cause acute or persistent infection, depending on the viral isolate and the dose of infection. High-dose infection with the fast-replicating strain LCMV-Docile (or strain Clone 13) results in virus persistence and exhausted virus-specific $CD8^+$ T cells. In contrast, low-dose infection is efficiently cleared in immunocompetent mice.

To study the role of IL-21 in acute and chronic viral infection, we infected control and *Il21r*$^{-/-}$ mice with low- [200 plaque-forming units (PFU)], intermediate- (2000 PFU), or high-dose (2×10^6 PFU) LCMV-Docile. Comparable expansion, cytokine production, and killing of virus-infected targets by viral epitope gp_{33-41}–specific $CD8^+$ T cells were observed 8 days after infection, indicating that the IL-21 receptor (IL-21R) was not required for priming and differentiation of virus-specific $CD8^+$ T cells during the acute response (Fig. 1, A to C, and fig. S1, A to G). As expected, control mice infected with low or intermediate doses mounted efficient long-term antiviral $CD8^+$ T cell responses and controlled the infection (Fig. 1, A to F), whereas infection with high-dose LCMV-Docile resulted in reduced frequencies of and interferon-γ (IFN-γ) production by virus-specific T cells (Fig. 1, A to C), in addition to viral persistence (Fig. 1F). We detected exhausted *Il21r*$^{-/-}$ LCMV-specific $CD8^+$ T cells in response to low and intermediate virus doses starting at day 15 after infection (Fig. 1, A to D). After 5 weeks, we observed reduced frequencies and total numbers of gp_{33-41}-specific *Il21r*$^{-/-}$ $CD8^+$ T cells in the blood and spleen. Moreover, the remaining gp_{33-41}-specific $CD8^+$ T cells failed to produce IFN-γ, tumor necrosis factor–α, and IL-2 and did not proliferate upon stimulation, all of which are characteristics of exhausted T cells (Fig. 1C and fig. S1, H and I). Consequently, *Il21r*$^{-/-}$ mice developed chronic viremia after exposure to low or intermediate doses of virus (Fig. 1E and fig. S1K). Even at high-dose exposure, when both control and *Il21r*$^{-/-}$ mice developed a chronic infection, viral titers were increased in the latter (Fig. 1F). The fre-

[1]Molecular Biomedicine, Institute of Integrative Biology, ETH Zurich, Switzerland. [2]Institute of Microbiology, ETH Zurich, Switzerland.

*To whom correspondence should be addressed. E-mail: Manfred.Kopf@ethz.ch

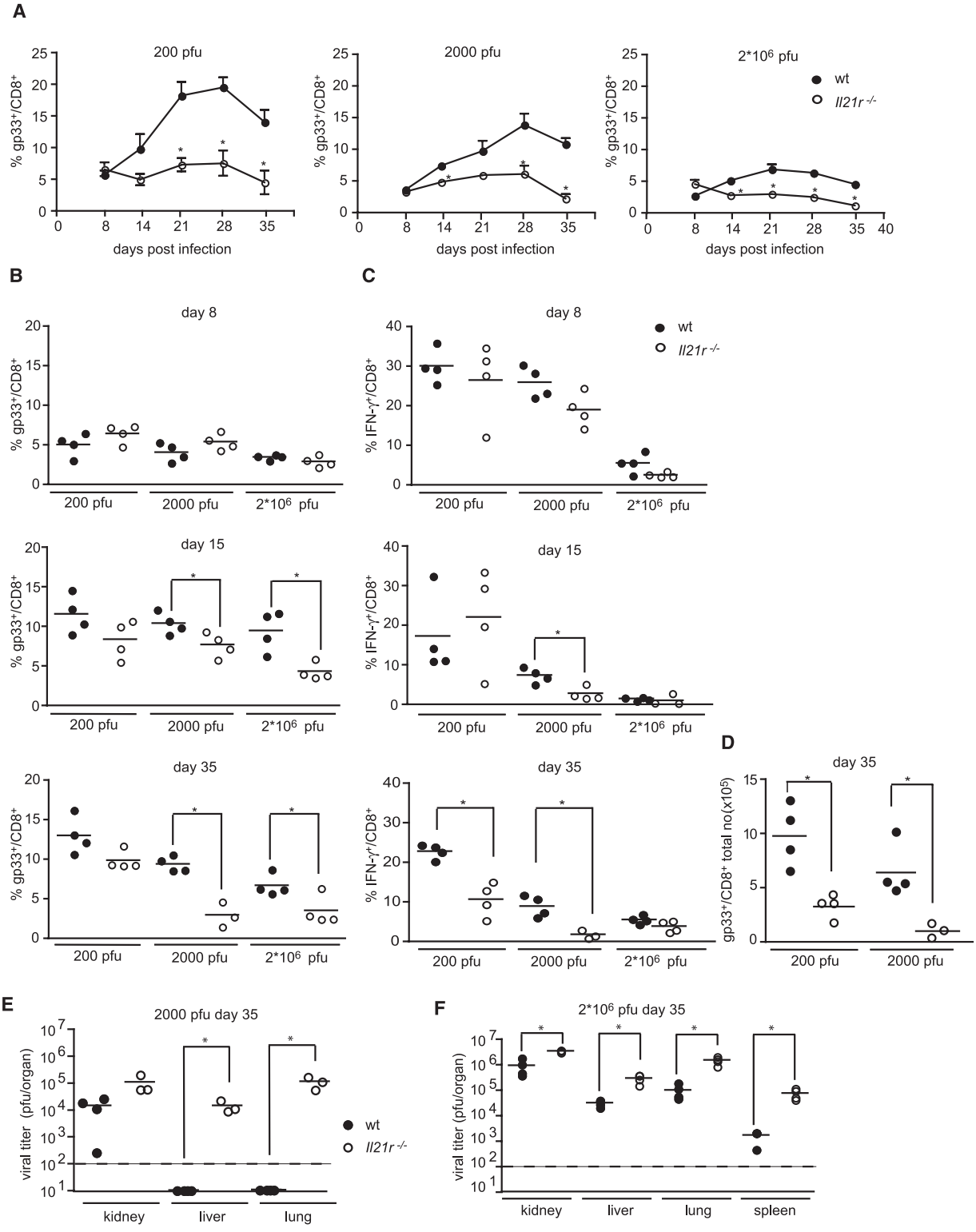

Fig. 1. IL-21R is essential for sustained antiviral $CD8^+$ T cell responses and control of viral infection. Control and *Il21r*$^{-/-}$ mice were infected with the indicated doses of LCMV-Docile. Blood samples (**A**) and splenocytes (**B** to **D**) were taken to monitor the presence of $CD8^+$ T cells specific for the gp_{33-41} epitope [(A), (B), and (D)] by flow cytometry. wt, wild-type control. Splenocytes were stimulated with gp_{33-41} peptide 4 hours before intracellular staining with antibodies to the indicated cytokines (C). Graphs show frequencies of $gp_{33-41}{}^+$ cells [(A) and (B)] and IFN-γ^+ cells (C) of $CD8^+$ T cells or total number of $gp_{33-41}{}^+$ $CD8^+$ T cells (D). Values indicate averages ± SEM of four mice per group (A) or individual mice [(B) to (D)]. Viral titers in indicated organs at day 35 after infection with 2000 PFU (**E**) or 2×10^6 PFU (**F**) of LCMV-Docile are shown. Symbols represent values of individual mice. *$P < 0.05$. Representative data are shown from three independent experiments.

quency of IL-2– or IFN-γ–producing gp_{61-80}-specific $CD4^+$ T cells was not affected in *Il21r*$^{-/-}$ mice (fig. S1L). LCMV-specific neutralizing antibodies appeared late after infection (*10*) and were undetectable in both control and *Il21r*$^{-/-}$ mice up to 70 days after infection, whereas we observed nonneutralizing LCMV-specific immunoglobulin G antibodies at day 19 in control mice and reduced by a factor of 3 in *Il21r*$^{-/-}$ mice infected with LCMV-Docile or LCMV-WE (fig. S1, M and N).

Il21r$^{-/-}$ mice showed normal acute $CD8^+$ T cell responses to and viral clearance of infection with both influenza virus and vaccinia virus (fig. S2). Together, these results suggest that IL-21R was dispensable for acute antiviral $CD8^+$ T cell responses, but was essential for maintenance of virus-specific $CD8^+$ T cells, sustained effector responses, and eventual control of chronic infection.

To address whether IL-21R was required for memory T cell responses, we studied infection with LCMV strain WE, which is less virulent than LCMV-Docile and is cleared by $CD8^+$ T cells by day 10 after infection. Antigen-experienced LCMV-specific $CD8^+$ T cells constitute a stable pool of memory cells over long periods of time (*11*–*13*). We observed no differences in gp_{33-41}-specific $CD8^+$ T cell frequencies in the blood between *Il21r*$^{-/-}$ and control mice up to 70 days after infection (Fig. 2A), At day 35, maintenance, cytokine production, and proliferation of memory gp_{33-41}–specific $CD8^+$ T cells were unaffected in *Il21r*$^{-/-}$ mice (fig. S3). Hence, virus was effectively controlled and undetectable in the blood from day 11 up to day 75 after infection (fig. S1O). Memory mice were then challenged with a high dose of LCMV-WE, which triggered rapid expansion and cytokine production of gp_{33-41}-specific memory $CD8^+$ T cells in both *Il21r*$^{-/-}$ and control mice, indicating efficient and protective recall responses in the absence of IL-21R (Fig. 2, B and C). In addition, we observed efficient recall responses of *Il21r*$^{-/-}$ mice after immunization with replication-incompetent virus-like particles and challenge with vaccinia virus. (fig. S4). Taken together, these data clearly demonstrate that IL-21R is dispensable for efficient CD8 T cell effector and memory responses during acute and resolved infection with nonpersistent viruses.

We next generated mixed bone-marrow chimeras in which the marrow of irradiated C57BL/6 (B6) mice ($CD45.1^+$) was reconstituted with a 1:1 mixture of bone marrow from *Il21r*$^{-/-}$ ($CD45.2^+$) and control ($CD45.1^+$) mice, and 1:1 chimerism was confirmed in both $CD4^+$ and $CD8^+$ T cells (fig. S5A). After infection with LCMV-Docile, both control and IL-21R–deficient $CD8^+$ T cells expanded comparably during the acute phase (Fig. 3A), whereas we saw dramatic differences in $CD8^+$ T cell maintenance starting at 2 weeks after infection (Fig. 3, A and B). At day 35, the frequency of gp_{33-41}-specific *Il21r*$^{-/-}$ $CD8^+$ T cells and IFN-γ–producing $CD8^+$ T cells was reduced as compared with that in controls (1.3 ± 0.5% versus 6.7 ± 2.2% and 1.22 ± 1% versus 4.9 ±1.8%,

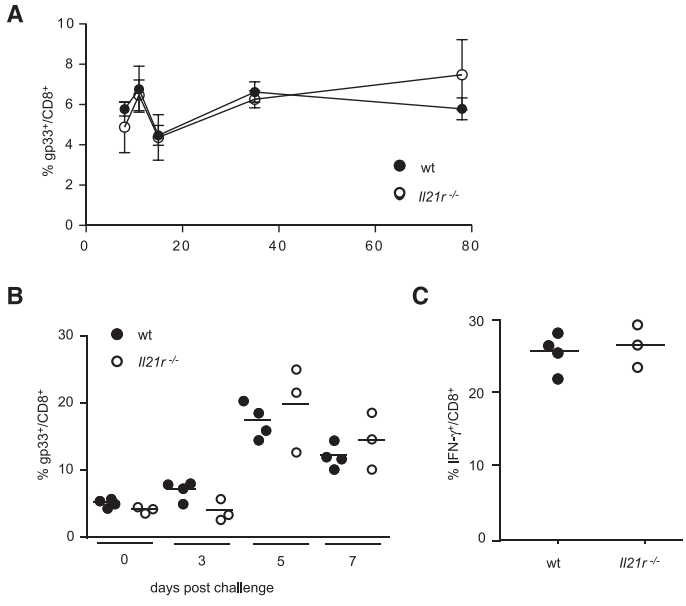

Fig. 2. IL-21R is not required for $CD8^+$ T cell memory and recall after resolved viral infection. Control and *Il21r*$^{-/-}$ mice were infected with 2000 PFU of LCMV-WE. (**A**) Gp_{33-41}-specific $CD8^+$ T cells were measured in the blood at indicated days. (**B** and **C**) LCMV-WE–infected mice were challenged with 2×10^6 PFU of LCMV-Docile at day 50. Frequencies of gp_{33-41}-specific $CD8^+$ T cells in the blood at indicated days (B) and IFN-γ–producing gp_{33-41}-specific T cells in the spleen at day 7 after challenge (C) are shown. Values indicate percentages and represent averages of groups of mice (n = 4 or 5 per group) ± SD (A). Symbols represent individual mice [(B) and (C)]. Representative data are shown from two independent experiments.

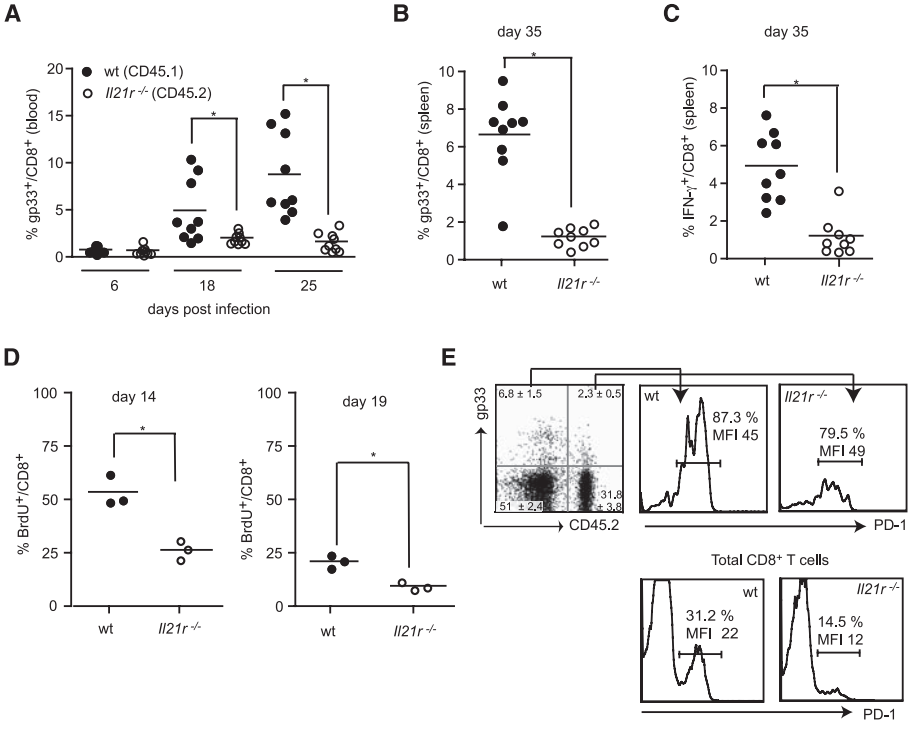

Fig. 3. IL-21R signaling is required for sustained in vivo proliferation of antiviral $CD8^+$ T cells. IL-$21R^{+/+}$ (wt) ($CD45.1$)/*Il21r*$^{-/-}$ ($CD45.2$) mixed bone-marrow chimeras were infected with 2000 PFU of LCMV-Docile, and antiviral $CD8^+$ T cell responses were measured in the blood (**A**) and in the spleen (**B** to **E**). Shown are frequencies of wt or IL-21R–deficient gp_{33-41}-specific $CD8^+$ T cells at indicated days [(A) and (B)] and gp_{33-41}-specific T cells producing IFN-γ at day 35 (C), as measured by intracellular staining. (D) At day 10 after infection, bone-marrow chimeras received daily injections of BrdU for 4 days, and BrdU incorporation by wt or IL-21R–deficient $CD8^+$ T cells was determined by BrdU staining and flow cytometry 1 and 5 days later (days 14 and 19). (E) Flow cytometric analysis of PD-1 expression by wt and IL-21R–deficient $CD8^+$ T cells at day 35 after infection. Graphs represent histograms of PD-1 expression by control ($CD45.1$) or *Il21r*$^{-/-}$ ($CD45.2$) cells gated on gp_{33-41}-specific $CD8^+$ T cells (top) or total $CD8^+$ T cells (bottom). MFI, mean fluorescence intensity. Graphs show a representative sample of a group of mice (n = 4). Values indicate average ± SD. Representative data are shown from two independent experiments.

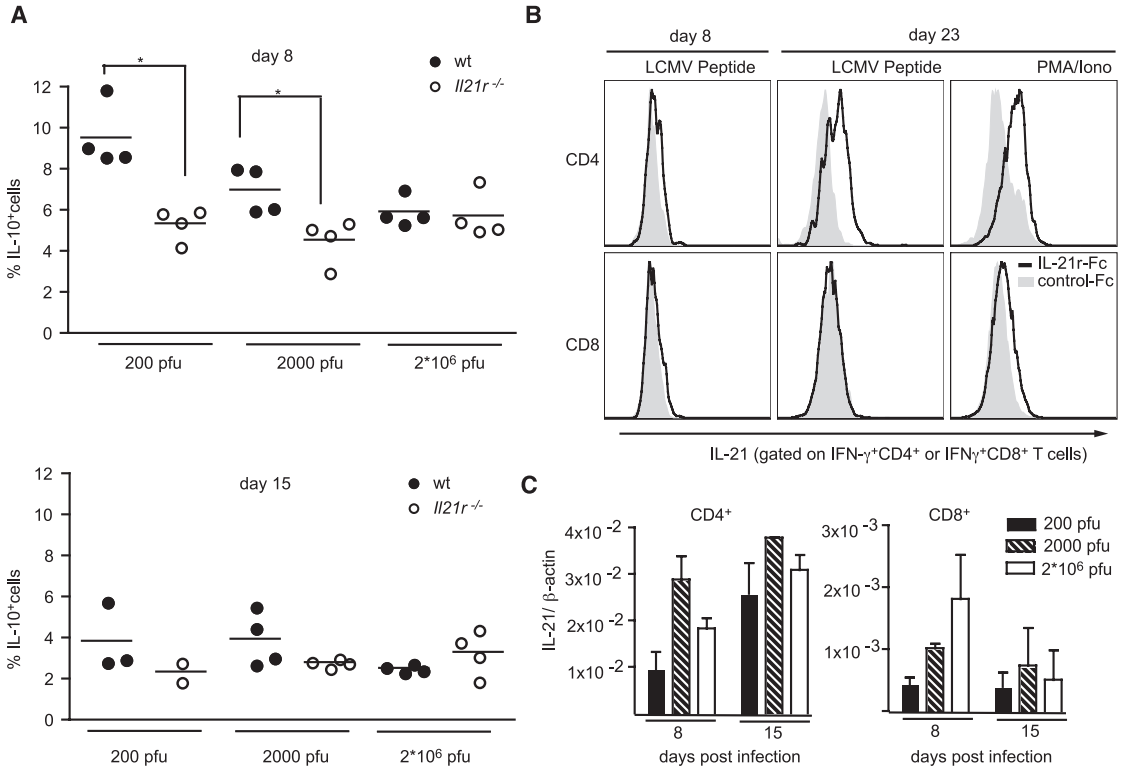

Fig. 4. IL-21 is mainly produced by virus-specific $CD4^+$ T cells. Groups of mice were infected with indicated doses LCMV-Docile. (**A** and **B**) At indicated days, splenocytes were cultured with gp_{33-41} or gp_{61-80} (100 nM) in the presence of monensin for 5 hours before staining of CD4, CD8, CD11c, and CD11b cells by specific monoclonal antibodies and intracellular IL-10 or IL-21, and then analyzed by flow cytometry. (A) Frequency of IL-10–producing cells gated on $CD11b^+$ cells. (B) Histograms show IL-21 production stained with an IL-21R–Fc fusion protein by gp_{61-80}-specific $CD4^+$ IFN-γ^+ cells (top) and by gp_{33-41}-specific $CD8^+$ IFN-γ^+ cells (bottom) at indicated days after infection with 2000 PFU of LCMV-Docile. Shaded curves represent staining with a control Fc fusion protein. IL-21$^+$ IFN-γ^{neg} cells were undetectable. PMA, phorbol 12-myristate 13-acetate; iono, calcium ionophore. (**C**) IL-21 expression by $CD4^+$ and $CD8^+$ T cells (purity >90%) from infected mice as measured by quantitative polymerase chain reaction. Representative data are shown from two independent experiments [(A) and (B)].

respectively) (Fig. 3, B and C), demonstrating that $CD8^+$ T cells required cell-autonomous IL-21R signaling for sustained responses during chronic LCMV infection. The virus was not cleared by day 35 in mixed bone-marrow chimeras (fig. S5B). Reduced frequencies of LCMV-specific IL-21R–deficient $CD8^+$ T cells may result from impaired proliferation or from increased cell death. To address this question, LCMV-Docile–infected mixed bone-marrow chimeras were injected with bromodeoxyuridine (BrdU) at 24-hour intervals from days 10 to 13 after infection. IL-21R–deficient $CD8^+$ T cells showed strikingly reduced proliferation as compared with control $CD8^+$ T cells (50% versus 25%) at day 14 after infection (Fig. 3D). Six days after the last pulse, $BrdU^+$ populations of control and *Il21r*$^{-/-}$ $CD8^+$ T cells were reduced by half (~20% versus 10%) (Fig. 3D) as compared with the respective populations at day 14, which indicated a similar contraction of control and IL-21R–deficient $CD8^+$ T cells. These data suggest that IL-21R–dependent signaling in $CD8^+$ T cells was required for their continuous proliferation during chronic infection and not for their survival.

Chronic viral infection and $CD8^+$ T cell dysfunction have been strongly associated with sustained expression of the inhibitory receptor programmed death 1 (PD-1) (*14*, *15*). We found that PD-1 was strongly expressed by the vast majority of both gp_{33-41}-specific control and *Il21r*$^{-/-}$ $CD8^+$ T cells in mixed bone-marrow chimeras 5 weeks after infection. (Fig. 3E). Similar results were obtained by comparing PD-1 expression on $CD8^+$ T cells in control and *Il21r*$^{-/-}$ mice (fig. S6).

Like PD-1, the inhibitory cytokine IL-10 can interfere with antiviral T cell responses and the clearance of LCMV (*16*, *17*). The frequency of IL-10–producing cells peaked in the acute phase of LCMV infection. Surprisingly, the frequency of IL-10–producing cells was decreased in *Il21r*$^{-/-}$ mice (Fig. 4A). Most $IL\text{-}10^+$ cells were macrophages (fig. S7). Thus, $CD8^+$ T cell exhaustion in *Il21r*$^{-/-}$ mice is not associated with up-regulation of IL-10.

The above results demonstrate that virus-specific $CD8^+$ T cells require IL-21 to prevent exhaustion during chronic viral infection. We next wanted to define the cellular source of IL-21. Intracellular staining showed that a fraction of gp_{61-80} epitope–specific $CD4^+$ T cells coproduced IFN-γ and IL-21 in response to LCMV-Docile infection, whereas substantial IL-21 production by virus-specific $CD8^+$ T cells was detectable only by combined phorbol ester and calcium ionophore stimulation (Fig. 4B). Consistent with protein expression, IL-21 mRNA expression was considerably higher in $CD4^+$ than in $CD8^+$ T cells (Fig. 4C). Thus, $CD4^+$ T cells are the likely source of IL-21 that helps to sustain $CD8^+$ T cell functionality, although autocrine-produced IL-21, or IL-21 produced by another immune cell, may also play a role. Among $CD4^+$ subsets, T helper cell 17 cells have been suggested to be the main producers of IL-21; however, we did not detect IL-17–producing gp_{61-80}-specific $CD4^+$ T cells at days 8 and 15 after infection (fig. S7C)

Our data show that IL-21–dependent signaling is critical for the prevention of T cell exhaustion and control of chronic viral infection. Comparison of IL-21R and IL-2R–dependent signaling in the regulation of antiviral T cell responses reveals interesting differences in the requirements for γ_c cytokines during viral infection. Although both IL-2Rα and IL-21R are dispensable for acute $CD8^+$ T cell expansion and effector function (*4*, *5*), they are both essential for the maintenance of $CD8^+$ T cells during chronic infection (*4*). In contrast, only IL-2Rα is required for recall responses. During the acute primary response, it is thought that IL-2 programs the long-term fate of $CD8^+$ T cells to mount a secondary response (*5*). IL-2 therapy during the chronic phase has been shown to enhance antiviral $CD8^+$ T cell responses and viral clearance (*18*). Our results imply that a combination therapy of IL-2 and IL-21 may be more beneficial for treatment of chronic viral infection.

References and Notes

1. H. Shin, E. J. Wherry, *Curr. Opin. Immunol.* **19**, 408 (2007).
2. M. Altfeld, E. S. Rosenberg, *Curr. Opin. Immunol.* **12**, 375 (2000).
3. L. J. Picker, V. C. Maino, *Curr. Opin. Immunol.* **12**, 381 (2000).
4. M. F. Bachmann, P. Wolint, S. Walton, K. Schwarz, A. Oxenius, *Eur. J. Immunol.* **37**, 1502 (2007).

5. M. A. Williams, A. J. Tyznik, M. J. Bevan, *Nature* **441**, 890 (2006).
6. T. C. Becker *et al.*, *J. Exp. Med.* **195**, 1541 (2002).
7. A. W. Goldrath *et al.*, *J. Exp. Med.* **195**, 1515 (2002).
8. J. T. Tan *et al.*, *J. Exp. Med.* **195**, 1523 (2002).
9. R. Spolski, W. J. Leonard, *Annu. Rev. Immunol.* **26**, 57 (2008).
10. L. Hangartner, R. M. Zinkernagel, H. Hengartner, *Nat. Rev. Immunol.* **6**, 231 (2006).
11. S. M. Kaech, E. J. Wherry, *Immunity* **27**, 393 (2007).
12. K. Murali-Krishna *et al.*, *Immunity* **8**, 177 (1998).
13. P. Wolint, M. R. Betts, R. A. Koup, A. Oxenius, *J. Exp. Med.* **199**, 925 (2004).
14. D. L. Barber *et al.*, *Nature* **439**, 682 (2006).
15. C. L. Day *et al.*, *Nature* **443**, 350 (2006).
16. D. G. Brooks *et al.*, *Nat. Med.* **12**, 1301 (2006).
17. M. Ejrnaes *et al.*, *J. Exp. Med.* **203**, 2461 (2006).
18. J. N. Blattman *et al.*, *Nat. Med.* **9**, 540 (2003).

19. This project was funded by Swiss National Science Foundation 310030_124922.

Supporting Online Material
www.sciencemag.org/cgi/content/full/1172815/DC1
Materials and Methods
Figs. S1 to S7
References

26 February 2009; accepted 20 May 2009
Published online 28 May 2009;
10.1126/science.1172815
Include this information when citing this paper.

Merkel Cells Are Essential for Light-Touch Responses

Stephen M. Maricich,[1]* Scott A. Wellnitz,[2] Aislyn M. Nelson,[2] Daine R. Lesniak,[3] Gregory J. Gerling,[3] Ellen A. Lumpkin,[2,4,5,6]† Huda Y. Zoghbi[1,2,5,6,7]†

The peripheral nervous system detects different somatosensory stimuli, including pain, temperature, and touch. Merkel cell-neurite complexes are touch receptors composed of sensory afferents and Merkel cells. The role that Merkel cells play in light-touch responses has been the center of controversy for over 100 years. We used *Cre-loxP* technology to conditionally delete the transcription factor *Atoh1* from the body skin and foot pads of mice. Merkel cells are absent from these areas in $Atoh1^{CKO}$ animals. Ex vivo skin/nerve preparations from $Atoh1^{CKO}$ animals demonstrate complete loss of the characteristic neurophysiologic responses normally mediated by Merkel cell-neurite complexes. Merkel cells are, therefore, required for the proper encoding of Merkel receptor responses, suggesting that these cells form an indispensible part of the somatosensory system.

Different qualities of touch are encoded by discrete touch receptors, each with distinctive coding properties (*1*–*3*). One form of light touch important for tactile discrimination of shapes and textures is mediated by Merkel cell-neurite complexes, which exhibit a characteristic response to light skin indentation (*4*, *5*). Merkel cell-neurite complexes are composed of nerve fibers associated with Merkel cells, an enigmatic skin cell population first described in 1875 (*6*). In mammalian skin, Merkel cells are normally found in whisker follicles of the face, specialized epithelial structures of the hairy skin called touch domes, and epidermal invaginations of the plantar foot surface called rete ridges (*7*). Merkel cells have been proposed to be the sensory receptor cells of the complexes because they form synaptic contacts with somatosensory afferents (*8*, *9*); however, studies that indirectly tested this model have yielded conflicting results (*10*–*16*).

Atoh1 is a basic helix-loop-helix transcription factor expressed by Merkel cells in all areas of the skin (*17*). *Atoh1* null mice die within minutes of birth, which prevents a detailed assessment of nonlethal phenotypes resulting from deletion of the gene. We used the $Hoxb1^{Cre}$ allele (*18*), which is expressed throughout the dermis and epidermis of body skin, but not head skin (Fig. 1, A to A″), to delete a floxed allele of *Atoh1* ($Atoh1^{flox}$) (*19*) in transgenic mice (*20*). Conditional knockout ($Atoh1^{CKO}$) animals were born in the expected Mendelian ratio, but roughly 50% of these animals died within 24 to 36 hours of birth.

The overall structure of the touch dome, including the palisading epithelium and location of the guard hair, was preserved in $Atoh1^{CKO}$ animals (Fig. 1, B and C, and Fig. 2, A and B). Atoh1 is a positive autoregulator of its own expression (*21*), so we analyzed β-galactosidase expression driven by the $Atoh1^{LacZ}$ knock-in allele (*22*) to demonstrate that *Atoh1* was deleted from the skin of E16.5 $Atoh1^{CKO}$ mice (Fig. 1, B and C). Xgal staining was found in touch domes and foot pads of heterozygous $Atoh1^{LacZ/+}$ mice but not $Atoh1^{CKO}$ animals (Fig. 1, B′ and C′). To determine whether Merkel cells were present, we

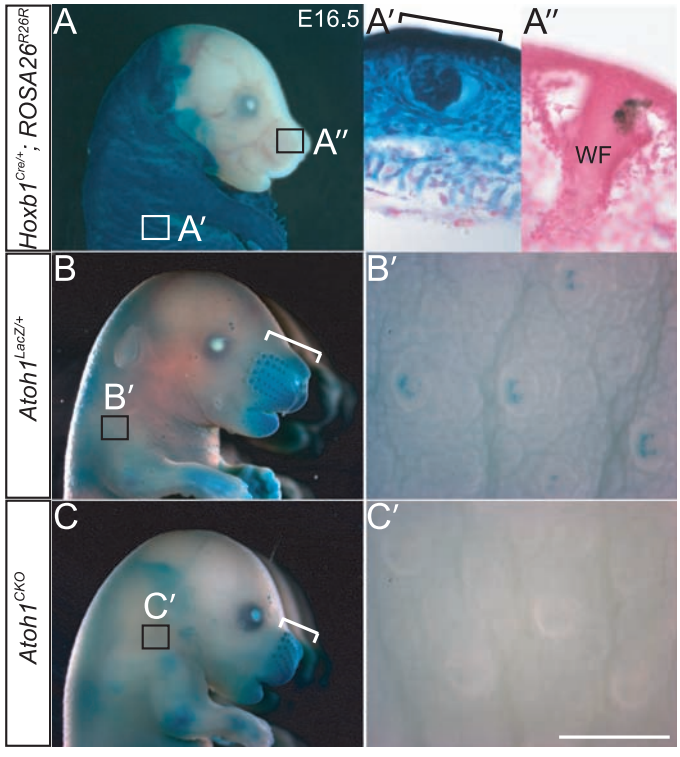

Fig. 1. $Hoxb1^{Cre}$ abolishes $Atoh1^{flox}$ expression in the body but not the face. Wholemount X-gal staining of E16.5 embryos revealed β-galactosidase expression driven from the $ROSA^{R26R}$ (**A** to **A″**) or $Atoh1^{LacZ}$ (**B** to **C′**) loci. (A) $Hoxb1^{Cre/+}$; $ROSA^{R26R}$ embryo. $Hoxb1^{Cre}$ expression is absent from the majority of the head. Boxes denote regions shown in (A′) and (A″). (A′ and A″) Body skin and whisker pad, respectively, from a $Hoxb1^{Cre/+}$; $ROSA^{R26R}$ embryo counterstained with nuclear fast red. Staining is present throughout the epidermis and dermis of the body skin, whereas virtually no staining is seen in the whisker pad. The bracket in (A′) denotes a developing touch dome. WF, whisker follicle. (B) $Atoh1^{LacZ/+}$ embryo showing β-galactosidase expression in the whisker pad (bracket) and touch domes of the skin. The box denotes the region shown in (B′). (B′) $Hoxb1^{+/+}$; $Atoh1^{LacZ/flox}$ embryo body skin showing staining in individual touch domes. (C) $Atoh1^{CKO}$ embryo showing β-galactosidase expression driven from the *Atoh1* locus in the whisker pad (bracket), but absent from touch domes of the skin (box). (C′) $Atoh1^{CKO}$ embryo body skin. Touch domes are present but lack the WT staining pattern. Scale bars, 5 mm [(A), (B), and (C)]; 400 μm [(B′) and (C′)]; 100 μm [(A′) and (A″)].

[1]Department of Pediatrics, Baylor College of Medicine, Houston, TX 77030, USA. [2]Department of Neuroscience, Baylor College of Medicine, Houston, TX 77030, USA. [3]Department of Systems and Information Engineering, University of Virginia, Charlottesville, VA 22904, USA. [4]Department of Molecular Physiology and Biophysics, Baylor College of Medicine, Houston, TX 77030, USA. [5]Department of Molecular and Human Genetics, Baylor College of Medicine, Houston, TX 77030, USA. [6]Program in Developmental Biology, Baylor College of Medicine, Houston, TX 77030, USA. [7]Howard Hughes Medical Institute (HHMI), Houston TX 77030, USA.

*Present address: Department of Pediatrics, Case Western Reserve University, Cleveland, OH 44106, USA.
†To whom correspondence should be addressed. E-mail: lumpkin@bcm.edu (E.A.L.); hzoghbi@bcm.edu (H.Y.Z.)

used immunocytochemistry to compare the expression pattern of keratin 8, an intermediate filament protein specifically expressed by Merkel cells in adult mammalian skin (*23*, *24*), with that of β-galactosidase protein expression driven from the *Atoh1*^{LacZ} locus (Fig. 2). Both proteins were expressed by Merkel cells in all regions of *Atoh1*$^{LacZ/+}$ animals but were absent throughout the body of *Atoh1*^{CKO} animals, except for the whisker pads where *Hoxb1*^{Cre} is not expressed. We also found that VGLUT2 and Rab3c, two synaptic vesicle proteins that robustly label Merkel cells (*8*, *25*, *26*), were absent from the epidermis of body skin and foot pads (Fig. 3, A and B, and fig. S2) but were present in whisker pads of *Atoh1*^{CKO} animals. We confirmed these findings by examining more than 100 touch domes,16 foot pads, and 8 whisker pads from four adult *Atoh1*^{CKO} mice. These results differ from a previous report from our group suggesting that Merkel cells are present in *Atoh1*-null embryos (*17*). That study was limited by the necessity of examining prenatal mice, because *Atoh1*-null animals die within minutes of birth secondary to respiratory failure (*22*). Here, our use of conditional knockout animals enabled us to examine specific Merkel cell markers in fully developed skin and to show Merkel cell loss in *Atoh1*^{CKO} mice. To our knowledge, *Atoh1* is the first gene shown to be necessary for the specification of Merkel cells. Our data also demonstrate that Merkel cells are not necessary to specify or maintain touch dome ultrastructure, as guard hairs and the overlying keratinocytes appear completely normal in the hairy skin of *Atoh1*^{CKO} mice.

Crescent-shaped clusters of Merkel cells are normally found within each touch dome, where they are innervated by a single sensory afferent that expresses neurofilament 200 (NF200) in large- and medium-sized branches and VGLUT2 in terminal branches (*8*, *26*) (Fig. 3A). Innervation of touch domes was present in wild-type (WT) and *Atoh1*^{CKO} animals, as revealed by NF200 immunocytochemistry (Fig. 3, A and B). However, there was exuberant branching of the VGLUT2-positive, NF200-negative terminal ends of touch dome afferent fibers of *Atoh1*^{CKO} animals (Fig. 3B). We confirmed this observation using in vivo subcutaneous injections of the styryl dye FM 1-43. FM 1-43 strongly labels sensory cells, including Merkel cells, and their afferent fibers in vivo (*27*) in WT mice, permitting whole-mount analysis of Merkel cell-neurite complex structure (Fig. 3C). Afferent terminal branches were labeled in the touch domes of *Atoh1*^{CKO} animals, despite the absence of Merkel cells (Fig. 3D). Both of these methods demonstrated that touch domes in *Atoh1*^{CKO} animals display excessive terminal branching compared with WT animals. These data suggest that, although Merkel cells are not necessary for the development or maintenance of touch dome innervation, they play a role in the acquisition of the typical terminal arborization pattern of touch dome afferents. Several neurotrophins have been implicated in the development and maintenance of Merkel cell innervation (*28*, *29*). Our data also demonstrate that Merkel cells cannot be the primary source of these trophic factors.

Many different afferent somatosensory fiber types innervate the skin (*30*). These fibers can be grouped by conduction velocity into three broad categories: Aβ, Aδ, and C fibers (table S1). Nociceptors and temperature receptors are primarily of the Aδ and C subtypes, whereas light-touch sensation is mediated by Aβ fibers. The Aβ fiber subclass can be further subdivided by the adaptation characteristics of the fibers: Slowly adapting type I (SAI) fibers innervate Merkel cell-neurite complexes (*5*), SAII fibers are thought to innervate Ruffini corpuscles, and rapidly adapting (RA) fibers innervate Meissner and Pacinian corpuscles (*1*). Each of these subclasses is important for detecting a specific form of touch (*1*). Together with the presence of touch dome innervation, the absence of Merkel cells in *Atoh1*^{CKO} animals provided the perfect opportunity to test whether Merkel cells are required for mechanotransduction by their innervating nerve fibers.

The overall population of cutaneous afferent receptors is normal in *Atoh1*^{CKO} animals (Fig. 3, J to L). We applied electrical and mechanical stimuli to the epidermal surface of ex vivo skin/saphenous nerve preparations from WT and *Atoh1*^{CKO} animals and simultaneously recorded extracellular responses from teased afferent fibers (Fig. 3, E to M). There were no differences between WT and *Atoh1*^{CKO} mice in the mechanical thresholds (Fig. 3J), conduction velocities (Fig. 3K), or proportions (Fig. 3L) of touch-sensitive fibers ($P > 0.1$ by Mann-Whitney *U* test).

We next focused specifically on the Aβ fiber population. The distribution of Aβ subtypes revealed a conspicuous loss of SAI responses among slowly adapting Aβ afferents in *Atoh1*^{CKO} animals [n = 0 out of 27 (0/27) afferents] compared with WT animals (n = 8/39 afferents) (Fig. 3M). We also observed a proportional expansion of other Aβ afferent subtypes (*20*) in *Atoh1*^{CKO} mice. These data are consistent with a complete loss of mechanosensitive SAI fibers.

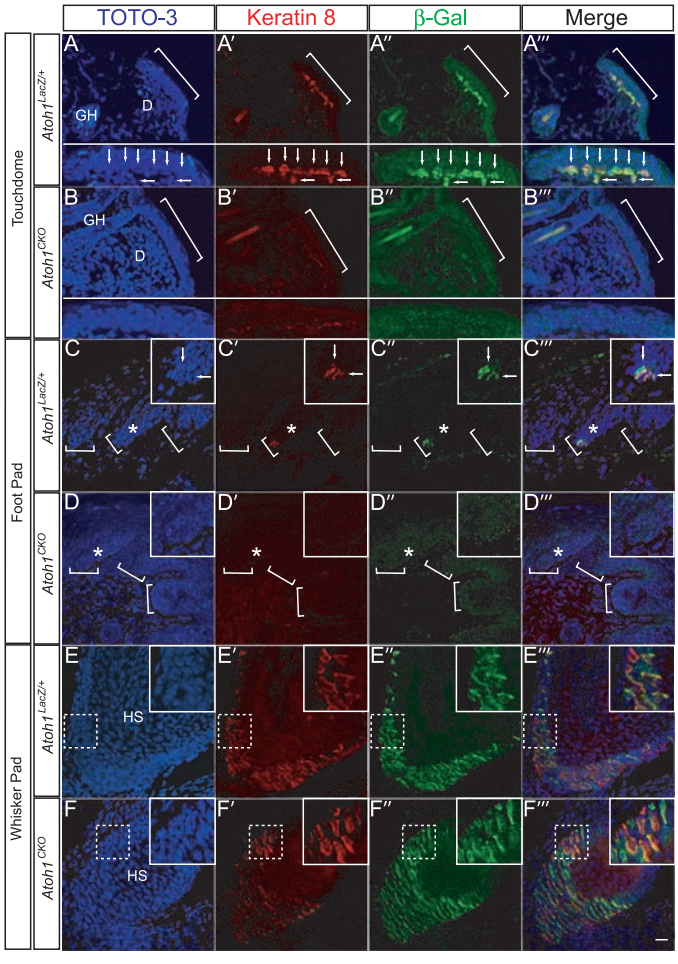

Fig. 2. Merkel cells are absent from the body skin and foot pads of *Atoh1*^{CKO} animals. All tissue is from P22 animals, and all images are z-stack projections of confocal images. (**A** to **B‴**) Skin from *Atoh1*$^{LacZ/+}$ (A to A‴) and *Atoh1*^{CKO} (B to B‴) animals. Brackets denote a single touch dome. Subpanels in (A) to (A‴) show Merkel cells (arrows) from the WT touch dome denoted by the bracket, whereas none are seen in the *Atoh1*^{CKO} animal [subpanels in (B) to (B‴)]. D, dermis; GH, guard hair. (**C** to **D‴**) Hind foot pad from *Atoh1*$^{LacZ/+}$ (C to C‴) and *Atoh1*^{CKO} (D to D‴) animals. Brackets denote epidermal rete ridges, asterisks denote areas shown in the insets, and arrows in (C to C‴) mark individual Merkel cells. Cells positive for keratin 8 and β-galactosidase are absent from *Atoh1*^{CKO} body skin and foot pad. (**E** to **F‴**) Whisker pad from *Atoh1*$^{LacZ/+}$ (E to E‴) and *Atoh1*^{CKO} (F to F‴) animals. There is no difference in the immunostaining patterns between the two genotypes. Dotted boxes outline areas shown in the insets. HS, whisker hair shaft. All keratin 8-positive cells were also β-galactosidase-positive and vice versa in all tissues of both genotypes. Scale bars, 25 μm in all panels; 12.5 μm in subpanels and insets.

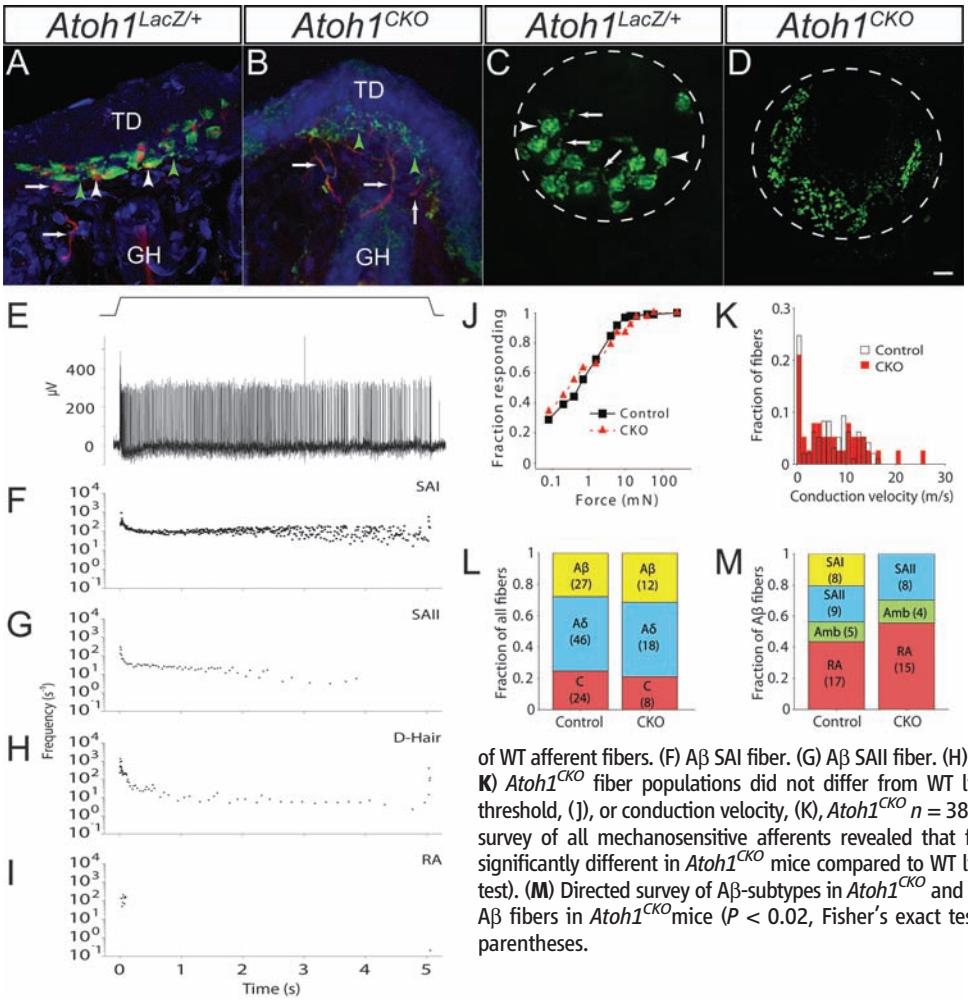

Fig. 3. Touch dome afferents are present but SAI responses are absent in *Atoh1*^{CKO} mice. (**A** and **B**) Touch dome sections from P22 *Atoh1*$^{LacZ/+}$ (A) and *Atoh1*^{CKO} (B) animals immunostained for NF200 (red) and VGLUT2 (green). White arrows mark nerve branches innervating the touch dome, white arrowheads mark nerve terminal branches contacting individual Merkel cells, and green arrowheads mark VGLUT2-positive, NF200-negative nerve terminal branches. Counterstain (blue) is TOTO3. Note the lack of cellular staining but increased nerve branching pattern in (B). GH, guard hair; TD, touch dome. (**C** and **D**) In vivo FM 1-43 dye labeling of adult *Atoh1*$^{LacZ/+}$ (C) and *Atoh1*^{CKO} (D) touch domes. Dotted lines delineate touch dome boundaries. Arrows (C) show sensory nerve branches; arrowheads denote Merkel cells. Note the excessive sensory nerve branching but absence of Merkel cells in (D). Scale bars, 12.5 μm in all panels. (**E**) Semi-intact recordings from touch-sensitive afferents innervating hairy skin of WT mice. (Top) Displacement trace showing a 5-s touch to the skin surface. (Bottom) SAI response to the 5-s mechanical stimulus shown above. (**F** to **I**) Representative plots of instantaneous firing frequency versus time for 5-s mechanical stimuli of WT afferent fibers. (F) Aβ SAI fiber. (G) Aβ SAII fiber. (H) Aδ down hair fiber (D-Hair). (I) Aβ RA fiber. (**J** and **K**) *Atoh1*^{CKO} fiber populations did not differ from WT littermates in mechanical sensitivity [by von Frey threshold, (J), or conduction velocity, (K), *Atoh1*^{CKO} $n = 38$, WT $n = 97$; $P > 0.10$, Mann-Whitney U test]. (**L**) A survey of all mechanosensitive afferents revealed that fiber type proportions (Aβ, Aδ, and C) were not significantly different in *Atoh1*^{CKO} mice compared to WT littermate control animals ($P > 0.10$, Fisher's exact test). (**M**) Directed survey of Aβ-subtypes in *Atoh1*^{CKO} and control mice. No SAI responses were found among Aβ fibers in *Atoh1*^{CKO}mice ($P < 0.02$, Fisher's exact test). Number of fibers in (L) and (M) is shown in parentheses.

Thus, canonical SAI responses elicited by touch require Merkel cells. It is possible that touch dome afferents lacking Merkel cells remain intrinsically touch sensitive but possess different electrophysiological properties. For example, they could be represented in the "ambiguous" class (fig. S1); however, they are unlikely to constitute the whole population because we observed similar responses in WT mice.

For more than a century, neurobiologists have postulated that Merkel cells are responsible for the specialized coding properties that allow their afferent nerves to resolve fine spatial details. Our genetic knockout approach has allowed us to directly test this hypothesis and to demonstrate that Merkel cells are essential for these responses. Because Merkel cells fail to develop in *Atoh1*^{CKO} mice, a key question that remains is whether Merkel cells, somatosensory neurons, or both are sites of mechanotransduction in the skin. Selective and acute control of Merkel cell signaling will be necessary to determine whether Merkel cells act as sensory receptor cells or serve another role in touch.

References and Notes

1. K. O. Johnson, *Curr. Opin. Neurobiol.* **11**, 455 (2001).
2. K. O. Johnson, G. D. Lamb, *J. Physiol.* **310**, 117 (1981).
3. K. O. Johnson, T. Yoshioka, F. Vega-Bermudez, *J. Clin. Neurophysiol.* **17**, 539 (2000).
4. A. Iggo, A. R. Muir, *J. Physiol.* **200**, 763 (1969).
5. C. J. Woodbury, H. R. Koerber, *J. Comp. Neurol.* **505**, 547 (2007).
6. F. S. Merkel, *Arch. Mikrosk. Anat.* **11**, 636 (1875).
7. Z. Halata, M. Grim, K. I. Bauman, *Anat. Rec. A Discov. Mol. Cell. Evol. Biol.* **271A**, 225 (2003).
8. H. Haeberle *et al.*, *Proc. Natl. Acad. Sci. U.S.A.* **101**, 14503 (2004).
9. W. Hartschuh, E. Weihe, *J. Invest. Dermatol.* **75**, 159 (1980).
10. P. M. Cahusac, S. S. Senok, *Synapse* **59**, 235 (2006).
11. J. Diamond, L. R. Mills, K. M. Mearow, *Prog. Brain Res.* **74**, 51 (1988).
12. B. M. Fagan, P. M. Cahusac, *Neuroreport* **12**, 341 (2001).
13. K. M. Gottschaldt, C. Vahle-Hinz, *Science* **214**, 183 (1981).
14. I. Kinkelin, C. L. Stucky, M. Koltzenburg, *Eur. J. Neurosci.* **11**, 3963 (1999).
15. E. G. Pacitti, G. S. Findlater, *Prog. Brain Res.* **74**, 37 (1988).
16. S. S. Senok, K. I. Baumann, Z. Halata, *Exp. Brain Res.* **110**, 325 (1996).
17. N. Ben-Arie *et al.*, *Development* **127**, 1039 (2000).
18. B. R. Arenkiel, G. O. Gaufo, M. R. Capecchi, *Dev. Dyn.* **227**, 379 (2003).
19. N. F. Shroyer *et al.*, *Gastroenterology* **132**, 2478 (2007).
20. Materials and methods are available as supporting material on *Science* Online.
21. A. W. Helms, A. L. Abney, N. Ben-Arie, H. Y. Zoghbi, J. E. Johnson, *Development* **127**, 1185 (2000).
22. N. Ben-Arie *et al.*, *Nature* **390**, 169 (1997).
23. R. Moll, I. Moll, W. W. Franke, *Differentiation* **28**, 136 (1984).
24. U. Vielkind, M. K. Sebzda, I. R. Gibson, M. H. Hardy, *Acta Anat. (Basel)* **152**, 93 (1995).
25. I. S. Hitchcock, P. G. Genever, P. M. Cahusac, *Neurosci. Lett.* **362**, 196 (2004).
26. M. G. Nunzi, A. Pisarek, E. Mugnaini, *J. Neurocytol.* **33**, 359 (2004).
27. J. R. Meyers *et al.*, *J. Neurosci.* **23**, 4054 (2003).
28. K. M. Cronk *et al.*, *Development* **129**, 3739 (2002).
29. B. T. Fundin *et al.*, *Dev. Biol.* **190**, 94 (1997).
30. E. A. Lumpkin, M. J. Caterina, *Nature* **445**, 858 (2007).

31. We thank M. Capecchi for generously providing us with *Hoxb1*^{Cre} animals; N. Ao, K. Firozi, E. Mathes, K. Morrison, and S. Vaishav for technical assistance; and G. Landreth, L. Landmesser, and R. Miller for critical reading of the manuscript. Funding sources are as follows: NIH grant 5K08NS53419 (to S.M.M.), McNair Scholars Program (to A.M.N.), National Library of Medicine grant T15LM009462 (to D.R.L.), Defense Advanced Research Projects Agency grant HR0011-08-1-0072 (to G.J.G.), NIH grant HD024064, and NIH grant AR051219 (to E.A.L.). H.Y.Z. is an investigator with HHMI.

Supporting Online Material

www.sciencemag.org/cgi/content/full/324/5934/1580/DC1
Materials and Methods
Figs. S1 and S2
Table S1
References

2 March 2009; accepted 1 May 2009
10.1126/science.1172890

Recruitment of an Area Involved in Eye Movements During Mental Arithmetic

André Knops,[1,2,3]* Bertrand Thirion,[2,4] Edward M. Hubbard,[1,2,3] Vincent Michel,[2,3,4] Stanislas Dehaene[1,2,3,5]

Throughout the history of mathematics, concepts of number and space have been tightly intertwined. We tested the hypothesis that cortical circuits for spatial attention contribute to mental arithmetic in humans. We trained a multivariate classifier algorithm to infer the direction of an eye movement, left or right, from the brain activation measured in the posterior parietal cortex. Without further training, the classifier then generalized to an arithmetic task. Its left versus right classification could be used to sort out subtraction versus addition trials, whether performed with symbols or with sets of dots. These findings are consistent with the suggestion that mental arithmetic co-opts parietal circuitry associated with spatial coding.

The human species is unique in its capacity to create revolutionary cultural inventions such as writing and mathematics, which dramatically enhance its native competence. From a neurobiological standpoint, such inventions are too recent for natural selection to have dedicated specific brain mechanisms to them. It has therefore been suggested that they co-opt or "recycle" evolutionarily older circuits with a related function (*1*), thus enriching (without necessarily replacing) their domain of use. For instance, learning to read recruits a left inferotemporal area originally engaged in object recognition, and even the seemingly arbitrary shapes of our letters may originate in a neural repertoire of junction detectors that are useful for scene recognition and available to all primates (*2*). In the case of mathematics, although foundational intuitions such as number sense (*3*) and spatial maps (*4*) are present in many animal species and in humans before their education, mathematical constructions vastly exceed these initial domains of inherited competence. It has been argued that analogies between number and space play a crucial role in the expansion of mathematical concepts (*5*). We investigated the role of brain areas for spatial coding in mental arithmetic.

Many behavioral experiments have demonstrated automatic links between number and space. Even young children and uneducated adults readily conceive of numbers as forming an internal spatial continuum or "mental number line" (*6*). Merely perceiving an Arabic digit suffices to elicit a spatial bias in both attentional orienting (*7*) and manual responses (*8*), with small numbers inducing a left-sided and large numbers a right-sided advantage in left-to-right readers. When adults perform approximate additions and subtractions, they overshoot toward larger numbers for addition and toward smaller numbers for subtraction, as if carried along by spatial momentum (*9*). Perhaps the most conclusive evidence for numerical-spatial links comes from the syndrome of spatial hemineglect, in which brain-lesioned patients fail to attend to one side of space, usually the left side. When such patients attempt to bisect a numerical interval, their responses are shifted toward larger numbers, as if neglecting the left half of the numerical segment, where small numbers are represented (*10*).

The brain mechanisms of these numerical-spatial interactions, however, remain largely unknown. In both monkeys and humans, number processing recruits a brain area deep within the horizontal aspect of the intraparietal sulcus (hIPS) (*11*, *12*). This site partially overlaps with the ventral intraparietal cortex (VIP), an area coding for multimodal spatial movement and tightly interconnected with the nearby lateral intraparietal cortex (LIP), which is involved in saccadic and attention control (*13*–*15*). A model of the VIP-LIP circuitry proposes that it implements a form of vector addition of eye and retinal

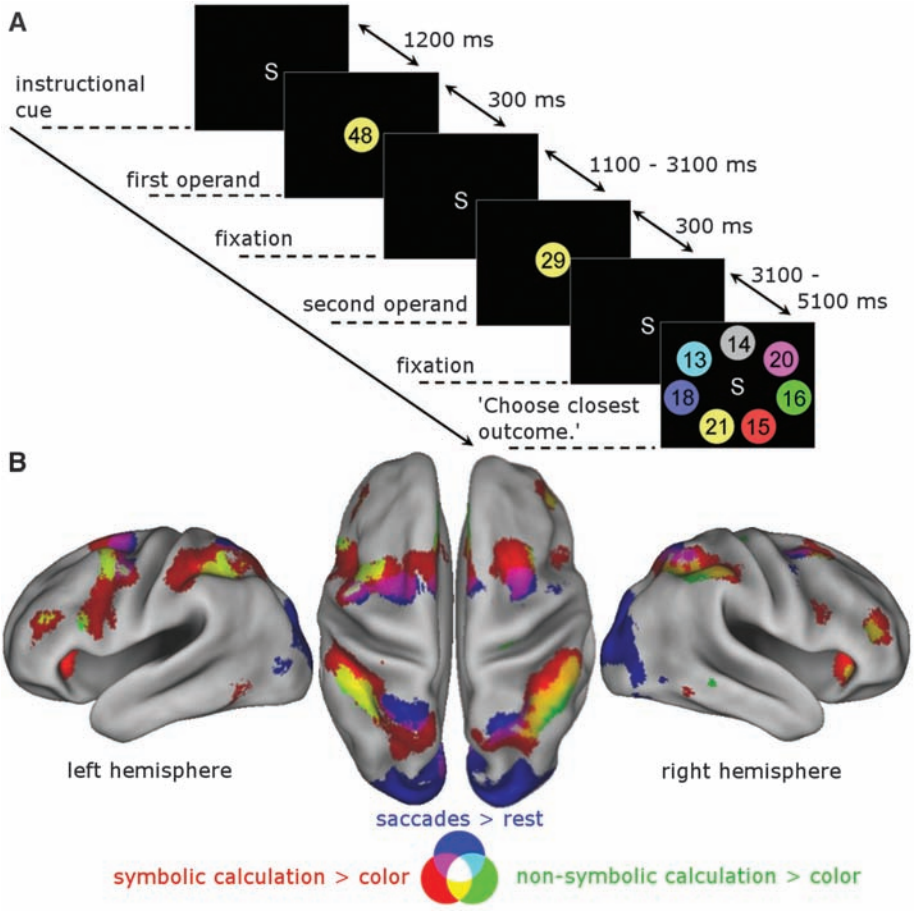

Fig. 1. (**A**) Schematic depiction of a calculation trial. After the initial presentation of an instructional cue [A, S, or C for addition, subtraction (shown here), or color task, respectively], two quantities were presented successively, either as dot patterns or Arabic digits. After a variable delay period, seven response alternatives appeared on the screen and participants had to choose the alternative closest to the actual outcome. (**B**) Brain activation in the calculation task and the saccades localizer task projected on lateral and top views of the brain. The images shown result from contrasting symbolic (red) or nonsymbolic (green) calculation to the color task and from contrasting saccades to rest (blue) ($P = 0.005$, uncorrected).

[1]INSERM, Cognitive Neuroimaging Unit, F-91191 Gif-sur-Yvette, France. [2]Commissariat à l'Energie Atomique (CEA), I2BM, NeuroSpin, F-91191 Gif-sur-Yvette, France. [3]Université Paris-Sud, F-91405 Orsay, France. [4]Institut National de Recherche en Informatique et en Automatique Saclay–Île de France, Orsay, France. [5]Collège de France, Paris, France.

*To whom correspondence should be addressed. E-mail: knops.andre@gmail.com

position information (*16*). We therefore reasoned that this circuit might be co-opted for a similar function in the arithmetic domain. Given the cultural link in left-to-right readers between small numbers and the left side of space, and large numbers and the right side of space, we predicted that mental addition, which increases number size, would be associated with a rightward shift of attention and subtraction with a leftward shift. Hence, the activation pattern in the parietal cortex during addition would resemble the activation pattern associated with a rightward eye movement, whereas subtraction would resemble a leftward eye movement.

In a 3 Tesla functional magnetic resonance imaging (fMRI) scanner, participants first performed a localizer task for eye movements. By contrasting eye movements against fixation, we isolated a set of six cortical regions that are classically associated with saccades, and we used them in all subsequent classifier-based analyses (*17*): the bilateral posterior superior parietal lobule (PSPL), at a site overlapping with the proposed human homolog of monkey area LIP (*18*); the bilateral frontal eye fields (FEF) proper; and two clusters of activation lateral to the FEF (lFEF; Fig. 1B).

Participants performed a second set of fMRI runs during which they moved their eyes either rightward or leftward on randomly intermixed trials. We adopted a machine learning approach to search for a linear combination of these voxel-based activation signals that reliably separated leftward and rightward saccades (*19*). We trained a linear support vector machine as a classifier, using a 10-fold cross-trial validation approach in which the classifier is first trained on a random subset of 90% of activation images (one image per trial), and then performance is evaluated on the remaining 10% of trials. The process was repeated 100 times, each time with a new random assignment of trials. Using only voxels from the bilateral PSPL region, we obtained a mean accuracy across all participants of 70.3 ± 2.4% (1 SE), which is significantly above the chance level of 50% [Student's *t* test $t(14) = 8.39$, $P < 0.001$]. Analysis by signal detection theory gave similar results [average sensitivity index d' across participants = 1.1 ± 0.15, $t(14) = 7.58$, $P < 0.001$]. Thus, saccade direction, which is known to be coded by neurons in monkey area LIP, could be inferred from fMRI of the human posterior parietal cortex.

We then examined whether the same classifier, without further training, would generalize to approximate arithmetic. In new fMRI runs, participants saw two successive numbers (presented as Arabic numerals or as sets of dots), mentally calculated their approximate sum or difference, and subsequently chose the closest number among seven possible outcomes. We concentrated on brain activation just after the presentation of the second operand, at which time the participants performed the calculation (Fig. 1A). Calculation activated a network of brain areas comprising the bilateral hIPS, prefrontal and premotor areas, with considerable overlap between both notations (Fig. 1B). Calculation overlapped only partially with saccades in the bilateral PSPL, but, as predicted, the classifier trained with bilateral PSPL activations during saccades generalized to calculation images. Equating addition with rightward saccades and subtraction with leftward saccades, the mean accuracy for inferring whether an addition or subtraction was performed, averaged over all participants, was 55.0 ± 1.8%, which is significantly greater than chance [$t(14) = 2.78$, $P = 0.015$; $d' = 0.31 \pm 0.10$, $t(14) = 2.85$, $P = 0.013$].

Further analyses showed that when the saccades classifier was tested with addition images, it classified them as rightward saccades 61% of the time (Fig. 2D), which is above the chance level [$t(14) = 2.35$, $P = 0.03$]. For subtraction, however, only 49.1% of images were classified as leftward saccades [$t(14) = -0.16$, n.s.]. This asymmetry, although unexpected, is congruent with earlier reports of larger rightward saccades in response to large numbers, relative to leftward saccades in response to small numbers (*20*), and might reflect reading habits in Western cultures.

A key aspect of the cortical recycling view is that saccadic areas of the posterior parietal lobule should contribute to calculation, not only when performed with concrete sets of objects but even with Arabic numerals, which are a recent product of human culture. We therefore tested the generalization from saccades to calculation in each notation separately. The saccade-trained classifier could distinguish addition from subtraction with an average accuracy of 54.3 ± 2% for Arabic numerals [$t(14) = 2.26$, $P = 0.02$; $d' = 0.38 \pm 0.11$, $t(14) = 2.1$, $P = 0.054$] and an average accuracy of 55.8 ± 2% for nonsymbolic notation [$t(14) = 2.93$, $P = 0.005$; $d' = 0.38 \pm 0.14$, $t(14) = 2.74$, $P = 0.016$]. Thus, both symbolic and nonsymbolic calculations rely in part on brain circuits for saccadic eye movements.

As a further test of this sharing of resources for nonsymbolic and symbolic arithmetic, we also

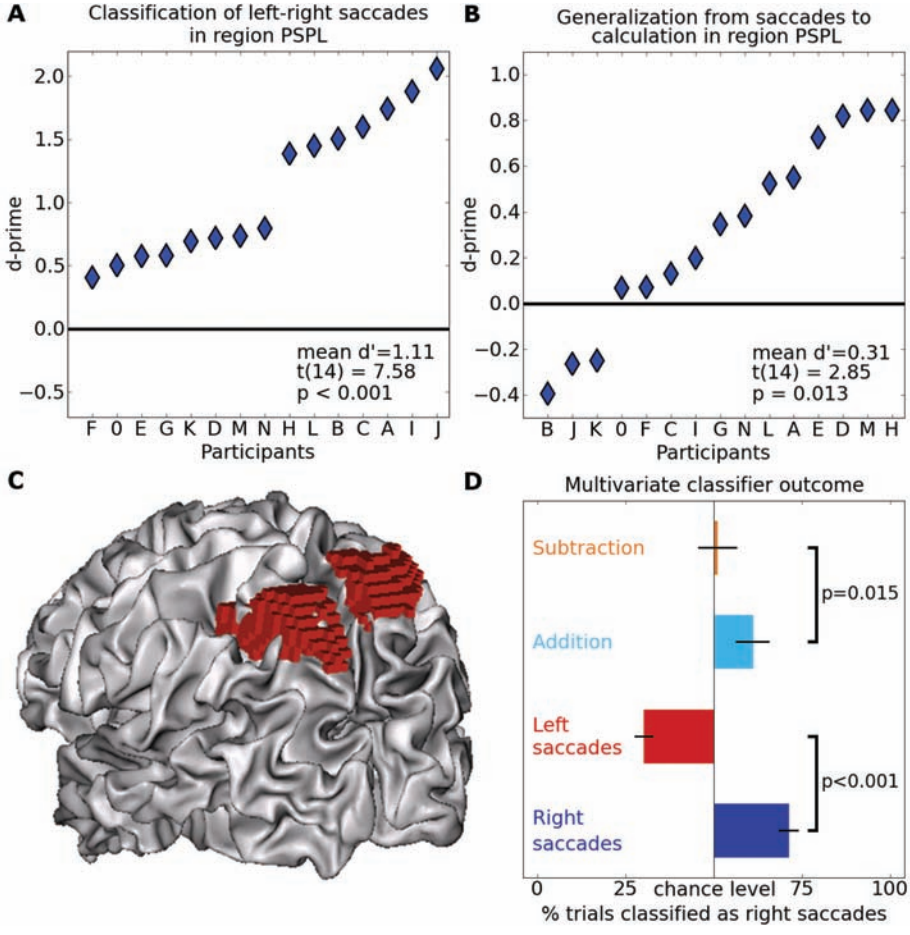

Fig. 2. (**A**) Classification performance (d') for each participant in the saccades task (participants are sorted according to d'). (**B**) Classification performance (d') per participant for generalization of the classifier trained on left/right saccades to subtraction/addition trials. (**C**) Voxel clusters in left and right PSPL region that resulted from the saccade localizer task and served as ROI for the classifier, rendered on the white matter/gray matter boundary. (**D**) Percentages of trials classified as right saccades for subtraction (orange), addition (light blue), and left and right saccades (red and dark blue, respectively).

examined the ability to predict which operation was being performed in one notation, on the basis of a classifier trained to sort additions from subtractions in the other notation. This cross-notation generalization yielded good results, both for the prediction of nonsymbolic calculation from the symbolic notation [mean accuracy 60.7 ± 2.5%, $t(14) = 4.37$, $P < 0.001$; $d' = 0.53 \pm 0.16$, $t(14) = 3.32$, $P = 0.005$] and vice versa [mean accuracy 62.2 ± 2.1%, $t(14) = 5.71$, $P < 0.001$; $d' = 0.75 \pm 0.14$, $t(14) = 5.39$, $P < 0.001$]. This finding indicates that the PSPL region is comparably involved in solving mental arithmetic problems in both notations. Approximate arithmetic with sets of dots is part of an inherited number sense available to infants (*21*) and nonhuman primates (*22*), but the cross-notation generalization proves that the corresponding brain circuitry is also used by arithmetic with culturally specific Arabic numerals.

Given the observed parietal cross-talk, one may wonder whether the arithmetic task, although involving only central visual presentations and a constantly present fixation point, led to overt eye movements. Eye position was continuously monitored throughout fMRI, and we found no detectable change in horizontal fixation at or around the time of the arithmetic calculation (*17*). Furthermore, the observed cross-talk was specific to the posterior parietal cortex. Activation patterns in FEF and lFEF could be reliably used to classify left versus right saccades [56.9 ± 2.4%, $t(14) = 2.87$, $P = 0.012$, and 57.8 ± 2.4%, $t(14) = 3.3$, $P = 0.005$, respectively], but this classification did not generalize to addition versus subtraction {49 ± 5.3% [$t(14) = –0.18$, $P = 0.86$] and 49.2 ± 6.3% [$t(14) = –0.12$, $P = 0.9$, respectively]}. The absence of decodable FEF activation during arithmetic confirms that calculation specifically engages parietal rather than frontal spatial mechanisms and involves covert visuospatial mechanisms, not overt eye movements. As a final test of the specificity of our results to the PSPL area, we repeated the major analyses with two control regions (hand motor area M1 and hIPS). None of these regions yielded better-than-chance generalization from saccades to calculation (*17*).

We demonstrated that a multivariate classifier can distinguish between brain activations during mental addition and subtraction, after having been trained on images from a separate experiment requiring saccades to the right or left. This generalization was observed with numbers presented either as Arabic symbols or as nonsymbolic sets of dots, which implies shared cognitive processes between both notations. The observed generalization goes beyond previous demonstrations of classifier-based decoding of line orientation and other pictorial contents from early visual areas (*23*–*26*); object identity and category from the ventral visual cortex (*27*); noun identity from distributed cortical regions (*28*); or intentions from premotor, prefrontal, and striatal sites (*29*). Although generalization was found across different image sizes (*27*), from real to imagined images (*26*), or from trained nouns to novel nouns (*28*), inference remained confined to the trained domain. In contrast, the present research demonstrates generalization from a low-level sensorimotor task to a high-level cognitive task involving learned cultural symbols.

Our results confirm a prediction first made by Hubbard *et al*. (*13*) that mental calculation can be likened to a spatial shift along a mental number line. In a certain sense, when a Western participant calculates 18 + 5, the activation moves "rightward" from 18 to 23. This spatial shift relies on neural circuits in the PSPL shared with those involved in updating spatial information during saccadic eye movements. The findings are reminiscent of the "embodied cognition" perspective, which stipulates that perceptual and action mechanisms lie at the core of human abstract thinking (*30*). However, the recycling view that we propose does not imply that all concepts originate in sensorimotor learning. Indeed, there is ample evidence that numerical concepts have a long evolutionary history and a dedicated neuronal circuitry in the intraparietal cortex, partially distinct from neighboring visuospatial circuits (*31*). Our proposal is that human mathematics builds from foundational concepts (space, time, and number) by progressively co-opting cortical areas whose prior organization fits with the cultural need. The PSPL area, perhaps because of its capacity for vector addition during eye movement computation (*16*), appears to have a connectivity or internal structure relevant to arithmetic.

The contribution of the PSPL appears to be fundamentally different from the function of other regions such as the FEF or hIPS, where no generalization from saccades to calculation was found. The PSPL is active not only during saccades but during a broad variety of tasks involving as a common denominator the representation, updating, or attention to spatial locations. This makes it an ideal site for explaining the broad variety of numerical-spatial interactions that have been observed behaviorally with eye, hand, or attention movements (*13*).

Like any fMRI study, the present work is correlative and cannot establish whether the observed PSPL activation plays a causal role in calculation. One interpretation is that the PSPL is causally recruited during the actual computation of the result of arithmetic operations. Another is that calculation is effected by other means and that the PSPL activation merely reflects a subsequent spread of activation to visuospatial areas, perhaps because the final numerical result attracts attention on the mental number line. To separate those alternatives, future work should evaluate the impact of temporary or permanent lesions; for instance, using transcranial magnetic stimulation of dorsal parietal areas, which has already been shown to cause joint impairments in attentive visual search and arithmetic (*32*).

References and Notes

1. S. Dehaene, L. Cohen, *Neuron* **56**, 384 (2007).
2. M. A. Changizi, Q. Zhang, H. Ye, S. Shimojo, *Am. Nat.* **167**, E117 (2006).
3. S. Dehaene, *The Number Sense: How the Mind Creates Mathematics* (Oxford Univ. Press, New York, 1997).
4. C. R. Gallistel, *The Organization of Learning* (MIT Press, Cambridge, MA, 1990).
5. G. Lakoff, R. E. Nuñez, *Where Mathematics Comes From* (Basic Books, New York, 2000).
6. S. Dehaene, V. Izard, E. Spelke, P. Pica, *Science* **320**, 1217 (2008).
7. M. H. Fischer, A. D. Castel, M. D. Dodd, J. Pratt, *Nat. Neurosci.* **6**, 555 (2003).
8. S. Dehaene, S. Bossini, P. Giraux, *J. Exp. Psychol. Gen.* **122**, 371 (1993).
9. K. McCrink, S. Dehaene, G. Dehaene-Lambertz, *Percept. Psychophys.* **69**, 1324 (2007).
10. M. Zorzi, K. Priftis, C. Umilta, *Nature* **417**, 138 (2002).
11. S. Dehaene, E. Spelke, P. Pinel, R. Stanescu, S. Tsivkin, *Science* **284**, 970 (1999).
12. S. Dehaene, M. Piazza, P. Pinel, L. Cohen, *Cogn. Neuropsychol.* **20**, 487 (2003).
13. E. M. Hubbard, M. Piazza, P. Pinel, S. Dehaene, *Nat. Rev. Neurosci.* **6**, 435 (2005).
14. J. R. Duhamel, C. L. Colby, M. E. Goldberg, *Science* **255**, 90 (1992).
15. C. L. Colby, M. E. Goldberg, *Annu. Rev. Neurosci.* **22**, 319 (1999).
16. A. Pouget, S. Deneve, J. R. Duhamel, *Nat. Rev. Neurosci.* **3**, 741 (2002).
17. Materials and methods are available as supporting material on *Science* Online.
18. M. I. Sereno, S. Pitzalis, A. Martinez, *Science* **294**, 1350 (2001).
19. K. A. Norman, S. M. Polyn, G. J. Detre, J. V. Haxby, *Trends Cogn. Sci.* **10**, 424 (2006).
20. M. H. Fischer, N. Warlop, R. L. Hill, W. Fias, *Exp. Psychol.* **51**, 91 (2004).
21. K. McCrink, K. Wynn, *Psychol. Sci.* **15**, 776 (2004).
22. J. F. Cantlon, E. M. Brannon, *PLoS Biol.* **5**, e328 (2007).
23. J. D. Haynes, G. Rees, *Nat. Neurosci.* **8**, 686 (2005).
24. Y. Kamitani, F. Tong, *Nat. Neurosci.* **8**, 679 (2005).
25. K. N. Kay, T. Naselaris, R. J. Prenger, J. L. Gallant, *Nature* **452**, 352 (2008).
26. B. Thirion *et al*., *Neuroimage* **33**, 1104 (2006).
27. E. Eger, J. Ashburner, J. D. Haynes, R. J. Dolan, G. Rees, *J. Cogn. Neurosci.* **20**, 356 (2008).
28. T. M. Mitchell *et al*., *Science* **320**, 1191 (2008).
29. J. D. Haynes *et al*., *Curr. Biol.* **17**, 323 (2007).
30. R. L. Goldstone, L. W. Barsalou, *Cognition* **65**, 231 (1998).
31. O. Tudusciuc, A. Nieder, *Proc. Natl. Acad. Sci. U.S.A.* **104**, 14513 (2007).
32. S. M. Göbel, M. F. Rushworth, V. Walsh, *Cortex* **42**, 774 (2006).

33. The fMRI experiment was part of a general research program on functional neuroimaging of the human brain that was sponsored by the Atomic Energy Commission (D. Le Bihan). We thank L. Hertz-Pannier, A. Jobert, and the NeuroSpin staff for their help. Supported by INSERM, CEA, a McDonnell Foundation centennial fellowship (S.D.), and a Volkswagen Foundation grant (S.D. and A.K.).

Supporting Online Material

www.sciencemag.org/cgi/content/full/1171599/DC1
Materials and Methods
Figs. S1 to S3
References

29 January 2009; accepted 27 April 2009
Published online 7 May 2009;
10.1126/science.1171599
Include this information when citing this paper.

PCR Products

Switch to Superior High Fidelity PCR

PrimeSTAR®

Top Five Reasons to Switch to PrimeSTAR®:

- **Higher Accuracy:** A strong exonuclease activity results in an extremely low error rate, with only 15 errors per 480,000 bp on a GC-rich template.
- **Higher Efficiency:** Higher than *Taq* Polymerase.
- **Robust Amplifications:** A single PCR cycling protocol can be used to amplify products of varying sizes.
- **Greater Specificity:** The antibody mediated Hot Start formulation prevents false initiation events during reaction assembly.
- **Excellent with GC-Rich Targets:** Robust performance with GC-rich templates using the GC buffer formulation.

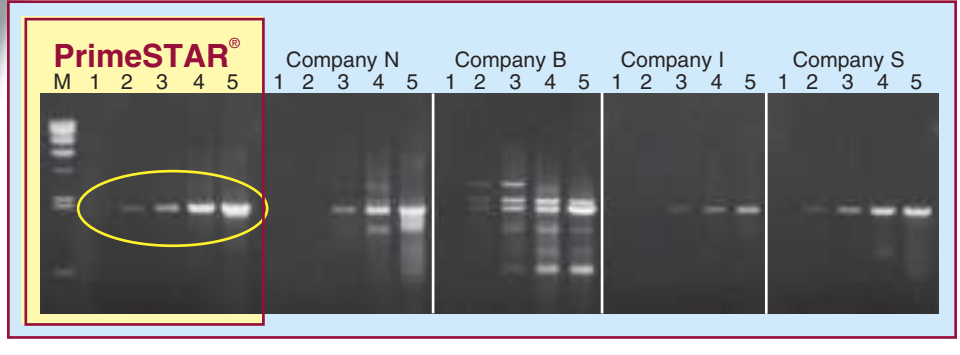

Amplification Efficiency of a 2 kb Human Genomic DNA Fragment (DCLRE1A)**.** Excellent sensitivity and yield are observed when amplifying with PrimeSTAR®. Quantities: Lane1: 0 ng (dH_2O), Lane 2: 100 pg, Lane 3: 1 ng, Lane 4: 10 ng, Lane 5: 100 ng.

TaKaRa

For more information
www.takara-bio.com

Japan:
Takara Bio Inc.
+81 77 543 7247
www.takara-bio.com

USA:
Takara Bio USA
A Division of Clontech Laboratories, Inc
888-251-6618
www.takarabiousa.com

Europe:
Takara Bio Europe S.A.S.
+33 1 3904 6880
www.takara-bio.eu

China:
Takara Biotechnology (Dalian) Co., Ltd.
+86 411 8764 1681
www.takara.com.cn

Korea:
Takara Korea Biomedical Inc.
+82 2 2081 2525
www.takara.co.kr

GENE TRANSFER:
TAMING DIVERSITY

Transferring specific nucleic acids into cells can modulate gene function, thereby revealing the mechanism of action and ultimate role of specific stretches of DNA. Nonetheless, getting the nucleic acids into the right cells efficiently and without damaging them creates challenges as diverse as the cells themselves. **By Mike May**

To study the processes behind gene expression, scientists often want to modify a specific cell's genome with selected nucleic acids. Making gene transfer work—getting nucleic acids from one cell into another—requires solving many problems. "Every cell type, especially cultured cells, has a different tolerance for each approach to gene transfer," explains Warren E. Zimmer, Scott Exter Professor in the department of systems biology and translational medicine at the **Texas A&M Health Science Center** in College Station.

Transfection experiments can be performed using a range of approaches: chemical, electrical, lipid- or protein-based, or viral. And within each category, a variety of protocols exists. These range from using different instruments to changing reagents or sample handling. Consequently, it's not always easy to get started working in this field. "It's good to know somebody in the business before you start trying these things," Zimmer says. This can help a researcher come up with a better approach to a gene transfer problem than simply going at it through trial and error.

As researchers try to apply gene transfer to a growing range of cells and situations, vendors keep improving on the tools for transfection. As a result, today's transfection tools are easier to use and more efficient.

> "Every cell type, especially cultured cells, has a different tolerance for each approach to gene transfer."

Chemical and Electrical Transfection

Among the various ways that a researcher can introduce genes into cells, chemical methods are some of the oldest. For example, a scientist can coat DNA with calcium carbonate, which forms a crystal on a cell's membrane. The cell takes up the crystal and releases the DNA in the cytoplasm. If the cell is dividing, the transfected DNA can end up in the nucleus.

In fact, many chemical approaches exist. For example, **Agilent Technologies' Stratagene Products Division** in La Jolla, California, uses a polyamine reagent in its GeneJammer Transfection product. "The transfection efficiency varies depending on the cell type," explains Scott O'Brien, product line manager for Stratagene. "For HeLa cells, the efficiency is 95–99 percent." The portion of cells killed in the process also varies among cell types. Again using HeLa cells as an example, O'Brien says, "the cell death is primarily a function of background—1–5 percent."

In addition, **Roche,** with its headquarters in Basel, Switzerland, offers the FuGENE HD Transfection Reagent. "It delivers plasmid DNA or shRNA with high transfection efficiency in a broad variety of cell lines, including many cell lines and primary cells that other reagents can't transfect," says Mike Leous, manager of marketing, discovery reagents, at Roche Applied Science. He adds, "FuGENE HD Transfection Reagent exhibits very low cytotoxicity, so more cells survive than with many other reagents. Just as important, but much less known: It generates fewer 'off-target effects.'" That is, the FuGENE HD Reagent itself does not cause the nonspecific up- or down-regulation of genes. "This allows researchers to truly measure the impact of their transfected sequence—not the impact of their transfection reagent," Leous says. continued >

Look for these **Upcoming** Articles

Label-free Technologies — September 18

Epigenetics — October 9

RNAi — October 16

Inclusion of companies in this article does not indicate endorsement by either AAAS or Science*, nor is it meant to imply that their products or services are superior to those of other companies.*

Featured Participants

Advalytix
www.advalytix.com

Agilent Technologies
www.agilent.com

Bio-Rad Laboratories
www.bio-rad.com

Broad Institute
www.broad.mit.edu

Life Technologies
www.lifetech.com

Massachusetts Institute of Technology
www.mit.edu

Oxford BioMedica
www.oxfordbiomedica.co.uk

Qiagen
www.qiagen.com

Roche
www.roche.com

Sigma-Aldrich
www.sigmaaldrich.com

Stratagene
www.stratagene.com

Texas A & M Health Science Center
medicine.tamhsc.edu

University of Glasgow
www.gla.ac.uk

Some of today's chemical techniques also use advanced materials. For instance, **Qiagen** in Hilden, Germany, offers a nanopolymer-based product called the NanoFect Transfection Reagent. Qiagen chemically synthesizes these nanopolymers, which include no lipids or animal-derived components. The nanopolymers and DNA form complexes that can enter a range of cells, including HeLa, MCF-7, and others.

Instead of introducing genes into cells with chemical methods, researchers can also use an electrical approach called electroporation. In this technique, a researcher places cells in a solution of DNA and runs current across the cell membrane. "The current blows holes in the cells that let in the DNA," says Zimmer. "This is quite efficient in some cells but it can be hard to control."

Electroporation can be a good choice when trying to transfect primary cells. Such cells come from cultures that are started directly from pieces of tissue or organ, and these cells usually die after a limited number of cell divisions. "We continue to see growing use of primary cells," says Steve Kulisch, division marketing manager in the gene expression division at **Bio-Rad Laboratories** in Hercules, California, making them an important target.

With Bio-Rad's Gene Pulser MXcell, researchers can take various approaches to electroporation. This instrument is compatible with sample chambers that accommodate both electroporation cuvettes and plates. Cuvettes are available in multiple "gap" sizes and allow for single transfections in a variety of volumes. For plates, researchers can select 12-, 24-, or 96-well versions and transfect in as little as 100 microliters. Kulisch adds, "This is an open system, and you can tune the conditions of electroporation to achieve higher transfection efficiency or increased cell viability."

Electroporation does not always take place in cuvettes. For example, **Life Technologies** (formally known as Invitrogen) in Carlsbad, California, developed its Neon Transfection Device that uses a modified pipette tip that also functions as the transfection chamber. "Unlike a cuvette, the pipette tip–based reaction vessel was designed to improve cell viability and the experimental workflow by reducing cell-handling steps," says Keith Farnsworth, product development manager for Invitrogen's molecular biology reagents. The Neon Transfection Device with its integrated buffer kit works with cell lines, primary cells, and stem cells. Depending on the cells being transfected with this technique, efficiency and cell survival can both be very high and range in different cell types from 53 percent to 94 percent and 59 percent to 97 percent, respectively.

Turning to Lipids and Protein

In the lipophyllic approach to transfection, genes are encapsulated in lipid micelles that fuse with cells, where the DNA is released. "With this technique a transfection efficiency of 30 percent is considered good," says Zimmer. "If you are looking for, say, a reporter with no background, that is okay, but often you need a higher transfection efficiency."

One of the most enduring lipid-based approaches is Life Technologies' Lipofectamine line. For example, Lipofectamine LTX works "great for immortalized cell lines and some primary cells," says Farnsworth. "Our customers tell us that it strikes the right balance—being potent enough to deliver a plasmid to many cell types but gentle enough to not disrupt cell viability." In addition, Lipofectamine RNAiMAX delivers short interfering RNA (siRNA). "Our customers are finding that they can achieve high gene knockdown results with minimal amounts of siRNA," says Farnsworth. "This improvement in transfection efficiency helps to reduce off-target effects."

Lipid-based transfection can also be used with in vivo applications. Life Technologies' Invivofectamine, for instance, was developed for in vivo delivery of siRNA. "This is more challenging than in vitro transfection," says Farnsworth. "The siRNA needs to transfect the targeted organs of a subject animal and provide extra stability to the siRNA so that the delivered material arrives intact and ready to perform gene knockdown." To help with that, this technology uses Life Technologies' Stealth siRNA, which Farnsworth says "has been modified to reduce off-target effects and to evade the host immune response."

Lipofectamine can also be used in conjunction with a range of tools, such as the AmpliCell from **Advalytix,** which is headquartered in Munich, Germany. "In order to do transfection, cell growth, and PCR [polymerase chain reaction] all in one place, we attached an eight-chamber device on top of the AmpliGrid," says Frank Feist, executive director at Advalytix. The AmpliGrid is a slide-based product for PCR. "You add the cells you want to transfect to the chamber, let them grow in a monolayer, and transfect them with just 100 microliters of volume." Moreover, eight different transfection reagents can be tried with the same slide-and-chamber combination. Later, a researcher can use the same slide to do PCR on the transfected cells, all without reformatting. "It cuts out handing steps, which minimizes cellular stress and leads to more representative gene expression, saves reagent, and it's multiplexed," Feist says. The AmpliGrid with

added chamber is called the AmpliCell, and is expected to launch later in 2009.

In addition to making the slides, chambers, and reagents, Advalytix provides protocols. "Many of our customers are oncologists, immunologists, and stem cell researchers," Feist says. "So we have many protocols related to clinical oncology, immunology, and stem cells."

Genes can also be introduced into cells with protein-based transfection. For example, some cell types—such as primary cells, neurons, and nondividing cells in general—can be difficult to transfect with traditional techniques. To overcome this challenge, **Sigma-Aldrich** developed its N-TER Nanoparticle siRNA Transfection System, which uses a peptide-based approach to delivering siRNA. For in vivo applications, says Heather Holemon, research and development manager in functional genomics at Sigma-Aldrich in St. Louis, Missouri, "a major limitation of RNA interference is getting reagents into the cells and with the right biodistribution." Moreover, such a system must work in a range of situations. "You want to use the same approach to test a knockdown in vitro and then move to in vivo," says Supriya Shivakumar, global commercial marketing manager for functional genomics at Sigma-Aldrich. This is possible with N-TER.

Viral Transfection

Virally mediated techniques provide an alternative means for transfection. For example, this can be done with adenoviruses or lentiviruses. "The good news is that virus-mediated gene transfer is highly efficient—virtually 100 percent," says Zimmer. "The bad news is that the virus can induce cellular responses."

When using short hairpin RNA (shRNA), Sigma-Aldrich scientists focus on a lentiviral approach. The company is part of the RNAi Consortium, led by the **Broad Institute** at the **Massachusetts Institute of Technology,** which is developing a library of shRNA against the whole-human and whole-mouse genomes, as well as lentiviral vectors for a variety of applications. "This virus offers extra advantages, because it is effective even in primary and nondividing cells, and you can manipulate it with things like antibiotic resistance or green fluorescent protein markers. Then, you can track it," says Shivakumar.

One of Stratagene's viral-based transfection systems, AdEasy, uses adenovirus. DNA is cloned into the viral particle which then infects the cell and undergoes replication. With this technique, researchers must employ high biosafety levels, because the virus remains active. In contrast, Stratagene's transfection reagents based on adeno-associated virus (AAV) do not allow viral replication. "This technique is very safe and can be used in a standard lab environment," O'Brien explains.

Therapeutic Challenges

The idea of transferring genes often leads to thinking about repairing genetic diseases. "If you look over the past 15 years or so, though, gene therapy has gone through a bit of a rough time," says Andrew Baker, professor of molecular medicine at the **University of Glasgow** in the United Kingdom. "There was an initial boom in the 1990s, but problems turned up regarding the safety of vectors." Today, some improved techniques might solve the safety issues that held back earlier approaches to gene therapies.

Baker focuses on adenovirus-based gene transfer. "The adenovirus family is very large, and there are some serotypes of adenovirus that are very rare," Baker says. "The more rare a serotype is, the more likely a patient will not have preexisting antibodies to it. That could make such a virus more useful in the clinical setting." Those rare adenoviruses, however, are sometimes the ones that researchers understand the least. "So we will need some basic studies to understand the biology of the virus as well as detailed safety studies," Baker says.

"The good news is that virus-mediated gene transfer is highly efficient—virtually 100 percent."

In addition, transfection used as therapy should not cause a patient's immune system to react. "The problem, though, with many vectors is that they do create an immune response—inflammatory issues or aberrant proliferation," says Stuart Naylor, chief scientific officer at **Oxford BioMedica** in the United Kingdom. Naylor and his colleagues focus on viral vectors. "We think they provide a gain in efficiency and work well for differentiated cell types," he says. But among viral vectors, clinical researchers must still pick from adenoviruses, adeno-associated viruses, and lentiviruses. "Adenoviruses are very immunogenic and perturb target cells in the dish or in man," says Naylor. "Adeno-associated viruses are less predictable in expression." He continues: "We use lentiviruses because of their larger cargo capacity and predictable kinetics of expression."

Some of Oxford BioMedica's gene therapies are already being tested. For example, ProSavin—a dopamine-replacement therapy intended for patients with Parkinson's disease—is in a clinical trial in France. This gene therapy gets injected directly into the striatum of the brain, where it converts cells into dopamine factories. It uses LentiVector, which is a lentiviral-based approach to gene-delivery technology that, Naylor says, was designed to overcome the problems associated with earlier generations of vector technology and can stably deliver genes. "So far, the clinical trials show that this approach is safe, and there are some signs in the subjects of dopaminergic activity," Naylor says.

The current range of research and medical science impacted by gene transfer is just the beginning. As more tools become available, even more basic researchers will find ways to put gene transfer to work. In addition, as medical scientists learn more about transfection vectors, additional clinical applications will emerge.

Mike May is a publishing consultant for science technology.

DOI: 10.1126/science.opms.p0900036

New Products

Transfection Device

The Neon Transfection device is a cost-effective benchtop tool for high-efficiency transfection of DNA and small interfering RNA into more than 150 different cell types, including very difficult to transfect cells such as primary cells, stem cells, and Jurkat cells. The device features a unique pipette tip transfection chamber designed to minimize cell death, open-program software for easy adjustment of transfection parameters, and an optimized reagent kit that works with all cell types.

Invitrogen, a division of Life Technologies
For information 650-638-6113
www.lifetech.com

Transfer Plasmids

A new range of transfer plasmids features unique signal sequences and promoters that increase cloning efficiency and expression of foreign genes. The pOET transfer plasmids have been designed to be smaller for improved cloning efficiency and ease of use. Both pOET-1 plasmids contain a large multiple cloning site (MCS), allowing foreign genes to be inserted in the correct orientation. Autographica californica multiple nuclear polyhedrosis virus (AcMNPV) sequences flanking the gene in the transfer plasmid's MCS allow recombination with FlashBAC DNA to insert the expression cassette into the polyhedron locus. In addition, pOET-1NTM has been designed for high-level expression of foreign genes fused to an N-terminal 6xHis tag, easing the purification of the recombinant protein. The pOET-1 is compatible with any baculovirus system that uses homologous recombination in insect cells.
Oxford Expression Technologies
For information +44-(0)-1865-483236
www.oetltd.com

DNA Isolation Kit

The BiOstic Bacteremia DNA Isolation Kit is optimized for the extraction of total DNA from cultured blood for the detection of bacteria. In the protocol, blood samples are inoculated into the BioMerieux BacT/Alert SA Culture Bottle for growth of potential pathogens. The kit removes the antibiotics in the sample and all inhibitors from the medium through patented inhibitor removal technology. The purity of the isolated DNA allows it to be used in sensitive detection assays, including Agilent BioAnalyzer assays for multiplex polymerase chain reaction (PCR) products and real-time PCR.
Mo Bio Laboratories
For information 800-606-6246
www.mobio.com

Sample Storage

The automated -20°C Sample Access Manager (SAM) is an affordable cold storage system for compounds and biological samples. The -20°C SAM ensures sample integrity by maintaining a precise storage environment at user-determined levels from +20°C to -40°C. Based on the technology behind Hamilton's -80°C storage system, the lower throughput, automated system offers sample format flexibility, cherry picking, sample tracking, and easy-to-use software, all within a compact footprint. The sample tracking software provides an audit trail and complete chain-of-custody documentation. The system's internal robotics are driven by patented external magnetic couplers to ensure consistent storage temperature and prevent sample degradation. The system can handle microplates or a variety of tube sizes and is suitable for the storage of nucleic acids, tissues, proteins, and compounds.
Hamilton Storage Technologies
For information 508-544-7000
www.hamilton-storage.com

Streptavidin Magnetic Beads

The Pierce Streptavidin Magnetic Beads are designed to streamline the isolation and purification of biotinylated biomolecules without columns or centrifugation. These superparamagnetic particles offer higher binding capacity and lower nonspecific binding than other commercially available magnetic beads, according to the manufacturer. They are validated and optimized for use with high throughput magnetic instrumentation, such as the Thermo Scientific KingFisher 96 and KingFisher Flex instruments. The particles also perform well in manual purification procedures. They can be stored refrigerated for one year.
Thermo Fisher Scientific
For information 815-968-0747
www.thermo.com/pierce

RNA Extraction

The QuickExtract RNA Extraction kit extracts RNA from cultured cells for reverse transcription polymerase chain reaction. The single-tube system requires only vortex mixing to lyse the cells and prepare the RNA for complementary DNA synthesis. The kit is free of toxic, organic solvents and is suitable for high throughput workflows. It has been tested on both mammalian and bacterial cell cultures.
Epicentre Biotechnologies
For information 800-284-8474
www.EpiBio.com

Electronically submit your new product description or product literature information! Go to **www.sciencemag.org/products/newproducts.dtl** for more information.

Newly offered instrumentation, apparatus, and laboratory materials of interest to researchers in all disciplines in academic, industrial, and governmental organizations are featured in this space. Emphasis is given to purpose, chief characteristics, and availabilty of products and materials. Endorsement by *Science* or AAAS of any products or materials mentioned is not implied. Additional information may be obtained from the manufacturer or supplier.

POSITIONS OPEN

ASSISTANT PROFESSOR

An accomplished scientist using biochemical, cellular, immunological, and/or molecular biology approaches to investigate human and animal infectious diseases and/or host response to infectious agents is sought for a tenure-track position (90 percent research, 10 percent instruction) in the Department of Veterinary Molecular Biology at Montana State University. We are seeking an individual to complement or expand existing expertise in the study of viral, protozoan, fungal, prion, and bacterial pathogens as well as host responses against these pathogens. This position is funded by a competitive institutional salary (nine months), technician support, and a generous startup package. The Department is housed in a state-of-the-art facility with core laboratories for flow cytometry, cell biology, and molecular sciences as well as pathogen containment facilities for small (BSL-3) and large animal research (ABSL-2). A doctoral degree in a biomolecular discipline and postdoctoral experience are required. The potential to establish or evidence of a competitive, independent research program is required. A completed application will include a letter of application, curriculum vitae, selected reprints, a summary statement concerning research plans and grant proposals, and three letters of reference to be sent to: **Chair, Search Committee, Veterinary Molecular Biology, Montana State University, Bozeman, MT 59717-3610.** Screening will begin August 3, 2009, and will continue until a suitable applicant is hired. For a full job description and additional information about our Department, visit **website: http://vmb.montana.edu.** To learn more about the position go to **website: http://www.montana.edu/cgi-bin/msuinfo/fpview/f/9866-2.** *ADA/Equal Opportunity/Affirmative Action/Veterans Preference.*

POSTDOCTORAL SCHOLAR. A Postdoctoral Scholar position in cardiovascular physiology research is available immediately in the Department of Physiology at Brody School of Medicine, East Carolina University in Greenville, North Carolina, in the laboratory of **Dr. David A. Tulis, F.A.H.A.,** Associate Professor. The overall research focus in our laboratory is vascular smooth muscle physiology and pathology. Specifically we are investigating molecular, cellular, and functional mechanisms that underlie abnormal growth of vascular smooth muscle as integral to cardiovascular disease and injury. Cyclic nucleotide signaling is of particular interest in these studies, as these events regulate a wide range of biological actions. Specific areas of study include elucidation of cyclic guanosine monophosphate–versus cyclic adenosine monophosphate–dependent processes, characterization of cyclic nucleotide-regulating systems, identification of downstream kinase events, analyses of matrix metalloproteinase and gap junction biology, and elucidation of the functional impact of these signals on vascular physiology. Experimental approaches include functional, molecular, cellular, and genetic assays and consist of whole animal models, in vitro cell culture, and ex vivo tissue explants. Salary and benefits will be commensurate with experience and in accordance with NIH guidelines. Women and minorities are encouraged to apply. Review of applications will begin immediately and will continue until the position is filled. Please visit **website: http://www.ecu.edu/cs-dhs/physiology/tulisd.cfm** for more information. Please send an updated curriculum vitae, a statement of research interests, and contact information for three references to **e-mail: tulisd@ecu.edu,** and include Postdoctoral Scholar in the Subject line.

POSTDOCTORAL POSITIONS available to study cytokinesis in a well-established model system, the trypanosomes. Research experience in molecular biology and cell biology is essential. Must have a recent Ph.D. degree. Send curriculum vitae and names and addresses of three references to: **Prof. C. C. Wang, Department of Pharmaceutical Chemistry, University of California, San Francisco, CA 94158-2280. Fax: 415-476-3382; e-mail: ccwang@cgl.ucsf.edu.**

POSITIONS OPEN

ENDOWED CHAIR IN CANCER BIOLOGY

The University of South Carolina (USC) in Columbia, South Carolina, in collaboration with the Medical University of South Carolina (MUSC) in Charleston, seeks applications and nominations for an Endowed Chair in Cancer Biology. The specific area of specialization is open, but preference will be given to individuals with interests in the action of anticancer agents. This position is sponsored by the South Carolina Centers of Economic Excellence Program (**website: http://www.sccoee.org/**) and resides within the South Carolina College of Pharmacy (**website: http://www.sccp.sc.edu/**). The successful candidate will be an established biomedical scientist who maintains a strong national and international research reputation, has a productive record of publications and extramural funding, and is qualified for a tenured appointment at the level of **FULL PROFESSOR.** The individual, as well as his/her laboratory, will be located on the Columbia campus of USC. Participation in professional and graduate education and maintenance of a nationally recognized, extramurally funded research program will be expected.

USC has undergone expansion of its biomedical research capabilities and has developed significant strength in basic investigations relating to cancer. This has been spearheaded by the university's Center for Colon Cancer Research (**website: http://www.cccr.sc.edu/**), which conducts interdisciplinary studies of the basic biology, epidemiology, detection, prevention, and therapy of colorectal cancer. MUSC is likewise experiencing rapid growth in its research environment, recently highlighted by the Hollings Cancer Center's being awarded National Cancer Institute designation (**website: http://hcc.musc.edu/**). State-of-the-art core research facilities exist at both institutions, fostering an atmosphere of collegiality and collaboration.

Interested candidates should submit curriculum vitae, statements of research interests and accomplishments, and the names of three references to: **Dr. Franklin G. Berger, Director, Center for Colon Cancer Research, Room 337 Sumwalt Building, University of South Carolina, Columbia, SC 29208. E-mail: berger@sc.edu.** Or submit to: **Dr. Kenneth Tew, Department of Cell and Molecular Pharmacology, Medical University of South Carolina, 173 Ashley Avenue, Charleston, SC 29425. E-mail: tewk@musc.edu.** Nominations are also welcome, and can be sent to one or both of these individuals. Review of applications will begin on August 1, 2009, and will continue until the position is filled.

The University of South Carolina and the Medical University of South Carolina are Affirmative Action/Equal Opportunity Employers.

Full-time **RESEARCH SCIENTIST** position available at Wright State University in the Department of Neuroscience, Cell Biology and Physiology. For consideration applicants are required to have a Ph.D. degree in biomedical sciences or a related field, experience with confocal microscopy and imaging analysis, and a track record using this instrumentation in the form of publications or communications to meetings. Preference will be given to candidates with additional experience with two-photon and/or electron microscopy and in managing a multiuser facility. Duties include maintaining an Olympus FV1000 two-photon microscope; training and supervising students and faculty; helping with administration and maintenance of all microscopes in the facility; involvement in searching for external funding. Applications are being reviewed starting June 15, 2009. Please send a cover letter, curriculum vitae, and names of three references electronically to **e-mail: jobs.wright.edu/applicants.** Position open until filled. *WSU is an Affirmative Action/Equal Opportunity Employer.*

Department of Health and Human Services
National Institutes of Health

National Eye Institute

Deputy Director

The National Eye Institute (NEI), a major component of the National Institutes of Health (NIH) and the Department of Health and Human Services (DHHS), is seeking exceptional candidates for the challenging position of Deputy Director, NEI. The NEI is responsible for a national and international program to conduct and support research, training, health information dissemination, and other programs with respect to blinding eye diseases, visual disorders, mechanisms of visual function, preservation of sight, and the special health problems and requirements of individuals who are visually impaired. These activities are conducted in hundreds of extramural laboratories and clinics throughout the United States and in NEI's own facilities in Bethesda, Maryland.

The Deputy Director, NEI, serves as second in command and principal advisor to the Director, NEI, in evaluating, planning, directing, and coordinating all activities related to the mission and function of the Institute, in the development and execution of policies, and in the allocation of resources to carry out these policies. On behalf of the Director, NEI, the Deputy Director represents the NEI in all matters and in this sense is the champion and guarantor for the intellectual and administrative envir onment at the Institute. The Deputy Director also serves as an ambassador and spokesperson for the Institute.

Applicants must possess a Ph.D., M.D., or equivalent doctorate degree in the biomedical sciences, with broad senior-level research experience and experience in direct administration of a research program. Applicants should be known and respected within their profession, both nationally and internationally, as distinguished individuals of outstanding scientific competence and administrative capability. Candidates should have demonstrated leadership; serving as a spokesperson; planning, program assessment, and analysis of program objectives; resolution of operational problems and issues; and the ability to manage financial and human resources including building, motivating, and maintaining a culturally diverse staff. Experience with NIH administrative policies, procedures, and operations is highly desirable but not essential. Salary is commensurate with experience and qualifications. Full Federal benefits are available including leave, health and life insurance, long-term care insurance, retirement, and retirement savings plan (401k equivalent).

Interested candidates should send a letter of interest, including a brief description of research and administrative experience, a curriculum vitae and bibliography, and the names of at least three references to: Chair, NEI Deputy Director Search Committee at **NEISearch@nei.nih.gov or 31 Center Drive, Room 6A03, 31 Center Drive, MSC 2510, Bethesda, MD 20892**. Applications should be received by **July 15, 2009**, and review of applications will begin soon thereafter, but applications will continue to be accepted and considered until the position is filled. For questions, contact **Dr. Paul A Sieving, Director, NEI, at paul.sieving@nih.gov**. Applicants are encouraged to browse the NEI Home Page at **http://www.nei.nih.gov/**.

NIMH
National Institute of Mental Health

Director, Division of Adult Translational Research and Treatment Development

The National Institute of Mental Health, a major research component of the National Institutes of Health (NIH) and the Department of Health and Human Services (DHHS), is seeking exceptional candidates for the position of Director, Division of Adult Translational Research and Treatment Development (DATR). This position provides overall scientific, programmatic, and administrative leadership for an extramural grants and contracts portfolio of approximately $250 million and manages a staff of 16 individuals (http://www.nimh.nih.gov/about/organization/datr/index.shtml). The DATR Director is responsible for developing a vision for research and training aimed at understanding the pathophysiology of mental illness and hastening the translation of behavioral science and neuroscience advances into innovations in clinical care and prevention strategies.

Applicants must possess an M.D. with a specialty in psychiatry and/or a Ph.D. in neuroscience, psychology, or related discipline with broad senior-level research experience and experience in direct administration of a research program. Applicants should be known and respected within their profession, both nationally and internationally, as distinguished individuals of outstanding scientific competence. Salary is commensurate with experience and accomplishments.

Interested candidates should send a letter of interest, including a brief description of research experience, contact information for at least three references, and a curriculum vitae and bibliography to: **Dr. Philip Wang, Chair, Search Committee for Director, DATR, at NIMHsearch@mail.nih.gov or at 6001 Executive Blvd. Room 8235, MSC 9669, Bethesda, MD 20892 (Rockville, MD 20852** for express or courier service). Review of applications will begin on June 22, 2009, but applications will continue to be accepted and considered until the position is filled.

NIEHS
National Institute of Environmental Health Sciences
National Institutes of Health

Chief, Toxicology Branch/Senior Scientist

Research Triangle Park, North Carolina

The National Institute of Environmental Health Sciences (NIEHS) of the National Institutes of Health (NIH) is seeking a dynamic, highly motivated scientist to serve as a Senior Scientist to oversee the operations of the Toxicology Branch (TB) of the National Toxicology Program (NTP). The Chief, TB, supervises senior scientists, staff scientists, and support staff who design, interpret, review, and report toxicology and carcinogenicity studies for substances studied by the NTP. As a senior official representing NTP, the Chief, TB, is the primary expert and interface on toxicology with many agencies and offices and provides guidance on relevant research, policy, and practices. He/she identifies, assesses, and integrates advancements in molecular and cellular techniques with traditional rodent toxicology testing methods.

To accomplish this, he/she builds strong relationships with intramural and extramural investigators to design and carry out studies that further our understanding of toxicological mechanisms. The Chief, TB, works with computational and bioinformatics scientists at NTP, NIEHS, and other institutes and agencies to organize data collection and analysis, works with NTP chemists to evaluate compounds, and works with other NTP staff to oversee the development of technical reports on study findings. He/she also evaluates and develops new methodologies and technologies for toxicology assessments, writes technical reports and prepares manuscripts in collaboration with investigators within and outside NTP. The training of NTP postdoctoral fellows to prepare outstanding future leaders in toxicological research is also a critical part of this position. Finally, the Chief, TB, develops collaborations and relationships with other agencies and institutes, including EPA, FDA, advocacy groups and industry coalitions.

Minimum qualifications include a Ph.D. or equivalent degree with research interests in a core toxicology discipline, and supervisory experience in managing other scientists in a toxicology laboratory or testing program. Experience in carrying out toxicology research and testing according to regulatory guidelines is desired. Salary will be commensurate with qualifications. To apply, submit a cover letter indicating interests, curriculum vitae and 3 letters of recommendation by **June 26, 2009** to:

Ms. Barbara Curtis (DIR09-01)
National Institutes of Health • National Institute of Environmental Health Sciences
P.O. Box 12233, Maildrop A2-06 • 111 Alexander Drive, Room A202
Research Triangle Park, NC 27709
e-mail: **dir-appls@niehs.nih.gov**
http://dir.niehs.nih.gov

DHHS and NIH are Equal Opportunity Employers

U.S. DEPARTMENT OF HEALTH AND HUMAN SERVICES
National Institutes of Health

Help Us Help Millions

Principal Deputy Director, Division of AIDS, NIAID, NIH, DHHS

The National Institute of Allergy and Infectious Diseases (NIAID) is seeking an exceptional and visionary leader for the position of principal deputy director in the Division of AIDS (DAIDS). The mission of DAIDS is to increase basic knowledge of the pathogenesis, natural history, and transmission of HIV disease and to support research that promotes progress in its detection, treatment, and prevention. DAIDS plans, implements, manages, and evaluates programs in fundamental basic research, discovery and development of therapies for HIV infection and its co-infections and complications, discovery and development of preventive vaccines, and development and evaluation of other biomedical strategies to prevent HIV and AIDS. DAIDS funds efforts through a comprehensive portfolio of research grants, cooperative agreements, and contracts, with a total annual budget of more than $1 billion.

The deputy shares responsibility with the director for providing overall scientific leadership and administrative management in planning, conducting, coordinating, and evaluating a global extramural research program focused on HIV/AIDS. The deputy serves as senior scientific advisor and key executive to the director and plays a lead role in coordinating DAIDS's research programs with internal and external stakeholders.

Qualifications: Applicants must possess an M.D. or Ph.D., have a strong science management background, and demonstrate extensive experience in 1) working both independently and collaboratively in planning, organizing, and conducting infectious disease research; 2) serving effectively in research program administration; and 3) effective communications and collaborations.

Application Information: Provide curriculum vitae, bibliography, and a three page summary explaining 1) your vision for HIV/AIDS research, 2) your reasons for being interested in the position, and 3) the specific leadership skills and experience you would bring to the HIV/AIDS research programs at NIAID.

Submit application package to Mr. Robert Gulakowski, Office of the Director, DAIDS, NIAID, 6700-B Rockledge Drive, Room 4143, Bethesda, Maryland 20892-7620 and reference announcement number DAIDS-09-02. All information provided by applicants will remain confidential and will be reviewed only by authorized NIAID officials.

NIAID

National Institute of Allergy and Infectious Diseases

Salary and Benefits: The successful candidate will be appointed under the Title 42(f) authority at a salary commensurate with experience. A full package of benefits is also available, including retirement; health, life, and long-term care insurance; annual and sick leave; and a thrift savings plan (401(k) equivalent). This position is subject to public financial disclosure requirements.

The deadline for receipt of applications is August 14, 2009.

Direct any inquiries to Mr. Gulakowski via e-mail at rgulakow@niaid.nih.gov or call 301-496-0545.

Additional information about working at NIAID can be found at **www.niaid.nih.gov/careers/pdd**.

U.S. DEPARTMENT OF HEALTH AND HUMAN SERVICES
National Institutes of Health

National Institute of Allergy and Infectious Diseases

Proud to be Equal Opportunity Employers

WWW.NIH.GOV

Help Us Help Millions

Director, Therapeutics Research Program, Division of AIDS, NIAID, NIH, DHHS

The National Institute of Allergy and Infectious Diseases (NIAID) is seeking an exceptional and visionary leader to be director of the Therapeutics Research Program in the Division of AIDS (DAIDS). The director plans, implements, and directs a global extramural research program, in excess of $120 million, for the preclinical development and clinical testing of therapies for HIV/AIDS and its associated co-infections and complications. This includes overseeing the largest collection of HIV/ AIDS therapeutic clinical trials networks in the world, which have an annual budget of more than $70 million and conduct all phases of clinical trials at research sites around the globe.

The director serves as a key scientific advisor to the directors of DAIDS and NIAID and ensures that the therapeutics research supported by DAIDS is integrated with and complements other programs in NIH, federal agencies, and external organizations conducting HIV/AIDS therapeutics research. The director formulates an overall scientific agenda for the development and clinical testing of therapeutic interventions, recommends resource allocation across competing initiatives, and continually assesses and reorients program priorities and activities, both anticipating and responding to changing research needs or redefined policies.

Qualifications: Applicants must possess an M.D. with board certification in internal medicine or infectious diseases and must demonstrate experience in 1) working both independently and collaboratively in planning, organizing, conducting, and/or overseeing clinical research in infectious diseases (experience in HIV/AIDS is a plus); 2) serving effectively in research program administration; and 3) effective communications and collaborations.

Application Information: Provide curriculum vitae, bibliography, and a three-page statement explaining 1) your vision for HIV/AIDS therapeutics research, 2) your reasons for being interested in the position, and 3) the specific leadership skills and experience you bring to the HIV/AIDS research programs at NIAID.

Submit your application package to Mr. Robert Gulakowski, Office of the Director, DAIDS, NIAID, 6700-B Rockledge Drive, Room 4143, Bethesda, Maryland 20892-7620, and reference announcement number DAIDS-09-01. All information provided by applicants will remain confidential and will be reviewed only by authorized NIAID officials.

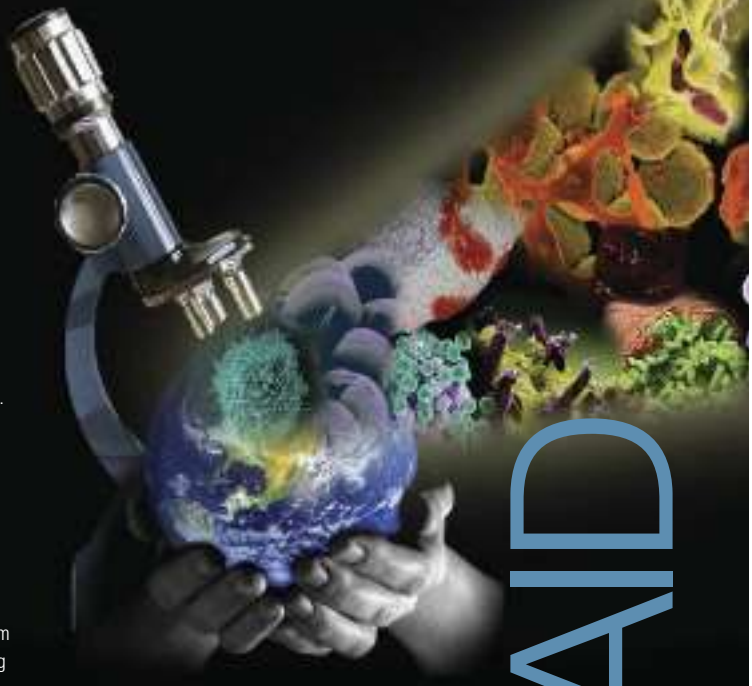

NIAID

National Institute of Allergy and Infectious Diseases

Salary and Benefits: The successful candidate will be appointed under the Title 42(f) authority at a salary commensurate with experience. A full package of benefits is available, including retirement; health, life, and long-term care insurance; annual and sick leave; and a thrift savings plan (401(k) equivalent). This position is subject to confidential financial disclosure requirements.

The deadline for receipt of applications is August 14, 2009.
Direct any inquiries to Mr. Gulakowski via e-mail at rgulakow@niaid.nih.gov or call 301-496-0545.

Additional information about working at NIAID can be found at **www.niaid.nih.gov/careers/pdd.**

U.S. DEPARTMENT OF HEALTH AND HUMAN SERVICES
National Institutes of Health

National Institute of Allergy and Infectious Diseases

Proud to be Equal Opportunity Employers

USDA ARS Agricultural Research Service
www.ars.usda.gov

"The premier food and agricultural research agency of USDA"

ASSISTANT AREA DIRECTOR

(Agricultural Administrator, GS-0401-15)

Pacific West Area Salary Range of $131,873.00 to $153,200.00
Midwest Area Salary Range of $111,760.00 to $145,290.00

Applications must be received by **July 21, 2009**

The USDA, Agricultural Research Service (ARS) is seeking highly qualified candidates for two permanent full-time leadership positions of Assistant Director for the Pacific West and Midwest Areas, located in Albany, California and Peoria, Illinois, respectively. The Assistant Director is a key member of a Senior Management Team that:

- Implements problem-solving research that provides an abundant, nutritious and safe food supply, protects the environment, and generates sustainable bioproducts and biofuels.
- Leads a large, talented cadre of scientists in an eight-state region.
- Works collaboratively with scientists and administrators within ARS, the Land-Grant Universities, State Agricultural Experiment Stations, other governmental agencies (Federal, state, local), Non-Governmental Organizations, private industry, and other stakeholder groups in the region, nation, and around the world.
- Manages human, fiscal and physical resources.

Candidates seeking a challenging leadership position that contributes to a secure and sustainable agricultural future are encouraged to apply. Applicants must have professional knowledge of research methods related to the biological sciences, environmental sciences, agricultural engineering, food technology or chemistry; knowledge of cooperative and user oriented programs directed toward agricultural research; and excellent leadership and communication skills.

Join us in Advancing the Health and Wealth of the Nation and Its Peoples, Solving Problems, Expanding Knowledge, Delivering Answers

To apply, print a copy of the vacancy announcement from the ARS Careers Website at **http://www.ars.usda.gov/Careers/Careers.htm** (Pacific West Area - **ARS-X9W-0188**) or (Midwest Area - **ARS-X9W-0194**) and follow the application directions provided. For questions about these positions, call **(510) 559-6015** (Pacific West Area) OR **(309) 681-6633** (Midwest Area).

USDA/ARS is an Equal Opportunity Employer and Provider.

CENTRAL DRUG RESEARCH INSTITUTE

(Council of Scientific & Industrial Research)
Chattar Manzil Palace, Lucknow-226001

Cancellation of Advt. No.2/2007 and 7/2008

It is notified for the information of all the candidates who have applied against the Advertisement No. 2/2007 of this Institute which appeared in the Employment News dated 13.05.07 that all the advertisement for the posts of Scientists Gr.(1) to Gr.IV(3) has been cancelled due to unavoidable reasons.

It is also notified that advertisement for the posts advertised vide Advertisement No.7/2008 which appeared in the Employment News dated 26.07.2008 have also been cancelled except that for technical Gr.III(1) post and the post of Scientists Gr.IV(1) reserved for PWD.

The notice is also available on our website **www.cdriindia.org**

Controller of Administration

UNIVERSITY OF LOUISVILLE

Assistant Professors, Tenure Track
The Department of Biochemistry and Molecular Biology

The Department of Biochemistry and Molecular Biology, University of Louisville, School of Medicine invites applications for two tenure-track positions at the Assistant Professor level. Our Department is under new leadership and we anticipate that several additional positions will be filled in the next 3 years. Thus, successful candidates will play vital roles in the future development of the Department. The Department of Biochemistry and Molecular Biology is part of a vibrant research environment on UofL's Health Sciences Campus, which houses the Schools of Medicine, Dentistry, Nursing, Public Health and Information Sciences. The Health Sciences Campus has experienced tremendous growth in funding over the past 10 years and has added 3 new research buildings.

Individuals with expertise in all areas of Biochemistry and Genetics are invited to apply. Those using comparative approaches with model organisms or human studies to understand disease processes are encouraged to apply. Candidates must hold a PhD, MD, DDS or equivalent degree and have a strong potential to maintain a productive research program. As part of an academic unit, successful candidates will also be expected to teach in graduate and either Medical or Dental Biochemistry courses. As new faculty, individuals will benefit from a competitive start-up package, customized laboratory space, and numerous opportunities for collaborative interactions with investigators focusing on cancer, cardiovascular disease, diabetes, obesity, embryonic development, aging, environmental health, and stem cell biology.

Applicants should send a single PDF file containing their research summary, curriculum vitae, and names with contact information of at least three individuals who may be contacted for letters of reference to **debbie.powell@louisville.edu** or by mail to: **Assistant Professor Search Committee, Department of Biochemistry and Molecular Biology, University of Louisville School of Medicine, Louisville, KY 40292**. Applicants must also apply on-line for **Job ID#24091** at **www.louisville.edu**. Application review will begin immediately and continue until the positions are filled. Applicants must be U.S. citizens, permanent residents, or have a valid H1B1 visa.

The University of Louisville is an Affirmative Action/Equal Opportunity Employer. Women and minorities are strongly encouraged to apply.

SOUTHWESTERN
THE UNIVERSITY OF TEXAS
SOUTHWESTERN MEDICAL CENTER
AT DALLAS

Faculty Positions in Infectious Diseases

The Division of Infectious Diseases in the Department of Internal Medicine at the University of Texas Southwestern (UTSW) Medical Center at Dallas is seeking new faculty members at the Assistant Professor level. Faculty will be expected to develop independent and externally funded research programs that focus on understanding the molecular pathogenesis of infectious diseases and/or host defense mechanisms. Preference will be given to applicants performing "cutting-edge" research on medically important pathogens, emerging pathogens, and/or agents of potential biothreat. Excellent opportunities exist for collaborations with faculty members in Infectious Diseases, the Department of Microbiology, and the Department of Immunology at UTSW and with the Regional Center of Excellence (RCE) for Biodefense and Emerging Infectious Diseases. UTSW is an outstanding scientific environment with established strengths in structural biology, biochemistry, molecular biology, genetics, and numerous other areas. Candidates will be expected to contribute to the teaching and research training of Infectious Diseases fellows. The positions offer attractive start-up packages and laboratory space. Candidates should have an M.D. and/or a Ph.D. degree with at least two years of postdoctoral experience and an outstanding publication record.

To apply, submit a C.V., three letters of reference, and a description of research interests to: **Dr. Beth Levine, Chief, Division of Infectious Diseases, UT Southwestern Medical Center, 5323 Harry Hines Blvd, Dallas, TX 75390-9113; E-mail: Cindy.Jozefiak@UTSouthwestern.edu**.

UT Southwestern is an Equal Opportunity/Affirmative Action Employer.

NORTHEASTERN OHIO UNIVERSITIES COLLEGES OF MEDICINE AND PHARMACY

announces a new endowed professorship

Ohio Research Scholar
Molecular and Cell Biology of Bone or Cartilage
Department of Anatomy and Neurobiology

The Ohio Research Scholar position presents an extraordinary opportunity for an outstanding scientist to lead a team of faculty researchers in the study of ***molecular and cell biology of bone or cartilage***. Research areas may include tissue engineering, medical applications of biopolymers, normal and abnormal skeletal development, orthopaedic diseases and cancer. There will also be substantial opportunities for the Ohio Research Scholar to translate research findings into clinical applications, intellectual property and economic development initiatives. The successful Scholar candidate will be an experienced and productive scientist and a capable faculty research team leader. She/he will have a record of sustained extramural funding and strong current funding and will interact with the members of a successful existing research collaboration focused on Skeletal Biology.

This position is generously supported through the Ohio Research Scholar Program, a program created by the State of Ohio that benefits from strong regional collaborative partnerships, including close arrangements with major hospitals and participation in a revolutionary initiative, the BioInnovation Institute in Akron. The Ohio Research Scholar Program requires that the Scholar be recruited from outside the State of Ohio.

For a full position description, please visit *http://www.neoucom.edu/job php?job=148*. Interested candidates should apply electronically using the link at the bottom of the position description page. Please include curriculum vitae, a statement of research interests and goals and the names of four references. For full consideration, application should be received by August 14, 2009.

Inquiries about the position may be directed to Jeffrey J. Wenstrup, Ph.D., Professor and Chair, Department of Anatomy and Neurobiology, at *jjw@neoucom.edu,* or to Walter E. Horton Jr., Ph.D., Professor of Anatomy and Vice President for Research, at *wehj@neoucom.edu.*

The Colleges' dedication to excellence is complemented by its strong commitment to building and sustaining a culturally diverse academic community. Individuals from historically underrepresented groups are encouraged to apply. NEOUCOM is an equal opportunity employer and educator.

Northeastern Ohio Universities
COLLEGES OF MEDICINE & PHARMACY

The NASA/Goddard Space Flight Center, Earth Sciences Division, is seeking applications for positions to support current and planned Decadal Survey satellite missions. Experimental scientists with expertise in instrument definition, design, development, or characterization related to the following focus areas are of special interest:

- Radar remote sensing of cloud processes and precipitation.
- Polarimetric instrumentation and design for measurements of aerosols and clouds.
- Lidar instruments for aerosols, tropospheric wind, and carbon dioxide profiles.
- Passive microwave instruments for cloud ice water path, soil moisture, sea surface salinity, and snow water content.
- Spectrometry, from the ultraviolet through the thermal infrared, for atmospheric chemistry and temperature profiles.
- Hyper-spectral and multi-spectral thermal imaging for carbon cycle and ecosystem studies, and hydrologic studies of evapotranspiration.
- Laser-based altimetry for calibration and validation of satellite measurements of sea ice and glacier.
- Sensor calibration and validation of optical and other instruments, particularly in the area of thermal sensor calibration and characterization to support critical long-term systemic measurements.

Applicant should have an advanced degree or equivalent experience. The position will be filled based on qualifications/experience.

To apply, please submit a curriculum vitae and a statement of interest of approximately 1000 words to **Ms. Emilie Rank**, email: **emilie.j.rank@nasa.gov**. For more information about position requirements and application procedures, please contact **Emilie Rank** by e-mail or call **(301) 614-5566**. For scientific questions, please contact **Dr. Franco Einaudi, Director of the Earth Sciences Division** at **(301) 614-5634**.

The Goddard Space Flight Center has and encourages a diverse work force. Equal Opportunity Employer.

EMORY UNIVERSITY SCHOOL OF MEDICINE

Chair, Department of Psychiatry and Behavioral Sciences

The Emory University School of Medicine is seeking a Chair of the Department of Psychiatry and Behavioral Sciences. The successful applicant will also serve as Director of Psychiatric and Behavioral Health Services, Emory Healthcare and Chief of the Psychiatry Section, The Emory Clinic. The School of Medicine, the Woodruff Health Sciences Center and Emory Healthcare all share an unprecedented agreement in vision, values, and goals, including a strong commitment to take a highly successful Department of Psychiatry to the next level of excellence.

Founded as an independent department in 1958, Psychiatry and Behavioral Sciences has emerged as one of the preeminent departments in the United States. It has expanded to over 150 faculty and is currently ranked #9 in NIH funding and #12 in clinical service delivery by US News and World Report. The Department is located throughout multiple sites in the Atlanta area, with many of its faculty world-renowned experts in the areas of affective disorders, anxiety disorders, neuroendocrinology, psychoneuroimmunology, neuroimaging and psychotherapy.

The next chair of the Department of Psychiatry and Behavioral Sciences will be an exceptional, currently funded, academic physician leader, with the proven values and skills needed to lead a highly successful research program, a large clinical enterprise, and extensive educational and training programs. He/she will expand the department's research efforts through strategic recruitments, as well as fostering development of existing faculty and promoting institutional collaborations through the Neuroscience Center. Applicants will have an MD or MD/PhD, be board certified in Psychiatry (or equivalent) and fellowship trained.

Korn/Ferry International is assisting Emory University with this important search. Please forward, as soon as possible, nominations of appropriate candidates to: **Glenn C. Davis, M.D. or Warren E. Ross, M.D., c/o Betsy Messina (betsy.messina@kornferry.com), Korn/Ferry International, 1835 Market Street, Suite 2000, Philadelphia, PA 19103.**

Emory University is an Affirmative Action/Equal Opportunity Employer. AA/EOE/ADA.

Memorial University Medical Center, Curtis & Elizabeth Anderson Cancer Institute is recruiting an outstanding scientist for the translational oncology research program.

This opportunity provides substantial support for an exceptional researcher (Ph.D., M.D., M.D./Ph.D. or equivalent) at the level of Assistant, Associate or Full Member (equivalent to assistant, Associate and full Professorships) who will conduct innovative, laboratory-based research and provide strong intellectual leadership in understanding, preventing, diagnosing or treating cancers. Our primary goal is to recruit an excellent scientist, and our secondary goal is to broaden the research base of the Department of Laboratory Oncology by recruiting an expert in an area not already well represented. Therefore, a strong record of scholarly contributions in one or more of the following fields is desirable, through not necessary: mouse models, epigenetics, cancer cell biology, systems biology or angiogenesis. A willingness to work in a collaborative environment is important. Appropriate resources are available to support the successful candidate.

Memorial Health University Medical Center (MHUMC) is a 530-bed tertiary care and teaching hospital located in Savannah, Georgia. MHUMC is one of two University hospitals associated with Mercer University School of Medicine (MUSM) for medical student education. Residency training programs exist in Medicine, Surgery, Obstetrics and Gynecology, Pediatrics, Radiology and Family Medicine. MHUMC and MUSM have started a new four-year medical school on the MHUMC campus in 2008. MHUMC was ranked among the top one hundred places to work by U. S. News and World Report for 2006 and 2007. MHUMC offers several disease management teams inclusive of translational researchers in oncology. In August 2006, MHUMC opened the William and Iffath Hoskins Center for Biomedical Research. This 60,000 sq. ft. building has 30,000 sq. ft. of new educational space and 30,000 sq. ft. devoted to research. The research space is devoted to laboratory research in the molecular genetics of human cancer. In addition, it houses the clinical research program at MHUMC. Our location in Savannah, GA provides access to world-renowned medical community and the exceptional cultural and recreational diversity of a sophisticated, small metropolitan area. Interested applicants should forward a copy of their C.V. and a letter of interest describing their academic interests to: **Frank Thayer, Manager, Executive and Physician Recruitment, Memorial University Medical Center, P.O. Box 23089, Savannah, GA 31403-3089; 912-350-8243; 877-693-5069 (Toll Free); 912-350-8541 (Fax); MDsearch@memorialhealth.com.**

Be One of Us.

MOUNT SINAI SCHOOL OF MEDICINE

Tenure Track Faculty Positions in Immunology

The Mount Sinai Immunology Institute is seeking outstanding scientists to develop rigorous independent research programs in basic or translational immunology. Applicants whose programs address inflammatory bowel disease, mucosal immunity, and intravital imaging are encouraged to apply. The Immunology Institute is a diverse, interactive group interested in basic and translational immunology and mechanisms of immune-mediated diseases, **www.iisinai.org**. Applicants may have an MD, PhD or MD/PhD degrees and may be appointed at the Assistant, Associate or Full Professor levels, at Mount Sinai School of Medicine with a generous start-up package.

Applicants should submit a CV, research plan and the names of three references to **Immunology Institute Faculty Search Committee, email: Zaida.Newman@mssm.edu.** Review of applications will begin **July 31, 2009**.

ECOLOGIST FACULTY POSITION FORDHAM UNIVERSITY

The Department of Biological Sciences of Fordham University invites applicants for a tenure-track faculty position in **animal ecology** and **conservation biology** at the **ASSISTANT PROFESSOR** level for **fall 2009**. The department has an active research program and provides excellent physical facilities, state-of-the-art equipment, start-up funds, and competitive salaries and benefits. Preference will be given to vertebrate ecologists interested in establishing research collaborations with the Wildlife Conservation Society. There are also research opportunities at Fordham's biological field station, the Louis Calder Center. We seek individuals who will establish a vigorous, extramurally funded research program. The successful candidate must have a Ph.D. and postdoctoral experience and is expected to teach at the undergraduate and graduate levels.

Applicants should submit a curriculum vitae and contact information for three references to: **Dr. William Thornhill, Chair, Department of Biological Sciences, Fordham University, 441 E. Fordham Road, Larkin Hall 160, Bronx, NY 10458** and/or by email (preferred) to **thornhill@fordham.edu**. Review of applications will begin immediately. The position will remain open until a suitable candidate is identified.

Fordham University is an independent, Catholic university in the Jesuit tradition that welcomes applications from men and women of all backgrounds. Fordham is an EOE.

NANYANG TECHNOLOGICAL UNIVERSITY

NANYANG ASSISTANT PROFESSORSHIP

Singapore's science and technology university, Nanyang Technological University, invites outstanding researchers and scholars to apply for appointments as Nanyang Assistant Professors. Up to 10 appointments will be made.

Successful candidates will

- Receive start-up research grants of up to S$1 million
- Enjoy attractive remuneration package and other benefits including assistance with accommodation
- Hold tenure track appointments and play lead roles in the university's new wave of multi-disciplinary, integrative research

Candidates should be within 10 years of gaining their PhD and ready for independent leadership of their own research groups.

For more details, please email to:
NanyangProfessorship@ntu.edu.sg

About the University

Nanyang Technological University, among the world's top 100 universities*, has made unprecedented research investments, emphasizing cutting-edge research and revolutionary technological innovations across multiple disciplines.

The University has already attracted world-leading researchers to its ranks. Take this opportunity to join one of the fastest-growing research universities and participate in the rapid rise of Asia, between India and China, linking East and West.

** Times Higher Education-QS World University Rankings 2008*

Application Period:

15 June 2009 - 15 September 2009, 11.59 pm (UTC/GMT + 8 hours)

Please note that only online applications will be accepted.

www.ntu.edu.sg/NAP

POSITIONS OPEN

ASSISTANT OR ASSOCIATE PROFESSOR
Center of Excellence for Infectious Diseases

The newly created Center of Excellence for Infectious Diseases at the Paul L. Foster School of Medicine, Texas Tech University Health Sciences Center, El Paso, Texas, is seeking candidates for tenure-track faculty positions at Assistant or Associate Professor level. This is part of a state-funded initiative to enhance research in infectious diseases. The Center is primarily interested in investigators with research interests in molecular immunology, host-pathogen interactions, vaccine development, and animal models for translational studies.

Successful candidates are expected to develop and maintain independently funded research programs in infectious diseases or a related field. The position reports to the co-directors of the Center of Excellence for Infectious Diseases.

Minimum qualifications: M.D. or Ph.D. degree in a related field and at least three years of postdoctoral experience with a strong publication record.

Preferred qualifications: Candidates with funded grant support and experience in emerging infectious diseases and cutting edge technologies are particularly encouraged to apply.

The Center offers competitive salary and startup packages, newly constructed laboratory space, BSL-2 and BSL-3 laboratories, and a supportive interactive environment. Interested candidates must apply online at **website: http://jobs.texastech.edu, requisition #77147** by submitting curriculum vitae, a short write-up of research interests, and three letters of recommendation. For further information, please e-mail or contact:

Manjunath Swamy, M.D.
E-mail: manjunath.swamy@ttuhsc.edu or
Premlata Shankar, M.D.
E-mail: premlata.shankar@ttuhsc.edu
Co-Directors of the Center of Excellence for Infectious Diseases

The positions are open until filled. Application review will begin immediately.

Texas Tech University Health Sciences Center is an Equal Opportunity/Affirmative Action Employer.

The College of Sciences and Mathematics at Auburn University located in Auburn, Alabama, (**website: http://www.auburn.edu/cosam**) is seeking candidates for the position of **POSTDOCTORAL FELLOW** in the sciences and mathematics. From time to time, postdoctoral positions become available under a variety of research grants and projects in the college. We are seeking applications from individuals with a Ph.D. in any one area such as: biology, chemistry, geology, geography, mathematics, statistics, physics, or related fields. The candidates selected for these positions must be able to meet eligibility requirements to work in the United States at the time appointment is scheduled to begin and continue working legally for the proposed term of employment; excellent communication skills required. The positions are available for a minimum of one year as full-time, 12-month with renewal possible. Salary will be commensurate with education and experience. Review of applications will begin after July 1, 2009, and continue throughout the year as positions become available. Please send curriculum vitae, statement of research interests, along with a list of three references and contact information to: **Dr. Marie Wooten, Associate Dean for Research, College of Sciences and Mathematics, 315 Roosevelt Concourse, Auburn University, AL 36849. E-mail: adcocba@auburn.edu; fax: 334-844-5525.** *Minorities and women are encouraged to apply. Auburn University is an Affirmative Action/Equal Opportunity Employer.*

POSITIONS OPEN

ENDOWED CHAIR IN PHARMACOLOGY/CHEMICAL BIOLOGY/ MEDICINAL CHEMISTRY

The University of South Carolina (USC) in Columbia, South Carolina, and the Medical University of South Carolina (MUSC) in Charleston are jointly seeking applications and nominations for an endowed chair to be located at either campus. Individuals with demonstrated expertise in the areas of pharmacology, chemical biology, or medicinal chemistry are encouraged to apply. The successful candidate will be an established scientist who has a strong reputation in research, has a productive record of publication and extramural funding, and is qualified for a tenured appointment at the level of **FULL PROFESSOR.** The chair holder will play a key role in the growth and development of research and drug discovery in the state of South Carolina. He/she will be expected to participate in professional and graduate education and to maintain a nationally recognized, extramurally funded research program.

USC and MUSC have several centers of economic excellence, including the Centers for Drug Discovery and Cancer Therapeutics, and are continuing a period of rapid growth in research. State-of-the-art research cores and facilities exist at both institutions, fostering a variety of collaborative research efforts and interactions.

Interested candidates should submit curriculum vitae, statements of research interests and accomplishments, and the names of three references to: **Dr. Charles D. Smith, Department of Pharmaceutical and Biomedical Sciences, Medical University of South Carolina, MSC 140, Charleston, SC 29425. E-mail: smithchd@musc.edu.** Nominations are also welcome. Review of applications will begin on August 1, 2009, and will continue until the position is filled.

The University of South Carolina and the Medical University of South Carolina are Affirmative Action/Equal Opportunity Employers.

The Center for Genomics and Bioinformatics (CGB) at Indiana University, Bloomington, carries out independent research in the fields of functional genomics, environmental toxicology, ecology, and evolution. The CGB has recently acquired an Illumina sequencer to partner with its Roche Titanium sequencer. We seek a **BIOINFORMATICS STAFF SCIENTIST** (at the level of **RESEARCH ASSOCIATE**) to handle the data from these platforms and to develop programs to analyze the data.

The ideal candidate will have strong programming skills in PERL, C++ and possibly Java. Understanding of basic biological language would be an asset. Ability to design and develop algorithms would also be highly preferred. We require a Master's degree in computer science or equivalent. For more details, visit our **website: http://cgb.indiana.edu/careers/.**

Applications received by June 15, 2009, will be assured full consideration for an immediate start date. Send questions to **e-mail: job@cgb.indiana.edu.** Submit curriculum vitae and a description of your background and interests and have three letters of recommendation sent to: **Bioinformatics Staff Scientist CGB-015, Center for Genomics and Bioinformatics, Indiana University, 1001 E. Third Street, Bloomington, IN 47405.**

Indiana University is an Affirmative Action/Equal Opportunity Employer.

POSTDOCTORAL/RESEARCH ASSOCIATE POSITIONS are available in the area of mechanism-based cancer prevention using plant-derived compounds and molecular mechanism of metal carcinogenesis in the laboratory of **Xianglin Shi,** Graduate Center for Toxicology, University of Kentucky. Send curriculum vitae to **e-mail: xianglin.shi@uky.edu.**

POSITIONS OPEN

COLLABORATIVE POSTDOCTORAL POSITION
Biological Modeling
California State University, Los Angeles and California Institute of Technology

A Postdoctoral position is open immediately to study the dynamics of layered biological systems with specific applications to the ecology of mussel beds. A Ph.D. is required. Candidates should have experience using mathematical modeling and computer simulation to study biological problems. Knowledge of cellular automata and spatial statistics is desired. Opportunities exist to collaborate with field ecologists and to gain teaching experience. Salary is $42,000 per year plus benefits, renewable for up to three years. The position is a joint appointment between California State University at Los Angeles and California Institute of Technology. Inquiries and applications (cover letter, curriculum vitae, and three references) to: **Dr. Robert Desharnais, Biological Sciences, California State University, 5151 State University Drive, Los Angeles, CA 90032. E-mail: rdeshar@calstatela.edu.** *California State University, Los Angeles UAS is an Affirmative Action/Equal Opportunity Employer.*

ASSISTANT PROGRAM DIRECTOR, Environment Program. Apply principles of biological sciences to provide scientific research management, interpretation, and communication working closely with organization members and Health and Environment Program managers to do the following: manage complex scientific projects, interpret and communicate results effectively to a wide array of technical and non-technical audiences for scientific, policy, and educational purposes, and design studies to produce scientific results collaboratively with the association's technological, communications, and marketing programs. Resumes to: **Raquel Jimenez, International Copper Association, Ltd., 260 Madison Avenue, 16th Floor, New York, NY 10016.**

MARKETPLACE

Choo-Choo Cloning® Kit

PCR cloning for Dummies

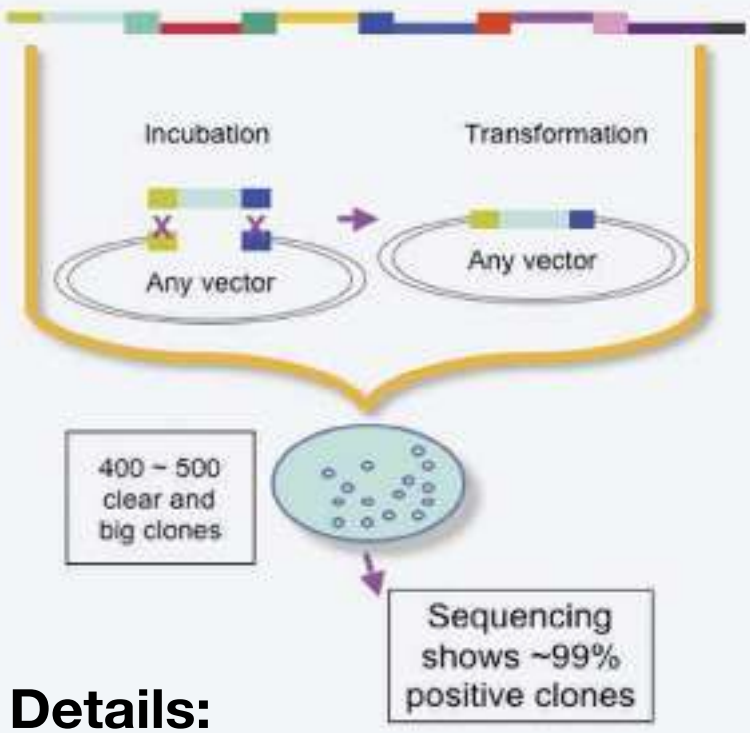

MCLAB
www.mclab.com

Now everyone can clone with confidence.

MCLAB offers a revolutionary way to do cloning/subcloning at a 99% rate of accuracy. You can get guaranteed clones in a day!

Details:

- *Simple protocol*
- *Directional cloning*
- *No vector limitations, restrictive digestion, or ligation*
- *Multiple fragments (up to 8 pieces)*
- *Broad PCR size up to 10kb*
- *Compatible for adaptor, linker and tag addition before and after the inserts*

MCLAB also provides custom cloning services as low as $250.00 per clone

384 Oyster Point Boulevard | South San Francisco, CA 94080 USA | Tel: (650) 872-0245 | Fax: (650) 872-0253
www.mclab.com

FROM START TO FINISH, ENDNOTE X3 KEEPS YOUR RESEARCH ON THE FAST TRACK.

Download your free demo or buy online today
www.endnote.com

With its world-class speed and track record, EndNote X3 puts your publishing in the lead and keeps you there. Out of the blocks with new features like faster start up times and seasoned favorites like our Cite While You Write™ technology, EndNote X3 is moving fast to deliver the world's most complete bibliographic solution.

It doesn't stop there. EndNote X3 is also meters ahead with a personal EndNote Web account that not only transfers groups swiftly between desktop and Web but also organizes your own publication list for the ResearcherID author community. You'll find new speed in Cite While You Write for Apple® Pages '09, Microsoft® Word, and now OpenOffice.org Writer 3 for Windows. EndNote X3 even sports new options for chemistry styles, multiple bibliographies within a Word document, and more.

Keep the lead, right to the finish line. Put EndNote X3 on your reference team today!

800-722-1227 • 760-438-5526 • rs.info@thomson.com

THOMSON REUTERS